Any Old Iron? – Astrochemical Modelling Of Star-Forming Regions At Low Metallicity

A thesis submitted to The University of Manchester for the degree of
Doctor of Philosophy
in the Faculty of Engineering and Physical Sciences

2010

Nadya Kunawicz
Jodrell Bank Centre for Astrophysics
School of Physics and Astronomy

Contents

List of Figures

List of Tables

The University of Manchester

ABSTRACT OF THESIS submitted by Nadya Kunawicz
for the Degree of Doctor of Philosophy and entitled
Chemical Modelling Of Extragalactic Regions September 2010

Two pseudo-time-dependent chemical models have been utilised – one of a dark cloud, and one of a hot core – in order to model these clouds in low metallicity environments, such as other galaxies. The dark cloud model uses gas-phase chemistry, whereas the hot core model includes both gas-phase and surface chemistry. The simulations have been calculated with varying initial elemental abundances of C, O, N, S and the heavy metals Fe, Mg and Na (henceforth, M). These initial abundances are taken from observations of HII regions in the Galaxy, the Large Magellanic Cloud and the Small Magellanic Cloud. The results have been used to identify species which potentially trace the underlying metallicity in dark clouds and hot cores. In the dark cloud models, the most useful tracers are ratios of two species, notably CO/OH and HCO^+/CO, which trace the underlying C and M abundances respectively. In the hot core models, the most useful metallicity tracer species are HNC and NH_3. The HNC abundance traces an underlying change in metallicity, independent of any changes to the dust/gas ratio. The NH_3 abundance traces the underlying N abundance.

The hot core model output abundances were used with RATRAN, a non-LTE radiative transfer code, to predict the integrated intensity as a function of hot core radius for various species. The RATRAN results are more directly comparable with observations than the results from the chemical models. Less common isotopes have been used to limit the optical depth of the species modelled. The results show that the extent of the emission may not reflect the size of the hot core. $HN^{13}C$ and NH_3 are confirmed as the most useful metallicity tracer species in hot cores.

Declaration

I declare that no portion of the work referred to in the thesis has been submitted in support of an application for another degree or qualification of this or any other university or other institute of learning.

Copyright Statement

(i) The author of this thesis (including any appendices and/or schedules to this thesis) owns certain copyright or related rights in it (the “Copyright”) amd she has given The University of Manchester certain rights to use such Copyright, including for administrative purposes.

(ii) Copies of this thesis, either in full or in extracts and whether in hard or electronic copy, may be made **only** in accordance with the Copyright, Designs and Patent Act 1988 (as amended) and regulations issued under it or, where appropriate, in accordance with licensing agreements which the University has from time to time. This page must form part of any such copies made.

(iii) The ownership of certain Copyright, patents, designs, trade marks and other intellectual property (the “Intellectual Property”) and any reporductions of copyright works in the thesis, for example graphs and tables (“Reproductions”), which may be described in this thesis, may not be owned by the author and may be owned by thirs parties. Such Intellectual Property and Reproductions cannot and must not be made available for use without the prior written permission of the owner(s) of the relevant Intellectual Property and /or Reproductions.

(iv) Further information on the conditions under which disclosure, publication and commercialisation of this thesis, the Copyright and any Intellectual Property and/or Reproductions described in it may take place is available in the University IP Policy (see http://www.campus.manchester.ac.uk/medialibrary/policies/intellectual-property.pdf), in any relevant Thesis restriction declarations deposited in the University Library, The University Library’s regulations (see http://www.manchester.ac.uk/libra and in The University’s policy on presentation of Theses.

Dedication

To my parents.

Acknowledgements

This thesis was typeset with LaTeX. I would like to thank Gary Fuller for all his fantastic help – without him, this thesis would not exist. I would like to thank Paul Woods, Estelle Bayet, David Tideswell and Andrew Markwick for their help with my work. I would like to thank Nicky for putting up with me on a daily basis. I would like to thank Mum, Dad, Sonya, Alex and Angela for all the family-based fun! I would like to thank Lyshia and Roisin for being awesome and never letting me give up. I would like to thank David, Danny and Stewart for fun, office-based hijinks. I would like to thank Mini and Ginger for being the best Jens I have ever met. I would like to thank Beckie and JB for giving me something to look forward to (their wedding!) during the long days of writing-up. I would like to thank all my friends in general for keeping me sane, or as sane as I ever was.

Supporting Publications

Dark cloud chemistry at low metallicity.

Nadya Kunawicz, Paul Woods and Andrew Markwick. In prep.

Chemical and radiative transfer modelling of hot cores at low metallicity.

Nadya Kunawicz, Gary Fuller and Estelle Bayet. In prep.

1

Introduction

1.1 Star Formation

Low-mass star formation is a reasonably well understood process. A cold, dark cloud of gas and dust collapses to form a low mass star. Figure 1.1 shows the key stages of this process. Figure 1.1 also shows what are thought to be the key stages in high mass and massive cluster star formation. The exact processes which occur in these types of star formation are unclear, as the formation of high-mass stars and massive clusters is not well understood. Newly-formed massive stars are shrouded in giant molecular clouds of gas and dust, and cannot be observed directly until this gas has been blown away by stellar winds.

Two stages of the star formation process are modelled in this thesis. Dark clouds, in which low mass stars form, and hot cores, which surround massive protostars. These regions are discussed in more detail in Sections 1.1.1 and 1.1.2 respectively.

1.1.1 Dark Clouds

Dark clouds mostly consist of gas-phase molecular hydrogen. They have a high density (e.g. $n(H_2)=10^5$ cm^{-3} – Hirota et al. 2003), a low temperature (e.g. 10K – Dickens et al. 2000) and a reasonably high visual extinction (e.g. 15 magnitudes in the cloud centre –

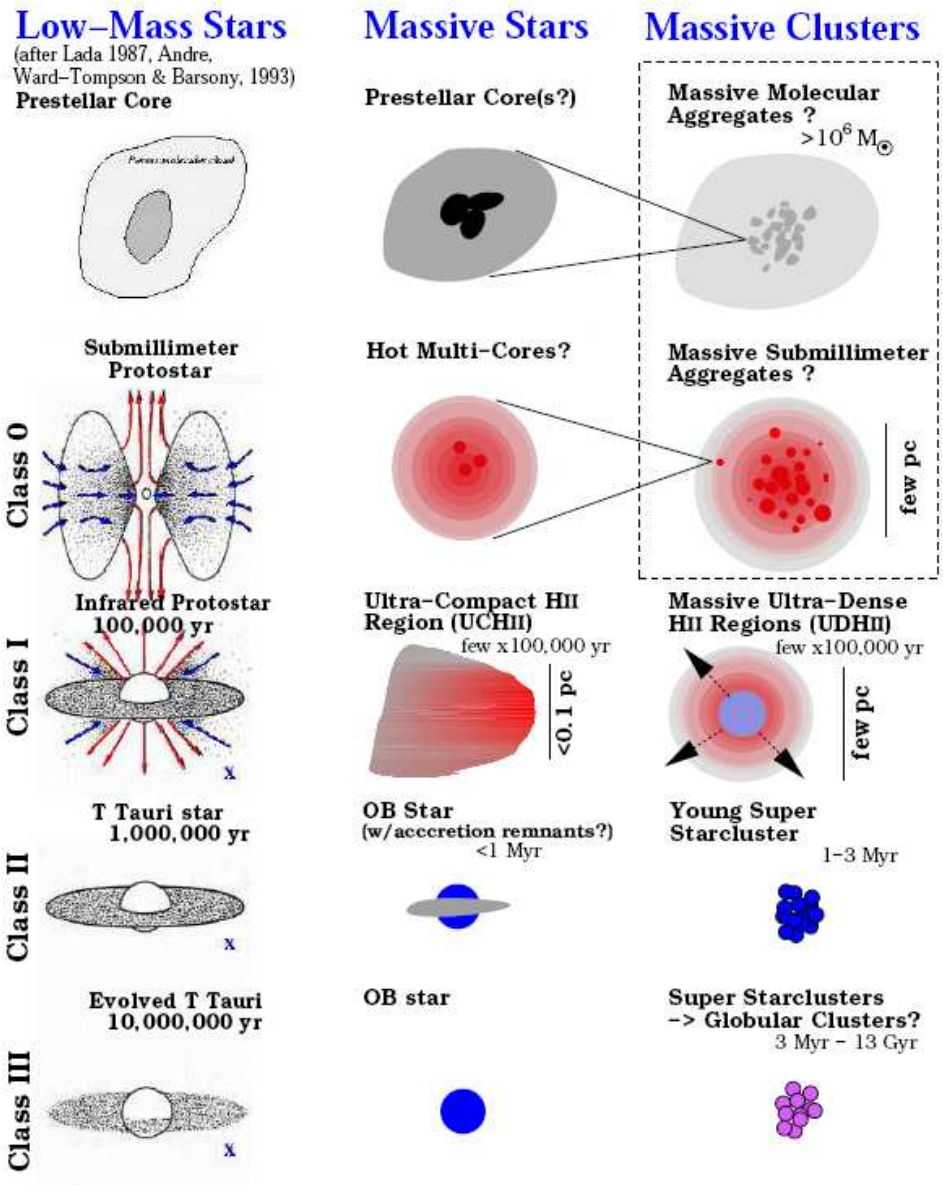

Figure 1.1: A diagram showing the suggested key stages in low mass, high mass and speculations about massive cluster star formation. This figure was taken from Kobulnicky & Johnson (2000).

Alves et al. 1999) which prevents photoreactions occurring within the region on a large scale. Dark clouds contain small quantities of elements heavier than hydrogen, such as helium, oxygen, carbon, nitrogen and sulphur (Caselli, 2005). These elements react with the hydrogen and with each other, to form various molecules, ions and radicals. It should also be noted that dark clouds contain dust grains, which are important in a number of ways. They provide shielding from UV photons for the chemical species in the cloud. They are a catalyst and formation site for some reactions, most notably the formation of H_2 molecules from atomic H. The scope of this thesis does not include the composition or formation of dust grains - they are regarded as simple surfaces on which reactions can occur. The low temperatures typical in a dark cloud also see the deposition of some species onto the dust grains, known as 'freezing out'. The species which freeze out are able to form a mantle on a dust grain - basically a layer of solid material is precipitated from the gas phase onto the grain. Dark clouds undergo gravitational collapse, resulting in the formation of low mass stars.

1.1.2 Hot Cores

Giant molecular clouds are similar in composition to a dark cloud, but they are much larger, with typical masses $>10^4 M_\odot$ (Brandner et al. 2008; Dowell et al. 2008). Hot cores typically have H_2 densities $>10^7$ cm^{-3} and gas temperatures >100K (Caselli, 2005). Hot cores are thought to form when a very dense clump within a giant molecular cloud collapses to form a massive protostar. A hot core is a spherical shell of gas which surrounds a newly formed massive star. In this thesis, a hot core is defined to have an inner radius of 1.31×10^{-3} pc from the protostar, and an outer radius of 1.12×10^{-1} pc. Hot cores have a temperature gradient, as the central protostar heats up the hot core from the inner regions outwards. The cloud collapse which forms the star results in a density gradient, where the inner hot core regions are more dense than the outer regions. The visual extinction in a hot core changes with the density, and is typically hundreds of magnitudes in the inner regions (Millar et al., 1997b). As hot cores form

from giant molecular clouds, they have a similar underlying chemical composition to dark clouds. Thus, hot cores are predominantly made up of molecular hydrogen with trace abundances of heavier elements. Hot cores have a more complex chemistry than dark clouds, as the higher temperatures sublimate the dust grain mantle species. A rich chemistry evolves on the dust grain surfaces, and when the grain species are desorbed, this chemistry is transferred to the gas phase, where it can be observed (van der Tak, 2004). Greater quantities of small, saturated species (e.g. NH_3) and complex species (e.g. CH_3CCH) are observed in hot cores than in dark clouds (Millar et al., 1997b).

1.1.3 Star Formation at Low Metallicity

In astrophysical terms, a metal is any element heavier than helium. In this thesis, the term 'metallicity' is used to describe the underlying elemental abundance of metals (specifically oxygen, carbon, nitrogen, sulphur, and the heavy metals: Mg, Fe and Na) within a region. Some authors define metallicity as the underlying fractional abundance of iron, [Fe/H], in a region. However, that definition does not apply to the work in this thesis.

The metallicity of a region can be used to examine how evolved that region is, in terms of cosmological timescales. When star formation began, in the early universe, the proportion of metals was virtually non-existent. Over billions of years, repeated cycles of star formation slowly enriched galaxies with metallic elements, which were formed in stars. New facilities, such as ALMA, will enable the observation of star-forming regions within high-redshift galaxies at an unprecedented level of detail. The aim of this thesis is to model such regions of low metallicity, in order that the model results can be compared with ALMA observations in the near future. The desired outcome is an increased understanding of star formation over cosmological time scales. Star-forming regions in the Large and Small Magellanic Clouds have been modelled as part of this thesis, as these dwarf galaxies provide observable examples of what star formation in a low metallicity galaxy may look like.

1.2 Chemical Modelling of Star-Forming Regions

1.2.1 Chemical Models of Dark Clouds

Computational models of the chemistry which occurs within a dark cloud were first built during the 1970s (e.g. Herbst & Klemperer 1973, Allen & Robinson 1977). Dark cloud models can be split into two types: steady state models and pseudo-time-dependent models. Figure 1.2 shows the chemical evolution of a typical species, and how it can be divided into 'early time' and 'steady state'.

The first models built were steady state models. These models are used to look at the end point of a dark cloud's chemical evolution - when the reactions have reached equilibrium and no changes in the concentrations of the various species occur. Steady state models are created by assuming the formation and destruction rates of all species are equal (e.g. Herbst & Klemperer 1973, Watt 1985).

Time dependent models are used to look at the evolution of a dark cloud during both early time and steady state. These models are created using differential equations to calculate the changing formation and destruction rates of all the species in the model, with respect to time (e.g. Herbst & Leung 1986, Millar & Nejad 1985). The model is based around a network of the (important) reactions which take place within a typical molecular cloud. An example of such a reaction network can be seen in Figure 1.3. Elemental abundances, reaction rates, and other physical parameters (e.g. temperature, density, cosmic ray ionisation rate) are entered into the model, to simulate the conditions of a dark cloud. Results can be produced for the abundances of all species at each time step looked at by the model. It should be noted that pseudo-time-dependent models are an approximation to truly time dependent models. The physical conditions under which the chemistry evolves in these models are held constant - in reality, it is likely these conditions would change with time (Millar et al. 1987, Wakelam et al. 2006).

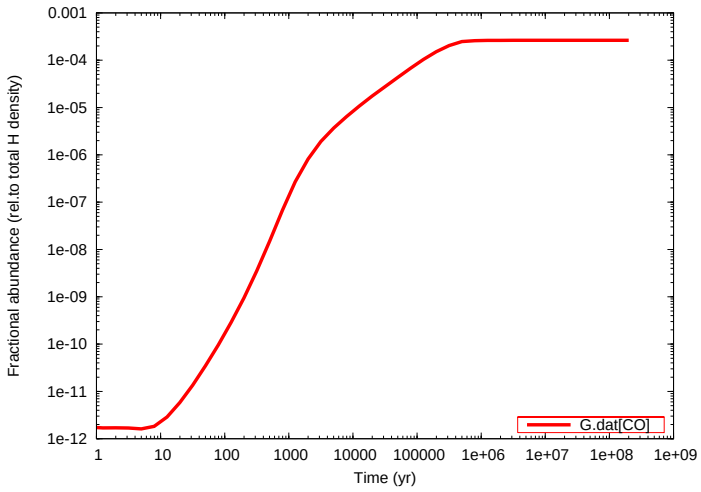

Figure 1.2: This graph demonstrates the concept of early time (up to approximately 10^6 years) and steady state (from 10^6 years onwards) chemistry. At early time, the graph shows a changing abundance of CO. At steady state the graph shows a constant amount of CO, as the cloud has reached a chemical equilibrium. The results shown are taken from a dark cloud model used in this thesis.

Steady State Models

The chemical modelling of a dense cloud was first attempted by Herbst & Klemperer (1973). Gas-phase reactions were considered the most important to the evolution of the cloud, as it was believed that grain surface chemistry would be subject to comparatively slow rates of reaction, which would only lead to negligible effects on the final concentrations of species. The exception to this was the reaction which forms H_2 from atomic hydrogen, which was assumed to take place on dust grains. The Herbst & Klemperer (1973) model was used to produce steady state abundances for polyatomic molecules, which could then be compared with observations in order to test the accuracy of the model.

It was assumed that the reaction networks in dense clouds begin with a cosmic ray ionisation of either H_2 of He. Other assumptions included:

- All neutral hydrogen was in the form of H_2, and almost all carbon was in the form of the CO molecule

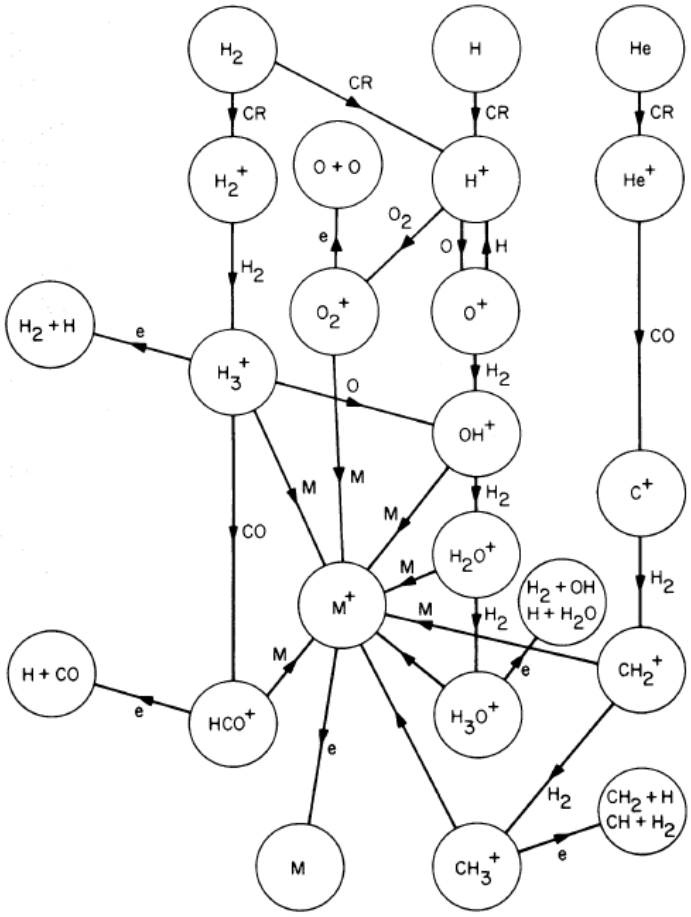

Figure 1.3: A reaction network for a dark, molecular cloud. Note that this is a simplified network, so all heavy metals (e.g. Mg, Na, Ca and Fe) are denoted as M. This figure was taken from Oppenheimer & Dalgarno (1974).

- The high density of the clouds led to a high visual extinction, which prevented photoreactions occurring within the clouds
- All reactions involved a maximum of two bodies, due to the low cloud density precluding reactions with more than two bodies
- The low temperatures (10K<T<50K) meant that only exothermic reactions were energetically feasible
- Exothermic reactions with an activation barrier were not permitted, as the low temperatures would not supply the energy needed to start the reaction

The Herbst & Klemperer (1973) model was a steady state model, which greatly simplified the numerical analysis of the differential equations used to calculate the species abundances. At steady state, the rate of formation of a species is equal to the rate of destruction of the same species. The authors noted that the steady state assumption only produces valid results if the time taken for the chemistry to reach equilibrium is shorter than the cloud lifetime. The authors calculated a steady state timescale for various species, and found that the cloud lifetime/collapse time was at least an order of magnitude longer than the time taken to achieve steady state. It was surmised that the model produced valid results. Comparison with observations from dark clouds and HII regions showed that the model results provided a reasonable estimate for the observed results.

The Herbst & Klemperer (1973) paper provided an excellent basis for much of the work which has been done today in the area of dark cloud chemical models. However, there are a number of aspects of the model which are now seen to be outdated in light of new observations, experimental evidence, and theoretical calculations. One example of this is the production of the NH_4^+ ion, via Reaction 1.1.

$$NH_3^+ + H_2 \rightarrow NH_4^+ + H \tag{1.1}$$

This reaction was thought to have such a low reaction rate that it could be considered negligible. In more recent models (e.g. Langer & Graedel 1989) it has been accepted that the rate of reaction for equation 1.1 increases as temperature decreases, and that it is key in the production of molecular NH_3. Herbst & Klemperer (1973) assumed that the role of dust grains in the cloud was limited to acting as a catalyst for the production of H_2 molecules from atomic hydrogen, as well as providing shielding from external photons which would affect the overall chemistry of the cloud. However, it has more recently been accepted that dust grains play a more central role in the cloud chemistry (e.g. Allen & Robinson 1977; Hasegawa et al. 1992; Shalabiea 2001). It was also stated by Herbst & Klemperer (1973) that, "The species CH^+ is an unimportant species in dense clouds; thus, its reactions will not affect our present results." A number of

authors (e.g. Watt 1985) have since disagreed with this assertion.

Watt (1985) used extremely similar assumptions to Herbst & Klemperer (1973), in order to create a dense cloud chemical model. This was used to investigate the effect of varying the initial C/O ratio on the steady state abundances of the species considered. The initial abundances used in the model were obtained from solar observations. A restricted reaction network was considered, as this greatly reduced the model run time. A range of C/O ratios from 0.1 to 2 were considered. In order to determine the ratios, the atomic carbon abundance was maintained at the solar value and the C/O ratio was thus obtained by varying the oxygen abundance. Watt (1985) noted that for C/O<1 (an oxygen-rich environment), almost all of the C was tied up in CO. The excess O abundance led to the production of such species as O_2, OH and H_2O. This result was reproduced by Millar & Herbst (1990) in their attempt to model dark clouds within the Large and Small Magellanic Clouds. Watt (1985) also showed that for C/O>1 (a carbon rich environment), the excess of C atoms resulted in CH_n species being formed. Watt (1985) used the CH^+ ion in the chemical network as a pathway to form carbon hydrides, such as CH, CH_2, CH_3 and CH_4. These carbon-chain reactions were crucial to the steady state abundances produced in the Watt (1985) model.

Pseudo-Time-Dependent Models

Herbst & Leung (1986) used a pseudo-time-dependent model of a dense cloud to investigate a number of different scenarios in which such a cloud could exist, in order to examine the varying chemistries which could evolve under these different conditions. The scenarios were:

1. Model 1: This model was based on a dense cloud model from a previous paper (Leung et al., 1984) - with updated rate coefficients taken from laboratory measurements. The following models were all based on this model.

2. Model 2: This model had a lowered visual extinction, which allowed some

photoreactions to occur within the cloud.

3. Model 3: This model had an increased temperature - from 10K up to 50K. This affected some of the reaction-rate coefficients, which were inversely proportional to temperature. The temperature increase caused the reaction rates to decrease.

4. Model 4: This model was carbon rich (e.g. C/O>1)

5. Model 5: This model had conditions which were somewhere between those of a diffuse cloud and a dense cloud. Compared with model 1, this included a lower density, a higher temperature, and a much-reduced visual extinction.

The results obtained from these models were intended to shed light on the various ways in which the initial physical/chemical conditions of a cloud can affect the resulting chemistry, at both early time and steady state. The steady state abundances of complex molecules were of particular interest to the authors, as previous models had failed to reproduce observations of these complex molecules. The abundances produced by the model of Leung et al. (1984) were much too small when compared with the observed abundances. The effect of the changes made to model 1, compared with the model from Leung et al. (1984), was that the steady state abundances of some complex molecules were increased by an order of magnitude. Overall however, the changes in reaction rate coefficients did not have a major affect on the results of the model compared with Leung et al. (1984).

The effects of the lowered visual extinction on the dense cloud chemistry in model 2 were seen to be fairly small. It was noted that the photodestruction of CO led to an increase in the amount of atomic C. This in turn led to an increased abundance of complex molecules at steady state. Conversely, it was found that there was a decreased abundance of complex molecules at early time, as photoreactions destroyed many of the larger molecules at this stage.

The increased temperature in model 3 caused the reaction rate coefficients to decrease. This, perhaps unsurprisingly, caused the abundances of complex molecules to decrease

both at early time and steady state, often by about an order of magnitude. When compared with observations of an appropriate region (e.g. a dense cloud at approximately 50K), the results from this model were more accurate than those from model 1.

The high C/O ratio in model 4 led to a large increase in the abundance of hydrocarbons - similar to that seen by Watt (1985). Herbst & Leung (1986) produced model results for both early time and steady state, unlike Watt (1985). Herbst & Leung (1986) found that the increased abundance of hydrocarbons was found at early time as well as steady state. When compared with observations from dense clouds, it was noted that for some complex molecules, the steady state abundances produced by the model were far too high.

Model 5, which was a borderline diffuse/dense cloud, produced a significantly reduced abundance of complex molecules, as the increased rate of photoreactions destroyed many molecules and their precursors. Those complex molecules which did form were often seen to be bare hydrocarbons, such as C_3 and C_4.

Millar & Nejad (1985) also created a time-dependent model of a dark cloud, in order to examine the formation of complex molecules. The authors argued that steady state models of dense clouds were less useful than time dependent models such as their own, as observed results of C^+ could not be recreated by steady state models, and these models also did not take dust grain sticking processes into account. It was also noted that the evolution of the cloud chemistry with time could not be followed in a steady state model. One of the reactions Millar & Nejad (1985) considered most important in their model was:

$$C + H_3^+ \rightarrow CH^+ + H_2 \tag{1.2}$$

They concluded that this reaction was vital in the formation route for the hydrocarbon species. This is in contrast to Herbst & Klemperer (1973), who argued that the reactions of CH^+ would not affect the results from their model. Millar & Nejad (1985) noted that when reacting efficiently, reaction 1.2 would lead to the production of methane, via a number of H_2 abstractions. This methane could then go to on to react with C^+ to form more complex hydrocarbons.

Millar & Nejad (1985) simplified the process of building a chemical model, by developing, "a computer code which writes the time-dependent chemical kinetic equations on the input of a set of chemical reactions and their rate coefficents". This type of code made building and altering existing chemical models a great deal faster and easier.
The assumptions used by Millar & Nejad (1985) were similar to those used by Herbst & Klemperer (1973) – however, a notable difference was that Millar & Nejad (1985) assumed the initial abundance of carbon was split evenly between C and C^+.
Millar & Nejad (1985) found that atomic carbon has a high fractional abundance at early time, but a sharp downturn at around 4×10^5 years, when most of the carbon is locked up in the CO molecule. This reduced the rate of production of hydrocarbons, as carbon is involved in the reaction (1.2) which drives this production. The production of complex molecules containing oxygen also decreased, as these were formed via reactions between hydrocarbon ions (produced initially from C atoms) and oxygen. At early time, atomic nitrogen was also highly abundant, which lead to its inclusion in complex molecules. After approximately 10^6 years, most of the atomic nitrogen was converted into N_2 molecules via reactions between neutrals. Coupled with the decrease in hydrocarbon ions, this lead to a reduction in the amount of nitrogen-bearing complex molecules at steady state.
Millar & Nejad (1985) also looked at the effects of including accretion of gas onto the dust grains in a cloud. It was found that all the species which were able to condense onto the dust grains were removed from the gas phase in around 10^6 yr. This calculation did not take into account any possible processes for returning the accreted matter to the gas phase. The authors noted that as observed dark clouds were shown to contain these species in the gas phase, there must be one or more methods which evaporate these species from the grains. It was postulated that the removal mechanism is unlikely to be shocks - however, there was some opposition to this view, e.g. Williams & Hartquist (1984). Millar & Nejad (1985) thought the species may be returned to the gas phase from the grain surfaces via either exothermic chemical reactions on the surfaces, or heating caused by cosmic rays.

Models have been seen to produce extremely different results, even when the mathematics and algorithm used in the models are the same. Millar et al. (1987) produced a paper which investigated the differences in results taken from two dark cloud models discussed above - Herbst & Leung (1986) (henceforth HL), and Millar & Nejad (1985) (henceforth MN). The two models were both aiming to produce fractional abundances of complex molecules which could be reconciled with observation. Neither of the models were able to do this successfully, and the results they produced also did not agree with one another. The HL model results compared more favourably with observations than the MN results at early time. Conversely, at steady state, the MN results were much closer to the observed abundances than the HL results were. A bridging analysis was undertaken to try and find the source(s) of the differing results. A number of reactions relating to complex species were added to the MN model, which was initially based on a smaller chemical network than the HL model. After the reactions were added to the model, the results produced by both models were extremely similar. It was found that the abundances of complex molecules were most strongly dependent on the choice of included reactions in which atomic oxygen was a reactant. The abundances of these complex molecules were also dependent on the branching ratios used in the dissociative recombination calculations for complex species. Millar et al. (1987) also found that carbon chain growth efficiency in dense clouds was effective at early time. However, at steady state it was found to be inefficient unless atomic oxygen was unreactive with carbon chain molecules.

Hasegawa et al. (1992) modelled a dark cloud with both gas-phase and grain-surface chemistry, in an attempt to match observed abundances of complex organic molecules. The authors considered physisorption[1] as the only adsorption[1] process, and the probability of a neutral species adsorbing to a grain upon collision was assumed to be 1. Grain surface species were able to traverse the grain surface, via thermal hopping[1]. Light species such as H and H_2 were able to diffuse across the grain surface via quantum

[1]These processes are defined in Section 2.2.2

tunnelling[2]. Several models were run, each with constant temperature (10K), density (2×10^4 cm^{-3}) and visual extinction (500 mag). The models had different initial gas-phase compositions, as follows:

1. Model A – Molecular hydrogen. Steady state molecular abundances of O, C, S and Si taken from Herbst & Leung (1989). Steady state heavy metal abundances
2. Model B – Atomic hydrogen. Neutral atomic O, C, S, Si and heavy metals
3. Model C – Molecular hydrogen. Neutral oxygen. Singly ionised C, S, Si and heavy metals
4. Model D – Identical to model C, except for exclusion of the surface reaction:
   $CO + O \rightarrow CO_2$

The only mechanism for returning the species which formed on the grains back into the gas-phase was thermal desorption[2]. This resulted in all neutral heavy species eventually accreting onto the grains, as the dark cloud model assumed a temperature of 10K. Complex molecules, such as CH_3OH and C_4H_2, were able to efficiently form on grain surfaces rather than in the gas-phase. The model which best matched dark cloud observations was model D, at early time ($\sim3\times10^5$ years). The authors planned to refine their calculations to try and better match observations.

Hasegawa & Herbst (1993a) attempted to improve the gas-grain dark cloud chemical modelling of Hasegawa et al. (1992) by considering cosmic-ray induced desorption. Hasegawa & Herbst (1993a) assumed that a cosmic-ray impact would heat a dust grain, and lead to thermal desorption of grain surface species. The authors also augmented the reaction rates and reaction networks. It was found that the formation of complex unsaturated species was more likely to occur in the gas-phase than on the grain surfaces. This was because quantum tunnelling of H and H_2 led to hydrogen-addition onto unsaturated grain-surface species. The addition of cosmic-ray induced desorption did not prevent the majority of the gas-phase species accreting onto the grain surfaces by

[2]These processes are defined in Section 2.2.2

later times (e.g. t>10^8 years). The best agreement between the models and observations was found to be at early times.

Hasegawa & Herbst (1993b) created a three-phase chemical model of a dark cloud. The three phases were: the gas phase, dust grain surfaces, and dust grain mantles. The grain mantles were layers of species which had accreted onto the dust grains. As more gas-phase species accreted on top of the already accreted species, a distinction was made between the two. The grain surface phase was defined to be the top layer of species. These species are mobile, reactive, and can desorb from the grain surface. The grain mantle phase was defined to consist of those species which have already been accreted, and remain under the top layer of the grain surface. These mantle species are immobile and unreactive. Hasegawa & Herbst (1993b) found that the model results did not differ greatly from those of their previous models (Hasegawa et al. 1992; Hasegawa & Herbst 1993b), particularly for inert species. The model results allowed the authors to obtain molecular abundances to represent the composition of the layers which built up at different times.

Fractional Ionisation and Reduced Chemical Networks

The fractional ionisation of a cloud can be described by the number density of charged particles as a proportion of the total number density of particles in the cloud (Oppenheimer & Dalgarno, 1974). This can be estimated from the number density of electrons divided by the number of hydrogen nuclei in a molecular cloud:

$$x_e = \frac{n(e)}{2n(\mathrm{H_2}) + n(\mathrm{H})} \tag{1.3}$$

where x_e is the fractional ionisation, *n(e)* is the number density of electrons, $n(\mathrm{H_2})$ is the number density of molecular hydrogen and n(H) is the number density of atomic hydrogen. The range of values taken by x_e are between 0 and 1. A value of 0 describes a neutral cloud, and a value of 1 describes an ionised cloud. Oppenheimer & Dalgarno (1974) wrote that the fractional ionisation is an important parameter in a dark cloud, as

it determines, "the coupling of the cloud to the galactic magnetic field". This controls the ambipolar diffusion time of the cloud, and when, or if, a star will form. If the cloud is strongly coupled to the magnetic field then collapse may be slowed down or prevented. Therefore, a low fractional ionisation is more likely to lead to star formation in a cloud, whereas a high fractional ionisation is likely to slow down or stop this process. Much work has been done to estimate the fractional ionisation in dark clouds (e.g. Oppenheimer & Dalgarno 1974; Elmegreen 1979; Caselli et al. 1998; Rae et al. 2002). Rae et al. (2002), produced a reduced chemical network (similar in principle to Figure 1.3) in order to accurately estimate the fractional ionisation in a molecular cloud. It was argued that using a reduced network resulted in a great reduction in calculation time (the reduced network was over sixty times faster to calculate) which was worth some loss of accuracy. The results produced by the model were seen to be in good agreement with those produced by a model using a full reaction network. Wiebe et al. (2003) also produced a reduced chemical network for a molecular cloud, and used it to analyse the abundance of CO as well as the fractional ionisation of a cloud. A gas phase model and a gas-grain model were used to test the network reduction method devised by Wiebe et al. (2003). The results produced for the fractional ionisation estimate compared reasonably well with results from models using a full reaction network. The reduced-network gas-phase model produced a fractional ionisation estimate which differed by less than 10% compared with a full-network gas-phase model. The CO estimate produced by the reduced-network model differed by around 15%. The reduced-network gas-phase model ran 10–20 times faster than the full-network gas-phase model. The reduced-network gas-grain model gave a fractional ionisation estimate which differed from the full-network gas-grain model results by 10% at early time, and 30% at steady state. The CO estimate produced by the reduced-network gas-grain model differed by 10%. The reduced-network gas-grain model ran 3–16 times faster than the full-network gas-grain model.

It will be interesting to see the effect of technological advances on this type of calculation. In the future, it is likely that greatly improved computer processing speeds will

Model	O	C	N	O/C	O-C
MH G	3.52(-4)	1.46(-4)	4.28(-5)	2.4	2.06(-4)
MH L1	4.80(-4)	1.58(-4)	1.74(-5)	3.0	3.22(-4)
MH L2	1.25(-4)	3.08(-5)	3.24(-6)	4.1	9.42(-5)
MH S1	2.20(-4)	2.80(-5)	8.00(-6)	7.9	1.92(-4)
MH S2	5.72(-5)	5.46(-6)	1.49(-6)	10.5	5.67(-5)

Table 1.1: Initial fractional elemental abundances used in the MH models. All abundances are given relative to H_2. Note: *a(-b)* refers to $a \times 10^{-b}$.

lead to this type of chemical network reduction becoming unnecessary.

Dark Cloud Chemical Modelling of The Magellanic Clouds

Millar & Herbst (1990) used a pseudo-time-dependent model previously developed to model galactic dark clouds, to try and model dark cloud chemistry in external galaxies. Observed chemical abundances from the Large Magellanic Cloud and the Small Magellanic Cloud (henceforth LMC and SMC) were used as model inputs. The inputs used were fractional elemental abundances for carbon, oxygen and nitrogen. The observations were taken from HII regions, rather than dark clouds (Bel et al., 1986). For this reason, two types of models were developed. The original HII region abundances were used in models L1 and S1, for the LMC and the SMC respectively. These abundances were then depleted according to factors previously calculated by the authors, while developing their dark cloud models (e.g. Millar et al. 1987; Millar et al. 1988). The depleted abundances were used in the models L2 and S2. Results were also produced using standard Galactic abundances, which were also depleted by the aforementioned factors. The results from the Galactic model were used as a base point from which the LMC and SMC results could be compared. The elemental abundance model inputs used in all five models are shown in Table 1.1. The five different models produced different final abundances for a variety of species – as would be expected

from the differing elemental input abundances. Millar & Herbst (1990) stated that the CO abundance produced by the model is directly related to the amount of available carbon at both early time and steady state. The authors explained that this result indicates that all of the available carbon in the cloud is locked-up in the stable C-O bond, as previously discussed by Watt (1985). It was then put forward that provided the oxygen abundance is greater than the carbon abundance, the CO abundance is independent of the oxygen abundance. This would allow CO observations in oxygen-rich regions to reveal the carbon abundance in these galaxies, and vice versa as in carbon rich regions all of the available oxygen will be locked up in stable CO and thus be the limiting factor for CO abundance.

Millar & Herbst (1990) noted that hydrocarbon abundances depend on a combination of factors, including (but not limited to);

1. the elemental carbon abundance, as hydrocarbons are formed from the carbon left over from CO production;

2. the oxygen abundance, as this can affect both the hydrocarbon formation and destruction rates;

3. the CO abundance, as formation of some hydrocarbons from precursor ions such as CH_5^+ depend on reaction with CO.

It was found that the atomic oxygen abundance was related to the quantity O−C, rather than the O/C ratio. The quantity O−C represents the amount of free oxygen atoms per unit volume, as almost all of the carbon atoms will bond with oxygen atoms, forming CO. The number density of oxygen atoms which are not bonded with carbon are then free to react with other species, so the quantity O−C represents the excess, or free oxygen atoms. Although model S2 had the highest O/C ratio, it also had the smallest value of O−C, and so the lowest atomic O abundance at both early time and steady state. It was concluded that the hydrocarbon abundances can be enhanced in models with low carbon and oxygen abundances (e.g. S2), provided that the O−C value is low.

This seems counterintuitive at first, as a more instinctive result would be that the hydrocarbon abundances would scale with the underlying carbon abundance. However, the stronger scaling of the hydrocarbon abundances with the quantity O−C gives an example of how the complex and highly inter-dependent chemical networks present in the clouds can interact in ways which are not immediately obvious.

The authors note that the abundances of nitrogen-containing species depend on the nitrogen abundance more strongly than hydrocarbon abundances depend on the carbon abundance. The steady state model results show that both the N_2 and NH_3 abundances directly scale with the elemental nitrogen abundance. At early time, the N_2 and NH_3 abundances have some co-dependence, as the formation of NH_3 involves N_2. However, the authors found that the association between N_2/NH_3 and the atomic nitrogen abundance at early times was less easily defined. The dependence was affected by the abundance of OH, and hence the elemental oxygen abundance. This dependence, combined with hydrocarbon/nitrogen reactions forming organo-nitrogen species, gave rise to a complex chemistry which was dominated by different reactions at different times.

Millar & Herbst (1990) also discussed the effect of reduced abundance of CO on the H_3^+ ion. This ion was more abundant in model S2 than G by more than an order of magnitude at both early time and steady state. It was stated that the increase could be attributed to the lower CO abundance, as H_3^+ is primarily destroyed by reaction with CO, and so a lower CO abundance leads to a lower destruction rate in model S2.

Millar & Herbst (1990) concluded that although it is generally hard to derive the C, O and N elemental abundances from molecular abundances, due to the complex nature of the reaction networks, it is a useful result that the CO abundance scales directly with the carbon abundance, provided the galaxy is oxygen rich. This result allows CO observations of such galaxies to determine the carbon abundance. The authors suggested that although it would be difficult to determine the elemental abundances of oxygen and nitrogen using molecular line observations of dark clouds, it may be possible to infer these abundances where the abundance of carbon is known, and a number of species containing C, O and N in various combinations could be observed. This demonstrates

how useful a chemical reaction network can be in deducing the abundance of a species in a dark cloud, even if the species itself is not directly observable.

1.2.2 Chemical Models of Hot Cores

Brown et al. (1988) created a chemical model of a hot core. The model included gas-phase and grain surface chemistry, and was pseudo-time-dependent. Brown et al. (1988) considered a three phase process for the hot core model.

1. Phase i: a cold, dark cloud collapsed to a density of 10^7 cm^{-3}
2. Phase ii: the gas was heated by the formation of a protostar and the grain mantles evaporated
3. Phase iii: the hot core chemistry was seen to evolve with time

Phase ii was thought to be sufficiently transient that the heating and evaporation of grain mantles was considered to be instantaneous by the authors. The grain surface chemistry was limited to hydrogenation reactions. In phase iii, the temperature (200 K) and density (10^7 cm^{-3}) were set as constant values throughout the hot core. Brown et al. (1988) discussed deuterium chemistry, but did not include it in the model as it would have substantially increased the run time of the model. The model results showed that the chemistry in the collapsing cold cloud, phase i, did not reach steady state, as the free-fall time (~9.3×10^5 years) was shorter than the time needed for the chemistry to reach equilibrium. All condensible species froze out onto the grain surfaces before the collapse was completed. The grain species formed were hydrogenated versions of the elemental atoms initially put into the model. For example, atomic nitrogen formed NH_3, and atomic oxygen formed H_2O. In phase iii, the destruction rates for many species were slow, as the reactive O and OH neutrals were 'locked up' in stable CO and H_2O. The abundance of ionic species produced by cosmic rays (e.g. H_3^+ and He^+) was reduced, as the fractional abundances of these species was known to be inversely proportional to density. The density in the hot core model was very high, and so few

of these ionic species were produced. The model overproduced some radical species, including CN and C_2H, as the hydrogenation of species other than C, N and O (and their hydrides) was ignored. Overall, the model produced results which could be used to explain observed abundances of various species in the Orion Hot Core.

Brown (1990) modelled the formation of complex molecules on dust grain surfaces. The author suppressed the reactions between atomic hydrogen and heavier species, in order to allow more complex species than hydrogenated atoms to form. Three reasons for the reduction in H atom surface reaction efficiency were put forward:

1. A reduced sticking coefficient for H atoms
2. Almost all hydrogen could be assumed to be in the form of H_2, with very little atomic H present
3. Reduced mobility of the H atoms on the grain surface

The Brown (1990) model results showed that complex species were efficiently produced by the new grain chemistry used in the model. A number of these complex species had been observed in hot cores, and other hot core models were not able to match the observed abundances. The Brown (1990) model represented an improved hot core model, which was more able to match observations from hot cores.

Charnley et al. (1992) used observations of mantles on dust grains as the starting point for their chemistry. These models did not include a collapse phase, but instead started with the injection of the grain mantle species into the gas phase. Charnley et al. (1992) modelled two different regions in the Orion-KL cloud which were both described as 'hot cores'. The two regions exhibited very different chemical abundances. The first region was known as the Hot Core. The Hot Core has a temperature of 200 K, a density $> 10^7$ cm^{-3}, and is relatively compact. The second region was known as the Compact Ridge. The Compact Ridge is cooler, with a temperature of around 100 K, and less dense with a density $> 10^6$ cm^{-3}. The Hot Core is known to have a largely neutral, nitrogen-rich chemistry, and the Compact Ridge has been observed to be dominated by oxygen-bearing species and ion-molecule reactions. Charnley et al. (1992)

attempted to reproduce the different chemistries seen in the two regions by increasing the initial abundance of CH_3OH in the Compact Ridge, and NH_3 in the Hot Core. The authors concluded that the complex gas phase species observed in hot cores could be formed in the gas phase, from simple hydrogenated parent species (e.g. NH_3, CH_4) which formed on the grain surfaces.

Caselli et al. (1993) also modelled the Hot Core and Compact Ridge in the Orion-KL cloud. Caselli et al. (1993) modelled the regions as two distinct shells of gas, collapsing around a common massive protostar. The Hot Core was the inner shell, and was hence hotter, denser, and closer to the protostar. The Compact Ridge was the outer shell, and was thus cooler and less dense. The Hot Core was assumed to be initially composed of molecular hydrogen and metallic ions. The Compact Ridge was assumed to contain atomic hydrogen, along with atomic metals. Both regions contained a temperature and density gradient (Scoville & Kwan, 1976). The model results reproduced some aspects of the contrasting chemistries seen in the two regions. However, some abundances could not be reproduced by the model. Caselli et al. (1993) suggested that further understanding of the grain surface chemistry was required, to reconcile the model results with observations.

Hot core models became more complex with time, as sulphur, silicon and phosphorus surface chemistry was added to the models, as dicussed by Charnley (1995). Millar et al. (1997b) created a complex model of a hot core and its surrounding region. The authors defined three regions in a molecular cloud surrounding a protostar, namely:

1. An ultracompact hot core (UCC)
2. A compact hot core (CC)
3. An extended halo

The definition of a general hot core which has been used in the models in this thesis corresponds to the ultracompact hot core and compact hot core regions only. The physical parameters used to define the three regions are shown in Table 1.2.

Component	$n(H_2)$	T	Outer radius	$N(H_2)$	A_V
	(cm^{-3})	(K)	(pc)	(cm^{-2})	(mag)
Ultracompact core	$2x10^7$	300	0.01	6×10^{23}	640
Compact core	10^6	$30\ r^{-0.4}$	0.1	2.7×10^{23}	288
Halo	$10^4\ r^{-2}$	$30\ r^{-0.4}$	3.5	2.9×10^{23}	310

Table 1.2: Physical parameters used in the Millar et al. (1997b) model. r is measured in cm.

Millar et al. (1997b) calculated a number of pseudo-time-dependent chemical models to represent the shells present in this scheme – two in the UCC, two in the CC and eighteen in the Halo. The cosmic ray ionisation rate used in the models was 1.3×10^{-16} s^{-1}, which is an order of magnitude larger than the standard interstellar value (as used in this thesis). The results were able to reproduce many observed abundances from the modelled hot core (G 34.3). It was suggested that more refined models could take into account the variation of grain mantle composition with radial distance.

Viti & Williams (1999) investigated what Brown et al. (1988) termed 'phase ii' of the hot core model, e.g. the evaporation of grain mantles via heating from a newly-formed protostar. Viti & Williams (1999) developed a hot core model in which the evaporation of icy mantles was time dependent. The authors hoped to use the model to constrain the age of the protostar, as it approached 'zero-age' main sequence (ZAMS), and the distance from the hot core to the protostar/ZAMS star. The time at which the star becomes a ZAMS star is called the contraction time, as at this time it reaches its minimum radius, highest mass (for a single star system) and greatest effective temperature. The model consisted of a uniform slab divided into 50 shells. The initial and final densities used were 10^4 H_2 cm^{-3} and 10^7 H_2 cm^{-3} respectively. The surface chemistry was limited to hydrogenation of species which were depleted onto grains, and conversion of a fraction of the CO into CH_3OH. In the time-dependent evaporation model, the different grain species evaporated according to their binding energy to the grain. As the temperature increased, different species were able to desorb from the grains. Four models were created, in which the temperature increased to a maximum of 200K over

four different timescales:

1. Instantaneous temperature increase to 200K (a traditional hot core model)
2. $T_{\rm dust}$ = 200K after 2.8×10^4 years. This corresponded to a $60M_\odot$ star.
3. $T_{\rm dust}$ = 200K after 7.0×10^4 years. This corresponded to a $25M_\odot$ star.
4. $T_{\rm dust}$ = 200K after 1.1×10^5 years. This corresponded to a $15M_\odot$ star.

The results showed that in the first 60,000 years following the birth of a star, very different fractional abundances were produced in the four models. This information could be used to estimate the age of a hot core, and the contraction time for a massive star.
Viti et al. (2001) considered the effects of shocks on hot core evolution. The shocks were postulated to be caused by winds from the protostar, as low-mass pre-ZAMS stars were known to have such winds. The authors assumed the shock to have a velocity of 10–20 km s^{-1}. It was assumed that the wind was steady – this would only cause one shock, rather than a series.The authors found that if all metallic species froze-out onto the grain surfaces prior to protostar formation and shock impact, then no shock tracer species could be identified. If this were not the case, HCO/H_2CO and NS/CS were found to be potentially useful shock tracers.
Charnley (1997) originally suggested the idea of using sulphur-bearing species as 'chemical clocks'. The author suggested using the ratios SO/H_2S and SO/SO_2 in order to determine the age of a hot core. Wakelam et al. (2004) further analysed sulphur chemistry in hot core chemical models. The authors found that a number of factors have a strong impact on the sulphur-bearing species, namely:

1. the gas temperature
2. the gas density
3. the atomic oxygen abundance
4. the form the sulphur takes when it is injected into the gas phase

As the sulphur-bearing species do not solely depend on the hot core age, the authors wrote that the use of sulphur-bearing species as chemical clocks was not straightforward. It was concluded that detailed hot core observations combined with rigorous modelling of the physical and chemical structure could be used to constrain the source age, along with the form of sulphur when it is injected into the gas phase.

Nomura & Millar (2004a) modelled a hot core in which the grain surface species sublimated at different temperatures, depending on the binding energy of the species to the grain surface. The grain mantle composition was chosen to match observations of ice absorption features in young stellar objects. The authors also created a model where the grain surface species were trapped within a water ice. Nomura & Millar (2004a) found that a hot core age of 10^4 years in the model was most appropriate when comparing the model results with observations of the hot core G34.3+0.15. The differing sublimation temperatures for different grain surface species produced a chemistry where parent species could be limited to an area within a certain radius (and hence temperature). The water-ice grain surface model produced distinctive results, where the abundance radii for parent and daughter species had changed, compared with the model where the grain species could evaporate according to their binding energy.

Extragalactic Chemical Models of Hot Cores

Lintott et al. (2005) investigated the possibility of observing emission from hot cores in galaxies at high redshift. The authors used a simple hot core model, with no internal structure and with instantaneous grain mantle evaporation. The initial elemental abundances used came from models of the yields from a zero-metallicity star. Bertoldi et al. (2003) estimated that the quasar SDSS J114816.64+525150.3 could have a star formation rate as high as 3000 solar masses per year. Lintott et al. (2005) thus estimated that high redshift galaxies could contain as many as 10^7-10^8 hot cores. The authors wrote that unresolved observations of molecular emission from the combined hot cores present in such galaxies should be possible.

Bayet et al. (2007) performed a preliminary investigation into hot core modelling in other galaxies, at low metallicity. For simplicity, Bayet et al. (2007) varied only the underlying elemental abundances in their models, and not the gas/dust ratio or the H_2 formation rate. The authors investigated a range of metallicities, from solar to solar/1000. Some hot core metallicity tracer species were identified. Those that varied linearly with metallicity included CO, NH_3, H_2O and CS. HCO^+ and SO were found to inversely trace the underlying metallicity. CH_3CN was found to be insensitive to metallicity. The effect of increasing the cosmic ray ionisation rate by an order of magnitude (from 1.3×10^{-17} s^{-1} to 1.3×10^{-16} s^{-1}) was investigated, and species that were both sensitive and insensitive to this parameter were identified.

Bayet et al. (2008) made a more detailed study of hot core modelling in other galaxies. The types of galaxies considered were spiral galaxies, active galaxies, low-metallicity galaxies and galaxies at high redshift. The parameters investigated were metallicity, dust/gas ratio, H_2 formation rate, relative initial elemental abundances, cosmic ray ionisation rate, and the hot core temperature. This comprehensive study identified a number of tracer species, which could identify hot cores in other galaxies. Bayet et al. (2008) found that even at very low metallicity, the hot core chemistry remained complex.

1.2.3 Time Scales

Some of the time scales over which important physical and chemical processes in star-forming regions occur can be approximated, using the equations given in this section. The free-fall time scale for gravitational collapse in a dark cloud is given by the following equation (Tielens, 2005):

$$\tau_{ff} = \left(\frac{3\pi}{32Gnm_{\mathrm{H}}}\right)^{1/2} \simeq \frac{4\times10^7}{n^{1/2}}\text{years} \tag{1.4}$$

where G is the gravitational constant, n is the cloud density in cm^{-3}, and m_H is the mass of a hydrogen atom.

The accretion rate for gas-phase species to freeze out onto dust grain surfaces is given in Section 2.2.2. This rate governs the freeze out time scale, which can be approximated (Tielens, 2005):

$$\tau_{freeze\_out} \simeq \frac{4 \times 10^9}{n} \text{years} \tag{1.5}$$

where n is the density of the gas in cm^{-3}. This time scale can be as short as $4{\times}10^4$ years in a cloud with a density of $1{\times}10^5$ cm^{-3}.

Ambipolar diffusion describes the process by which magnetic fields diffuse out of a region, affecting if/when a cloud is able to collapse to form a protostar. Charged particles within the cloud couple to the magnetic field which exist in the star forming region and can slow or prevent the cloud collapse, as they will not cross the magnetic field lines. The charged particles diffuse/drift to the edge of the cloud, as the neutral species are attracted inwards by gravity. The charged particles exert a friction against the gravitational collapse, as they slow or prevent this process. The ambipolar diffusion time scale is thus strongly affected by the fractional ionisation of the cloud, as the higher the proportion of charged material in the cloud, the longer it takes for the gravity to overcome the supportive magnetic field. The ambipolar diffusion time scale, τ_{AD}, is given by (McKee, 1989):

$$\tau_{\rm AD} \simeq 1.6 \times 10^{14} \phi_{\rm AD} x_e \text{ years} \tag{1.6}$$

where x_e is the fractional ionisation of the cloud and ϕ_{AD} is a constant of order unity, which is used to allow for deviations from this estimate.

The chemical time scale is "the time taken to create molecular coolants from the initially atomic gas assuming that nearly all of the hydrogen is molecular" (Banerji et al., 2009). At this time, enough hydrogen has been ionised so that C and O can be totally converted into molecules (Banerji et al., 2009). The chemical time scale, τ_{chem} is approximated by (Banerji et al., 2009):

$$\tau_{chem} \simeq \frac{5 \times 10^6 \xi}{\zeta / 1 \times 10^{-17}} \text{ years} \tag{1.7}$$

where ξ is the metallicity of the cloud and ζ is the cosmic ray ionisation rate. This time scale is more important for collapsing diffuse clouds rather than dense or dark cores. Rough estimates of some of these time scales for a typical dark cloud, with density n $\approx$ 2×10^4cm^{-3} are given in Table 1.3. It is worth noting that the ambipolar diffusion time scale is much longer than the free-fall collapse time scale. The ambipolar diffusion time scale thus provides the limiting factor for the time taken to form a star within a cloud. The freeze-out time scale is much shorter than the ambipolar diffusion time scale. The differences (and similarities) between the times taken for these processes to occur can have interesting consequences for the chemistry. This is discussed further in Section 3.2.1.

	Ambipolar diffusion	**Free-fall collapse**	**Freeze-out**
Dark Cloud	10^7	1.3×10^5	4×10^4

Table 1.3: The typical time scales, in years, for some physical processes to occur in a dark cloud, with density 1×10^5cm^{-3}.

1.2.4 Summary

When ALMA becomes fully functional, observations of star-forming regions in other galaxies will be made at much higher levels of resolution than are currently possible. Previously unseen molecular emission from galaxies at high redshift will be detected. The chemical models of dark clouds and hot cores at low metallicity in this thesis will help observers to interpret and understand their findings.

2

Chemical Modelling

2.1 Modelling

When referring to the models used, it is useful to define some commonly used terms. The notation [X] is used to refer to the concentration (cm^{-3}) of a species, X. When the term 'abundance' is used with reference to chemical models, it can be assumed to mean fractional abundance, with respect to H_2 concentration, unless otherwise stated.

2.1.1 Chemical Networks

A chemical network is a representation of the various chemical reactions occurring between species in a region. An example reaction network is shown in Figure 1.3. Chemical models are built around reaction networks – the various species are connected via reactions, which in turn are governed by reaction rates. A computational chemical model can be used to calculate the abundances of species within a cloud, given appropriate physical conditions (e.g. temperature, H_2 density and extinction).

2.1.2 Abundance calculations

In a chemical model, the abundances of species with respect to time are calculated using differential equations, for example:

$$\frac{dn(\mathrm{X})}{dt} = \text{Formation(X)} - \text{Destruction(X)} \tag{2.1}$$

where n(X) is the concentration of species X. The formation rate of X is calculated by summing the amount of X produced by all possible reactions. An example of a formation reaction might be:

$$\mathrm{XH^+ + C \rightarrow CH^+ + X} \tag{2.2}$$

The rates of the forward and backward reactions can be represented using the following equation:

$$k_1 \left[\mathrm{XH^+}\right] \left[\mathrm{C}\right] = k_2 \left[\mathrm{CH^+}\right] \left[X\right] \tag{2.3}$$

where k_1 is the rate of the forward reaction, and k_2 is the rate of the backward reaction. The concentration of X formed via Reaction 2.2 can be calculated thus:

$$n(\mathrm{X}) = \frac{k_1}{k_2} \frac{n(\mathrm{XH^+}).n(\mathrm{C})}{n(\mathrm{CH^+})} \tag{2.4}$$

where k_1 and k_2 are the reaction rate coefficients described above. The formation rate of X is dependent on the concentrations of the reactants and the reaction rate for each reaction. The reaction rates are often temperature dependent, either proportionally or inversely, and so the reactions which have a high rate in cold, dark clouds will be different in warmer regions, including hot cores. The destruction rate of X is calculated in the same way as the formation rate, the only difference being that the reactions considered are those which destroy X.

In a steady state model, the species' abundances are found by setting the differential equations (e.g. equation 2.1) equal to zero and solving them. This follows, as steady state is defined as the time when the formation and destruction rates of a species are equal. In a time-dependent model, the abundances are calculated at a series of predefined time steps, where derivatives are typically non-zero.

2.1.3 Gas-phase and gas-grain models

Gas-phase chemical models (e.g. Millar & Herbst 1990) use chemical networks which consider only the gas phase reactions that are possible within a cloud. Gas-grain models (e.g. Hasegawa et al. 1992) include dust grain surface reactions in the chemical network. A grain population is input into the model, with an overall dust mass and a range of grain sizes. It is assumed that some gas phase species can freeze out of the gas phase onto the grain surfaces. A 'sticking' probability is used to determine what proportion of a gas-phase species freezes out, when it comes into contact with a grain surface. Surface chemistry is added to the model, as the species undergo a range of reactions on the grain surfaces. In a pseudo-time-dependent dark cloud chemical model, the low temperature would eventually lead to almost all species (except H_2) being depleted from the gas phase. In a hot core model, the increased temperature caused by the protostar 'switch-on' allows the frozen out species to evaporate from the grains, producing a complex gas-phase chemistry.

2.2 Chemistry

2.2.1 Gas-phase chemistry

The dark cloud and hot core models used in this thesis contain a gas-phase chemistry which is based on the reactions in the UMIST Database for Astrochemistry (Woodall et al., 2007). The gas-phase reaction classes included are shown in Table 2.1.

In a dark cloud, the chemistry is initiated by the cosmic-ray ionisation of H_2 or He. The most important reaction types are ion-molecule, dissociative recombination, charge exchange and neutral-neutral. This is because there are high concentrations of neutral species and positive ions in dark clouds. Photoreactions are less important in the interior of a dark cloud, as the high extinction reduces the number of photons able to enter the cloud, and therefore the efficiency of these reactions.

In a hot core, the neutral-neutral reactions are the most important. The fraction of

Type	**Process**	**Rate Coefficient**
Ion-molecule	$A^+ + B \rightarrow C^+ + D$	$\sim 10^{-9}$ cm^3 s^{-1}
Dissociative Recombination	$AB^+ + e \rightarrow A + B$	$\sim 10^{-6}$ cm^3 s^{-1}
Radiative Association	$A + B \rightarrow AB + h\nu$	$\sim 10^{-16}10^{-9}$ cm^3 s^{-1}
Neutral-neutral	$A + B \rightarrow C + D$	$\sim 10^{-12}10^{-10}$ cm^3 s^{-1}
Photodissociation	$AB + h\nu \rightarrow A + B$	$\sim 10^{-9}$ s^{-1}
Charge-transfer	$A^+ + B \rightarrow A + B^+$	$\sim 10^{-9}$ cm^3 s^{-1}

Table 2.1: Classes of gas-phase reactions used in chemical models. Taken from Caselli (2005).

ionic species is much lower in a hot core than a dark cloud, as the increased density combined with the (assumed) constant cosmic ray ionisation rate results in a smaller fraction of charged species. Thus, the reactions involving charged species are less frequent than those involving only neutral species. Photoreactions are also infrequent in a hot core, as the high density results in an even higher extinction than in a dark cloud.

Branching ratios

One of the factors affecting the evolution of a chemical reaction network within a cloud is the branching ratios of certain reactions. The branching ratio of a reaction is the proportion of the reactants which go on to form certain products. This can be shown in the following generalised example of dissociative recombination:

$$ABC^+ + e^- \longrightarrow AB + C \tag{2.5}$$

$$ABC^+ + e^- \longrightarrow A + BC \tag{2.6}$$

where the products are different for the two reactions. If the A–B bond is much stronger than the B–C bond then it is likely that most of the time, Reaction 2.5 will occur preferentially to Reaction 2.6. However, Reaction 2.6 will sometimes occur. This may result in a branching ratio of x% for Reaction 2.5 and (100-x)% for Reaction 2.6, where x>0. The number of possible reactions which could occur is not limited to two, and for

polyatomic species the number of possible outcomes will usually be higher than this (Millar et al., 1988). If the reaction can be performed in a laboratory, the data for the branching ratios will be taken from experimental results. Otherwise, an estimate will be made as to the likelihood of each reaction taking place, based on data from similar reactions, bond strengths and calculations using known reaction rates. Many of the reactions which occur in dark clouds, hot cores, or other astrophysical environments, take place under conditions which are impossible/difficult to recreate in an Earth-based laboratory. For this reason, many of the branching ratios for the reactions which occur in dark clouds are not known, or easily estimated. Other parameters, such as the reaction rate coefficients, activation barriers and energetic feasibility of reactions are also unknown and difficult to estimate as these parameters are also difficult to measure in a laboratory under 'dark cloud'/'hot core' conditions. Quantum-chemical calculations are sometimes utilised to study the likelihood of various bonds breaking within a species. However, these calculations are time-consuming as they are extremely complicated and computationally intensive.

2.2.2 Surface Chemistry

Figure 2.1 shows the interaction between gas-phase species and grain surfaces. It also shows the different types of reactions which can occur on the grain surface. These processes are individually discussed below.

Accretion

Accretion of gas-phase species onto dust grain surfaces is included in the hot core model. The probability of a species freezing out, or accreting, onto a grain surface upon collision is known as the 'sticking coefficient'. Most species are assumed to have a sticking coefficient of 1, which means they will accrete upon collision. Atomic hydrogen has a sticking coefficient of 0.3. As in Brown (1990), the reduced H atom sticking coefficient is used to suppress the reactions between elemental atoms and hy-

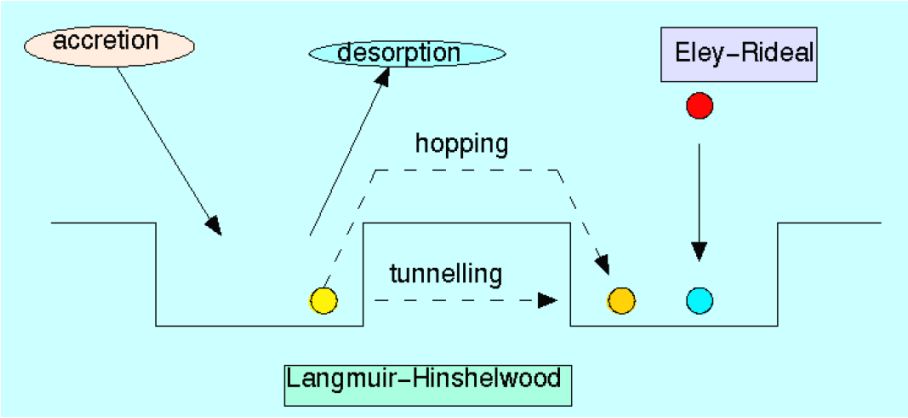

Figure 2.1: Assorted processes on dust grain surfaces. This image is taken from Herbst (2000), Minh & van Dishoeck (2000).

drogen, in order to increase the formation of complex molecules. The following species have a sticking coefficient of 0, and are not accreted; H^+, H_2, H_2^+, H_3^+, He, He^+ and HeH^+. Electrons are also not accreted, as the grains are assumed to be negatively charged. Positively charged gas-phase species are assumed to undergo dissociative recombination when accreting onto the negatively charged dust grains, resulting in the accretion of two or more neutral species. Neutral gas-phase species accrete onto the grains without dissociating. The following equation can be used to calculate the accretion rate, R_{acc}, for a species, i, (Millar & Williams, 1993):

$$R_{\rm acc}(i) = s_i \sigma_{\rm d} \langle v(i) \rangle n(i) n_{\rm d} \tag{2.7}$$

where s_i is the sticking coefficient, σ_d is the grain cross section (in cm^2), $\langle v(i)$ is the thermal velocity of the species, $n(i)$ is the gaseous concentration (cm^{-3}) of the species and n_d is the grain number density (cm^{-3}). When a gas-phase species is adsorbed onto a binding site, the species can become physisorbed or chemisorbed to the surface.

Desorption

Grain surface species thermally desorb from the grain surfaces when the temperature rises in the hot core model, as the dust temperature is assumed to be equal to the gas

temperature. Different species thermally desorb at different temperatures. The rate for thermal desorption of a species is given by the following equation (Millar & Williams, 1993):

$$t_{\text{desorb}}^{-1} = \nu_0 \exp\left(-E_{\text{D}}/\text{k}_{\text{b}}T\right) \tag{2.8}$$

where ν_0 is the oscillation frequency between the species and the grain surface (10^{12}-10^{13} s^{-1}), E_D is the binding energy between the species and the grain surface, k_b is Boltzmann's constant and T is the dust grain temperature. The harmonic oscillator approximation can be used to estimate the oscillation frequency, as follows:

$$\nu_0 = \sqrt{2n_s E_{\text{D}}/\pi^2 m} \tag{2.9}$$

where n_s is the surface density of binding sites per cm^2 and m is the mass of the adsorbed species.

Grain surface species can also desorb when the grain is impacted upon by a cosmic-ray, or a photon (photodesorption). The energy from the impact allows some surface species to desorb into the gas phase. In a hot core, thermal desorption is by far the most important type of desorption. The high extinction precludes photodesorption, particularly in the inner regions. Cosmic-ray induced desorption only has a tiny impact in dense regions, such as dark clouds and hot cores (Hartquist & Williams, 1990).

Physisorption

A physisorbed species undergoes van der Waals bonding with the surface atoms of the dust grain, as a mutually-induced dipole moment occurs. There is usually no activation energy to physisorption, and binding energies can be in the range 0.01–0.2eV. This weak bonding allows the species to move across the grain surface, either by thermal hopping or quantum tunnelling. These processes are represented in Figure 2.1. The rate of thermal hopping to an adjacent site is given by the following equation (Millar & Williams, 1993):

$$t_{\text{hop}}^{-1} = \nu_0 \exp\left(-E_{\text{b}}/kT\right) \tag{2.10}$$

where ν_0 is the same as in Equation 2.8, and E_b is the barrier energy between different sites. Millar & Williams (1993) wrote that geometrical arguments indicate that E_b is around 0.25-0.30 times the value of E_D, the binding energy. The rate of quantum tunnelling can be approximated by the following equation (Millar & Williams, 1993):

$$t_{\mathrm{q}}^{-1} \approx \nu_0 \exp\left[-(2a/\hbar)\sqrt{2mE_{\mathrm{b}}}\right] \tag{2.11}$$

where a is a rectangular barrier and $\hbar$ is the reduced Planck constant. The diffusion of grain species across the surface leads to Langmuir-Hinshelwood reactions, which can occur between two mobile species.

Chemisorption

A chemisorbed species undergoes chemical bonding (covalent or ionic) with the surface atoms of the dust grain. This creates a strong bond, with a typical binding energy of 1eV. The bond does not allow the species to diffuse across the grain surface. The species can react via Eley-Rideal reactions – where another species accretes on top of, or diffuses near to, the chemisorbed species. The Eley-Rideal reactions dominate over the Langmuir-Hinshelwood reactions at temperatures above 300K, as the physisorbed species tend to desorb at these temperatures.

2.3 The Dark Cloud Model

A pseudo-time-dependent gas-phase chemical model of a homogeneous dark cloud was constructed, similar to that of Herbst & Leung (1986), for example. The reactions used in the model were taken from the UMIST 06 database (Woodall et al., 2007). The model contained 3816 reactions and 312 species. The models were calculated using the parameters shown in Table 2.2. These physical conditions were all held to be constant for the duration of the simulations. Only gas-phase reactions were considered, except for the case of H_2 formation, where a rate was adopted appropriate for its formation on dust grain surfaces.

Parameter	Value
Temperature	10K
H_2 density	$2x10^4$ cm^{-3}
A_V	15 magnitudes
CR ionisation rate	1.3×10^{-17} s^{-1}

Table 2.2: The physical conditions used in the dark cloud models.

2.4 The Hot Core Model

The hot core model consists of two distinct parts – the first stage is the isothermal collapse of a dark cloud. This is followed by a multidepth hot core model.

2.4.1 The Isothermal Collapse Model

The Isothermal Collapse model (henceforth the Collapse model) is a modified version of the dark cloud model as described in Section 2.3. The Collapse model follows a 'packet' of gas in a dark cloud as the cloud collapses. The physical parameters used in the Collapse model can be seen in Table 2.3. The rate of change of the gas number density is modelled using the following equation:

$$\frac{\mathrm{d}n(t)}{\mathrm{d}t} = B\left(\frac{n(t)^4}{n_0}\right)^{1/3}\left\{24\pi \mathrm{G m_H} n_0\left[\left(\frac{n(t)}{n_0}\right)^{1/3} - 1\right]\right\}^{1/2} \mathrm{cm^{-3}s^{-1}}, \quad (2.12)$$

where t is time, B is the retardation factor, n_0 is the initial density of the cloud, G is the gravitational constant and m_H is the mass of a H atom. This is the modified free-fall collapse of an isothermal dark cloud, as used by Spitzer (1978). The retardation factor is used to account for the effect of external magnetic fields acting on the charged species and grains. The presence of a magnetic field causes the cloud to collapse more slowly than if the collapse were completely due to gravity (an unmodified free-fall collapse), as the charged species must cross the magnetic field lines. Once the pre-determined final density is reached ($2x10^7$ cm^{-3} in this model – a typical value for a

hot core), the collapse is halted. The temperature is constant in the Collapse model, as the collapse is assumed to be isothermal.

Dark Cloud Temperature (Collapse Model)	10K
Initial Density (Collapse Model)	2×10^{4} cm^{-3}
Final Density	2×10^{7} cm^{-3}
Visual Extinction (Collapse Model)	15 magnitudes
Cosmic Ray Ionisation Rate	1.33×10^{-17} s^{-1}
Dust/Gas Mass Ratio	100
Relative Dust Grain Number Density	1.33×10^{-12}
Dust Grain Albedo	0.5
Dust Grain Radius	1×10^{-5} cm
Surface Density of Grain Sites	7.9×10^{14} cm^{-2}
Retardation Factor (Collapse Model)	0.7

Table 2.3: The physical parameters used in the Hot Core Model. Those marked "Collapse Model" are used in the Collapse Model only. The others are used in both the Collapse Model and the Multidepth Model.

2.4.2 The Multidepth Hot Core Model

The Multidepth Hot Core model (henceforth the Multidepth model) consists of seventeen concentric shells, which extend outwards from a distance of 1x10^{-3}pc from the central protostar to a distance of 1.12x10^{-1}pc, and are separated on a logarithmic scale. The inner and outer radii of the shells, as a distance from the central protostar, are given in Table 2.4.2. Each shell has different physical conditions. The temperature profile for the hot core is given by the following equation:

$$T(r) = T_{\mathrm{C}}\left(\frac{r}{r_0}\right)^{-0.4} \mathrm{K}, \tag{2.13}$$

where T_C is the central hot core temperature and r_0 is the distance from the protostar to the inner radius of the hot core. This closely matches the expression used by Viti

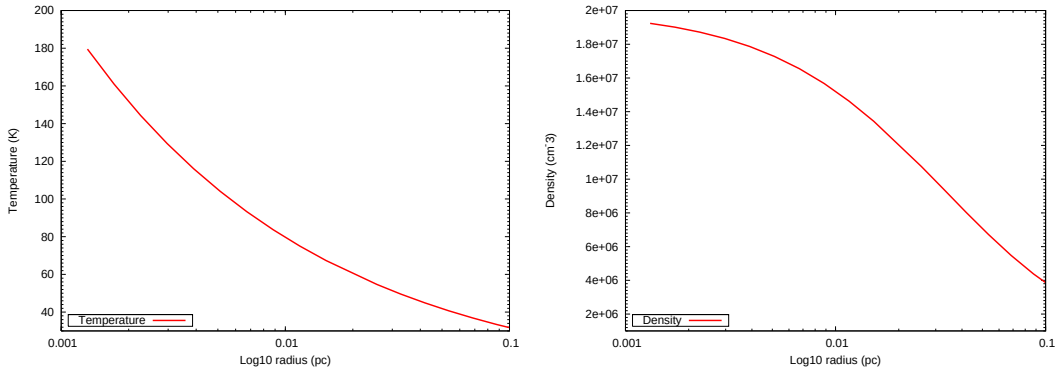

(a) The hot core temperature profile

(b) The hot core density profile

Figure 2.2: The temperature and density profiles used in the Multidepth hot core model.

& Williams (1999). The temperature distribution as a function of distance from the protostar be seen in Figure 2.2(a). The density profile adopted for the hot core model is given by the following equation:

$$n(r) = n_c \left(1 + \frac{r}{r_c}\right)^{-1.5} \text{ cm}^{-3}, \tag{2.14}$$

where n_C is the central hot core density, and r_C is the transitional radius between isothermal and non-thermal (Nomura & Millar, 2004b). Figure 2.2(b) shows the density profile as a function of distance from the protostar. For each shell, the distance from the hot core centre was used to identify the appropriate temperature and density, using equations 2.13 and 2.14.

The visual extinction is calculated using the assumption that a column density of N_H=3.1×10^{21} cm^{-2} corresponds to an A_V of 1.6 magnitudes (Millar et al., 1997b). The total hydrogen column density outside of a depth, *r*, is calculated using the following equation:

$$N(r) = \int_r^\infty n(r)\text{d}r, \text{cm}^{-2}, \tag{2.15}$$

where *n(r)* is the density profile seen in equation 2.14. The total visual extinction is then calculated by scaling the total column density using the factor described by Millar et al. (1997b).

The initial fractional abundances of the gas and grain species are different in each shell of the Multidepth model. These abundances come from the Collapse model. The density of each shell is compared with the density in the Collapse model – at the point where the densities match, the output abundances from the Collapse model are taken as the inputs for the Multidepth Hot Core model.

Once the physical and chemical inputs for each shell have been determined, a model is run for each shell, independently of the others. The physical and chemical conditions in each shell are assumed to be homogenous, and the increase in temperature is assumed to be instantaneous (the Collapse model runs at 10K). The temperature increase causes grain species to sublimate. These species are then further processed in the gas phase chemistry. The models are run up to a time of 10^7 years, which ensures the chemistry reaches steady state.

Shell	Inner radius (pc)	Outer radius (pc)	Density (cm^{-3})	Temp (K)	A_V (mag)
1	1.00E-003	1.50E-003	1.92E+007	179.4	5540.6
2	1.50E-003	1.98E-003	1.90E+007	160.8	5512.3
3	1.98E-003	2.59E-003	1.87E+007	144.2	5475.6
4	2.59E-003	3.41E-003	1.83E+007	129.4	5428.3
5	3.41E-003	4.47E-003	1.79E+007	116.0	5367.7
6	4.47E-003	5.87E-003	1.73E+007	104.0	5290.3
7	5.87E-003	7.71E-003	1.65E+007	93.3	5192.6
8	7.71E-003	1.01E-002	1.57E+007	83.7	5070.4
9	1.01E-002	1.33E-002	1.46E+007	75.0	4919.6
10	1.33E-002	2.00E-002	1.34E+007	67.3	4736.3
11	2.00E-002	2.89E-002	1.08E+007	54.7	4288.4
12	2.89E-002	3.70E-002	9.40E+006	49.6	4029.7
13	3.70E-002	4.73E-002	8.03E+006	44.9	3743.9
14	4.73E-002	6.06E-002	6.71E+006	40.7	3435.0
15	6.06E-002	7.75E-002	5.48E+006	36.9	3108.5
16	7.75E-002	9.91E-002	4.38E+006	33.4	2771.2
17	9.91E-002	1.27E-001	3.43E+006	30.3	2430.1

Table 2.4: The Multidepth Model Shell Physical Parameters

3

Dark cloud modelling at low metallicity

3.1 Introduction

Dark clouds are cold clouds of gas and dust which can condense and collapse to form stars (see Table 2.2 for typical conditions). Observations and models of these regions are important, as they provide insight into the star formation process, as well as yielding information regarding metallicity and chemical enrichment on both solar and galactic scales. In this chapter, a dark cloud is modelled at low metallicity, in an attempt to model the extragalactic environments of the Large and Small Magellanic Clouds (henceforth LMC and SMC). The wider motivation behind this work is a desire to increase understanding of how individual star-forming regions have evolved, and influenced galaxies, over cosmological timescales. The advent of new facilities, such as ALMA[1], will allow components of distant galaxies to be resolved at a higher level of detail than is currently possible. ALMA will be able to detect radiation from abundant molecules up to a redshift of z=10, effectively showing us the contents of these galaxies as they were over 12 billion years ago. Figure 3.1 shows which rota-

[1] www.almaobservatory.org

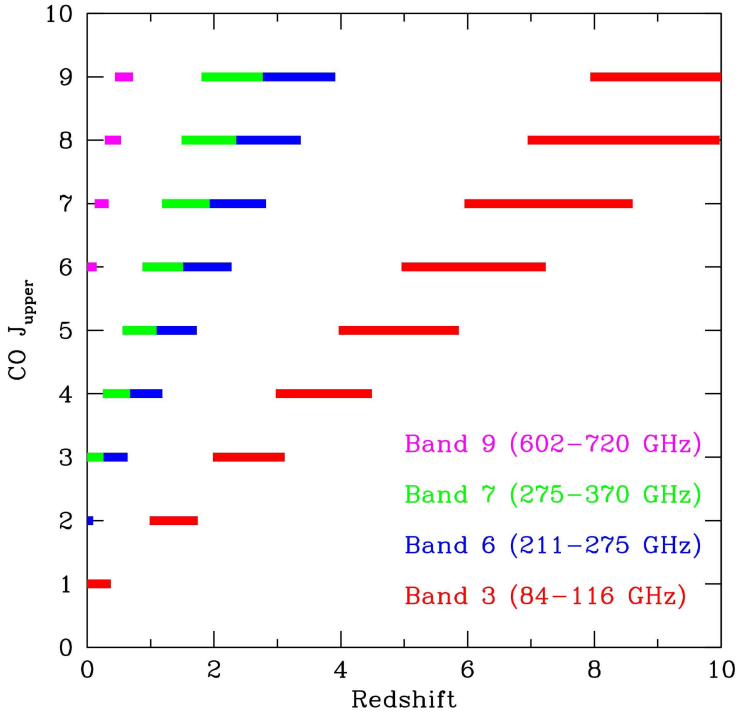

Figure 3.1: Credit: www.mma.nrao.edu/science/sciencegoals.html. This figure shows which rotational (J) CO transitions can be observed with ALMA, and to which redshift they correspond. The higher rotational transitions of CO are not observable at sub-mm wavelengths in the Galaxy. However, at high redshifts their wavelengths move into the observing bands of ALMA, whereas transitions commonly observed in the Galaxy, such as J=3-2, move out of these bands.

tional transitions of CO ALMA will be able to observe as a function of redshift. The LMC and SMC are particularly interesting to model, as the low degree of metallicity in these dwarf galaxies is thought to be similar to that which existed in galaxies in the early Universe. The results from the LMC and SMC modelling could therefore be used to explain/predict observations of other galaxies at a high redshift.

A metallicity tracer species (i.e. a certain molecule or molecular or atomic ion) provides a measure of the underlying abundance of metals in a region. The region modelled in this chapter is a dark cloud, and the metals included in the model are carbon, oxygen, nitrogen, sulphur and the heavy metals (iron, magnesium and sodium, collectively referred to as M). A general metallicity tracer would give an estimate of the underlying metallicity in a cloud e.g., how much C, O, N, S and M there was

in total. An elemental metallicity tracer would give an estimate for the underlying abundance of one element in a cloud, e.g. carbon. It is useful to know the metallicity of dark clouds, as the star formation process begins in these regions. The degree of metallicity in a cloud can be used to infer the cosmological age of the region, and/or how processed the material is. The metallicity of a dark cloud will also have an effect on whether/how a star forms, as the ionisation fraction in a cloud is affected by the metallicity. If a star does form in a particular cloud, the metallicity of the cloud will also determine the initial composition of the star, and will affect the surrounding region through circumstellar chemistry, and dust formation.

3.2 The NK Dark Cloud Chemical Model

A pseudo-time-dependent gas-phase chemical model of a homogeneous dark cloud was used, as described in Section 2.3, to model such regions under low metallicity conditions which are found in other galaxies – in particular, the LMC and SMC. This model is henceforth known as the NK dark cloud chemical model. The model does not contain depletion onto grain surfaces, or grain surface chemistry. The gas-phase results are considered to be sufficiently accurate for use in comparison with extragalactic observations, which have a low level of resolution. When referring to the models used, it is useful to define some commonly used terms. When ‘early time’ is used in reference to the dark cloud models, it is referring to the time before the abundances in the model have reached steady state - e.g. when the abundances are still changing. Steady state refers to the time when the abundances have reached chemical equilibrium, and no changes occur.

3.2.1 Time Scales

As discussed in Section 1.2.3, the time scales over which physical processes, such as free-fall collapse and freeze-out, occur can impact the chemistry. The steady state gas-

phase chemistry examined in this model may not occur in reality. The freeze-out time scale estimated for this model is 4×10^4 years. It is likely that the gas-phase species will all freeze out onto grain surfaces beyond this time, and so the chemistry seen at 10^7 years may not be a physical representation of what is occuring in SFRs. Accretion onto dust grains and the ensuing surface chemistry are not included in the NK dark cloud model. If these processes were modelled, a more accurate estimate for the freeze-out time scale could be obtained. This could provide the basis for future work.

3.2.2 Initial elemental abundances

The model inputs are taken from observed chemical abundances in the Milky Way, the LMC and the SMC (e.g. Woodall et al. 2007, Garnett 1999). Twelve models were produced, each with different metallicity. All of the initial elemental fractional abundances used in the models are shown in Table 3.1. The initial elemental abundances came from several sources. In models G, L and S, the carbon, oxygen, nitrogen, sulphur and M abundances were taken from observations in the Galaxy, the Large Magellanic Cloud and the Small Magellanic Cloud respectively. The Galactic abundances were taken from TMC-1, a well-studied Galactic dark cloud. The Magellanic abundances were taken from HII region observations in the LMC and SMC. The observed sulphur abundances in the Magellanic Clouds were depleted by a ratio found from Galactic HII region/dark cloud sulphur observations. This was done as follows. An observed fractional abundance of sulphur was taken from a Galactic HII region ($4.36\text{x}10^{-6}$ taken from García-Rojas et al. 2007). This number was divided by a dark cloud fractional abundance of sulphur, taken from the Galactic dark cloud TMC-1 ($2.00\text{x}10^{-8}$ taken from Woodall et al. 2007), to give a ratio of 217. This ratio was used to deplete the fractional sulphur abundances in the LMC and SMC models, L and S. It is possible that the depletion factor would be different in the Magellanic Clouds, owing to the lower dust/gas ratio in these galaxies. However, it is unclear if/how the ratio would change when compared with the Milky Way, and so the factor of 217 was used to deplete both

the LMC and SMC HII sulphur observations.

The models DC2-DC5 used intermediate abundance values, which were interpolated between the observed abundances used in models G, L and S. For example, models DC2 and DC3 had abundances scaled to be 1/3 and 2/3 of the way between those in models G and L. Models DC6-DC9 used abundances which were reduced to further test the results from the G, L and S models, and model DC1 used fractional abundances greater than those found in the Milky Way.

The dust/gas ratio was also changed in the models - the L and S model values were taken from Millar & Herbst 1990. The DUST parameter in Table 3.1 reflects how the dust/gas ratio used in Model G was scaled up or down in the other models. In models DC2-DC5, the DUST parameter was interpolated between the G, L and S values. For example, models DC2 and DC3 have DUST values which are respectively 1/3 and 2/3 of the way between the DUST values in models G and L. Models DC1 and DC6-9 used extrapolated DUST parameters, which are outside of the range used in models G, L and S.

3.3 Verification of the NK Dark Cloud Model

3.3.1 Comparison of the NK Dark Cloud Model with the Woodall et al. (2007) TMC1 Model

The results of model G were compared with those from the model of TMC-1 by Woodall et al. (2007). The input parameters for the two models are identical, the only difference between the models is that the NK TMC1 model does not contain the species F, P, Si or Cl. Table 3.2 shows the steady state fractional abundances of some common species in both models. The results from the two models are very similar. As seen in the third column of Table 3.2, the fractional abundance outputs tend to differ by only a few percent between the two models. The largest difference seen is in CS, where the NK TMC1 abundance is higher.

Model	Initial fractional elemental abundances					
	Carbon	**Oxygen**	**Nitrogen**	**Sulphur**	**M**	**DUST**
DC1	1.85E-004	3.87E-004	1.42E-004	1.48E-007	1.95E-008	1.750
G[1]	1.32E-004	3.19E-004	7.50E-005	8.57E-008	1.50E-008	1.000
NK TMC1	7.30E-005	1.76E-004	2.14E-005	2.00E-008	9.00E-009	1.000
DC2	1.14E-004	2.96E-004	5.26E-005	6.48E-008	1.35E-008	0.750
DC3	9.70E-005	2.74E-004	3.03E-005	4.39E-008	1.20E-008	0.500
L[2]	7.94E-005	2.51E-004	7.94E-006	2.30E-008	1.05E-008	0.250
DC4	6.13E-005	2.01E-004	6.35E-006	1.84E-008	7.59E-009	0.186
DC5	4.32E-005	1.50E-004	4.76E-006	1.38E-008	4.70E-009	0.123
S[2]	2.51E-005	1.00E-004	3.16E-006	9.16E-009	1.82E-009	0.059
DC6	7.94E-006	3.98E-005	1.26E-006	3.65E-009	3.16E-010	0.014
DC7	3.97E-006	1.99E-005	6.29E-007	1.82E-009	1.58E-010	0.007
DC8	3.18E-006	1.59E-005	5.03E-007	1.46E-009	1.26E-010	0.006
DC9	2.38E-006	1.19E-005	3.78E-007	1.09E-009	9.48E-011	0.004

Table 3.1: The initial fractional elemental abundances used in the dark cloud models. All abundances are given relative to H_2. The abundances in models G, L and S are taken from observations in the corresponding galaxy, where G is the Milky Way, L is the LMC and S is the SMC. The abundances in models DC2-DC5 are interpolated between the G, L and S values. The abundances in models DC1 and DC6-DC9 are extrapolated outside the G, L and S values. [1] The Galactic abundances were taken from Woodall et al. (2007). [2] The LMC and SMC abundances were taken from: Garnett (1999); García-Rojas et al. (2007); Lebouteiller et al. (2008).

Figures 3.2, 3.3 and 3.4 show the fractional abundance of some common species, as a function of time, in the models NK TMC1 and Rate 06 TMC1. By comparing Figure 3.2(a) with Figure 3.2(b) it is apparent that most of the sulphur-bearing species evolve in a similar manner in the two models. However, the fractional CS abundance in model NK TMC1 behaves quite differently to that seen in Rate 06 TMC1. This is caused by

	NK TMC	**Rate 06 TMC**	**NK as a % of Rate 06**
CH_3OH	1.97E-012	1.69E-012	116.33
CH_4	6.94E-008	6.58E-008	105.47
CO	1.45E-004	1.46E-004	99.59
CS	2.65E-010	1.69E-010	156.63
e^-	3.70E-008	3.70E-008	99.86
H_2O	2.43E-006	1.99E-006	121.86
H_2S	7.64E-011	6.67E-011	114.54
HCN	6.61E-009	5.89E-009	112.19
HCO^+	8.50E-009	9.09E-009	93.53
HNC	1.12E-008	1.02E-008	109.9
NH_3	1.82E-007	1.93E-007	94.09
NO	6.93E-006	8.23E-006	84.17
O	6.89E-005	4.91E-005	140.33
O_2	6.36E-005	7.32E-005	86.9
OCS	2.53E-010	2.32E-010	108.84
OH	1.26E-007	1.46E-007	85.96
S	1.53E-008	1.27E-008	120.16
SO	1.06E-008	1.06E-008	99.62
SO_2	1.35E-008	1.62E-008	83.33

Table 3.2: A comparison of steady state fractional abundances (to H_2) for NK TMC1 and Rate 06 TMC1 (Woodall et al., 2007).

the exclusion of the elements Cl, Si, P and F from model NK TMC1, as this is the only difference between the two models. Figure 3.3 shows how some oxygen-bearing species evolve in the two models. Between 10^3 and 10^4 years, the species CO, OH, H_2O, NO and O_2 behave quite differently in model NK TMC1 when compared with model Rate 06 TMC1. This can again be attributed to the exclusion of Cl, Si, P and F from NK TMC1. It can be seen that H_2O has a noticeably higher steady state fractional

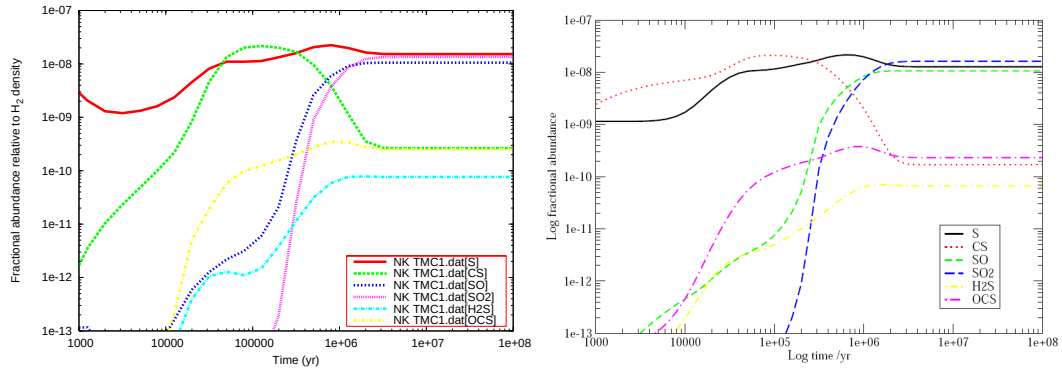

(a) NK TMC1 (b) Rate 06 TMC1

Figure 3.2: Some sulphur-bearing species in models NK TMC1 and Woodall et al. (2007) TMC1. Figure 3.2(b) is taken from Woodall et al. (2007).

abundance in model NK TMC. The other species have similar steady state abundances in both models. Figure 3.4 shows the fractional abundance of CH_3OH in models NK TMC and Rate 06 TMC. The fractional CH_3OH abundance seen in both models is similar at most times. Overall the results from the dark cloud model NK TMC compare well with the results from the TMC model results in Woodall et al. (2007). For this reason, the NK dark cloud model results can be considered comparable with results from similar chemical models, in terms of accuracy.

3.3.2 Comparison of the NK Dark Cloud Models with the Millar & Herbst (1990) Models

Millar & Herbst (1990) created pseudo-time-dependent gas-phase chemical models of dark clouds in the Milky Way, the LMC and the SMC (henceforth these models shall be referred to as the MH models). The initial fractional abundances and dust/gas ratios used in the MH and NK models are shown in Table 3.3. The DUST parameter refers to the dust/gas ratio as a fraction of the dust/gas ratio used in the Galactic model. The dust/gas ratios used in the NK models are taken from the MH models. The input

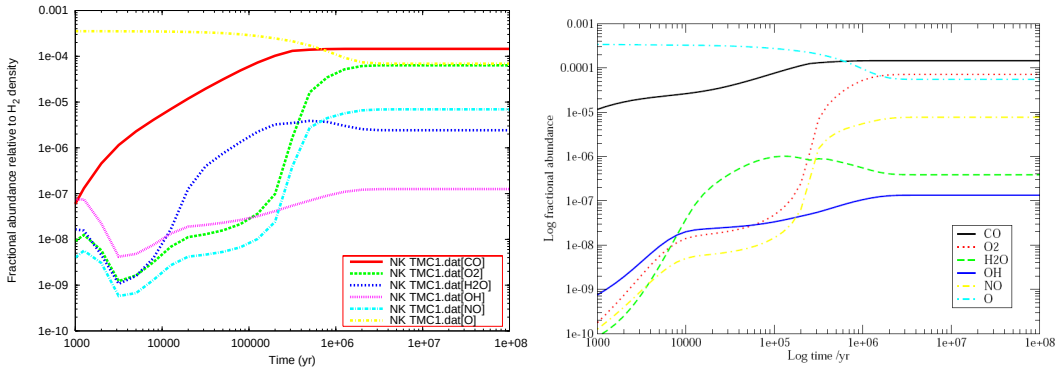

(a) NK TMC1 (b) Rate 06 TMC1

Figure 3.3: Some oxygen-bearing species in models NK TMC1 and Woodall et al. (2007) TMC1. Figure 3.3(b) is taken from Woodall et al. (2007).

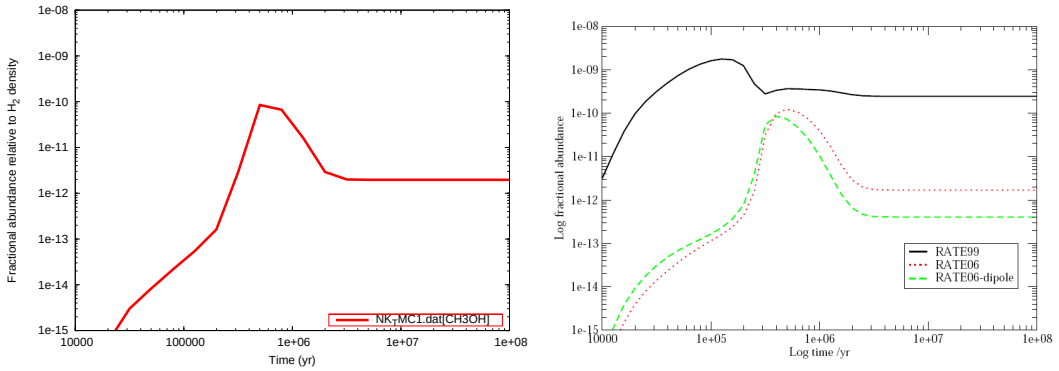

(a) NK TMC1 (b) Rate 06 TMC1

Figure 3.4: The fractional CH_3OH abundance in models NK TMC1 and Woodall et al. (2007) TMC1. The red dotted line in Figure 3.4(b) represents model Rate 06 TMC1. Figure 3.4(b) is taken from Woodall et al. (2007).

abundances are different, as more recent observations were used to determine the inputs for the NK models. The NK models include sulphur, unlike the MH models. The MH models include two LMC and two SMC models. Models L1 and S1 use observations of HII regions in the LMC and SMC for the input abundances. These values are taken from Bel et al. (1986). Models L2 and S2 use depletion factors taken from

the authors' previous dark cloud models, to deplete the Bel et al. (1986) abundances to a level thought to be representative of a dark cloud. The NK model inputs are taken from several sources, as shown in Table 3.1.

The results from the models will be different for a number of reasons. Some of the

Model	**Initial fractional elemental abundances**					
	Carbon	**Oxygen**	**Nitrogen**	**Sulphur**	**DUST**	**O/C**
NK G	1.32E-004	3.19E-004	7.50E-005	8.57E-008	1.000	2.4
NK L	7.94E-005	2.51E-004	7.94E-006	2.30E-008	0.250	3.2
NK S	2.51E-005	1.00E-004	3.16E-006	9.16E-009	0.059	4.0
MH G	1.46E-004	3.52E-004	4.28E-005	-	1.000	2.4
MH L1	1.58E-004	4.80E-004	1.74E-005	-	0.250	3.0
MH L2	3.08E-005	1.25E-004	3.24E-006	-	0.250	4.1
MH S1	2.80E-005	2.20E-004	8.00E-006	-	0.059	7.9
MH S2	5.46E-006	5.72E-005	1.49E-006	-	0.059	10.5

Table 3.3: The NK and MH dark cloud model input fractional abundances and dust/gas ratios. The fractional abundances used in the MH models were taken from Bel et al. (1986).

reaction sets, rates and branching ratios have changed since Millar & Herbst (1990) was written. The initial fractional abundances are different in each model. Sulphur is added to all the NK models, but is not included in any of the MH models. This will obviously cause some changes to the results, but these should be fairly small as the fractional sulphur abundance is low in all of the NK models. The initial abundances of the heavy metals (M) are also different in the NK models. The MH models each contain the same fractional M abundance - the abundance is not quoted by Millar & Herbst (1990).

The O/C ratios used in models NK G and MH G, and L and L1, are similar, as seen in Table 3.3. However the O/C ratios in models S1 and S2 are very different to that in model S. Tables 3.4 and 3.5 summarise the comparison between the models at early time and steady state respectively. A sample of twenty-three common species were

compared. The species were grouped by how good the comparison was between the NK and MH model pairs (the NK model L was compared with both MH L1 and L2, and NK model S was compared with both MH S1 and S2). For example, Table 3.4 shows that in models NK G and MH G, there are five species which differ by less than 50% between the two models at early time. There are twelve species which vary within one order of magnitude, four which vary within two orders of magnitude, and two species which vary by more than two orders of magnitude. Tables 3.6– 3.15 show the fractional abundances produced by the NK and MH model pairs at early time and steady state. The column on the right in each table shows the NK model abundance as a fraction of the MH model abundance. If this parameter is greater than one, then more of this species is produced in the NK model. If the parameter is less than one, more of the species is produced in the MH model. A very high or very low number shows that the model results differ quite dramatically. These changes are caused by the different fractional abundance inputs, as well as the changes in the reaction rates and branching ratios which have been implemented in the models since Millar & Herbst (1990) was written. For example, the modelling of methanol was changed in the UDfA 2006 by Woodall et al. (2007), when improved rates for methanol formation were experimentally deduced (Geppert et al. 2006, Luca et al. 2002). A reduced branching ratio for the formation of methanol from $CH_3OH_2^+$ via dissociative recombination was included in the 2006 version of the UDfA. Additionally, the formation rate of $CH_3OH_2^+$ via reaction between CH_3^+ and H_2O was found experimentally to be two orders of magnitude lower than assumed. This was also included in the UDfA 2006, and the combination of these two changes led to much lower abundances of methanol being produced in the dark cloud chemical models.

Tables 3.6 and 3.7 show that the NK G and MH G model results compare reasonably well at both early time and steady state. At early time, much less methanol is produced in the NK G model compared with the MH G model. By steady state, the fractional CH_3OH abundances in the two models are much more similar. This shows that the reaction rates and formation routes for CH_3OH have considerably changed

EARLY TIME	**Difference**			
	<±50%	**<factor of 10**	**<factor of 100**	**>factor of 100**
NK G vs MH G	5	12	4	2
NK L vs MH L1	9	9	3	2
NK L vs MH L2	3	10	8	2
NK S vs MH S1	6	13	3	1
NK S vs MH S2	0	10	13	0

Table 3.4: Summary of NK and MH model comparison at early time (3.6×10^5 years).

STEADY STATE	**Difference**			
	<±50%	**<factor of 10**	**<factor of 100**	**>factor of 100**
NK G vs MH G	4	10	7	2
NK L vs MH L1	6	10	5	2
NK L vs MH L2	3	10	7	3
NK S vs MH S1	2	15	5	1
NK S vs MH S2	3	12	5	3

Table 3.5: Summary of NK and MH model comparison at steady state ($>10^7$ years).

in the chemical models since 1990. The changes made to the CH_3OH modelling are discussed earlier in Section 3.3.2. H_2CO is modelled differently in the NK models, compared with the MH models. Much less H_2CO is produced in the NK models, as the results tables show. The modelling of this species has changed a lot since the Millar & Herbst (1990) models were created, both at early time and steady state. Woodall et al. (2007) implemented a large decrease to the reaction rate for H_2CO formation via reaction between C_2H_3 and O_2. This change results in the much lower H_2CO abundance in the NK models. The species CH_3CN and HCO^+ are formed in similar quantities in models NK G and MH G, at both early time and steady state. The formation and destruction of these species are modelled in a similar way in the MH and NK models. Tables 3.8, 3.9, 3.10 and 3.11 show that the NK L model compares slightly more fa-

3.6×10^5 years	**NK G**	**MH G**	**NK G / MH G**
C	3.17E-005	5.40E-006	5.86
C^+	6.33E-009	1.50E-009	4.22
C_2H	7.28E-009	3.50E-008	0.21
C_3H	6.13E-009	2.70E-007	0.02
C_3H_2	8.44E-009	1.00E-007	0.08
CH_3CN	3.33E-008	2.90E-008	1.15
CH_3OH	3.77E-013	1.70E-008	0.00
CN	1.46E-008	2.80E-008	0.52
CO	2.04E-004	1.10E-004	1.85
e^-	4.84E-008	2.30E-008	2.10
H_2CO	4.74E-010	2.30E-006	0.00
H_2O	5.22E-006	3.00E-006	1.74
H_3O^+	5.66E-009	4.00E-009	1.42
HC_3N	8.33E-008	9.20E-009	9.06
HCN	2.52E-007	3.80E-008	6.63
HCO^+	3.79E-009	6.70E-009	0.57
HNC	2.01E-007	2.10E-008	9.58
N	5.71E-005	3.50E-005	1.63
N_2	4.61E-005	3.70E-006	12.45
NH_3	7.72E-008	9.40E-009	8.21
NO	3.01E-008	5.90E-008	0.51
O	4.28E-004	2.20E-004	1.95
OH	2.01E-008	2.60E-007	0.08

Table 3.6: The NK G and MH G model results at early time (3.6×10^5 years).

10^7 years	**NK G**	**MH G**	**NK G / MH G**
C	6.72E-009	3.30E-010	20.37
C^+	1.13E-009	9.80E-010	1.15
C_2H	2.25E-011	2.00E-009	0.01
C_3H	8.44E-013	2.00E-009	0.00
C_3H_2	9.79E-011	6.00E-010	0.16
CH_3CN	1.16E-011	1.50E-011	0.77
CH_3OH	1.32E-012	1.10E-011	0.12
CN	3.09E-011	5.90E-010	0.05
CO	2.63E-004	1.50E-004	1.75
e^-	4.32E-008	2.60E-008	1.66
H_2CO	7.87E-012	1.00E-008	0.00
H_2O	4.33E-006	7.10E-007	6.10
H_3O^+	5.17E-009	1.40E-009	3.69
HC_3N	4.04E-012	2.70E-012	1.50
HCN	7.07E-009	3.90E-010	18.13
HCO^+	6.54E-009	1.20E-008	0.55
HNC	1.40E-008	1.10E-009	12.76
N	5.59E-006	9.20E-007	6.07
N_2	6.95E-005	2.10E-005	3.31
NH_3	2.65E-007	3.60E-008	7.37
NO	5.14E-006	1.80E-007	28.53
O	1.89E-004	3.70E-005	5.10
OH	5.51E-008	7.30E-007	0.08

Table 3.7: The NK G and MH G model results at steady state (>10^7 years).

3.6×10^5 years	**NK L**	**MH L1**	**NK L / MH L1**
C	5.65E-007	6.70E-006	0.08
C^+	9.77E-009	1.70E-009	5.75
C_2H	5.97E-009	2.10E-008	0.28
C_3H	4.12E-009	2.30E-007	0.02
C_3H_2	8.11E-008	8.60E-008	0.94
CH_3CN	2.13E-010	8.90E-009	0.02
CH_3OH	2.41E-012	1.90E-008	0.00
CN	4.62E-009	1.20E-008	0.38
CO	1.49E-004	1.20E-004	1.24
e^-	4.56E-008	2.20E-008	2.07
H_2CO	1.10E-010	1.90E-006	0.00
H_2O	3.84E-006	3.90E-006	0.98
H_3O^+	7.23E-009	4.90E-009	1.47
HC_3N	4.65E-009	3.10E-009	1.50
HCN	9.90E-009	1.40E-008	0.71
HCO^+	4.52E-009	6.10E-009	0.74
HNC	7.40E-009	7.80E-009	0.95
N	4.95E-006	1.60E-005	0.31
N_2	5.33E-006	8.20E-007	6.50
NH_3	1.58E-008	2.40E-009	6.57
NO	1.44E-007	4.10E-008	3.50
O	3.45E-004	3.30E-004	1.05
OH	4.56E-008	2.40E-007	0.19

Table 3.8: The NK L and MH L1 model results at early time (3.6×10^5 years).

10^7 years	NK L	MH L1	NK L / MH L1
C	3.00E-009	9.60E-010	3.13
C^+	8.36E-010	5.80E-010	1.44
C_2H	1.98E-011	8.30E-010	0.02
C_3H	4.46E-013	6.50E-010	0.00
C_3H_2	3.73E-011	1.60E-010	0.23
CH_3CN	2.48E-012	2.90E-012	0.86
CH_3OH	7.98E-013	7.20E-012	0.11
CN	7.94E-012	1.10E-010	0.07
CO	1.59E-004	1.60E-004	0.99
e^-	3.86E-008	2.50E-008	1.55
H_2CO	1.76E-011	6.20E-009	0.00
H_2O	3.57E-006	8.40E-007	4.25
H_3O^+	6.19E-009	1.60E-009	3.87
HC_3N	3.53E-013	3.10E-013	1.14
HCN	1.52E-009	8.30E-011	18.33
HCO^+	7.62E-009	1.30E-008	0.59
HNC	2.32E-009	2.30E-010	10.08
N	1.03E-006	3.50E-007	2.94
N_2	5.23E-006	8.40E-006	0.62
NH_3	6.52E-008	1.30E-008	5.01
NO	4.31E-006	1.80E-007	23.96
O	9.57E-005	4.20E-005	2.28
OH	1.21E-007	7.20E-007	0.17

Table 3.9: The NK L and MH L1 model results at steady state (>10^7 years).

3.6×10^5 years	**NK L**	**MH L2**	**NK L / MH L2**
C	5.65E-007	8.20E-009	68.91
C^+	9.77E-009	9.20E-010	10.62
C_2H	5.97E-009	2.60E-008	0.23
C_3H	4.12E-009	6.90E-008	0.06
C_3H_2	8.11E-008	2.70E-008	3.00
CH_3CN	2.13E-010	3.30E-010	0.65
CH_3OH	2.41E-012	4.90E-010	0.00
CN	4.62E-009	2.60E-009	1.78
CO	1.49E-004	2.90E-005	5.13
e^-	4.56E-008	3.30E-008	1.38
H_2CO	1.10E-010	1.90E-007	0.00
H_2O	3.84E-006	9.30E-007	4.12
H_3O^+	7.23E-009	2.40E-009	3.01
HC_3N	4.65E-009	1.30E-010	35.75
HCN	9.90E-009	6.20E-010	15.97
HCO^+	4.52E-009	6.50E-009	0.70
HNC	7.40E-009	5.50E-010	13.45
N	4.95E-006	8.20E-007	6.04
N_2	5.33E-006	1.00E-006	5.33
NH_3	1.58E-008	2.70E-009	5.84
NO	1.44E-007	3.30E-007	0.44
O	3.45E-004	3.00E-005	11.51
OH	4.56E-008	1.70E-006	0.03

Table 3.10: The NK L and MH L2 model results at early time (3.6×10^5 years).

10^7 years	NK L	MH L2	NK L / MH L2
C	3.00E-009	3.80E-010	7.90
C^+	8.36E-010	7.90E-010	1.06
C_2H	1.98E-011	8.50E-010	0.02
C_3H	4.46E-013	3.60E-010	0.00
C_3H_2	3.73E-011	1.30E-010	0.29
CH_3CN	2.48E-012	1.30E-012	1.91
CH_3OH	7.98E-013	3.60E-012	0.22
CN	7.94E-012	2.60E-007	0.00
CO	1.59E-004	3.10E-005	5.11
e^-	3.86E-008	3.60E-008	1.07
H_2CO	1.76E-011	6.00E-009	0.00
H_2O	3.57E-006	4.60E-007	7.76
H_3O^+	6.19E-009	1.40E-009	4.42
HC_3N	3.53E-013	1.20E-013	2.94
HCN	1.52E-009	4.10E-011	37.10
HCO^+	7.62E-009	8.10E-009	0.94
HNC	2.32E-009	5.80E-011	39.97
N	1.03E-006	9.10E-008	11.31
N_2	5.23E-006	1.40E-006	3.74
NH_3	6.52E-008	2.70E-009	24.14
NO	4.31E-006	2.60E-007	16.58
O	9.57E-005	1.00E-005	9.57
OH	1.21E-007	2.50E-006	0.05

Table 3.11: The NK L and MH L2 model results at steady state (>10^7 years).

3.6×10^5 years	**NK S**	**MH S1**	**NK S / MH S1**
C	1.98E-009	3.40E-009	0.58
C^+	3.17E-009	5.10E-010	6.21
C_2H	2.21E-009	5.40E-009	0.41
C_3H	1.04E-009	3.80E-008	0.03
C_3H_2	6.85E-008	1.50E-008	4.57
CH_3CN	3.62E-011	1.80E-010	0.20
CH_3OH	7.11E-011	6.40E-010	0.11
CN	1.35E-010	5.00E-010	0.27
CO	4.91E-005	2.70E-005	1.82
e^-	3.15E-008	2.70E-008	1.17
H_2CO	2.25E-010	1.40E-007	0.00
H_2O	4.25E-006	2.30E-006	1.85
H_3O^+	1.16E-008	4.60E-009	2.51
HC_3N	2.93E-010	1.20E-010	2.44
HCN	9.58E-009	5.70E-010	16.81
HCO^+	5.39E-009	4.50E-009	1.20
HNC	9.02E-009	4.80E-010	18.80
N	1.45E-006	2.80E-006	0.52
N_2	1.50E-006	2.50E-006	0.60
NH_3	5.41E-008	6.70E-009	8.07
NO	1.67E-006	2.50E-007	6.68
O	1.00E-004	8.70E-005	1.15
OH	1.65E-007	1.00E-006	0.17

Table 3.12: The NK S and MH S1 model results at early time (3.6×10^5 years).

10^7 years	**NK S**	**MH S1**	**NK S / MH S1**
C	1.97E-009	1.20E-010	16.45
C^+	1.21E-009	2.90E-010	4.18
C_2H	6.71E-011	1.50E-010	0.45
C_3H	1.71E-012	3.70E-011	0.05
C_3H_2	4.10E-011	1.00E-011	4.10
CH_3CN	5.67E-012	9.30E-013	6.10
CH_3OH	5.22E-013	1.50E-012	0.35
CN	1.48E-011	4.90E-007	0.00
CO	5.01E-005	2.80E-005	1.79
e^-	3.18E-008	3.40E-008	0.94
H_2CO	2.53E-010	2.30E-009	0.11
H_2O	1.72E-006	5.30E-007	3.25
H_3O^+	6.04E-009	1.50E-009	4.02
HC_3N	1.34E-013	1.40E-014	9.59
HCN	2.62E-009	3.20E-011	81.72
HCO^+	9.36E-009	7.80E-009	1.20
HNC	3.45E-009	4.70E-011	73.43
N	3.61E-007	1.00E-007	3.61
N_2	5.67E-007	3.70E-006	0.15
NH_3	1.00E-007	5.80E-009	17.31
NO	4.69E-006	4.90E-007	9.57
O	1.82E-005	9.50E-006	1.91
OH	4.43E-007	2.90E-006	0.15

Table 3.13: The NK S and MH S1 model results at steady state (>10^7 years).

3.6×10^5 years	**NK S**	**MH S2**	**NK S / MH S2**
C	1.98E-009	8.10E-010	2.44
C^+	3.17E-009	2.20E-010	14.40
C_2H	2.21E-009	2.90E-008	0.08
C_3H	1.04E-009	4.80E-008	0.02
C_3H_2	6.85E-008	1.70E-008	4.03
CH_3CN	3.62E-011	1.70E-011	2.13
CH_3OH	7.11E-011	5.00E-012	14.23
CN	1.35E-010	6.40E-009	0.02
CO	4.91E-005	4.70E-006	10.45
e^-	3.15E-008	6.60E-008	0.48
H_2CO	2.25E-010	3.80E-009	0.06
H_2O	4.25E-006	4.50E-007	9.44
H_3O+	1.16E-008	1.70E-009	6.79
HC_3N	2.93E-010	1.00E-010	2.93
HCN	9.58E-009	8.30E-010	11.54
HCO^+	5.39E-009	2.00E-009	2.69
HNC	9.02E-009	8.10E-010	11.14
N	1.45E-006	7.20E-008	20.15
N_2	1.50E-006	4.40E-007	3.42
NH_3	5.41E-008	5.90E-010	91.66
NO	1.67E-006	5.10E-007	3.27
O	1.00E-004	2.90E-006	34.47
OH	1.65E-007	6.10E-006	0.03

Table 3.14: The NK S and MH S2 model results at early time (3.6×10^5 years).

10^7 years	NK S	MH S2	NK S / MH S2
C	1.97E-009	1.10E-010	17.95
C^+	1.21E-009	2.50E-010	4.85
C_2H	6.71E-011	2.60E-010	0.26
C_3H	1.71E-012	5.50E-011	0.03
C_3H2	4.10E-011	2.00E-011	2.05
CH_3CN	5.67E-012	1.10E-012	5.15
CH_3OH	5.22E-013	7.50E-013	0.70
CN	1.48E-011	2.80E-007	0.00
CO	5.01E-005	5.40E-006	9.28
e^-	3.18E-008	6.20E-008	0.51
H_2CO	2.53E-010	9.10E-010	0.28
H_2O	1.72E-006	4.70E-007	3.67
H_3O^+	6.04E-009	1.80E-009	3.35
HC_3N	1.34E-013	3.60E-014	3.73
HCN	2.62E-009	3.00E-011	87.17
HCO^+	9.36E-009	2.30E-009	4.07
HNC	3.45E-009	3.00E-011	115.03
N	3.61E-007	4.50E-008	8.02
N_2	5.67E-007	5.80E-007	0.98
NH_3	1.00E-007	8.90E-010	112.81
NO	4.69E-006	2.80E-007	16.75
O	1.82E-005	2.80E-006	6.50
OH	4.43E-007	6.50E-006	0.07

Table 3.15: The NK S and MH S2 model results at steady state (>10^7 years).

vourably with model L1 than L2, at both early time and steady state. Most of the species modelled are different by one order of magnitude or less when comparing model L with L1. Fewer of the species match so closely when comparing model L with L2. Generally, most species are underproduced in model L when compared with L1, and overproduced in model L when compared with L2. This makes sense, as the input abundances in model L are partway between those for models L1 and L2, as seen in Table 3.3.

Tables 3.12, 3.13, 3.14 and 3.15 show that the NK S model results are closer to those of model S1 than S2. Table 3.3 shows that the input abundances in model S are closer to model S1 than model S2, so this result is sensible. The fractional carbon input abundance is particularly similar in models S and S1. The oxygen abundance is higher in S1 than S, by a factor of 2.2. However, as the models are oxygen rich, the results should not be strongly affected by this. The nitrogen input abundance in model S1 is also higher than than in model S, by a factor of 2.5. This explains why many nitrogen-bearing species are underproduced in model S when compared with model S1, at early time. The results from model S2 tend to be quite different to those seen in model S, particularly at early time, when most of the species are produced in abundances which differ by more than one order of magnitude between models S and S2. This differing chemistry is caused by the different O/C ratio in the two models, as seen in Table 3.3.

Overall, the differences in the results produced by the NK and MH models can be explained. The differing input abundances, and the changes in dark cloud chemical modelling since 1990, account for these differences. The results produced are reasonably similar, as few species are produced in abundances which differ by more than two orders of magnitude.

3.3.3 Comparison of the NK Dark Cloud Model with Observations

Table 3.16 shows some observed fractional abundances from the dark cloud TMC-1, as well as the corresponding fractional abundances from the model NK TMC1 at 1.3×10^5

years. Overall, the comparison between the NK TMC1 model and the TMC-1 observations shows that the chemical model is reasonably consistent with observations. Most of the species shown are somewhat overproduced by the model when compared with the observations – particularly HCN, HNC and CH_3CN. A number of species are underproduced – most notably H_2CO. The overproduction/underproduction of some species by the model could be caused by a number of factors, including errors in the chemical modelling of these species, such as incorrect reaction rates or branching ratios. Certain formation or destruction reactions may be missing from the reaction network, and this could cause over/underproduction of these species. The exclusion of grain surface depletion and chemistry from the model could also explain the discrepancies between the modelled and observed values. However, the model is not able to reproduce certain observed fractional abundances, and so the resulting modelled abundances for some species must be considered more uncertain than for other species which appear to be modelled more accurately.

3.4 Results from the NK Dark Cloud Models

The models were used to identify potential metallicity tracer species or ratios – e.g. observable species which could be used to predict or constrain the underlying metallicity of a dark cloud and could trace the abundance of all metals, or a particular metal. As most Galactic dark clouds are thought to be between 10^5 and 10^6 years old, the model results were mainly analysed between these ages, as well as at later times when the chemistry had reached steady state (usually around 10^7 years). Only species which have been observed in extragalactic regions[2] are discussed, as the intention of this work is to predict tracer species which it is possible to observe. As a rough estimate, a fractional abundance greater than 10^{-10} could be observed in an extragalactic dark cloud.

[2] www.astro.uni-koeln.de/site/vorhersagen/molecules/extragalactic

Species	Observed	Modelled	Mod/Obs
CO	3.00E-005	3.66E-005	1.22
CN	4.00E-009	1.42E-008	3.56
OH	3.00E-008	1.60E-008	0.53
HCN	6.00E-009	2.58E-008	4.30
HNC	4.00E-009	2.52E-008	6.31
C_2H	4.20E-009	4.27E-009	1.02
HCO^+	8.00E-009	1.37E-009	0.17
NH_3	5.00E-008	1.82E-008	0.36
H_2CO	6.00E-009	9.48E-010	0.16
HC_3N	(0.3-1.0)E-008	7.50E-009	(1.50-2.50)
CH_3CN	3.40E-010	2.84E-009	8.36

Table 3.16: A comparison of some observed fractional abundances from the dark cloud TMC-1 (Millar & Freeman 1984 and the references therein) and the fractional abundances produced by model NK TMC1 at 1.3×10^5 years.

3.4.1 Elemental fractional abundances

In Figures 3.5(a), 3.5(b), 3.5(c) and 3.5(d) the fractional abundances of atomic carbon, oxygen, nitrogen and sulphur are seen to evolve with time in models G, L and S. It can be seen that model G has the highest fractional abundance of each element, at all times. Model L has the next highest fractional abundance of each element, and model S has the lowest fractional abundance. As the fractional abundances seen in the models are representative of the underlying abundance of that element in the model, the species themselves can be considered metallicity tracers. However, these species are not easily observable in the central regions of dark clouds. The fractional abundance of C in models G, L, S and DC1-DC6 is shown in Figure 3.6. This shows that the carbon abundance in each model at each time is directly related to the underlying carbon abundance in the model - so model DC1 has the highest fractional abundance of atomic

Model	Elemental abundance ratios				
	O/C	C/N	C/S	O/N	N/S
DC1	2.82	3.20	2208.50	9.04	690.10
G	2.42	1.76	1540.26	4.25	875.15
NK TMC1	2.10	1.30	1243.73	2.72	957.26
DC2	3.16	10.00	3453.48	31.63	345.35
DC3	3.27	9.66	3335.39	31.63	345.32
L	2.41	3.41	3650.00	8.22	1070.00
DC4	3.48	9.09	3138.19	31.63	345.28
DC5	3.98	7.94	2742.36	31.63	345.20
S	2.59	2.17	1766.62	5.63	812.46
DC6	5.01	6.31	2177.67	31.63	345.05
DC7	5.01	6.31	2177.67	31.63	345.05
DC8	5.01	6.31	2177.67	31.63	345.05
DC9	5.01	6.31	2177.67	31.63	345.05

Table 3.17: Underlying fractional abundance ratios in the NK dark cloud models.

C, and model DC6 has the lowest. The C abundance in all the models drops rapidly between 5×10^4 and 1×10^5 years, as most of the atomic carbon is incorporated into the CO molecule at this time, where it remains, owing to the stability of this molecule.

3.4.2 CO

As seen in Figure 3.7(a) the CO abundance traces the carbon abundance in each model fairly well at early time, and very well at steady state. However, unless the age of the cloud is known fairly accurately then it is impossible to identify the underlying carbon abundance using these models, as the same CO abundance can occur in different models at different times. For example, a CO fractional abundance of 1×10^{-5} occurs in models G, L and S between the times of 10^4 and 10^5 years. This can be seen more

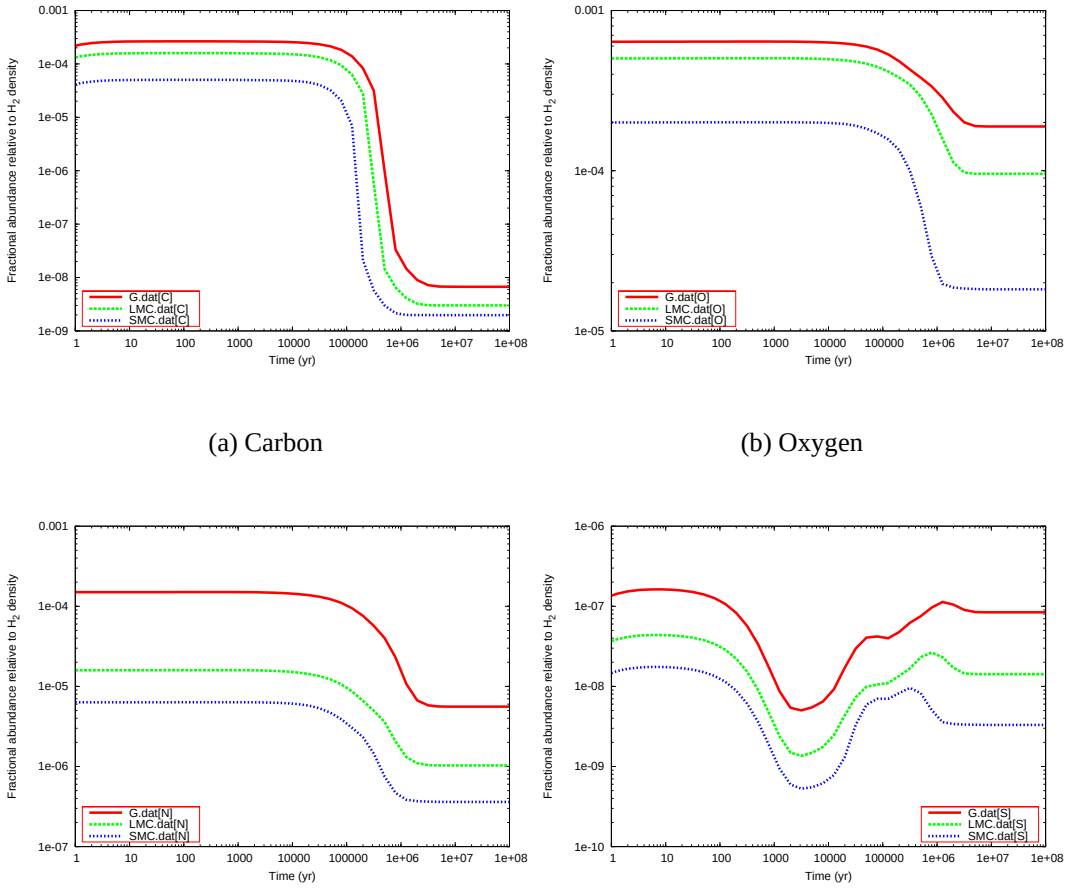

(a) Carbon

(b) Oxygen

(c) Nitrogen

(d) Sulphur

Figure 3.5: The fractional abundances of atomic carbon, oxygen, nitrogen and sulphur in models G, L and S.

clearly in Figure 3.7(b), where the early time fractional abundances of CO are shown for models G, L and S.

3.4.3 Species containing Nitrogen

Figure 3.8(a) shows the fractional abundance of NH_3 as a function of time for models G, L and S. Although NH_3 is abundant, it is a poor metallicity tracer. It is impossible to identify the underlying metallicity of a cloud from an observation, as the fractional abundance of NH_3 changes so much in each model. For example, an observation of

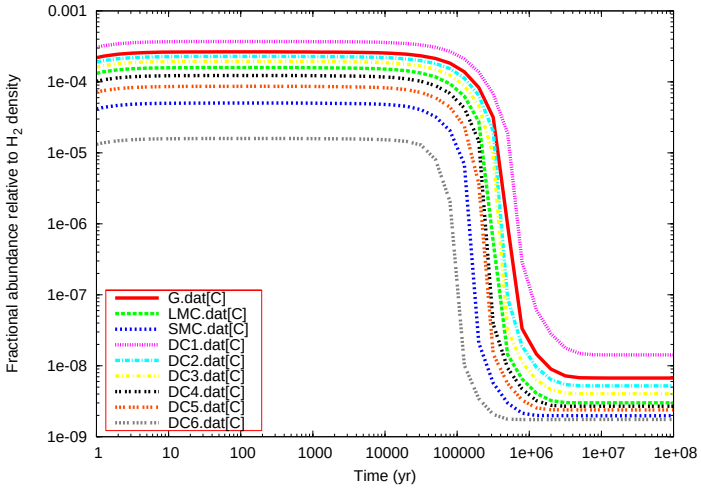

Figure 3.6: The fractional abundance of elemental C to H_2 in models G, L, S and DC1-DC6.

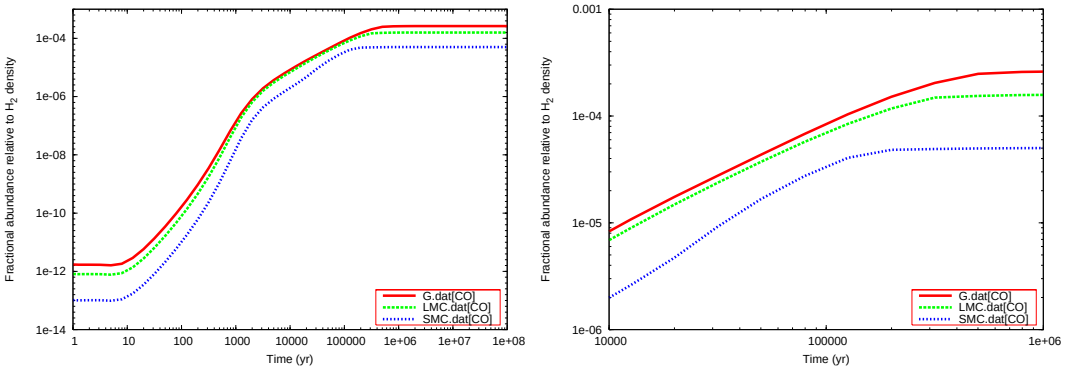

(a) CO (b) CO at early time

Figure 3.7: The fractional abundance of CO in models G, L and S.

$X(NH_3) = 1\times10^{-8}$ could potentially be produced by all three of the models in the time period 10^4–10^5 years. Even knowing the exact age of the cloud does not clarify this issue, as several models produce the same NH_3 abundance at the same time, even with different underlying metallicities. This can be seen in Figure 3.8(b).

Figures 3.9(a) and 3.9(c) show the fractional abundances of HCN and HNC in the three models. In both figures, HCN and HNC are much more abundant in G than in L and S. This order of magnitude difference in abundance could potentially be observed. However, the fractional abundances seen in the L and S models are very similar from

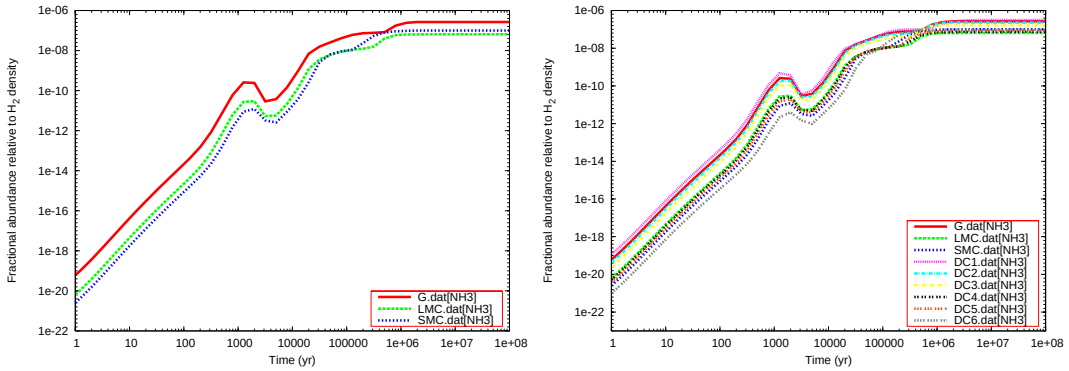

(a) NH_3 in G, L and S

(b) NH_3 in G, L, S, and DC1-DC6

Figure 3.8: The fractional abundance of NH_3 in models G, L, S, and DC1-DC6.

approximately 2×10^5 years onwards. It would be impossible to distinguish between the two models (and hence underlying metallicities) after that time. An observation of HCN or HNC in a dark cloud could therefore be used to provide an upper limit to the underlying metallicity. If a fractional abundance greater than 10^{-8} were observed, a Galactic metallicity level could be inferred. If an observation of HCN or HNC showed a fractional abundance below 10^{-8}, then a sub-Galactic metallicity could be assumed. Figures 3.9(b) and 3.9(d) show the fractional HCN and HNC abundances in models G, L, S and DC1-DC6. It can be seen that those species with a metallicity equal to or lower than model L have a similar fractional abundance of HCN and HNC from around 5×10^4 years onwards. An observation of HCN or HNC could thus be used to identify if a cloud had a metallicity above or below the level used in the L model, as seen in Table 3.1. These species could therefore be used to identify dark clouds with low metallicity, but could not be used to determine the metallicity level more precisely. At steady state, HCN and HNC could not be used to trace the underlying metallicity of a dark cloud, as the highest fractional abundances are seen in model G, then S, then L – this does not reflect the underlying metallicity of the models. A common factor shared by many of the nitrogen-bearing species studied is that the chemical behaviour of the species is similar in models G, L and S. The timing may be different – e.g. in model S the species

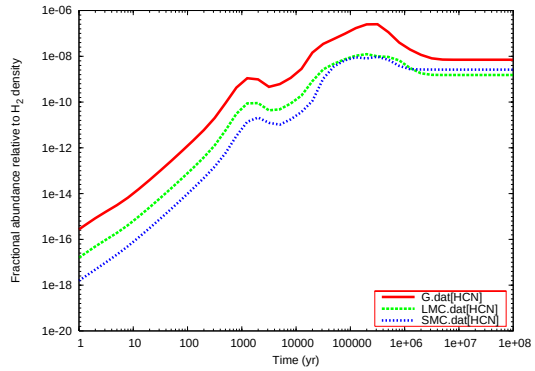

(a) HCN in models G, L and S

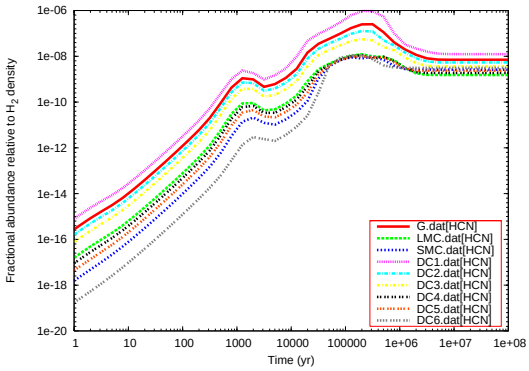

(b) HCN in models G, L, S and DC1-DC6.

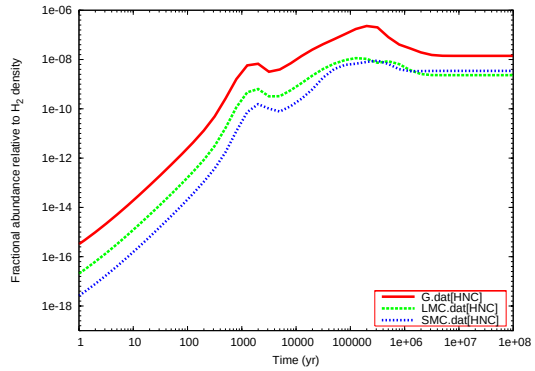

(c) HNC in models G, L and S

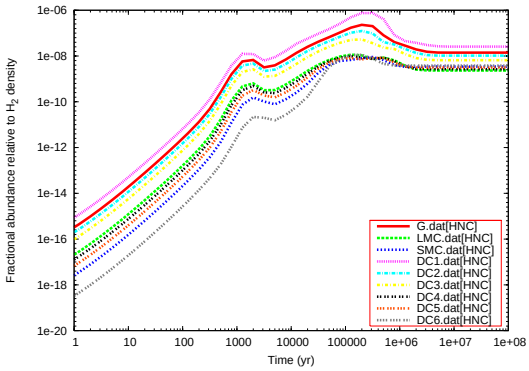

(d) HNC in models G, L, S and DC1-DC6.

Figure 3.9: The fractional abundances of HCN and HNC in models G, L, S and DC1-DC6.

may reach steady state at an earlier time due to the lower metallicity in this model, but the shape of the fractional abundance curve will be similar for each model. A good example of this is HC_3N, which is shown in Figure 3.10(a). The curve for each model has a very similar shape in this figure. However, the fractional abundances peak at different times, with the most metallic model (G) peaking at the latest time. This species could be used as a tracer to provide an upper limit to the underlying metallicity of a cloud, in a similar way to that described above for HCN and HNC. A fractional abundance above 10^{-8} is only seen in model G, and so an observation which showed a lower fractional HC_3N abundance than this would reveal a sub-Galactic metallicity. It would

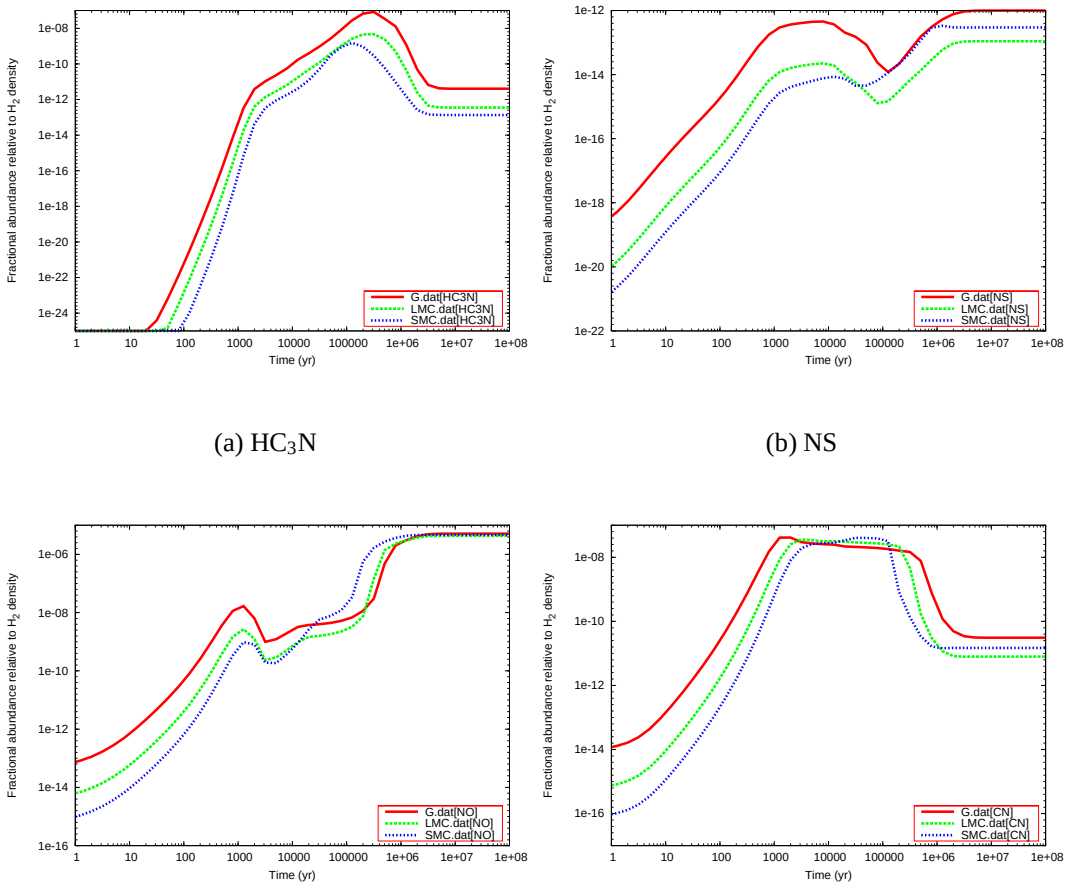

(a) HC_3N (b) NS

(c) NO (d) CN

Figure 3.10: The fractional abundances of HC_3N, NS, NO and CN in models G, L and S.

not be possible to further determine the metallicity using HC_3N, as similar abundances are seen in models L and S at early time. If a dark cloud were known to have a steady state chemistry, it may be possible to use this species as a tracer, as the steady state fractional abundances of HC_3N do appear to reflect the underlying metallicity of the models. However, the fractional abundances at steady state are all below 10^{-11}, and so it may not be possible to observe HC_3N in a dark cloud in another galaxy.

The NS fractional abundance in models G, L and S is shown in Figure 3.10(b). NS could not be used to trace the underlying metallicity of a dark cloud. Although the fractional NS abundances are distinct in the three models at early time, no fractional

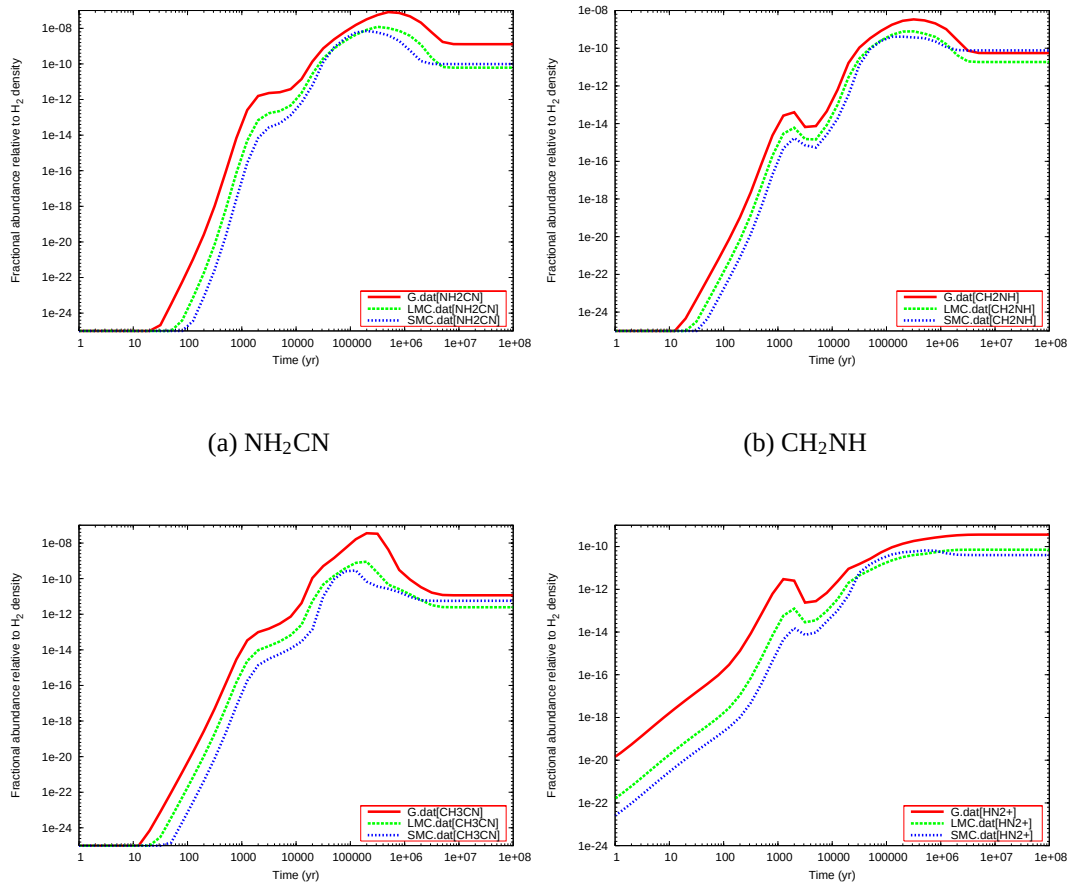

(a) NH_2CN (b) CH_2NH

(c) CH_3CN (d) HN_2^+

Figure 3.11: The fractional abundances of NH_2CN, CH_2NH, CH_3CN and N_2H^+ in models G, L and S.

abundances are seen which are unique to one model, and of a level which it is possible to observe. If the age of a dark cloud was accurately known, an estimate of the metallicity could be made, if the age was between 10^3 and 5×10^4 years. These specific conditions make it unlikely that NS could be used as a metallicity tracer.

Figures 3.10 and 3.11 show the fractional abundances of the other nitrogen-bearing species which have been observed in extragalactic regions. It can generally be seen that these species are not useful metallicity tracers at early time. The fractional abundances in the three models are often similar, and sometimes there is crossover between

the different models. Figure 3.11(c) shows that CH_3CN could be used to provide an upper limit for the underlying metallicity at early time, in a similar way to that described above for HC_3N, HCN and HNC.

Figure 3.11(d) demonstrates that at steady state, N_2H^+ could be used to trace the underlying metallicity, as the highest fractional abundance of this species is seen in model G, and the lowest in model S. However, the fractional abundances are very low, and it may not be possible to observe them. The values in models L and S are also quite similar, and it may not be possible to distinguish between these models from an observed value with errors. Figures 3.10 and 3.11 show that NO, CN, NH_2CN and CH_2NH are not useful metallicity tracers at early time or steady state.

The metallicity-tracing abilities of the nitrogen-bearing species which have been observed in extragalactic regions, and are included in the dark cloud reaction network, are summarised in Table 3.18.

Species	**Early-time tracer?**	**Steady state tracer?**
NH_3	No	No
HCN	Yes – provides lower limit	No
HNC	Yes – provides lower limit	No
HC_3N	Yes – provides lower limit	No- low abundance
NS	No	No
NO	No	No
CN	No	No
NH_2CN	No	No
CH_2NH	No	No
CH_3CN	Yes – provides lower limit	No
N_2H^+	No	Possibly

Table 3.18: A summary of the observed extragalactic nitrogen-bearing species and their potential as metallicity tracers.

Tracing an underlying ratio

Amongst the species NH_3, HCN, HNC, NS, CN, NH_2CN, and CH_3CN at steady state, the highest fractional abundance is seen in model G, then S, then L. This pattern does not follow the underlying metallicity of the dark cloud models, as G is the most metallic, and S is the least metallic. However, Figure 3.12(a) shows that these fractional abundances represent the N/O ratio at steady state, in each of the models. Figure 3.12(b) shows the N/O ratio in models DC1-DC6, along with G, L and S. It can be seen that up until 2×10^5 years, five of the models have the same N/O ratio. This is because the initial, or underlying, N/O ratio in these models is the same, as can be seen in Table 3.19. After 2×10^5 years, the N/O ratios in the models diverge, with each model producing a unique ratio at steady state.

The N/O ratio has a strong effect on the nitrogen-bearing species. Figure 3.12(c) shows the N/O ratio in the dark cloud models between 10^5 and 10^8 years. By comparing this with Figure 3.12(d), it can be seen that the fractional NH_3 abundance at steady state represents the underlying N/O ratio at that time. The higher the N/O ratio (e.g. the more nitrogen per unit oxygen), the more NH_3 there is. At a lower ratio, there is more oxygen per nitrogen atom, and so a greater proportion of the nitrogen reacts with oxygen to form oxides such as NO and NO_2. At a higher ratio, more nitrogen is available to become hydrogenated to form NH_3.

Model	**G**	**L**	**S**	**DC1**	**DC2**	**DC3**	**DC4**	**DC5**	**DC6**
N/O	0.24	0.03	0.03	0.37	0.18	0.11	0.03	0.03	0.03

Table 3.19: The initial N/O ratio in models G, L, S and DC1-DC6

Tracing another species

The fractional C^+ abundance is shown in Figure 3.13(a). It can be seen that initially, the C^+ abundance is very similar in models G and L. At steady state, similar fractional

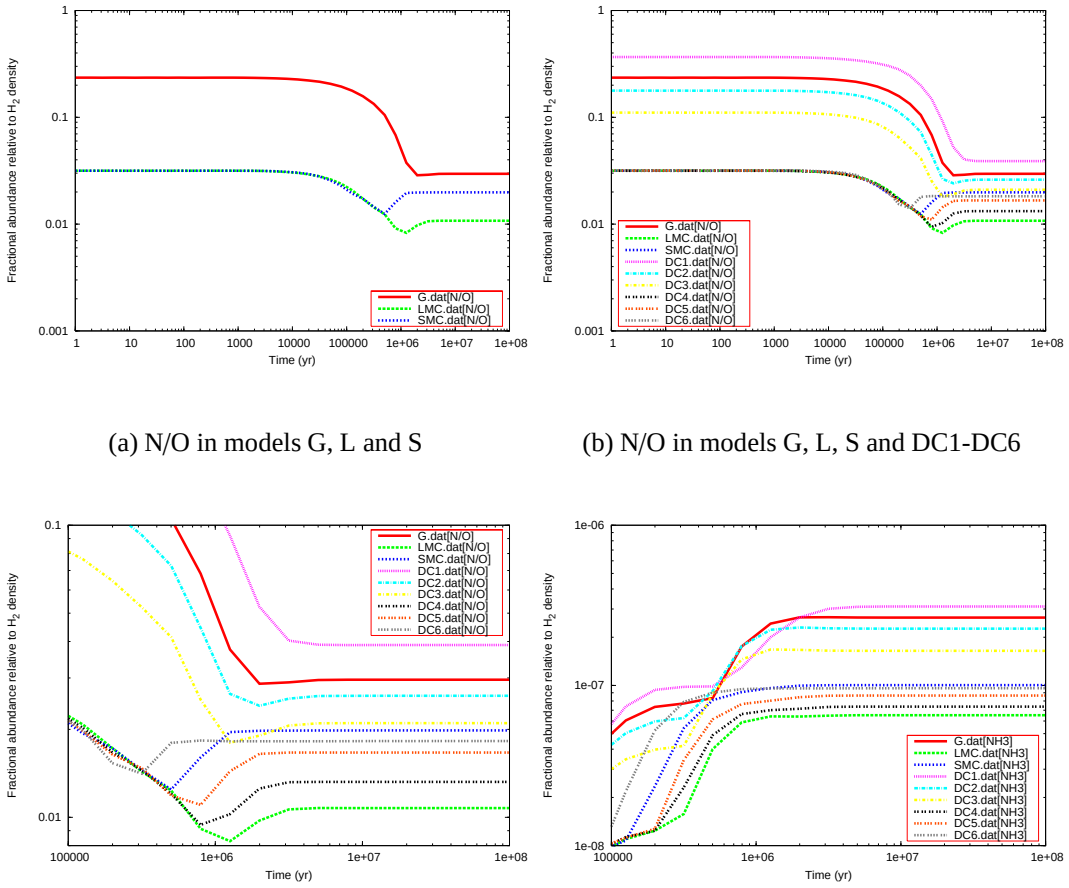

(a) N/O in models G, L and S

(b) N/O in models G, L, S and DC1-DC6

(c) N/O between 10^5 and 10^8 years

(d) NH_3 between 10^5 and 10^6 years

Figure 3.12: The N/O ratio and the NH_3 fractional abundance in models G, L, S and DC1-DC6.

abundances are seen in models G and S. The C^+ abundance is closely linked to the NH_3 abundance. It can be seen in Figure 3.13(b) that from 5×10^4 years onwards the C^+ and NH_3 abundances for each model behave in a similar and opposite way. In each model, the fractional abundances are reflected through a line at approximately 1×10^{-8}. This relationship is caused by a complicated web of reactions within the reaction network. Around 99% of the time, NH_3 is destroyed by reaction with a cosmic ray photon in the dark cloud models (or by reaction with He^+ at very early time). This leads to products such as NH_3^+ and NH_2, which eventually reform NH_3 in the chemical network. However, around 0.1% of the time, NH_3 is destroyed by reaction with C^+.

In this case, H_2NC^+ is formed. This species undergoes a number of reactions, and forms species including CN, HCN and HNC. If these species are broken down, they produce atomic carbon, which sometimes goes on to form C^+, which is then able to remove more NH_3 from the cloud. In this way, the C^+ and NH_3 eventually reach a balance where the fractional abundances are in a steady state chemistry. This occurs slightly before the model reaches a steady state chemistry for all species - a little before 1×10^6 years. This relationship could be used to estimate the fractional abundance of C^+ in a dark cloud at a certain time (rather than the underlying abundance of C or C^+). If the cloud was known to be at, or approaching, steady state, the fractional C^+ abundances could be estimated using a graph such as Figure 3.13(b). This could then be used to provide limits to the fractional carbon abundance at that time, using a graph such as Figure 3.13(c) which shows the relationship between the C^+ and the fractional C abundance. This estimate relies on the underlying metallicity of the region being "guessed" fairly accurately. However, the spread of C^+/C ratios at steady state is quite small (between 0.1 and 1), and so the error made on an estimate may not be excessively large. Alternatively, Figure 3.13(d) shows the relationship between the fractional C^+ and e^- abundances in the models. The C^+/e^- ratio is between 0.02 and 0.04 in models G, L and S at steady state - this range of values is fairly small. An estimate of the fractional C^+ abundance could thus be used to estimate a range for the fractional ionisation of the dark cloud at that time.

3.4.4 Hydrocarbons

The hydrocarbons shown in Figure 3.14 have all been observed in extragalactic regions. None of the species shown are useful metallicity tracers. The fractional abundances in the different models have values which cross over at different times. For example, in Figure 3.14(c) the fractional abundances in models G, L and S between 1×10^4 and 5×10^5 years are indistinguishable from one another. Figure 3.14(f) shows that at steady

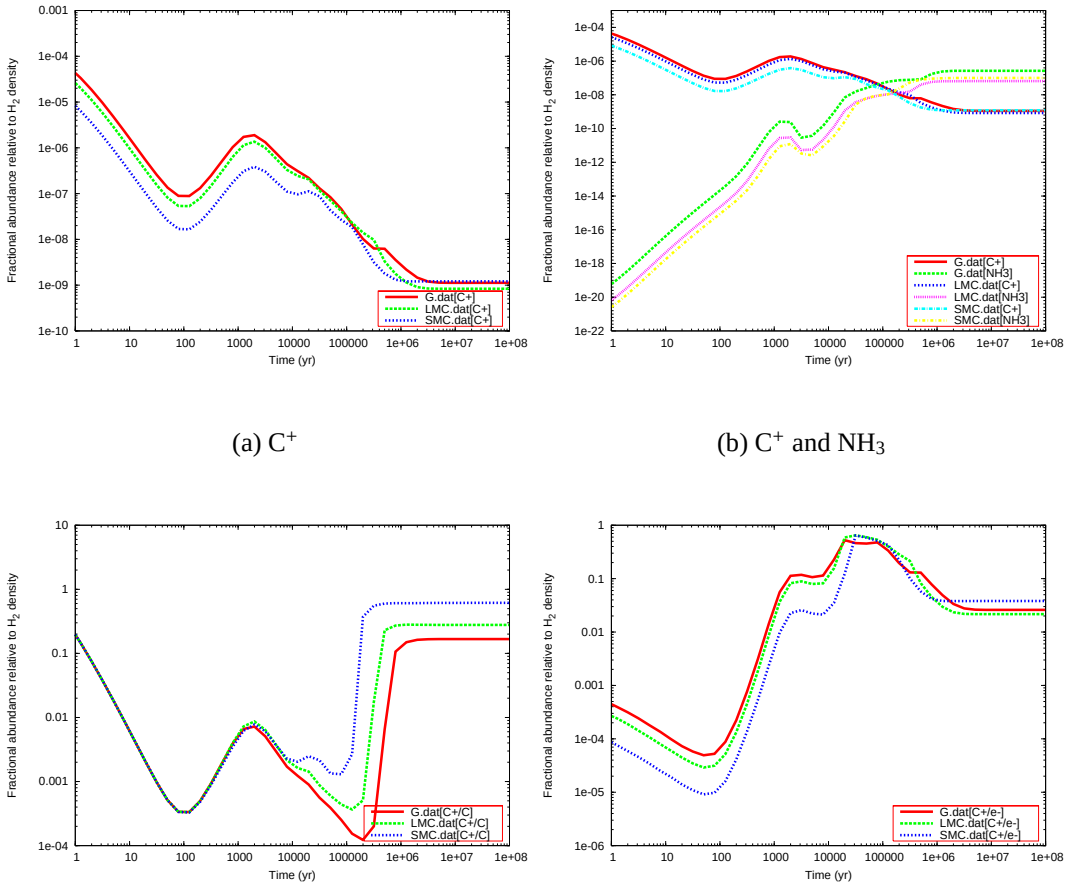

(a) C^+

(b) C^+ and NH_3

(c) C^+/C ratio

(d) C^+/e^- ratio

Figure 3.13: The C^+ and NH_3 fractional abundances, and C^+/C and C^+/e^- ratios, in models G, L and S.

state, it may be possible to identify the underlying metallicity of a cloud using the fractional CH_3CCH abundance. From around 10^6 years onwards, the highest abundance is seen in model G, and the lowest in model S. However, the fractional abundances seen are very low (around 1×10^{-14}) and so it is unlikely that extragalactic observations of these abundances could be made. Figure 3.14(a) shows that the fractional CH abundance at steady state inversely traces the underlying metallicity of the dark cloud. The fractional abundances seen are fairly low (between 10^{-10} and 10^{-11}) and thus may not be observable in other galaxies. As the relationship between metallicity and CH

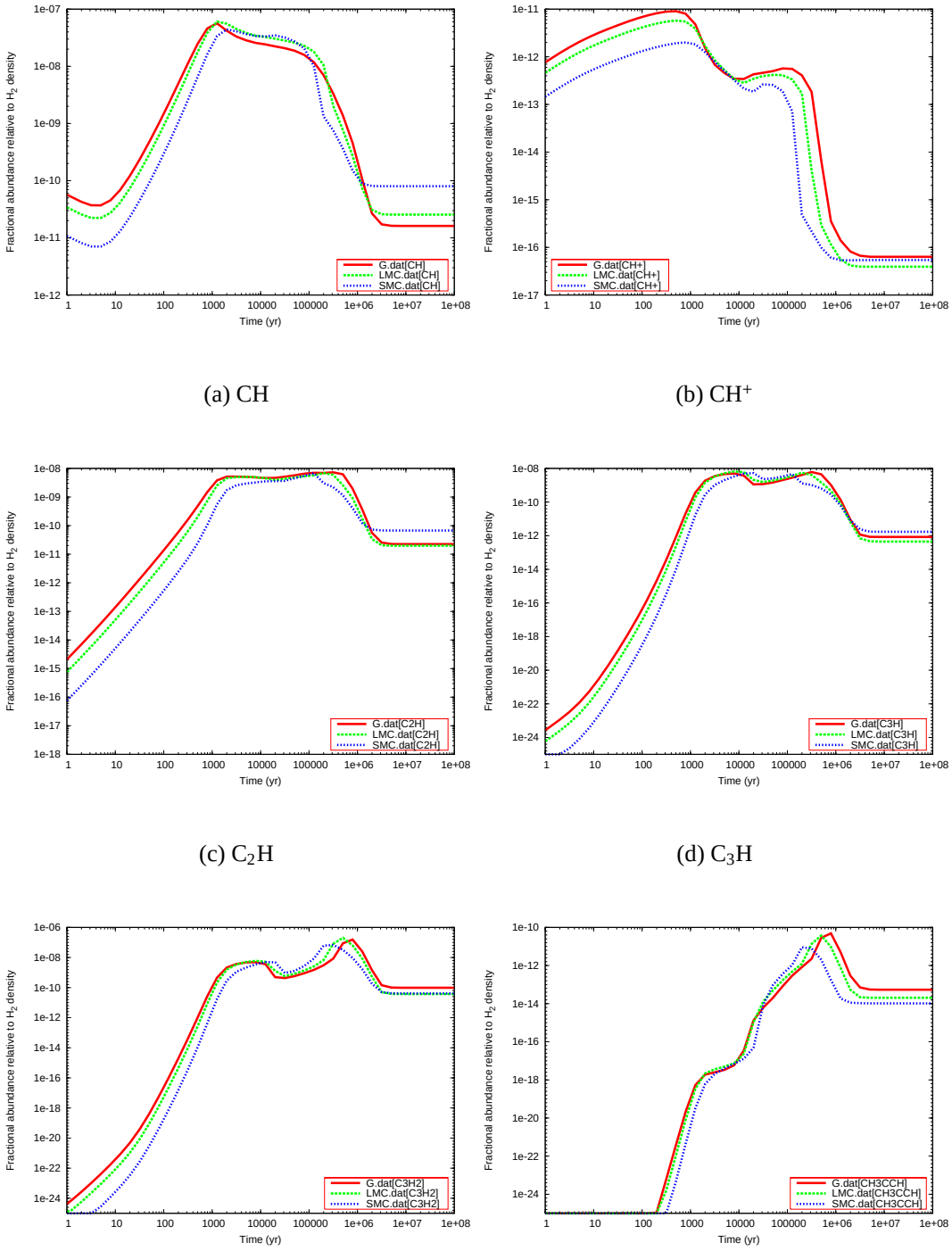

(a) CH (b) CH^+

(c) C_2H (d) C_3H

(e) C_3H_2 (f) CH_3CCH

Figure 3.14: The CH, CH^+, C_2H, C_3H, C_3H_2 and CH_3CCH fractional abundances in models G, L and S.

abundance is inverse, a CH observation could potentially be made from a dark cloud in another galaxy, if the dark cloud were at very low metallicity. This type of observation would only be valid if the cloud age was accurately known, and the chemistry was determined to be at steady state, as at early time the fractional CH abundance in all three models is fairly high (between 10^{-7} and 10^{-8}). The likelihood of such a specific observation being made is minimal. Figures 3.14(c) and 3.14(d) show that at steady state, the highest fractional abundances of C_2H and C_3H are seen in model S. This pattern holds for the carbon chain species C_4H, C_5H, C_6H, C_7H, C_8H and C_9H, as shown in Figure 3.15. The next highest fractional abundance of these species is seen in model G, and the lowest in model L. As model S has the lowest underlying carbon abundance, it is clear that these species cannot be used to trace metallicity. Table 3.20 summarises the ability of the hydrocarbons to trace underlying metallicity in a dark cloud.

Species	**Early-time tracer?**	**Steady state tracer?**
CH	No	Possibly
CH^+	No	No
C_2H	No	No
C_3H	No	No
C_3H_2	No	No
CH_3CCH	No	No – low abundance
C_4H	No	No
C_5H	No	No
C_6H	No	No
C_7H	No	No
C_8H	No	No
C_9H	No	No

Table 3.20: A summary of the hydrocarbons and their potential as metallicity tracers. This shows that none of these species are good metallicity tracers.

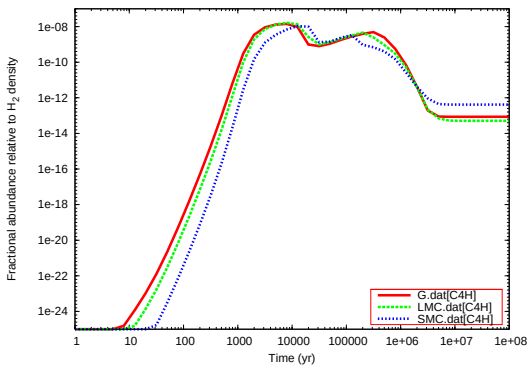

(a) C_4H

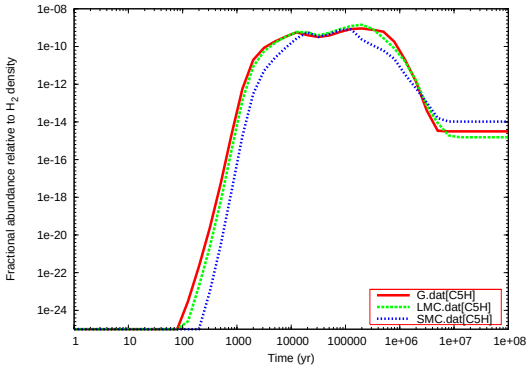

(b) C_5N

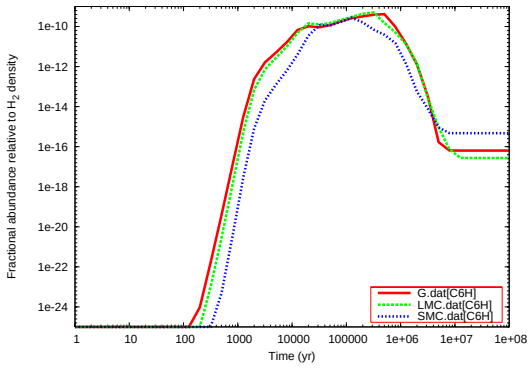

(c) C_6H

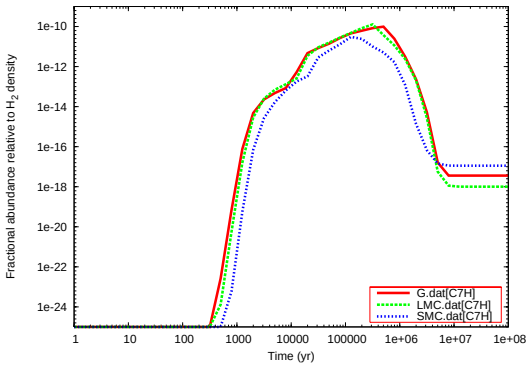

(d) C_7H

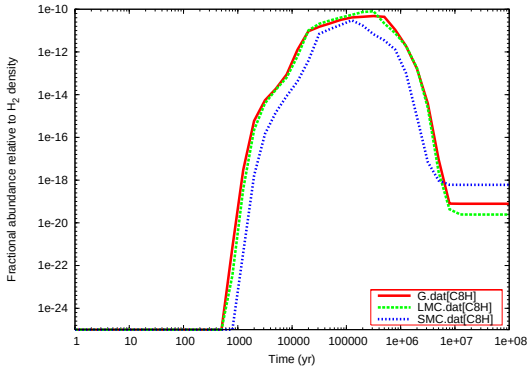

(e) C_8H

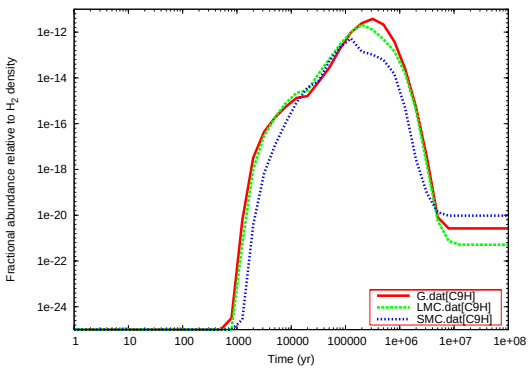

(f) C_9H

Figure 3.15: The C_4H, C_5H, C_6H, C_7H, C_8H and C_9H fractional abundances in models G, L and S.

3.4.5 Species containing oxygen

All of the models are oxygen-rich, as seen in Table 3.17. Figures 3.16 and 3.18 show the fractional abundances of some observed extragalactic oxygen-bearing species, in models G, L and S, as a function of time. The species seen in Figure 3.16 are not good metallicity tracers, in general. The fractional abundances produced by models G, L and S are often similar, and there is crossover between the models. Figure 3.16(a) shows that H_2O could potentially be used to identify low metallicity dark clouds at steady state. The fractional H_2O abundance is fairly high in all three models, and from around 3×10^6 years onwards the abundance is each model can be distinguished from the others. If a dark cloud with an evolved chemistry was observed in another galaxy, an H_2O observation could be used to estimate the underlying metallicity. Figure 3.16(e) shows that H_2CO inversely traces the underlying metallicity from 10^6 years onwards. The fractional abundances produced are quite low (between 10^{-9} and 10^{-12}), but as the H_2CO abundance increases with decreasing metallicity, it may be possible to observe this species in dark clouds in other galaxies. Figure 3.17 shows the fractional H_2CO abundance between 10^5 and 10^8 years, in models G, L and S. It can be seen that the steady state abundances in models G and L are very similar. These values could probably not be distinguished from one another in an observation. The fractional H_2CO abundance could thus be used to provide a lower limit to the underlying metallicity of a cloud. Figure 3.18 shows the fractional abundances of HCO and HCO^+ as a function of time, in models G, L and S. Figure 3.18(a) shows that HCO appears to trace the underlying metallicity of the cloud, to some extent. This species could potentially be used to estimate underlying metallicity from around 1×10^6 years onwards, as the chemistry approaches a steady state, as the three models produce fractional HCO abundances which differ by a factor of a few. The fractional abundances of HCO are fairly low at all times (between 10^{-11} and 10^{-13} at steady state), and it therefore may not be possible to observe this species in another galaxy. At early time, the HCO fractional abundance could be used to provide limits to a cloud's underlying metallicity, if the age

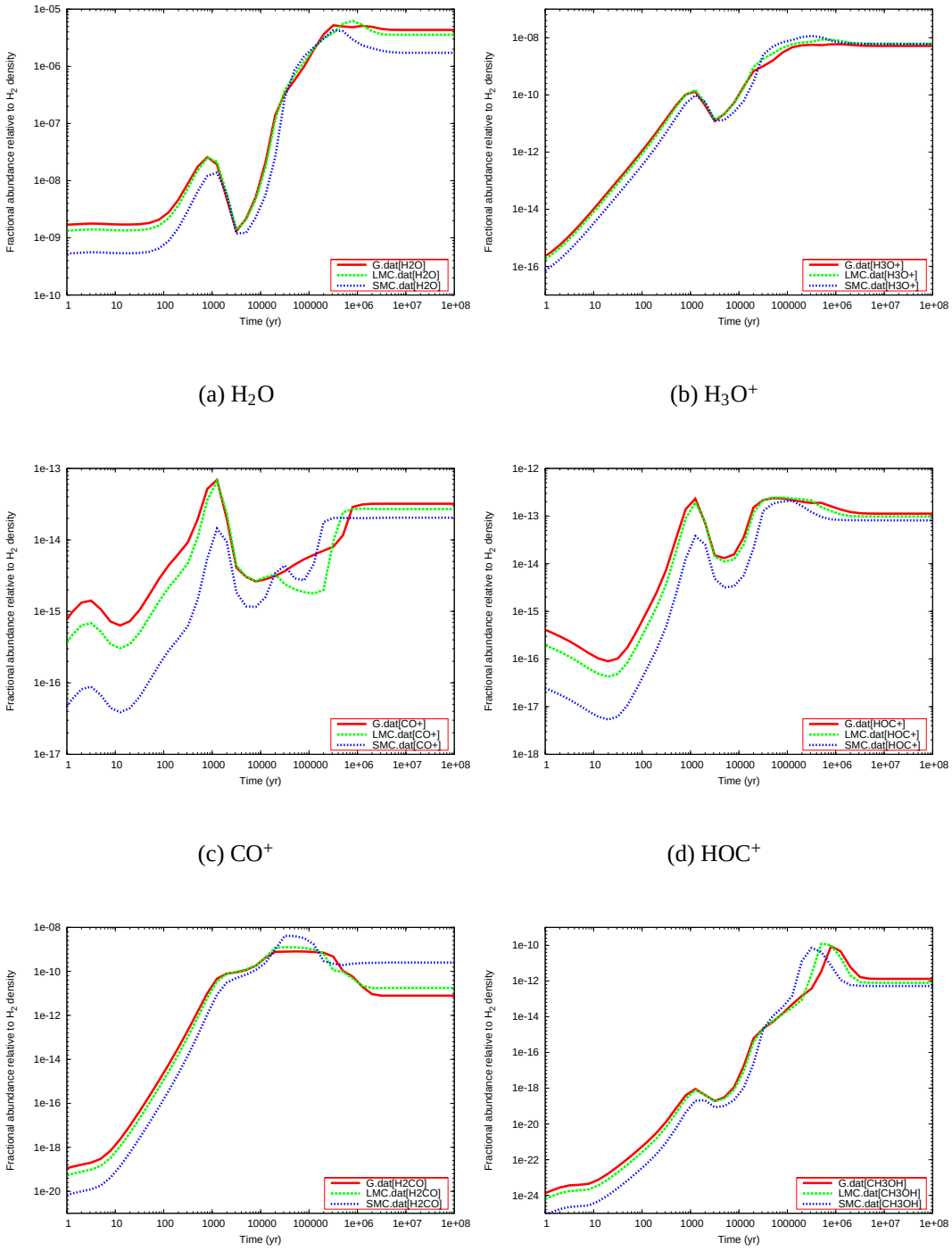

(a) H_2O (b) H_3O^+

(c) CO^+ (d) HOC^+

(e) H_2CO (f) CH_3OH

Figure 3.16: The H_2O, H_3O^+, CO^+, HOC^+, H_2CO and CH_3OH fractional abundances in models G, L and S.

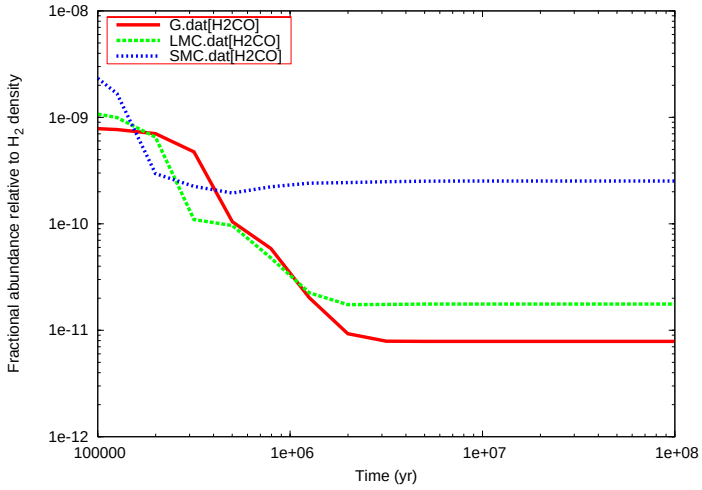

Figure 3.17: The H_2CO fractional abundance between 10^5 and 10^8 years, in models G, L,and S.

of the cloud were known accurately. For example, an observation of a fractional HCO abundance of 5×10^{-12} could only come from a low metallicity cloud such as in model S, in the time period 10^3-10^5 years. As seen in Figure 3.18(b), the fractional HCO^+ abundance produced by the three models is very similar from around 3×10^4 years onwards. This species could not be used to trace the underlying metallicity. However, this species is potentially a useful tracer as part of a ratio with CO. This is discussed further in Section 3.4.7.

Figure 3.18(c) shows the fractional OH abundance as a function of time in models G, L and S. This species is the best tracer of underlying metallicity amongst the oxygen-bearing species. Beyond 3×10^5 years, the fractional OH abundance inversely traces the underlying metallicity. The fractional abundances seen differ by a factor of a few between the models, and the species is abundant (the fractional abundances in the models vary between 10^{-6} and 10^{-8} at steady state). OH could therefore be a useful metallicity tracer in a dark cloud with a steady state chemistry. Before 3×10^5 years, OH is not a useful metallicity tracer, as the fractional abundances in the three models are similar, and have some crossover. Table 3.21 provides a summary of the oxygen-bearing species, and their ability to trace the underlying metallicity of a dark cloud.

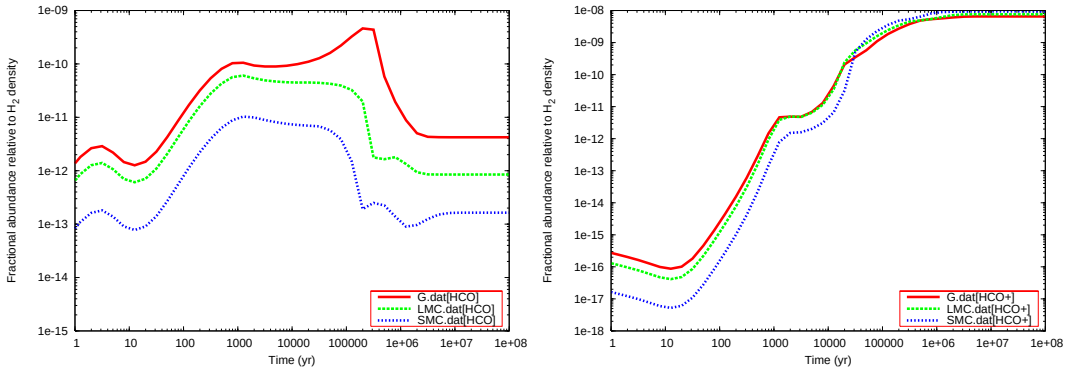

(a) HCO (b) HCO^+

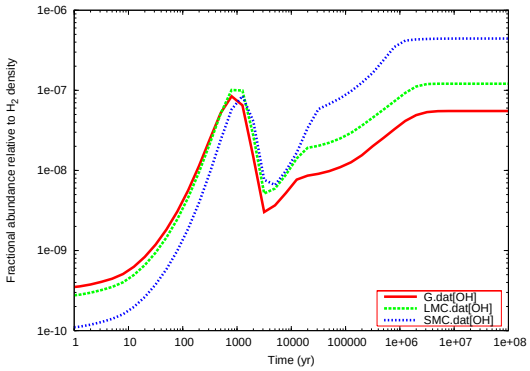

(c) OH

Figure 3.18: The HCO, HCO^+ and OH fractional abundances in models G, L and S.

3.4.6 Species containing sulphur

Figures 3.19 and 3.20 show the fractional abundances of some sulphur-bearing species in models G, L and S. It can be seen that at steady state, all these species trace the underlying metallicity, with the highest fractional abundance being seen in model G, and the lowest in model S. The species in Figure 3.19 contain oxygen and sulphur only. These species could not be used to trace metallicity at early time, as the fractional abundances in the three models cross over at certain points, and the abundances

Species	Early-time tracer?	Steady state tracer?
H_2O	No	Yes
H_3O^+	No	No
CO^+	No	No – low abundance
H_2CO	No	Yes – could provide lower limit
HOC^+	No	No
CH_3OH	No	No
HCO	Possibly	No – low abundance
HCO^+	No	No
OH	No	Yes

Table 3.21: A summary of the oxygen-bearing species and their potential as metallicity tracers.

produced in the models are very similar. At steady state, these species have reasonably high and distinct fractional abundances. They could be used as metallicity tracers for clouds older than 2×10^6 years, where the chemistry has reached a steady state.

The species in Figure 3.20, namely CS, H_2S, H_2CS and OCS, have distinct fractional abundances for each model at all times. The species CS, H_2CS and OCS all contain both carbon and sulphur. It appears that these two elements in combination produce species which are closely linked to the underlying metallicity. The underlying sulphur abundance provides a limiting factor, as it is less abundant than the carbon, hydrogen and oxygen, but the underlying carbon abundance also plays a role. Although all the species in Figure 3.20 produce distinct fractional abundances in each model at each time, there are some common values between the model outputs which prevent these species being used as metallicity tracers at early time. For example, in Figure 3.20(a) between 10^4 and 10^5 years, the CS fractional abundance is 1×10^{-9} in models G, L and S at various times. Unless the age of a cloud could be extremely accurately determined, these species are therefore not useful as metallicity tracers at early time. At steady state, all these species trace the underlying metallicity of the cloud. The best metallicity tracers are abundant, and have values which are easily distinguished from

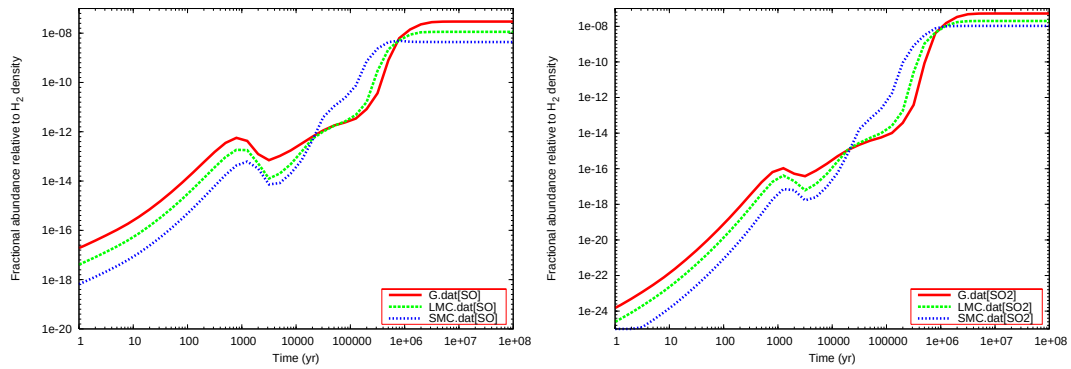

(a) SO (b) SO_2

Figure 3.19: The SO and SO_2 fractional abundances in models G, L and S.

one another. As discussed earlier, at a rough estimate, a fractional abundance greater than 10^{-10} could be observed in an extragalactic dark cloud. Of the species in Figure 3.20, OCS is perhaps the best metallicity tracer at steady state. This species reaches a steady state a little earlier than the other species, at around 10^6 years. The fractional abundances are above 10^{-11} in each model, and they differ by around one order of magnitude from model to model. Table 3.22 summarises the sulphur-bearing species examined, and their potential as tracers of the underlying metallicity in a dark cloud.

Species	**Early-time tracer?**	**Steady state tracer?**
SO	No	Yes
SO_2	No	Yes
CS	No	Yes
H_2S	No	Possibly – low abundance
C_2S	No	No – low abundance
H_2CS	No	Possibly – low abundance
OCS	No	Yes

Table 3.22: A summary of the sulphur-bearing species and their potential as metallicity tracers.

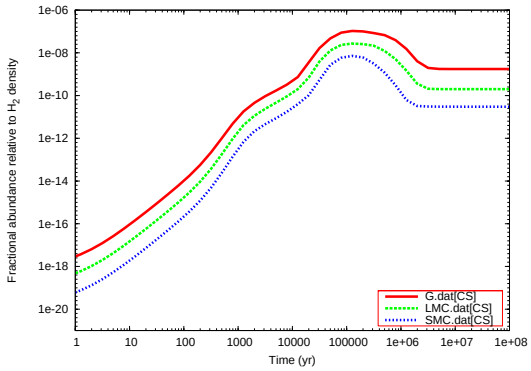

(a) CS

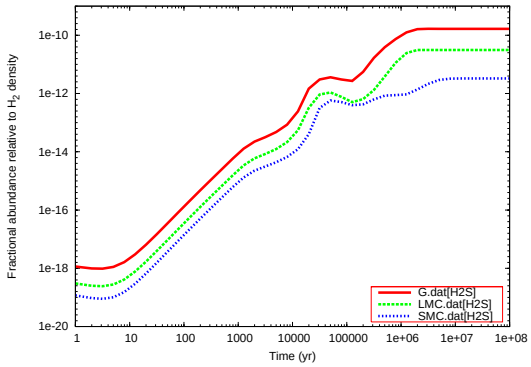

(b) H_2S

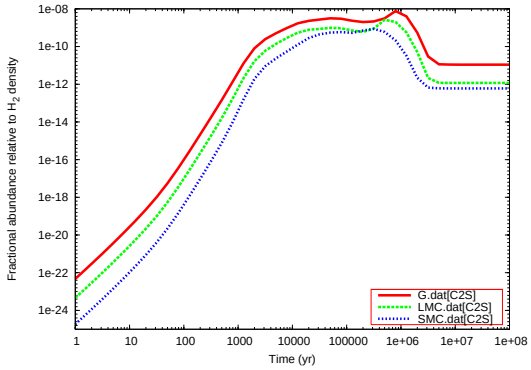

(c) C_2S

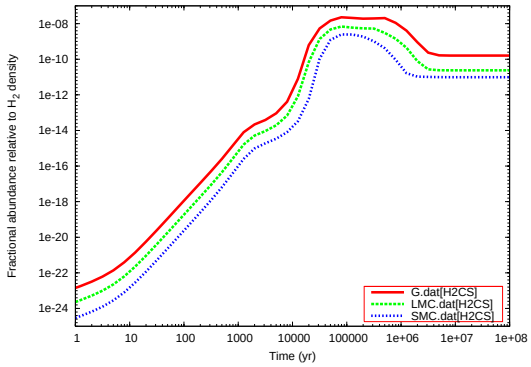

(d) H_2CS

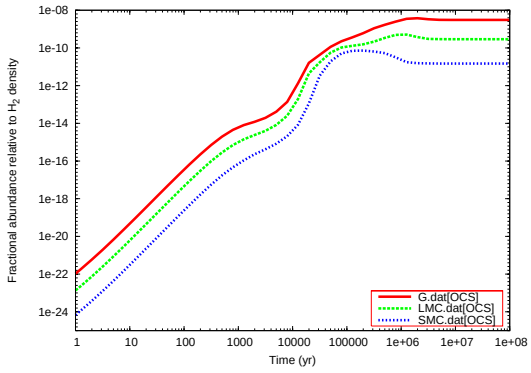

(e) OCS

Figure 3.20: The CS, H_2S, C_2S, H_2CS, and OCS fractional abundances in models G, L and S.

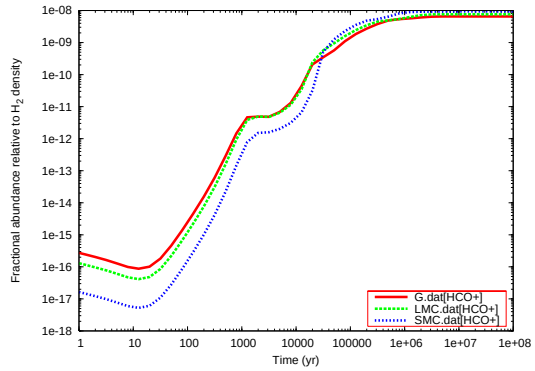

(a) HCO^+

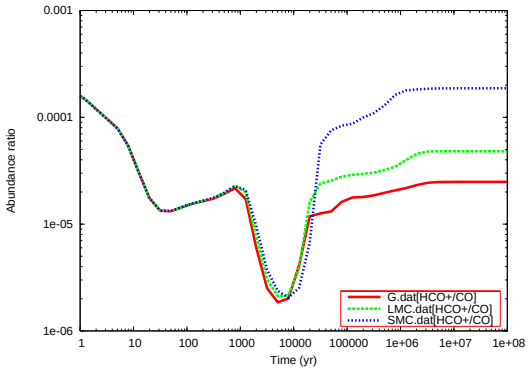

(b) HCO^+/CO

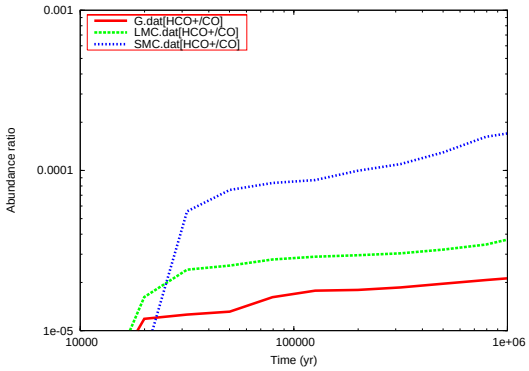

(c) HCO^+/CO between 10^4 and 10^6 years

Figure 3.21: The HCO^+ fractional abundance and HCO^+/CO ratio in models G, L and S.

3.4.7 Ratios of species

Some species in the NK dark cloud models are not metallicity tracers when observed alone, but can be used as metallicity tracers as part of a ratio.

HCO^+/CO

The CO abundance can be used in conjuction with other species as part of a ratio, to trace the underlying metallicity of a dark cloud. Figure 3.21(a) shows the fractional HCO^+ abundance in models G, L and S. It can be seen that the abundances are fairly similar in all three models, particularly from 10^4 years onwards. The species could

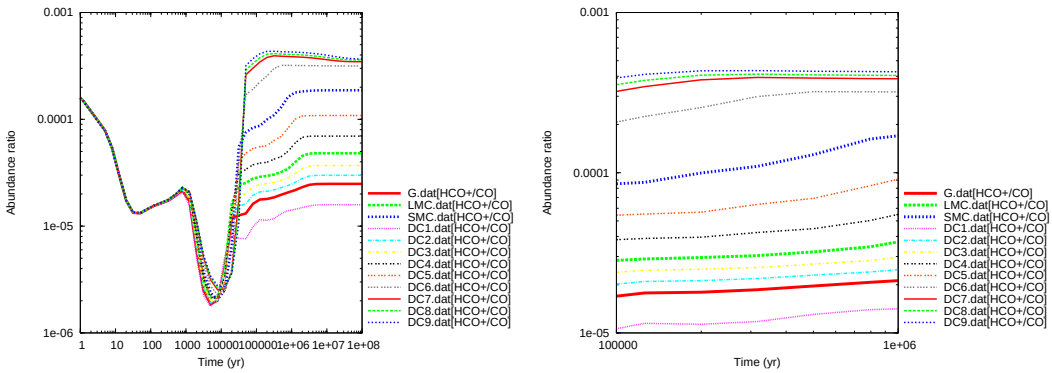

(a) HCO^+/CO (b) HCO^+/CO between 10^5 and 10^6 years

Figure 3.22: The HCO^+/CO fractional abundance in models G, L, S and DC1 - DC9. Figure 3.22(b) shows the same data between 10^5 and 10^6 years only.

not be used as a metallicity tracer, as the fractional abundances in the different models are too similar, and there is crossover between the models at different times. However, Figure 3.21(b) shows that the ratio HCO^+/CO can be used as a metallicity tracer, as the flat gradient of the lines allows the different models to be easily distinguished from around 5×10^4 years onwards. Before 5×10^4 years, models G, L and S have extremely similar HCO^+/CO ratios. Figure 3.21(c) shows the HCO^+/CO ratio between 10^4 and 10^6 years. It can be seen that the ratio in each model occupies a distinct region with no crossover between the G, L and S model ratios. The underlying metallicity used in the models could therefore potentially be determined using this graph. The relationship between HCO^+/CO and the underlying metallicity is inverse. The most metallic model, G, has the lowest HCO^+/CO ratio, and the model with the lowest metal abundance (model S) has the highest ratio.

Figure 3.22(a) shows that the evolution of the HCO^+/CO ratio is extremely similar in all of the models. The ratio itself is barely affected by the underlying metallicity until around 5×10^4 years, when the ratio increases dramatically. The extent of the increase is proportional to the metallicity/underlying M abundance of the model. The ratio is then seen to be fairly constant in each model, before the chemistry reaches steady state.

However, a given ratio is not always exclusively linked to one model during this time frame. For example, an HCO^+/CO ratio of 2.14×10^{-5} can be seen in both models G and DC2 between 10^4 and 10^5 years. This means that instead of linking an observed HCO^+/CO ratio to one underlying metallicity, the observation could be used to estimate an underlying metallicity range. If the age of the dark cloud where the observations were made was known fairly accurately, then the underlying metallicity could be determined more definitively. As an illustration of this, Figure 3.22(b) shows the HCO^+/CO ratio for the different models during the time frame 10^5-10^6 years. Between these times, the range of HCO^+/CO ratios produced by each model is much narrower, and so identifying the underlying metal abundance from an observed ratio becomes more precise.

The HCO^+/CO ratio appears to scale with the heavy metal abundance (M) in the models. This can be used to deduce the electron abundance and hence the fractional ionisation of a cloud. Figure 3.23 shows the HCO^+/CO ratio taken at 1.26×10^6 years for all the models shown in Table 3.1. The ratio for each model is plotted against the natural log of the underlying fractional M abundance in that model. The data can be fitted with a straight line, with the equation:

$$\ln(\mathrm{M/H_2}) = -12451.45x - 17.82 \tag{3.1}$$

where x is the HCO^+/CO ratio at 1.26×10^6 years in that model, and $\mathrm{M/H_2}$ is the underlying heavy metal abundance. The Pearson correlation coefficient (R^2) for this relationship is 0.998, which shows strong correlation between the two variables. At 1.26×10^7 years, the relationship is still very similar, as seen in Figure 3.24(d). At 1.26×10^5 years, the data does not fit as well to a straight line, with a Pearson correlation coefficient (R^2) of 0.952. However, this still shows a reasonable fit, and the underlying M abundance could be estimated by either using the line shown in Figure 3.24(b), or by fitting a more suitable function to the data. The line parameters and Pearson coefficients for the straight line fits to these data are shown in Table 3.23. This shows that at any time beyond 1.26×10^5 years, the HCO^+/CO ratio provides a useful tracer

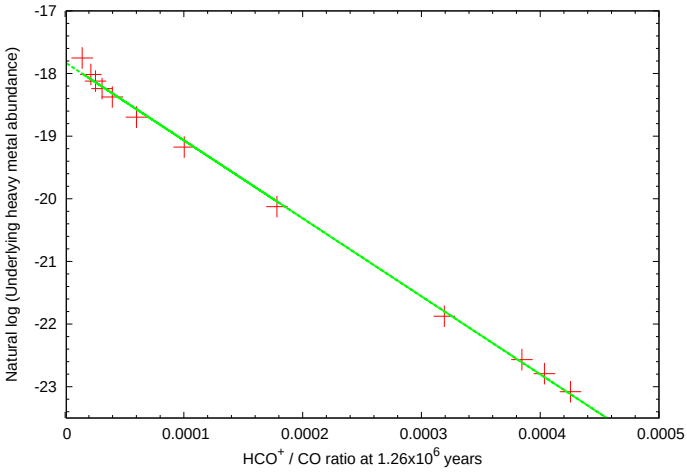

Figure 3.23: The HCO^+/CO ratio taken at 1.26×10^6 years for models G, L, S, and DC1-DC9 is plotted against the natural log of the underlying M abundance in the appropriate model.

of the underlying M abundance in a cloud. However, at earlier times the relationship between the HCO^+/CO ratio and the underlying M abundance is completely different. Figure 3.24(a) shows the relationship at 1.26×10^4 years. There is no obvious function to approximate the correlation between the HCO^+/CO ratio and the underlying M abundance at this time. Although, at higher values of the HCO^+/CO ratio, the underlying heavy metal abundance could be estimated using this graph. At 10^5 years, the relationship between the HCO^+/CO ratio and the underlying heavy metal abundance is represented by the line shown. This graph could be used to estimate the underlying M abundance, from observations of HCO^+ and CO. The relationship is not linear at this time, although it becomes linear as the chemistry reaches steady state. HCO^+/CO is most useful as a metallicity tracer if the cloud is thought to be older than 10^5 years, and may only produce approximate results if using a straight line fit.

Figure 3.22(a) shows that the HCO^+/CO ratio becomes flatter as metallicity becomes lower. At very low metallicities, the ratio is the same between approx 10^5 years to 10^8 years. At Galactic abundances, the ratio remains similar over this time period but is not constant. It increases between 10^5 and 10^6 years before reaching steady state sometime after this. The lower metallicity models reach steady state at an earlier time

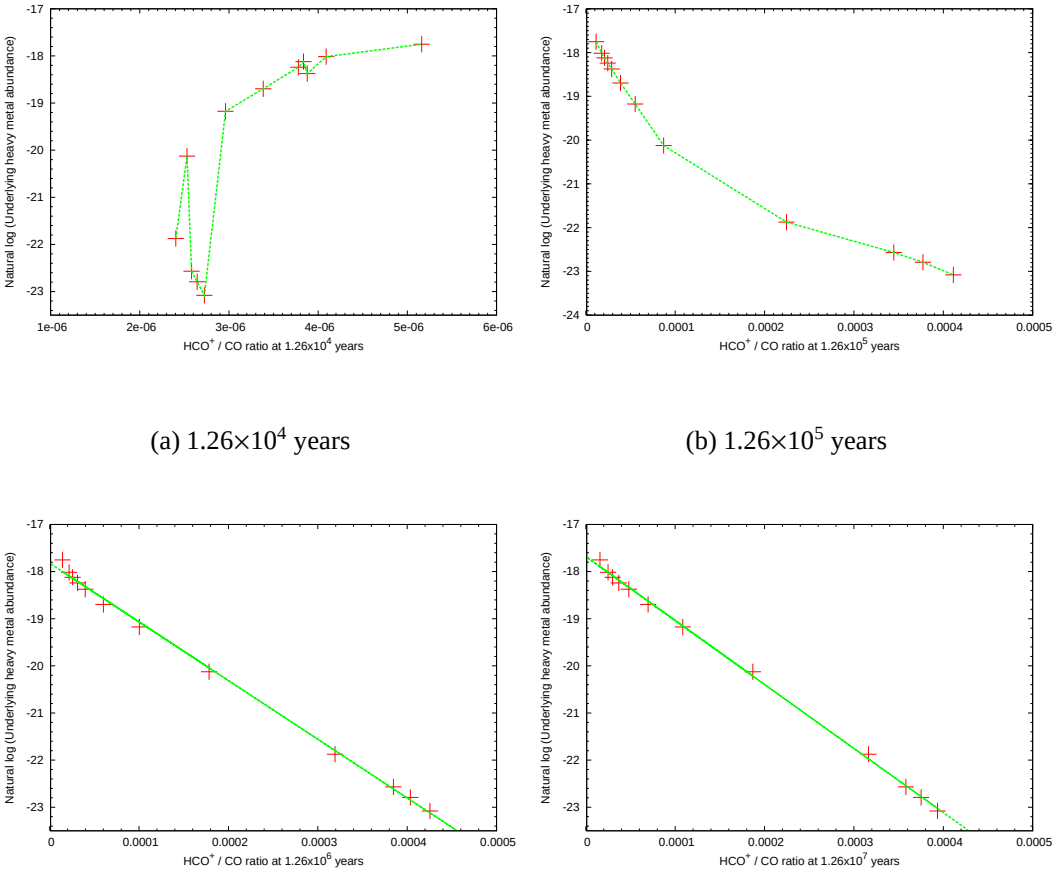

(a) 1.26×10^4 years

(b) 1.26×10^5 years

(c) 1.26×10^6 years

(d) 1.26×10^7 years

Figure 3.24: The correlation between the HCO^+/CO ratio and the underlying M abundance in models G, L, S, and DC1-DC9.

	1.26×10^4yrs	**1.26×10^5yrs**	**1.26×10^6yrs**	**1.26×10^7yrs**
Slope	2015432.27	-12993.84	-12451.45	-13580.21
Intercept	-26.614	-18.122	-17.822	-17.679
R^2	0.654	0.952	0.998	0.999

Table 3.23: The line parameters and Pearson correlation coefficient values for the linear relationship between HCO^+/CO and the natural log of the underlying M abundance in the dark cloud models, at various times.

than the higher metallicity models. This means that the steady state abundances could be used to estimate the underlying M abundance using observations from a dark cloud in a galaxy at very low metallicity.

The M abundance is the sum of the underlying abundances of Mg^+, Na^+ and Fe^+. In the model, these ions are involved in electron transfer only, and do not react to form any species other than their neutral atoms and positive ions. The underlying M abundance can therefore be used to estimate the electron abundance in a cloud, and hence the proportion of charged species within it, or 'fractional ionisation' of the cloud. As discussed in Chapter 1.2.1, this parameter is thought to be useful in determining the collapse timescale of a cloud. Figure 3.25(a) shows the fractional abundances of HCO^+ and e^- in models G, L and S. It can be seen that as the HCO^+ abundance increases in all the models, the e^- abundance decreases. The HCO^+ and e^- graphs for each model asymptotically approach a value of $y=3x10^{-8}$.

The cosmic ray ionisation rate is a parameter which affects the electron abundance in the dark cloud model. As such similar electron abundances were seen in the G, L and S models, a set of models with a higher CR ionisation rate of $1.3x10^{-16}$ s^{-1} was run. The CR ionisation rate is poorly constrained, particularly for extragalactic regions. This value is used to test the effect of an order of magnitude change in CR ionisation rate on the chemistry. These models had the same initial abundances and physical inputs as the models G, L and S, seen in Tables 2.2 and 3.1. The models are henceforth denoted GHCR, LHCR and SHCR to show their higher CR ionisation rate. Figure 3.25(b) shows the electron and HCO^+ abundances in the HCR models. When compared with Figure 3.25(a), it can be seen that the electron abundance has a wider spread between the HCR models than between the initial set of GLS models. The HCR models reach steady state at a similar time to the GLS models, for both e^- and HCO^+. It can be seen in Figure 3.25(b) that the electron abundance is related to the HCO^+ abundance in each model, as the HCO^+ and e^- graphs for each HCR model asymptotically approach a value of $y=2x10^{-8}$. This "reflection line" value is slightly lower than that seen in Figure 3.25(a) and must result from the change in the CR ionisation rate, as this is the

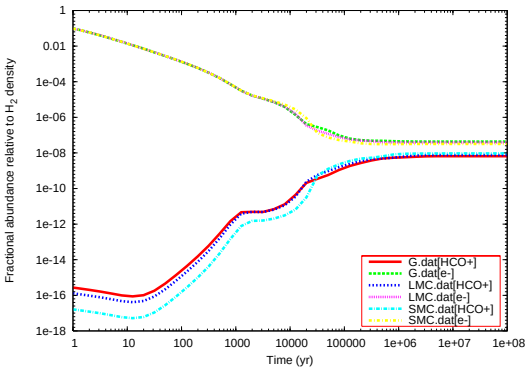

(a) HCO^+ and e^- in G, L and S

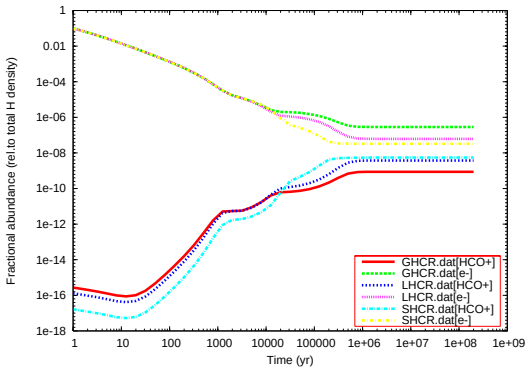

(b) HCO^+ and e^- in GHCR, LHCR and SHCR

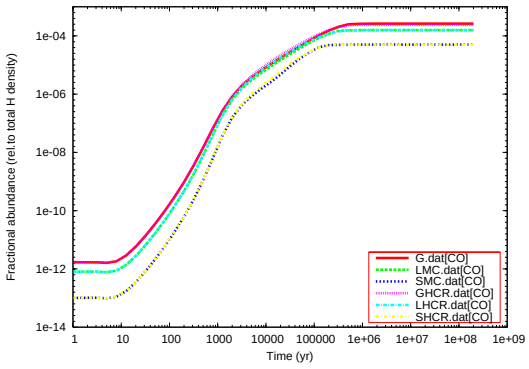

(c) CO in G, L, S, GHCR, LHCR and SHCR

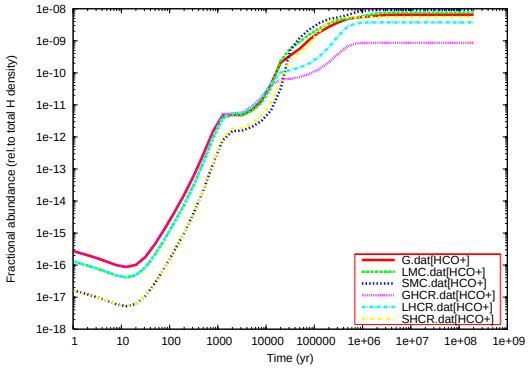

(d) HCO^+ in G, L, S, GHCR, LHCR and SHCR

Figure 3.25: The fractional abundances of HCO^+, e^- and CO in models G, L, S, GHCR, LHCR and SHCR.

only parameter which has been changed in the HCR models. It thus appears that the higher CR ionisation rate changes the steady state chemical equilibrium in the HCR models. The spread of values is increased for both HCO^+ and e^- in the HCR models. A steady state analysis of the GLS and HCR models shows that the e^- abundance is 6.5 times larger in the GHCR model than the G model, and the HCO^+ abundance is 7 times smaller in the GHCR model than in the G model. The similiarity in these numbers suggests that an increase in the steady state e^- abundance leads to a reduction in

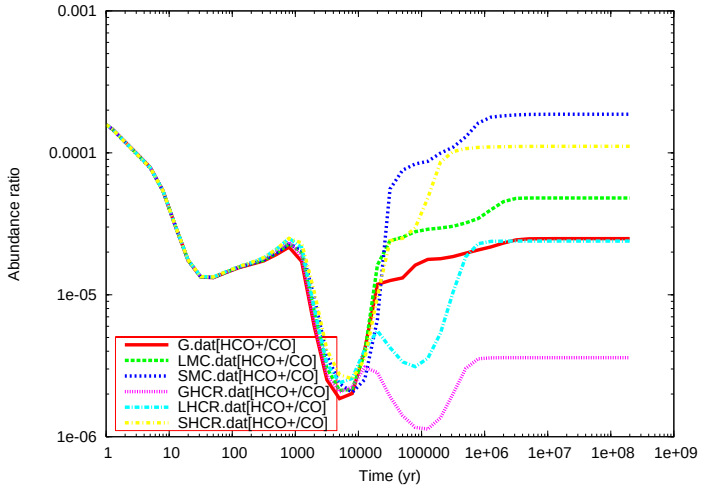

Figure 3.26: The HCO^+/CO ratio in models G, L, S, GHCR, LHCR and SHCR.

the steady state HCO^+ abundance. The CR ionisation rate was increased by an order of magnitude, and the changes in the e^- and HCO^+ abundances approximately reflect this. The LHCR and L model e^- abundances differed by a much smaller factor, with the fractional e^- abundance being 60% higher in the LHCR model. The HCO^+ fractional abundance in model L was twice as big as that in model LHCR, again showing a link between the e^- and HCO^+ abundances. In the SHCR and S models, the steady state fractional e^- abundance differed by around 2%, being slightly larger in the SHCR model. The fractional HCO^+ abundance is 70% bigger in the S model.

In the dark cloud model, the e^- abundance is a conserved parameter, which forces the model to conserve charge. The strongest influence on the e^- abundance in the model is the initial proportion of charged species. The increase in steady state e^- abundance seen in the GHCR model is a result of the increased CR ionisation rate which causes the chemistry to reach steady state at a different equilibrium to the G model. The effect of this on the LHCR and SHCR models is less strong, as there are fewer metals in the models to transfer the increased charge between species. It seems the effects of a change in CR ionisation rate are felt less strongly at lower metallicity. This is useful, as the CR ionisation rate is not well-known for extragalactic regions. If the HCO^+ and CO abundances are not strongly affected by a change in CR ionisation rate at low

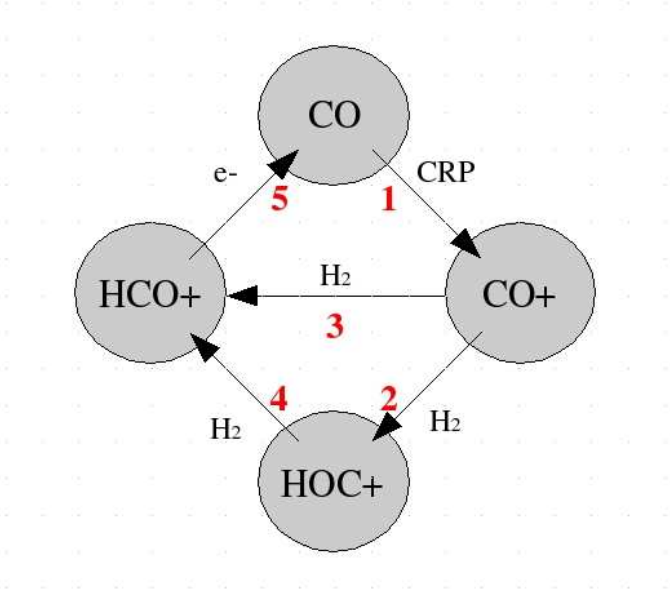

Figure 3.27: Part of the reaction network in the GLS models. This shows the reactions which govern the HCO^+/CO ratio from approximately 5×10^4 years onwards.

metallicity, then the HCO^+/CO ratio could be a very useful tracer of heavy metals under these conditions.

From Figure 3.25(c), it can be seen that the equilibrium chemistry for CO is not affected by the CR ionisation rate. At both early time and steady state, the GLS models and their counterpart HCR models have extremely similar abundances of CO.

The steady state HCO^+ fractional abundance for the two sets of models is seen in more detail in Figure 3.29. It can be seen that the HCO^+ abundance is at higher in the GLS models than in the corresponding HCR models. The steady state abundance of HCO^+ in models G, L and S exists over a smaller range than the fractional abundances in the HCR models. The chemical networks which govern the HCO^+ and CO abundances in the GLS and HCR models are shown in Figures 3.27 and 3.28 respectively. The reactions involved in these networks are listed in full in Table 3.24, along with their rates.

In the GLS models, the HCO^+ abundance at steady state is governed by reaction 1, as seen in Figure 3.27. The rate of this reaction determines the rate at which HCO^+ is

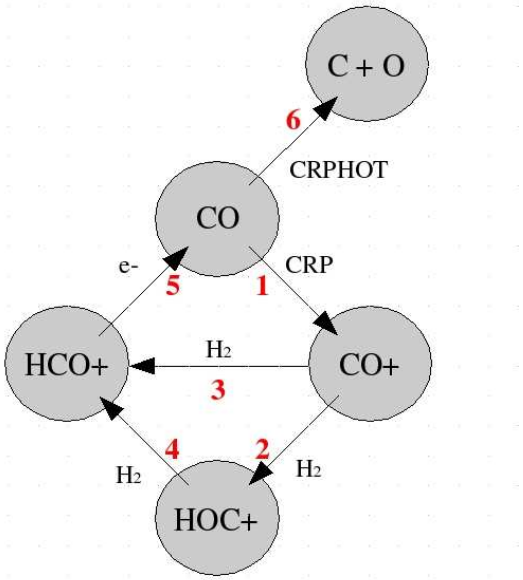

Figure 3.28: Part of the reaction network in the HCR models. This shows the reactions which govern the HCO^+/CO ratio from approximately 5×10^4 years onwards.

Reaction number	Reaction	GLS Rate	HCR Rate
1	$CO + CRP \longrightarrow CO^+ + e^-$	3.90E-17	3.90E-17
2	$CO^+ + H_2 \longrightarrow HOC^+ + H$	7.50E-10	7.50E-10
3	$CO^+ + H_2 \longrightarrow HCO^+ + H$	7.50E-10	7.50E-10
4	$HOC^+ + H_2 \longrightarrow HCO^+ + H_2$	3.80E-10	3.80E-10
5	$HCO^+ + e^- \longrightarrow CO + H$	2.51E-06	2.51E-06
6	$CO + CRPHOT \longrightarrow O + C$	3.41E-15	3.41E-14

Table 3.24: The reactions which govern the HCO^+/CO ratio in the dark cloud models. The numbers are referred to in Figures 3.27 and 3.28. CRPHOT refers to a cosmic-ray photon, and CRP to a cosmic-ray proton, as used in Woodall et al. (2007).

formed, as the CO^+ which is a product of reaction 1 quickly goes on to form HCO^+ via reactions 2 and 3. Reaction 1 has the slowest rate, and is thus the rate determining step.

In the HCR models, the HCO^+/CO ratio is much more strongly affected by reaction 6, as seen in Figure 3.28. This reaction is enhanced in the HCR models, as the number

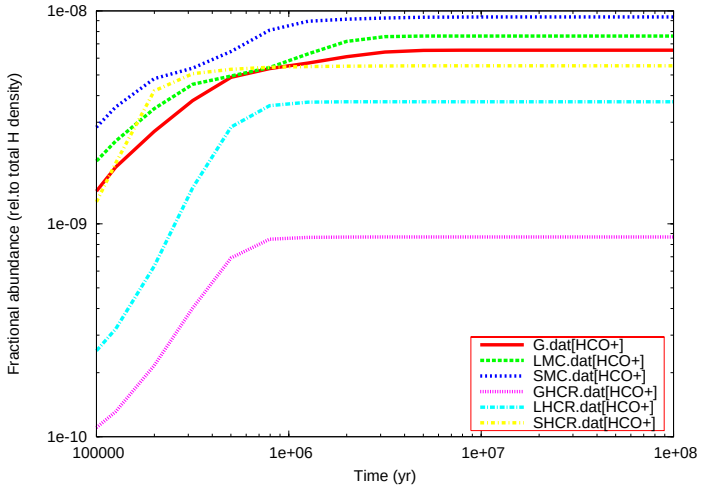

Figure 3.29: The steady state HCO^+ abundance in models G, L, S, GHCR, LHCR and SHCR.

density of CR induced photons is increased by the higher CR ionisation rate. The reaction rate is increased by an order of magnitude, when compared with the rate in the GLS models. For this reason, more of the CO which is destroyed is photodissociated to atomic carbon and oxygen. This changes the HCO^+/CO ratio considerably. In the GLS models, much of the CO which is destroyed becomes HCO^+, as seen in Figure 3.27, and the two species form an interdependent quasi-steady-state chemistry from around 5×10^4 years. In the HCR models, more of the CO which is destroyed becomes atomic carbon and oxygen. Although this will be eventually be formed into species including CO and HCO^+, this obviously reduces the HCO^+/CO ratio when compared with the GLS models.

It can be shown by the differences between the GLS and HCR model results that the HCO^+/CO ratio does trace metallicity. However, in some instances this ratio is more sensitive to changes in the CR ionisation rate than change in the underlying metallicity. A further investigation of the effect of the CR ionisation rate on the model results would be interesting, and could provide a method for determining the CR ionisation rate in other galaxies.

Comparison with Caselli et al. (1998)

Langer (1985) used steady state chemical models to show that the DCO^+/HCO^+ and HCO^+/CO ratios can be used to estimate the underlying fractional ionisation of a dark cloud and the CR ionisation rate in the region. Caselli et al. (1998) constructed a formula which allows the underlying fractional ionisation and CR ionisation rate to be calculated from these ratios at steady state. The results from the NK models indicate that this relationship holds for early time as well as steady state. Although there is no deuterium chemistry in the model, the HCO^+/CO ratio has a high level of correlation with the underlying M abundance. A chemical model investigation into the DCO^+/HCO^+ ratio at early time could be used to verify if this relationship holds at early time as well as steady state. This could provide the basis for future work.

CO/H_3O^+

The CO/H_3O^+ abundance ratio for models G, L and S is seen in Figure 3.30(a). This ratio is a useful metallicity tracer from around 3×10^4 years onwards, as it is fairly constant in each model beyond this time. The ratio is highest in model G (the highest metallicity model), and lowest in model S. The age of a typical dark cloud is estimated to be around 1×10^5 years, and so this ratio could prove useful in determining the underlying metallicity of a dark cloud. Between 3×10^4 and 5×10^5 years, there is some crossover in CO/H_3O^+ value ranges for models G and L. This means that unless the age of a dark cloud could be accurately determined, the CO/H_3O^+ ratio could only be used to provide a range for the underlying metallicity, rather than a specific value. For example, if an observation of the ratio gave a value of 2.6×10^4, and the age of the dark cloud was not certain, then this could indicate a metallicity similar to the G or L models. This provides a range of values for the underlying metallicity, but not a definitive value. At steady state, the ratios in the three models are easily discernable, as they differ by a factor of a few between models. Figure 3.30(b) shows the CO/H_3O^+ ratio in the DC1–DC6 models. It can be seen that the ratio decreases with decreasing

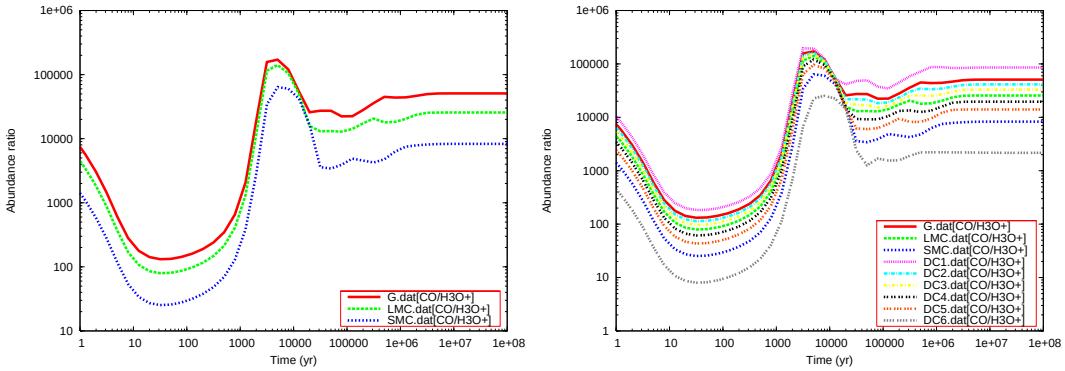

(a) CO/H_3O^+ in models G, L and S

(b) CO/H_3O^+ in models G, L, S and DC1-DC6

Figure 3.30: The CO/H_3O^+ ratio in models G, L, S and DC1-DC6.

metallicity across the whole range of models shown here.

The CO/H_3O^+ ratio correlates with the underlying carbon abundance in the dark cloud models. Figure 3.31 shows this correlation at various times in the model. The line parameters and Pearson correlation coefficients are shown in Table 3.25. These figures, and straight line equations, could be used to estimate the underlying carbon abundance in a dark cloud, if observations of the CO and H_3O^+ abundances were made.

	1.26×10^4yrs	**1.26×10^5yrs**	**1.26×10^6yrs**	**1.26×10^7yrs**	**1.26×10^8yrs**
Slope	2.19	1.15	0.98	0.91	0.89
Intercept	-33.19	-20.39	-19.33	-18.73	-18.53
R^2	0.963	0.997	0.995	0.999	0.999

Table 3.25: The line parameters and Pearson correlation coefficient values for the linear relationship between the natural log of CO/H_3O^+ and the natural log of the underlying carbon abundance in the dark cloud models, at various times.

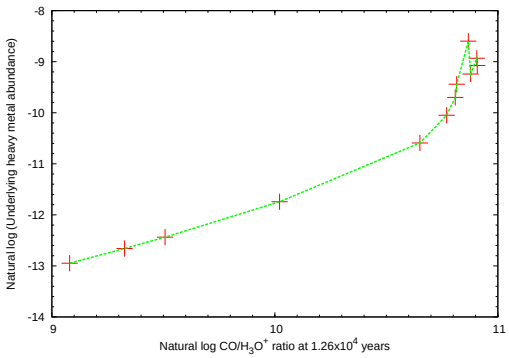

(a) CO/H_3O^+ at 1.26×10^4 years

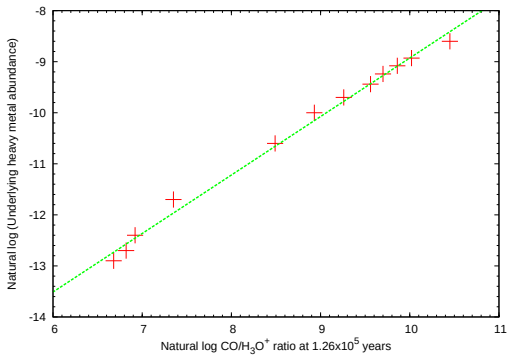

(b) CO/H_3O^+ at 1.26×10^5 years

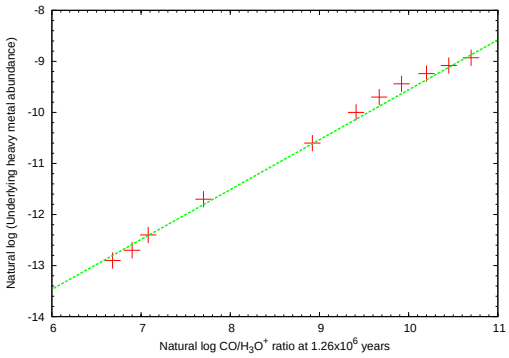

(c) CO/H_3O^+ at 1.26×10^6 years

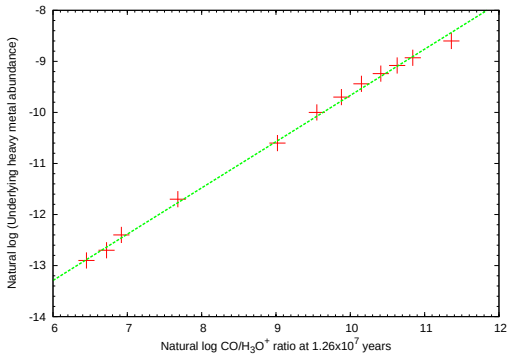

(d) CO/H_3O^+ at 1.26×10^7 years

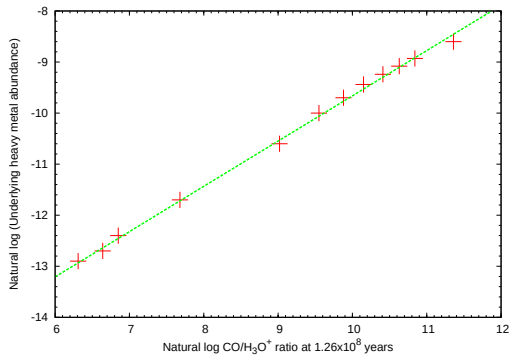

(e) CO/H_3O^+ at 1.26×10^8 years

Figure 3.31: The correlation between the CO/H_3O^+ ratio and the underlying carbon abundance in models G, L, S and DC1–DC9, at various times.

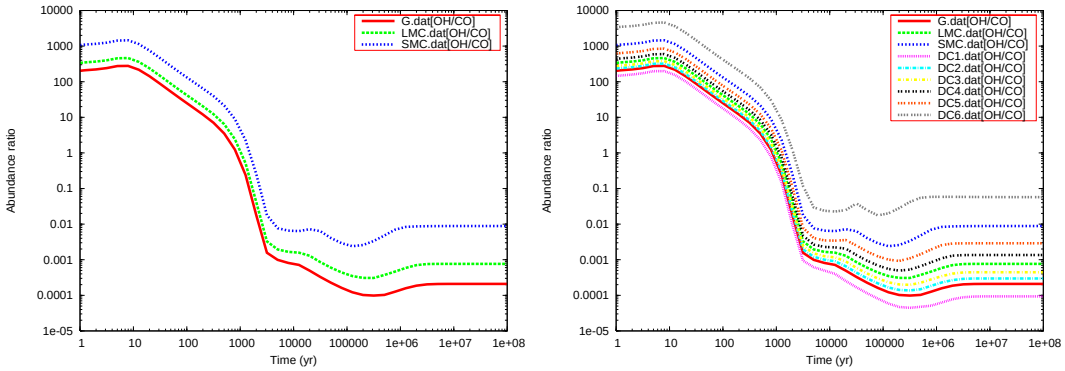

(a) OH/CO in models G, L and S

(b) OH/CO in models G, L, S and DC1-DC6

Figure 3.32: The OH/CO ratio in models G, L, S and DC1-DC6.

OH/CO

The fractional abundance of OH/CO is shown as a function of time for the models G, L and S in Figure 3.32(a). The abundance ratio OH/CO is a good metallicity tracer from around 10^5 years onwards. Figure 3.32(b) shows the OH/CO ratio for the models G, L, S and DC1-DC6. It can be seen that for most of these models, there is a definitive range of OH/CO values which identify that model (and therefore, the underlying metallicity). For some of the models shown, e.g. DC4 and DC5, an observed OH/CO ratio of 0.001 could indicate the underlying metallicity in either model, as this number is included in the range for both models. If the age of the cloud is unknown, this result can be used to provide a constraining range of values for the underlying metallicity, rather than a definitive metallicity value. The abundances of both OH and CO are also sufficiently high as to be observable, which is an important consideration when identifying a tracer. Figure 3.18(c) shows that the fractional OH abundance increases with decreasing metallicity, so it is likely that this species could be observed, even in dark clouds with very low metallicity. However, OH and CO gas are not typically observed together, owing to the very different frequencies at which they are observed - typically 1.7GHz for OH (e.g. Cappa de Nicolau & Poppel 1991, Crutcher et al. 1993) and 115GHz for CO (e.g. Young et al. 1982, Thampi & Dave 2006). This makes the result

less useful, as two separate observations would be needed to investigate this ratio in a dark cloud.

Figure 3.33 shows the OH/CO ratio as a function of the underlying fractional carbon abundance in models G, L, S and DC1–DC9, at various times. This ratio seems to trace the underlying carbon abundance even at 10^4 years. However, Figure 3.32(b) shows that at 10^4 years, the OH/CO ratio is still changing, particularly in the more metallic models, and so the results from Figure 3.33(a) are not very useful. Figures 3.33(b) - 3.33(e) show the relationship between OH/CO and the underlying carbon abundance from 10^5 years onwards. Observed values for the OH/CO ratio from dark clouds in other galaxies, or low metallicity regions, could be used in conjunction with these graphs to estimate the underlying carbon abundance in a dark cloud. This could be done most accurately if the age of the cloud were known. Overall, the OH/CO ratio could be a reasonably useful tool for estimating the underlying carbon abundance in a dark cloud.

3.5 Estimating the Age of a Dark Cloud

Figure 3.34 shows the NH_3/C^+ and NH_3/CH^+ ratios for models G, L and S. It can be seen that these ratios increase with increasing chemical age of the dark cloud, and that the increases are largely independent of temperature. If these species were observed in a dark cloud, and a ratio made, this could be used to constrain the chemical age of the dark cloud. The fractional NH_3 abundance increases with time, as atomic nitrogen becomes hydrogenated to form NH_3. The C^+ and CH^+ fractional abundances decrease with time, as more of the carbon becomes locked-up in the stable CO molecule. The balance between the NH_3 and the C^+/CH^+ abundances thus changes steadily with time, and each provides a ratio which can be used to estimate the chemical age of the dark cloud.

Suzuki et al. (1992) proposed that the C_2S/NH_3 ratio could be used as an indicator of

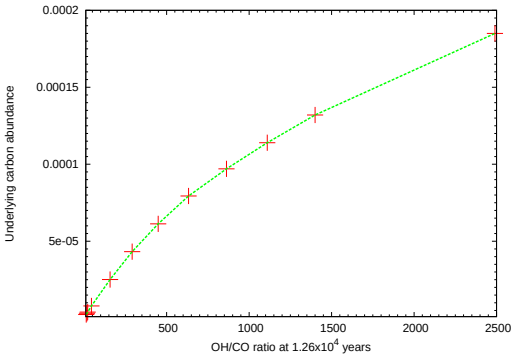

(a) 10^4 years

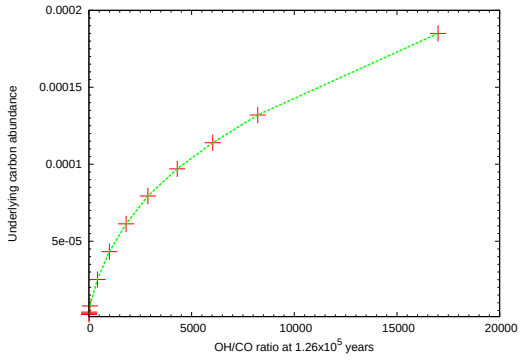

(b) 10^5 years

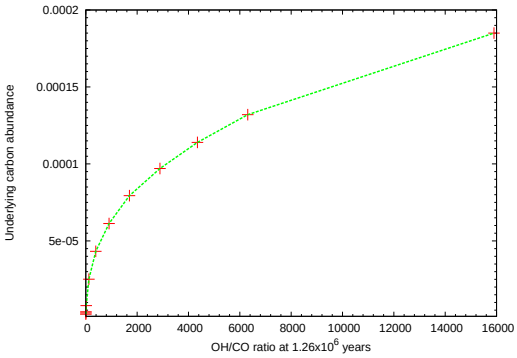

(c) 10^6 years

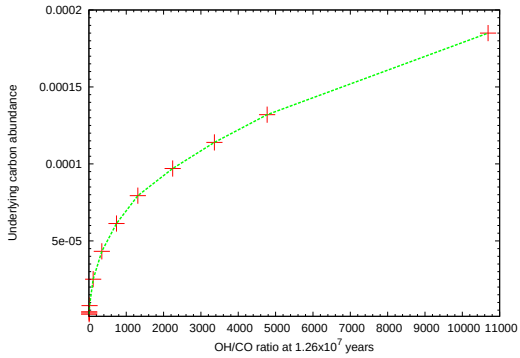

(d) 10^7 years

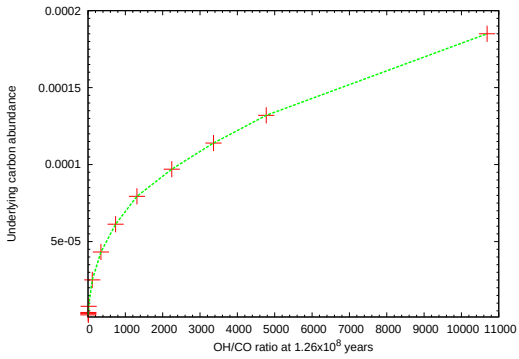

(e) 10^8 years

Figure 3.33: The OH/CO ratio as a function of the underlying carbon abundance in models G, L, S and DC1–DC9 and the underlying C abundance in each model, at various times.

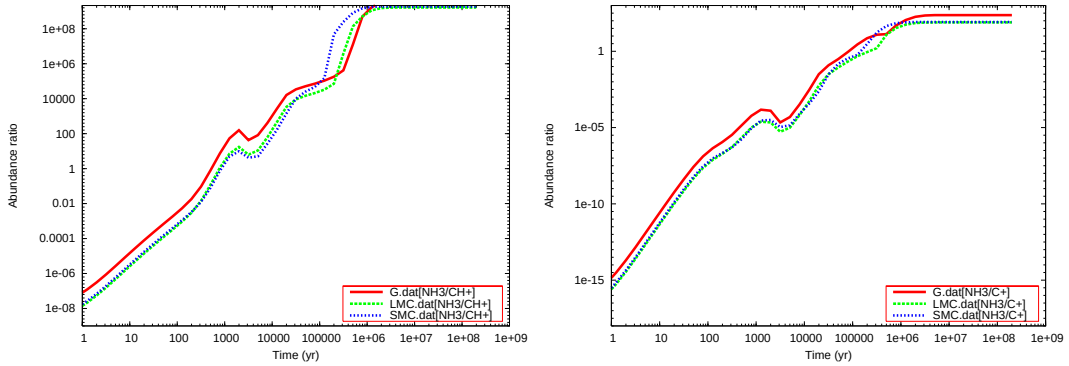

(a) NH_3/C^+ in models G, L and S

(b) NH_3/CH^+ in models G, L and S

Figure 3.34: The NH_3/C^+ and NH_3/CH^+ ratios in models G, L and S. These ratios appear to be largely independent of underlying metallicity. If observed, these ratios could be used to estimate the age of a dark cloud.

dark cloud evolution. Figure 3.35 shows the C_2S/NH_3 for models G, L and S. The ratio could be used to constrain the age of a dark cloud, as if a ratio greater than 1 were observed (as seen in Figure 3.35(b)) then the age of the dark cloud could be assumed to be within the range 2×10^3 and 2×10^4 years, irrespective of the underlying metallicity of the dark cloud.

3.6 Conclusions

The different chemical evolution seen in each model for various species (e.g. CO^+, HCO, NS) demonstrates that a change in the underlying metallicity of a region does not translate directly into scaling up or down the expected abundances for a dark cloud. If the metallicity is halved in a model, the fractional abundances of each species will not automatically be halved. This is because the chemical network used in the models has many interdependencies, and when the amount of one species is reduced, a different reaction may dominate and cause an unexpected increase in another species.

The model results show that many abundant species (e.g. NH_3 and C_2H) are poor

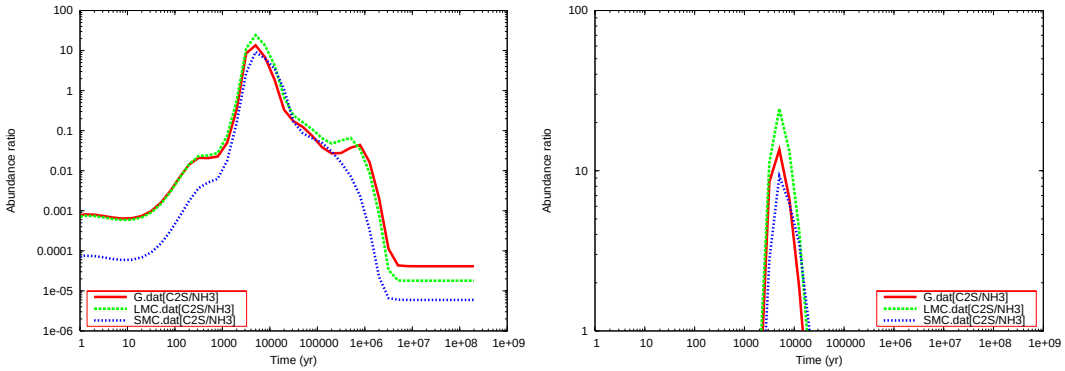

(a) C_2S/NH_3 in models G, L and S

(b) Reduced range C_2S/NH_3 in models G, L and S

Figure 3.35: The C_2S/NH_3 ratio in models G, L and S. If observed, this ratio could be used to constrain the age of a dark cloud.

metallicity tracers.

Several species (e.g. HCN, HNC, H_2O, SO) could be used as metallicity tracers if the age of a dark cloud were specifically known. However, these species could not be used if the cloud age/chemical evolution were uncertain.

Some ratios of species could be used to determine the underlying metallicity of a dark cloud, provided the cloud were older than a minimum age (different for each ratio). The HCO^+/CO ratio traces the underlying heavy metal (M) abundance of a cloud, and hence could give information regarding the fractional ionisation of a cloud. The CO/H_3O^+ and OH/CO ratios trace the underlying carbon abundance in a dark cloud.

These results can potentially be extrapolated, so that tracer ratios observed in galaxies at high redshift can be used to estimate the underlying metallicity of an extragalactic dark cloud.

The chemical age of a dark cloud can be estimated using the NH_3/C^+ and NH_3/CH^+ ratios. The ratios increase with increasing chemical age, and appear to be independent of underlying metallicity.

The results from the NK dark cloud model represent a single point with high visual

extinction, assumed to be at the centre of a dark cloud. In reality, a dark cloud is likely to exist as part of a larger cloud complex, with a lower visual extinction in the outer regions. For example, a dark cloud could be embedded within a more diffuse cloud. The observed values predicted here only apply to the dark cloud environment, and the chemistry seen in a more diffuse cloud may be quite different. For example, a lower visual extinction would allow more photoreactions to occur within the cloud. Larger species would be broken down, and so lower abundances of these species would occur. More charged species, e.g. C^+, would exist in a dark cloud with a lower density and visual extinction. A more elaborate model, with a density/visual extinction gradient could be used to more accurately reflect observations which could be made in an extragalactic star-forming region. This could form the basis of future work.

4

Hot core modelling at low metallicity

4.1 Introduction

A pseudo-time dependent gas-grain hot core model has been used to model a hot core under conditions thought to be typical of such a region in the Galaxy, the Large Magellanic Cloud and the Small Magellanic Cloud.

As described in Section 2.4, the Hot Core Model consists of two stages – the first models the isothermal collapse of a dark cloud, the second is the Multidepth Hot Core model. The temperature profile seen in Figure 2.2 is applied to the Multidepth Model. This approximation assumes an instantaneous temperature increase throughout the hot core, when the protostar "switches on". The hot core model used in this thesis contains a well-defined physical structure which represents a progression from models such as Millar et al. (1997b). The model used in Millar et al. (1997b) contained a number of concentric shells and a density/temperature gradient, similar to that seen in the model used in this thesis. However, the models used here contain a greater number of shells, and hence more detailed information about the radial hot core structure. The instantaneous temperature increase which is assumed at the start of Multidepth phase of this hot core model is unlikely to be a truly accurate reflection of the physical processes which occur in reality. Viti & Williams (1999) created a hot core model in which the protostar

switching on results in a gradual temperature rise. The Viti & Williams (1999) model incorporated a less complex surface chemistry than that used in this thesis. Viti & Williams (1999) found that the first 60,000 years were affected by the gradual temperature increase, and that at times greater than 60,000 years the chemistry was not affected by the speed of the temperature increase. In this thesis, the chemistry is generally examined at 10^4, 10^5 and 10^6 years. The findings of Viti & Williams (1999) serve as a caveat to the results of the hot core models at 10^4 years. However, the results at 10^5 and 10^6 years should not be affected by the instantaneous temperature increase used in this model.

4.1.1 The Chemistry in the Hot Core Model

The same chemical reaction network is used in both stages of the Hot Core Model. The reaction network includes all 4605 gas-phase reactions from the UMIST Rate 06 database (Woodall et al., 2007), as well as 63 gas-phase reactions as used in Tideswell et al. (2010) to model gas-phase HNCO. The grain surface chemistry consisted of a network of 273 reactions (Allen & Robinson 1977; Hasegawa et al. 1992; Hasegawa & Herbst 1993b; Garrod et al. 2008) which were added to the model by Tideswell et al. (2010). The number of gas-phase species used in the model is 420, and the number of grain surface-species is 215.

The Chemical and Physical Input Parameters

Twelve models were run, with varying initial chemical abundances, dust/gas ratio and visual extinctions. From these models, three were selected to model a typical hot core in the Galaxy, the LMC and the SMC. These models are discussed in this chapter, along with some of the other models which were used to isolate certain effects, for example the effect of changing the input abundances without changing the dust/gas ratio.
Two Galactic models are included in this chapter. The input parameters used in these models, along with the other models which are discussed, are included in Table 4.1.

The Galactic model, G1, uses input abundances taken from Hubble Space Telescope observations of Galactic interstellar clouds. Another Galactic model, G TMC, is also included. The initial elemental abundances used in the G TMC model come from Woodall et al. (2007). These abundances are representative of the Taurus Molecular Cloud, a Galactic star-forming region which contains depleted abundances of most elements. The initial abundances used in these models, as well as the LMC and SMC models, are shown in Table 4.1.

Observations of HII regions in the LMC and SMC were used to determine the initial elemental abundances of carbon, oxygen, nitrogen and sulpur used in the LMC and SMC Collapse models. The initial S abundances used in these models were depleted using a ratio of 217. This ratio was found by comparing the Galactic S abundance in an HII region (García-Rojas et al., 2007) with the Galactic S abundance in a depleted dark cloud (Woodall et al., 2007). This depletion factor was used in an attempt to produce model results which accounted for the sulphur depletion problem, as discussed by Ruffle et al. (1999). The heavy metal (in the form of Fe in these models) abundances for the LMC and SMC models were taken from Lebouteiller et al. (2008). These abundances were depleted by a factor of 166. This factor is taken from Okada et al. (2008), and represents the depletion of Fe between an HII region and a star-forming region. The iron is depleted as it is incorporated into the dust grains. These initial abundances, and the physical parameters used, can be seen in Table 4.1. Millar & Herbst (1990) and Stanimirovic et al. (2000) were used to choose the dust/gas ratios for the LMC and SMC respectively. The input abundances used in the Multidepth Model are taken from the output of the Collapse Model, at the appropriate density. Some example species are shown in Table 4.2. The species which begin with the letter G are grain-surface species. It can be seen that the fractional abundances of many of the species are very low. The atomic species freeze out onto the grain surfaces very quickly within the isothermal collapse model (within the first few thousand years). This allows for little formation of molecular gas. Once the atomic elements have adhered to the grain surface, they are most likely to react with hydrogen. This results in large

Model	C	O	N	S	Fe	DUST	EXT
G1[1,2,3]	1.32E-004	3.19E-004	7.50E-005	8.57E-008	1.50E-008	1	1
G TMC[4]	7.30E-005	1.76E-004	2.14E-005	4.00E-008	2.10E-008	1	1
L1[4,5,6]	7.94E-005	2.51E-004	7.94E-006	2.30E-008	1.05E-008	1	1
L2[4,5,6]	7.94E-005	2.51E-004	7.94E-006	2.30E-008	1.05E-008	0.25	0.25
S1[4,5,7]	2.51E-005	1.00E-004	3.16E-006	9.16E-009	1.82E-009	1	1
S2[4,5,7]	2.51E-005	1.00E-004	3.16E-006	9.16E-009	1.82E-009	0.03	0.03

Table 4.1: The Hot Core Collapse Model Input Abundances relative to the total number of hydrogen nuclei. [1]Savage & Sembach (1996); [2]Meyer et al. (1997); [3]Meyer et al. (1998); [4]Woodall et al. (2007); [5]Garnett (1999), García-Rojas et al. (2007), Lebouteiller et al. (2008), Okada et al. (2008); [6]Millar & Herbst (1990); [7]Stanimirovic et al. (2000). The 'DUST' parameter shows the dust/gas ratio used in that model, as a proportion of that used in the G1 model. The 'EXT' parameter shows the visual extinction used in that model, as a proportion of that used in the G1 model.

amounts of hydrogenated species forming – example, atomic carbon forms CH, CH_2, CH_3 and CH_4 on the grain surfaces. These hydrogenated species are returned to the gas phase when the protostar switches on. They tend to be destroyed quite quickly by species such as atomic oxygen and OH.

4.2 The Galactic Hot Core Models

The initial elemental abundances used in the G1 and G TMC models can be seen in Table 4.1, as can the references from where the abundances came. It can be seen that the Galactic (G1) model has higher abundances of all elements, except Fe, than the G TMC model. The dark cloud TMC-1 is thought to be depleted in most elements, to some extent (Woodall et al., 2007), compared with an 'average' Galactic star forming region. The purpose of running models G1 and G TMC was to investigate the effects of this depletion on the model results. The species analysed are those which are abundant

	Fractional Abundance to H		
Species	**Shell 1**	**Shell 9**	**Shell 17**
CO	4.09E-015	4.45E-014	8.36E-010
GCO	6.22E-008	6.25E-008	6.80E-008
CS	1.12E-019	1.02E-018	2.06E-014
GCS	2.15E-025	1.79E-024	1.88E-020
CH_3OH	0.00E+000	0.00E+000	1.15E-024
GCH_3OH	3.56E-006	3.56E-006	3.56E-006
HCN	3.19E-019	1.62E-018	2.67E-014
GHCN	6.65E-007	6.65E-007	6.65E-007
HNC	2.01E-020	7.88E-020	5.97E-016
GHNC	3.61E-007	3.61E-007	3.61E-007
HNCO	5.99E-020	2.85E-019	7.15E-017
GHNCO	3.12E-021	1.38E-020	3.30E-017
HC_3N	0.00E+000	1.52E-025	1.18E-019
GHC_3N	0.00E+000	0.00E+000	2.78E-025
HCO^+	7.36E-023	4.43E-022	2.26E-014

Table 4.2: Some example fractional abundance inputs for three shells of the Multidepth Model. These fractional abundances come from the Collapse Model, with initial abundances taken from model G1. The listed fractional abundances which begin with the letter G are adhered to a grain surface. Shell 1 is the innermost shell of the hot core, and shell 17 is the outermost shell. Shell 9 is one of the intermediate shells, roughly halfway between shells 1 and 17.

in hot cores, and likely to be observable in star-forming regions in other galaxies.

4.2.1 Results from the Galactic Hot Core Model and the 'TMC-1 type metallicity' Hot Core Model

CO

As seen in Figure 4.1(a), the CO abundance in the G1 model at 10^4 years does not vary much with increasing radius, with a fractional abundance of around 1.5×10^{-6} from the centre up to a distance of 0.06pc. After this, the CO abundance falls dramatically, suggesting it is readily destroyed in the outer shells of the hot core. At 10^5 years, the same pattern is seen, although the abundance in the inner regions of the hot core has increased by a factor of around 4, giving a fractional abundance of around 6×10^{-6}. The abundance begins to drop at around 0.04pc. At 0.07pc, a sharp decrease in abundance leads to the CO abundance in the outer shells (approximately 0.085pc onwards) to be the same as at 10^4 years. By comparing the fractional abundance graphs, it can be seen that CO has been forming in the time interval between 10^4 and 10^5 years, in all shells except the outer two. This shows that the CO in the outer two shells has already reached a chemical steady state by this time. This is caused by the lower density and higher fractional ionisation in these shells, compared with the intermediate and inner shells of the hot core. More discussion of the behaviour in these shells can be found in Section 4.5.10.

The CO abundance at 10^6 years is not as steady in the inner shells, and the abundance falls, then peaks towards the edge of the hot core, with a fractional abundance of 5.6×10^{-5} at a distance of 0.05pc from the centre. A sharp drop in abundance follows, and the abundance in the outermost shells is the same as in the model at 10^4 and 10^5 years. This shows that a chemical equilibrium for CO is reached more quickly in the outer shells. The destruction and formation rates for CO in the two outer shells are very similar, at both 10^5 and 10^6 years. The species that destroy CO in this region are charged species only - namely, He^+, H_3^+ and CH_5^+. Additionally, all the CO which is formed in these shells at 10^5 and 10^5 years comes from the destruction of HCO^+. For all other shells at 10^6 years, the CO abundance is higher than at 10^5 years, as CO is still

being formed in the gas phase. The uneven shape of the curve shows that more CO is formed in some shells, and less in others. In the inner/intermediate shells of the hot core, OH is the primary destructor species for CO at 10^5 and 10^5 years. The majority of the CO in these shells at these times is formed from neutral HCO, the remainder being formed from HCO^+ and CO_2. The neutral chemistry which dominates in the inner/intermediate shells is slower to reach equilibrium than the chemistry of the outer two shells. The most important results here are those for the hot core at 10^5 years, as this is a typical hot core age and it is unlikely that the chemistry will evolve beyond this point.

Figure 4.1(b) shows the CO fractional abundance for the G TMC model, at 10^4, 10^5 and 10^6 years. It can be seen that the abundances of CO are similar in models G1 and G TMC for all times. The greatest difference occurs at 10^6 years, when the CO abundance in some of the intermediate shells in G TMC falls to a lower level than at 10^5 years. The lower input abundance of carbon in the G TMC model is the cause of this. However, as stated above, it is unlikely a hot core would chemically evolve to this point without being dissociated.

The results from models G1 and G TMC show a characteristic pattern for a Galactic-type chemistry in a hot core - a fairly constant CO abundance across the centre, with a reduced CO abundance (by one or two orders of magnitude) at the outer edge.

HCO^+

Low fractional abundances of HCO^+ are produced in the G1 model at all times, as seen in Figure 4.2(a). At 10^4 years, the HCO^+ abundance is fairly constant for the inner regions of the hot core, increasing slowly up to a radius of 0.05pc. At this point, the fractional abundance increases sharply to a maximum at 0.07pc, before decreasing sharply again as the radius increases. The same shape is also seen at 10^5 and 10^6 years, although the fractional abundance increases with time, showing HCO^+ is formed in the gas phase. The abundances produced in this model are very low, and may not be high enough to detect. It is possible that at the peak abundance a detection may be

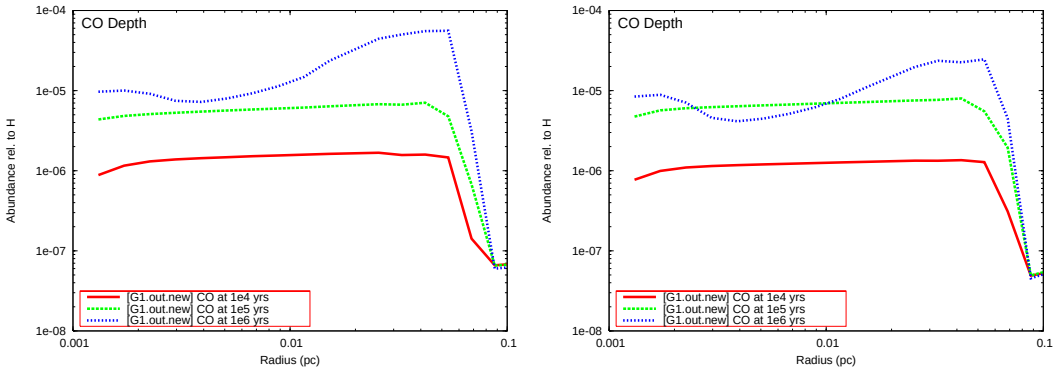

(a) G1 CO (b) G TMC CO

Figure 4.1: The fractional abundance of CO to H in models G1 and G TMC at 10^4, 10^5 and 10^6 years.

made - if so, a ring of HCO^+ would be detected at a distance of around 0.07pc from the centre of the hot core. The HCO^+ 'spike', or 'ring' at a radius of 0.07pc is caused by reactions with H_2CO, which form and (to a lesser extent) destroy HCO^+, at all times examined. A higher fractional abundance of H_2CO is formed at this radius. Beyond this radius, all of the gas phase H_2CO is formed via thermal desorption from grain surfaces. At smaller radii, H_2CO is formed via neutral-neutral reactions, whereas at 0.07pc the H_2CO is formed via ion-neutral reactions. These ion-neutral reactions have faster reaction rates than the neutral-neutral reactions, and so more H_2CO is formed at 0.07pc than further inside the hot core.

Figure 4.2(b) shows that the HCO^+ abundance in the G TMC model behaves in a very similar fashion to that seen in the G1 model, with respect to both depth and time. The main difference is that there is slightly more HCO^+ formed in G TMC at all times and depths. This is because the heavy metal (Fe) abundance is higher in model G TMC. This produces a greater proportion of charged species, such as HCO^+.

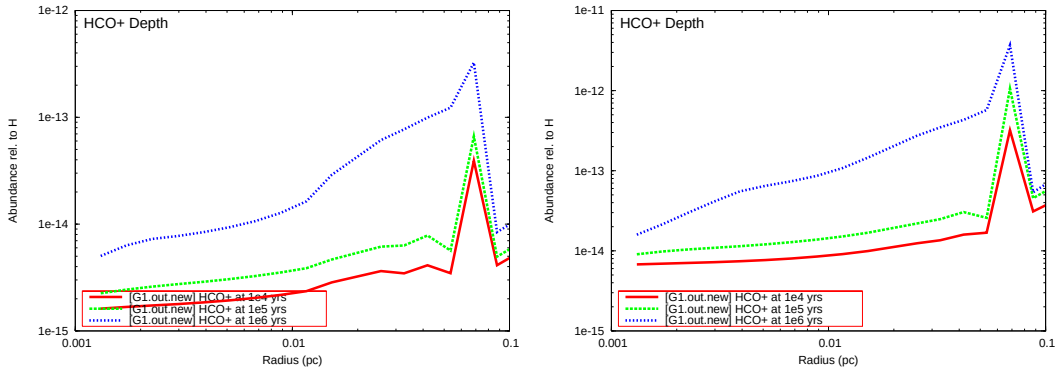

(a) G1 HCO^+ (b) G TMC1 HCO^+

Figure 4.2: The fractional abundance of HCO^+ to H in models G1 and G TMC at 10^4, 10^5 and 10^6 years.

HCN

The fractional abundance of HCN at 10^4 and 10^5 years is similar, as can be seen in Figure 4.3(a). The fractional abundance is approximately $7x10^{-7}$ across most of the hot core, from the centre up to a radius of 0.07pc. At this radius, the abundance drops, more sharply at 10^4 years than at 10^5 years. This means that the outer layers produce HCN in the intervening time period. As the HCN fractional abundance is fairly constant between 10^4 and 10^5 years, it is not a useful evolution tracer, or 'chemical clock'. However, at 10^6 years, the HCN abundance changes dramatically across the whole hot core. The HCN fractional abundance is seen to be highest at the inner and outer edges of the hot core, with a lower abundance seen inbetween. The different shells contain very different abundances, with some sharp jumps in abundance from one shell to the next. This could be interpreted as the hot core shell model 'breaking down', as it is unlikely that this is representative of what would happen in reality, if the shells were not discrete.

Figure 4.3(b) shows that the behaviour of HCN in model G TMC is similar to that seen in model G1. The HCN abundance seen at 10^4 and 10^5 years in G TMC is about half of that seen in model G1. The C and N abundance ratios for (G TMC)/(G1) are

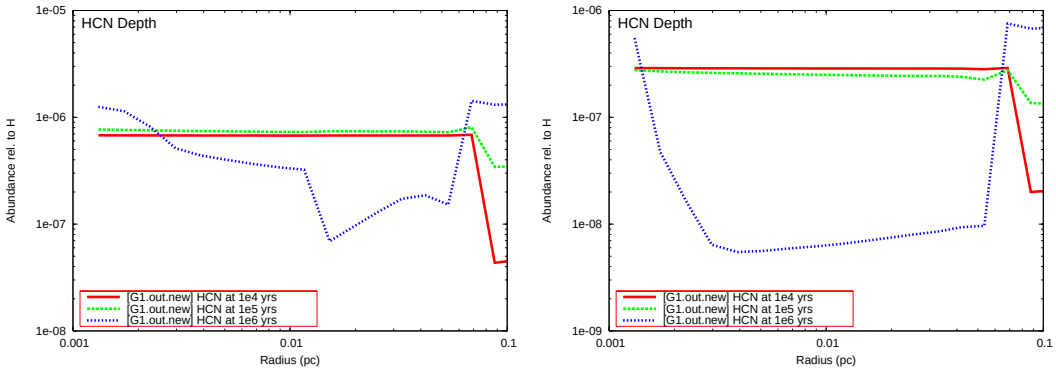

(a) G1 HCN

(b) G TMC HCN

Figure 4.3: The fractional abundance of HCN to H in models G1 and G TMC at 10^4, 10^5 and 10^6 years.

0.55 and 0.29 respectively. It is likely that the HCN fractional abundance ratio for (G TMC)/(G1) is governed by a combination of the C and N abundance ratios between the two models. At 10^6 years, the HCN abundance distribution differs between the two models. In G TMC, the fractional HCN abundance increases at the very inner and outer edges, and falls by a factor of 30 inbetween these peak abundances. The lower abundance in the intermediate regions is quite flat, with a smooth transition from shell to shell. As a whole, the hot core in G TMC at 10^6 years would be observed to have a high abundance of HCN in the very centre and at the edges. If this were seen in a region such as the TMC, it would imply the hot core contains a well-evolved chemistry, and provide an age constraint for the hot core.

The HCN abundances seen in both models at 10^4 and 10^5 years would be observed across the hot core as a fairly constant abundance, with a reduced fractional abundance at the edges of the hot core. At early time, the fractional abundances seen in both models are fairly high (between 2×10^{-6} and 2×10^{-8}) and could potentially be observed.

HNC

In the G1 model, the fractional abundance of HNC in the inner shells of the hot core is very similar to that of HCN at all times, as can be seen by comparing Figure 4.4(a) with Figure 4.3(a). At 10^4 and 10^5 years, the HNC abundance is lower than the HCN abundance by a factor of 1.9. This is because HCN forms approximately twice as efficiently as HNC on the grain surfaces, during the Collapse phase, as can be seen in Table 4.2. At 10^6 years the fractional abundances of HCN and HNC are very similar, as the two species have been processed in the gas phase. Both species form $HCNH^+$ upon reaction with charged species. $HCNH^+$ then goes on to form HCN and HNC, with a branching ratio of 50% in each case. By 10^6 years, this set of reactions leads to equal abundances of HCN and HNC being produced. The main differences between the species arise in the outermost shells of the hot core. The HNC abundance is stable across the whole hot core, whereas the HCN abundance drops in the outer shells, particularly at 10^4 years. This is because HNC continues to be produced in the gas-phase across the whole hot core radius, whereas HCN is mainly formed via thermal desorption from grain-surfaces in the outermost shells of the hot core. This is partly because HCN thermally desorbs from the grain surface at a faster rate than HNC, and partly because more HCN than HNC forms on the grain surfaces during the Collapse phase, as described above. Some of the gas-phase HCN is then processed into HNC.

In the G TMC model, the abundance and behaviour of HNC is similar to that of HCN. This can be seen by comparing Figure 4.4(b) with 4.3(b). The HNC abundance at 10^4 years is lower than the HCN abundance by a factor of 5, and at 10^5 years it is lower by a factor of 3. The HNC abundance can thus be seen to increase with time, across the whole hot core. The HNC abundance drops less dramatically at the outer edges of the hot core than the HCN abundance, so at 10^4 years there is more HNC than HCN in the outer shells. At 10^6 years, the evolved chemistry produces a HNC abundance pattern which is very similar to that seen in HCN. This would again produce an observation of a high HNC abundance in the centre and edge or the hot core, with a lower abundance

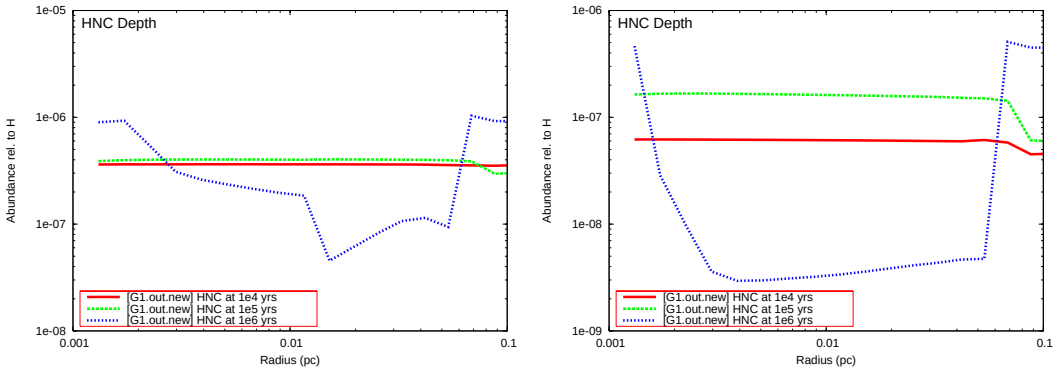

(a) G1 HNC (b) G TMC HNC

Figure 4.4: The fractional abundance of HNC to H in models G1 and G TMC at 10^4, 10^5 and 10^6 years.

in the regions inbetween.

In models G and G TMC, the HNC fractional abundance at early time is constant for most of the hot core radius. If an observation of HNC were made in which the abundance were lower in the intermediate shells, it could indicate an evolved chemistry, as this is characteristic of the chemistry at 10^6 years.

HNCO

HNCO, a typical hot core species, is seen in Figure 4.5(a). At 10^4 and 10^5 years, in model G1, the fractional abundance changes across the hot core in a similar pattern. Consistently higher abundances are seen at 10^5 years, which shows that HNCO is being actively produced in the gas phase in all shells of the hot core after 10^4 years. The abundance is fairly constant up to a radius of 0.015pc. The abundance then follows a general downward trend to the outer edge of the hot core, with fractional abundances falling by a factor of several thousand at both times. From this, it can be seen that the HNCO is tracing the hotter, denser gas in the middle of the hot core. At 10^6 years, the fractional abundance falls in the intermediate regions of the hot core, and increases in the extreme inner and outer regions. Aside from these changes, the graph retains a

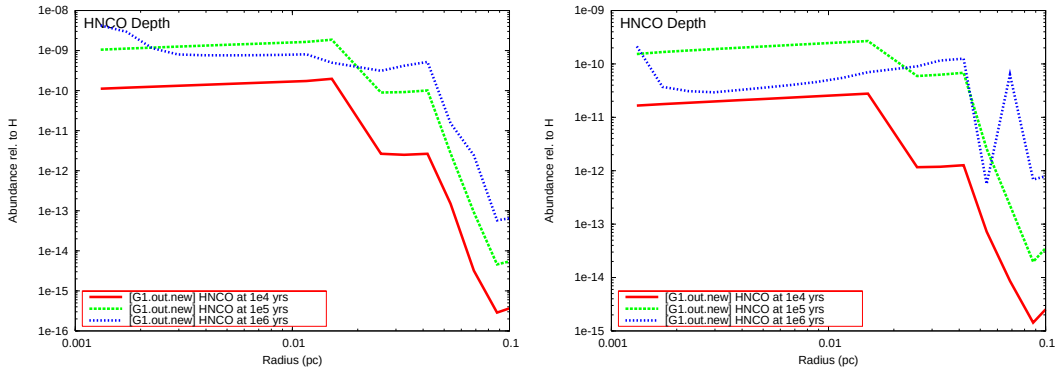

(a) G1 HNCO

(b) G TMC HNCO

Figure 4.5: The fractional abundance of HNCO to H in models G1 and G TMC at 10^4, 10^5 and 10^6 years.

similar shape to that seen at early time, with the bulk of the HNCO tracing the inner parts of the hot core, and tailing off considerably towards the edges.

The HNCO fractional abundance patterns in model G TMC, as shown in Figure 4.5(b), are similar to those seen in model G1. The main difference between the two models is the HNCO abundance, which is an order of magnitude lower in the G TMC model. The cause of this is the lower initial elemental abundances in model G TMC, as seen in Table 4.1. At 10^6 years, the fractional abundance falls in the inner regions of the hot core, and increases in the outer regions. The behaviour is seen to be quite different from shell to shell, particularly in the outer regions. This may show that the shell model is not as appropriate for the evolved/steady state chemistry as for the early time chemistry, as the shells exist in isolation and it is unlikely that this abundance pattern would occur in reality.

Overall, both the G1 and G TMC models show a similar HNCO abundance pattern at all times. The fractional abundance is very high in the centre of the hot core, and extremely low at the outer edge.

HC_3N

Figure 4.6(a) shows the fractional HC_3N abundance in the G1 model. It can be seen that HC_3N could potentially used as a 'chemical clock', in order to constrain the age of a hot core. The abundance of HC_3N increases with time in the model, showing it is produced in the gas phase. The fractional abundance varies by around one order of magnitude at each time shown on the graph – e.g. at 10^4 years it varies between 10^{-10} and 10^{-11}. However, even with this variation, each time has its own distinct fractional abundance 'window', which could be used to estimate an age for the hot core.

Figure 4.6(b) shows the fractional abundance of HC_3N across the hot core in model G TMC. The fractional abundances seen at 10^4 and 10^5 years are extremely similar to those seen in model G1. However, at 10^6 years, the G TMC model stops producing HC_3N. At this time, the HC_3N fractional abundance has increased at the inner and outer edges of the hot core, but has remained similar in the shells inbetween. This is a similar pattern of behaviour to HCN and HNC as seen in Figures 4.3(b) and 4.4(b) respectively. This is explained, in part, by the behaviour of N_2, as seen in Figures 4.6(c) and 4.6(d). As the hot core age increases, more N_2 is formed in models G1 and G TMC, particularly in the middle shells at 10^5 and 10^6 years. A greater proportion of the nitrogen is thus 'locked up' in the N_2 molecule, and is unable to form nitrogen-bearing species including HCN, HNC and HC_3N. At the inner and outer edges of the hot core, a much smaller proportion of the nitrogen forms N_2, and so more nitrogen is available to form the other nitrogen-bearing species.

HC_3N is thought to be a density tracer, but its abundance does not appear to clearly trace the density changes across the hot core models. Furthermore, its variability with time demonstrates that it may not be a reliable tracer of density if the age of the observed region is unknown.

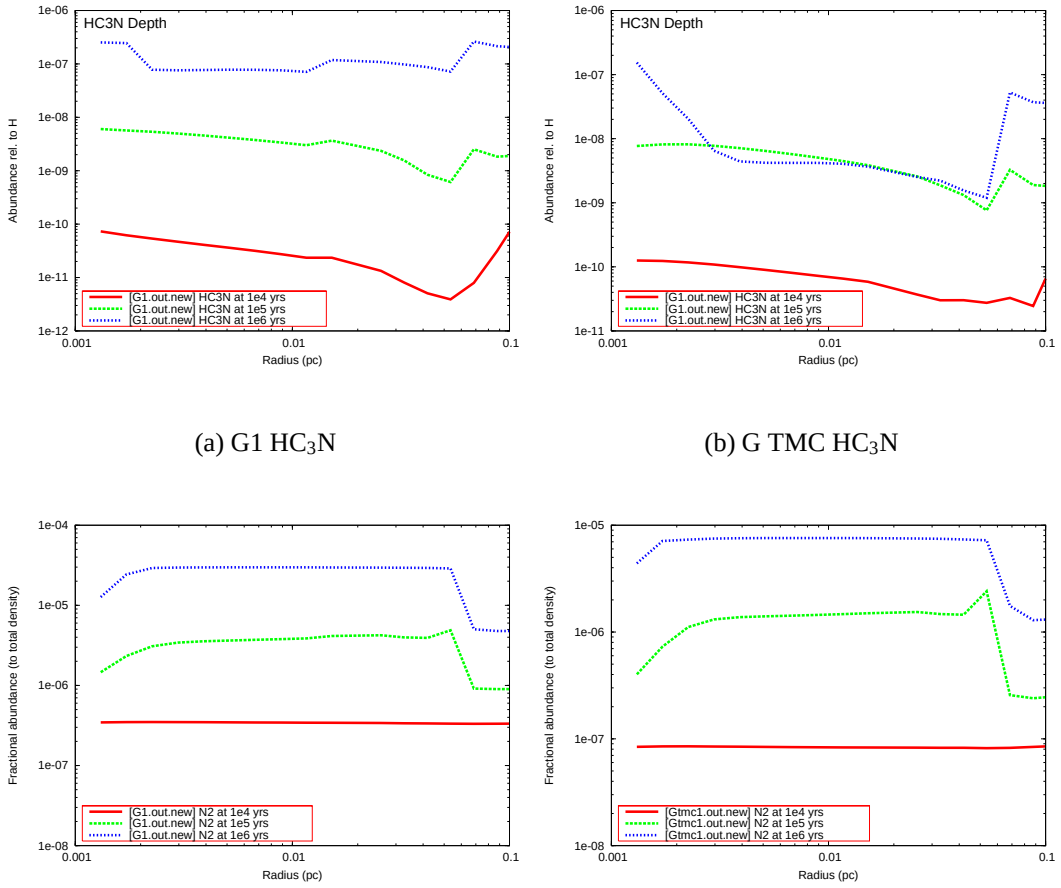

(a) G1 HC_3N (b) G TMC HC_3N

(c) G1 N_2 (d) G TMC N_2

Figure 4.6: The fractional abundance of HC_3N and N_2 to H in models G1 and G TMC at 10^4, 10^5 and 10^6 years.

CH_3OH

Figure 4.7(a) shows the fractional abundance of CH_3OH across the hot core. At 10^4 and 10^5 years, the abundance is fairly constant across the inner parts of the hot core. At 10^4 years there is a fractional abundance of around 3.3×10^{-6} and at 10^5 years this has slightly decreased to around 1.8×10^{-6}. Beyond a radius of 0.04pc, the fractional abundance falls rapidly, by around 10 and 6 orders of magnitude at 10^4 and 10^5 years respectively. The fractional abundances seen at 10^4 years shows the CH_3OH has uniformly thermally desorbed from the grain surfaces up to a distance of 0.04pc, which

corresponds to a minimum temperature of around 42K. The CH_3OH abundance beyond this radius comes from the gas phase. By 10^5 years, the CH_3OH abundance in the inner shells has begun to drop, as in the gas phase the species is destroyed more efficiently than it is produced. At the outer edges of the hot core, the fractional abundance increases by several orders of magnitude. In this region, the existing CH_3OH was produced in the gas phase of the collapsing dark cloud. The switching on of the protostar increases the temperature in this region, and so more CH_3OH is produced with time. At 10^6 years, the CH_3OH fractional abundance has dropped by up to 4 orders of magnitude, showing that this species is efficiently destroyed. The species is mainly destroyed by the oxygen bearing species H_3O^+, via the following reaction:

$$H_3O^+ + CH_3OH \rightarrow CH_3 + H_2CO \tag{4.1}$$

The abundances seen at 10^6 years are very low, and so less easily observable than the high fractional abundances seen at 10^4 and 10^5 years. Therefore, a low observed abundance of CH_3OH could show that a hot core is chemically old, with a lower age limit provided by a model such as this one.

Figure 4.7(b) shows the fractional abundance of CH_3OH across the hot core in model G TMC. The fractional abundances seen are slightly higher than those from model G1, with a similar pattern of behaviour. At 10^4 years there is a fractional abundance of around 4.5×10^{-6} and at 10^5 years this has slightly decreased to around 1.5×10^{-6}. Beyond a radius of 0.04pc the fractional abundance falls rapidly, by around 6 orders of magnitude. At 10^6 years, the CH_3OH fractional abundance has dropped by up to 5 orders of magnitude.

It can be seen that CH_3OH is abundant in both models at early time. This species behaves in a similar fashion to HNCO, with a high abundance in the inner regions of the hot core, and an extremely low abundance in the outer regions.

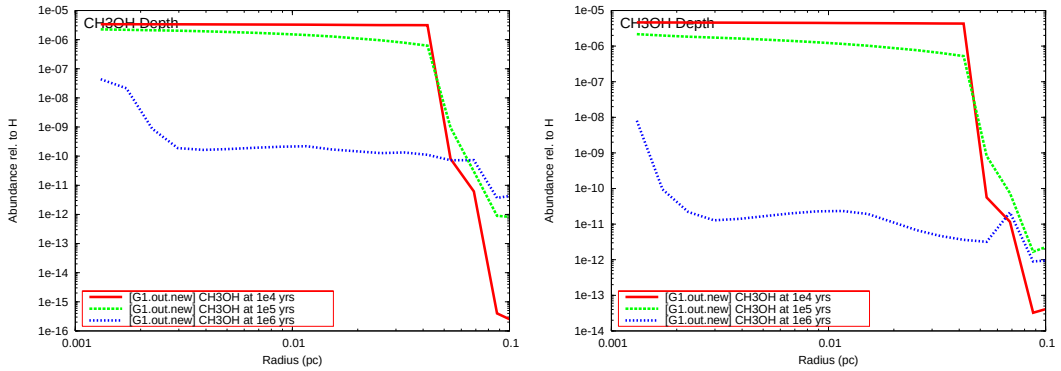

(a) G1 CH_3OH (b) G TMC CH_3OH

Figure 4.7: The fractional abundance of CH_3OH to H in models G1 and G TMC at 10^4, 10^5 and 10^6 years.

CS

The fractional abundance of CS in model G1 across the hot core is seen in Figure 4.8(a). At 10^4 years, CS is most abundant in the inner part of the hot core. The abundance decreases fairly steadily with radius, although there is a secondary peak at around 0.06pc. After this, the fractional abundance falls swiftly, with a small increase at the outer edge. At 10^5 years, a similar abundance pattern is seen. However, the fractional abundance has increased throughout the hot core, with the exception of the outer edge where the abundance remains constant. CS is thus being produced in the gas phase, in most parts of the hot core. It appears that CS has reached a chemical equilibrium in the outermost parts of the hot core. At 10^6 years, the fractional CS abundance has increased in the innermost part of the hot core, and also towards the outer edge, at the site of the secondary peak.

The CS fractional abundances from the G TMC model are shown in Figure 4.8(b). At 10^4 and 10^5 years, the abundances seen in the inner regions of the hot core follow a similar pattern to those seen in the G1 model, although the G TMC abundances are lower. The abundance at 10^4 years is fairly consistent across the hot core, with a fractional abundance just below 10^{-9}. By 10^5 years, the fractional abundances have

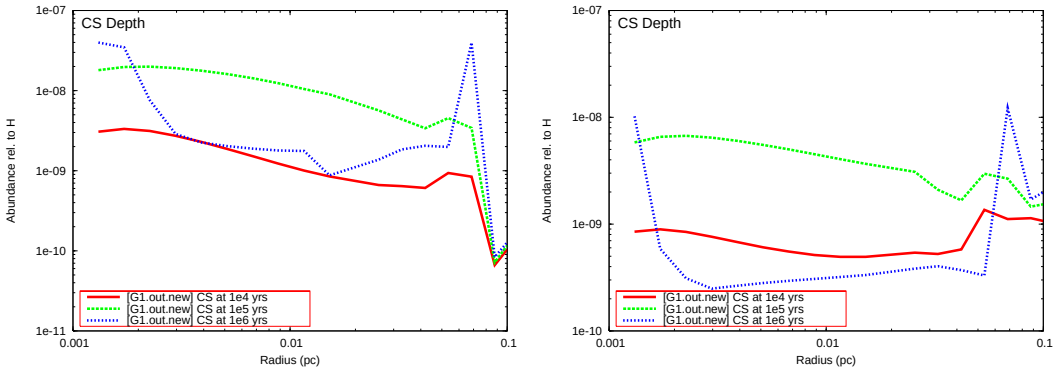

(a) G1 CS (b) G TMC CS

Figure 4.8: The fractional abundance of CS to H in models G1 and G TMC at 10^4, 10^5 and 10^6 years.

increased, particularly in the inner regions of the hot core. At 10^6 years, the fractional abundance follows the pattern of HCN, HNC, etc, with a higher value at the inner and outer shells, and a lower value inbetween.

The CS fractional abundance pattern seen in both models is fairly consistent - a reasonably flat abundance of CS is seen across the whole hot core. In the G1 model, the outer shells show a much lower abundance than the G TMC model, but the general appearance of the graphs is similar. To an observer, this should look as though the CS is found uniformly across the hot core at early time. If a larger abundance is observed in the centre and at the edges, this could indicate the hot core is chemically old.

NH_3

Figure 4.9 shows the fractional NH_3 abundance in models G1 and G TMC, at 10^4, 10^5 and 10^6 years. Figure 4.9(a) shows that the same fractional NH_3 abundance is seen across the whole hot core at 10^4 years in model G1. This is because the species forms on grain surfaces during the collapse phase, and is thermally desorbed in all shells when the protostar 'switches on'. The fractional NH_3 abundance drops slightly in model G1 between 10^4 and 10^5 years. At both times, the fractional abundance seen

in all shells across the hot core is identical. The NH_3 is being destroyed at the same rate in each shell, irrespective of the shell temperature and density. In model G1, NH_3 is destroyed by a mixture of charged and neutral species in all shells. By 10^6 years, the fractional abundance pattern has changed across the hot core. The highest fractional NH_3 abundances are formed in the inner and outer shells, and the fractional abundance in the intermediate shells is reduced by over two orders of magnitude. This is caused by the nitrogen atoms becoming locked up in the N_2 molecule at steady state, as seen in Figure 4.6(c).

Figure 4.9(b) shows the NH_3 fractional abundance in model G TMC. The fractional abundances seen at 10^4 and 10^5 years in this model are lower than the abundances seen in G1, by a factor of ~ 4. Table 4.1 shows that model G1 has a higher underlying abundance of nitrogen than model G TMC, by a factor of ~ 9. The decreased abundance of nitrogen in model G TMC leads to a lower fractional NH_3 abundance in that model. In model G TMC, the NH_3 fractional abundance evolves with time in a similar manner to that seen in model G1. The fractional abundance is flat as a function of radius at 10^4 years, and nearly flat at 10^5 years. At 10^6 years, the fractional NH_3 abundance is much reduced in the middle shells. Again, this can be attributed to the nitrogen becoming locked up in molecular N_2, as seen in Figure 4.6(d).

4.2.2 Comparison of the G1 Model with Observations

Table 4.3 shows a comparison of some observed fractional abundances (in the hot core G34.3+0.15) with the fractional abundances produced by the model G1 at 10^5 years. The modelled and observed abundances compare reasonably well in most cases. It is hard to directly compare the observed isotopologues (e.g. $HN^{13}C$) with the modelled abundances, as these isotopologues were not included in the model. Estimates of the fractional abundances of these isotopologues in the G1 model were made by scaling down the modelled abundances by an appropriate factor - e.g. the $^{12}C/^{13}C$ ratio in the Milky Way.

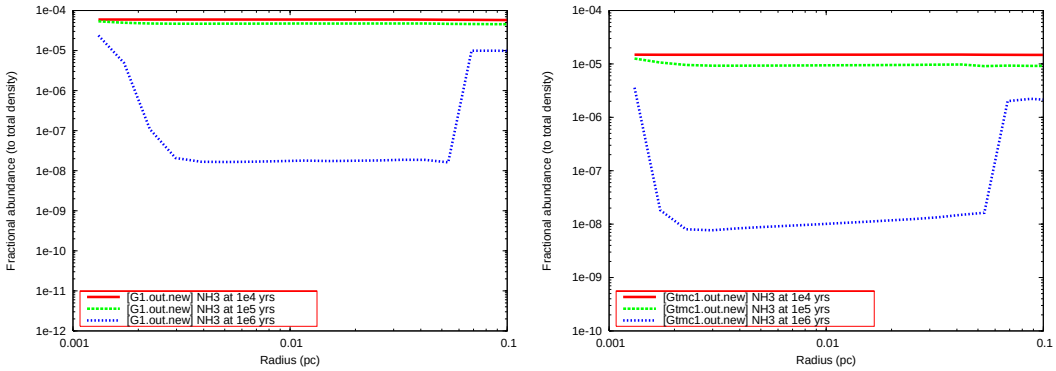

(a) G1 NH_3 (b) G TMC NH_3

Figure 4.9: The fractional abundance of NH_3 to H in models G1 and G TMC at 10^4, 10^5 and 10^6 years.

The modelled values which do not compare well to the observations are the fractional isotopologue abundances. The isotopologues are not included in the hot core model. The inclusion of isotopologues in the hot core model would improve the estimates of these fractional abundances, as it appears that the fractionation of the isotopes does not scale directly with the underlying isotopic ratio in a hot core.
Overall, the G1 model produces reasonable estimates for the fractional abundances of these common hot core species.

4.3 The LMC and SMC Hot Core Models

The initial parameters used in the LMC and SMC models can be seen in Table 4.1. Models L1 and S1 contain reduced elemental input abundances, and the same dust/gas ratio and visual extinction as in model G1. These models can be thought of as depleted Galactic models, as the physical conditions resemble those found in the Milky Way. Models L2 and S2 contain the same reduced elemental abundances seen in models L1 and S1, but the dust/gas ratio and visual extinction is depleted in these models.
The models which are thought to most closely resemble the low metallicity environ-

Species	Observed	Modelled		
		Shell 1	Shell 8	Shell 17
CH_3OH	1.80E-008	2.25E-006	1.58E-006	7.80E-013
$H^{13}CO^+$	1.15E-011	2.96E-017	4.64E-017	8.76E-017
HCN	3.60E-011	7.69E-007	7.33E-007	3.49E-007
$HN^{13}C$	5.00E-012	5.12E-009	5.29E-009	3.98E-009
HC_3N	1.15E-011	7.31E-011	2.75E-011	1.46E-010
	2.35E-011	7.31E-011	2.75E-011	1.46E-010
HNCO	2.65E-010	1.05E-009	1.56E-009	6.34E-015
	1.40E-010	1.05E-009	1.56E-009	6.34E-015
CS	8.00E-011	1.80E-008	1.24E-008	1.77E-010
NH_3	1.00E-006	5.37E-005	4.72E-005	4.53E-005

Table 4.3: This table shows some observed fractional abundances (relative to H) from the hot core G34.3+0.15, along with some modelled fractional abundances (relative to H) from the G1 model. The observed abundances are taken from MacDonald et al. (1996), with the exception of NH_3 which is taken from Heaton et al. (1989). Where two observed values are given for one species, both values were observed in the hot core. Isotopologues were not modelled in the hot core model, and so for observations of species such as $H^{13}CO^+$, the modelled fractional abundance is reduced by the isotopic ratio $^{12}C/^{13}C = 76$ (Stahl et al., 2008). The modelled values are taken from model G1 at 10^5 years, in shells 1, 8 and 17.

ments in the LMC and SMC are models L2 and S2. Models L1 and S1 are used to isolate the effects of changing the dust/gas ratio and visual extinction.

4.3.1 Results from the LMC and SMC Hot Core Models

Figures 4.10(a) and 4.10(b) show the fractional HC_3N abundances at 10^4 years, for models G1, L2 and S2 and models G1, L1 and S1 respectively. The difference between the two figures is that the dust/gas ratio has been reduced for models L2 and S2, but is maintained at a Galactic level for L1 and S1. It can be seen that changing this

parameter (and thus, the visual extinction) has a profound effect on the chemistry of HC_3N. The HC_3N fractional abundance is much higher in model L2 than L1 (and S2 than S1). This is because HC_3N is most efficiently formed in the gas phase, and when the dust/gas ratio is reduced, the amount of carbon and nitrogen available in the gas phase is greatly increased. HC_3N forms more readily in the gas phase than on grain surfaces, as this species contains many unsaturated bonds. If the species were deposited onto a grain surface, or were formed there, it would undergo hydrogen addition(s), and produce a more saturated species which would be returned to the gas phase when the protostar 'switches on'. The species which form on the grain surfaces, or which are deposited there, tend to become much more saturated. Example species include C_3H_2N and C_3H_3N, which only form on grain surfaces during the collapse phase. They are desorbed when the protostar switches on, and then processed by the hot core gas phase chemistry. In the gas phase, HC_3N is destroyed by reaction with H_3^+ in models L2 and S2. This does not happen to any appreciable extent in models L1 and S1.

At 10^4 years, in models L1 and S1, most of the HC_3N forms via the following reaction with C_2H_2:

$$CN + C_2H_2 \rightarrow HC_3N + H \tag{4.2}$$

Whereas in models L2 and S2 at 10^4 years, most of the HC_3N forms via the following reactions:

$$CH_3OH + HC_3NH^+ \rightarrow HC_3N + CH_3OH_2^+ \tag{4.3}$$

$$NH_3 + HC_3NH^+ \rightarrow HC_3N + NH_4^+ \tag{4.4}$$

$$HC_3NH^+ + e^- \rightarrow HC_3N + H \tag{4.5}$$

In models L2 and S2, there is a cycle of HC_3N production, with the previous production reactions being followed by these destruction reactions:

$$HC_3N + H_3^+ \rightarrow HC_3NH^+ + H_2 \tag{4.6}$$

$$HC_3N + H_3O^+ \rightarrow HC_3NH^+ + H_2O \tag{4.7}$$

The species HC_3NH^+ is much more abundant in models L2 and S2 than in models L1 and S1, as seen in Figures 4.10(c) and 4.10(d). This species is not formed on the grain surfaces, and so when the dust/gas ratio is lowered, proportionally more of the C and N atoms are available to form this species. The HC_3NH^+ then goes on to form HC_3N. Figures 4.11(a) and 4.11(b) show the fractional HC_3N abundances in the same models at 10^6 years. By this time, the differences between models L2 and L1, and S2 and S1, are far less great. This is because the gas-phase chemical reactions have thoroughly processed the material, over a very long time period. Many of the differences which were caused by species which form on grain surfaces have been eradicated by this time, as the larger species which form on the grains are broken down into smaller species.

Figure 4.12(a) shows the HNC fractional abundance in the three models at 10^4 years. The abundance range seen in each model is distinct from the other models, and so potentially this species could be a useful metallicity tracer. Figure 4.12(b) shows the fractional HNC abundances in models G1, L1 and S1 at the same time. By comparing these figures, it is apparent that the HNC abundance is not as sensitive to the changing gas/dust ratio as species such as HC_3N are. Although there is a change in abundance between models L1 and L2, the change is reasonably small. The change in fractional HNC abundance seen between models S1 and S2 is bigger, with a definite reduction in HNC in model S2. This is because HNC forms on the grain surfaces, as does HCN, from which HNC is formed (via $HCNH^+$). The lowered dust/gas ratio in model S2, results in fewer HNC (and HCN) molecules being formed during the collapse phase, as the total grain surface area is smaller in model S2 compared with S1. This results in less HNC existing in the gas-phase of the hot core at early time.

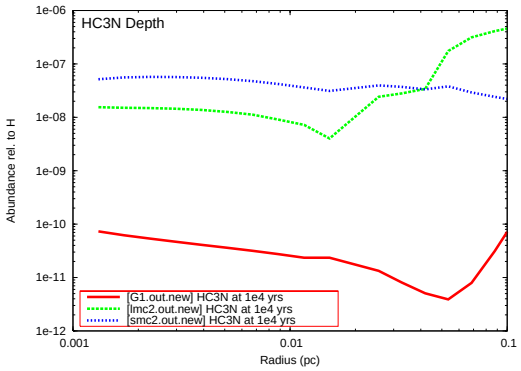

(a) HC_3N in models G, L2 and S2 at 10^4 years

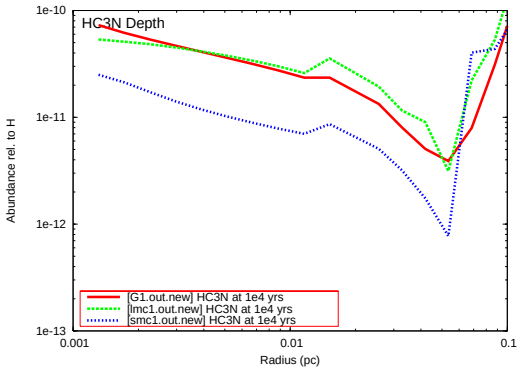

(b) HC_3N in models G, L1 and S1 at 10^4 years

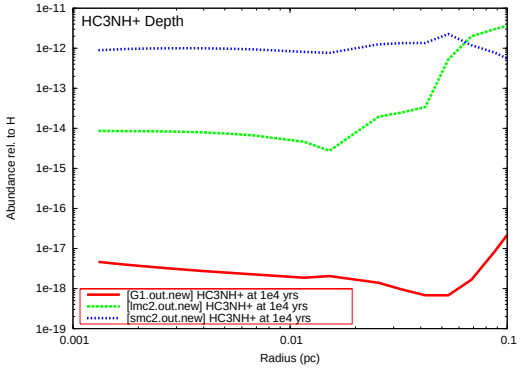

(c) HC_3NH^+ in models G, L2 and S2 at 10^4 years

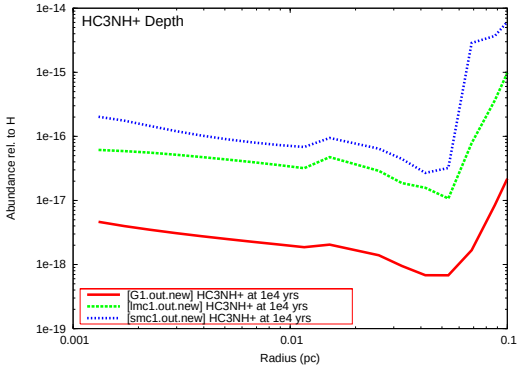

(d) HC_3NH^+ in models G, L1 and S1 at 10^4 years

Figure 4.10: The fractional abundance of HC_3N and HC_3NH^+ to H in models G1, L2, S2, L1 and S1 at 10^4 years.

4.4 Verification of the Model – Comparison with Bayet et al. (2008)

Bayet et al. (2008) investigated hot core models at low metallicity. The parameters which were varied included initial elemental abundances, dust/gas ratio, hot core temperature, hot core density and the cosmic ray ionisation rate. The hotcore models used

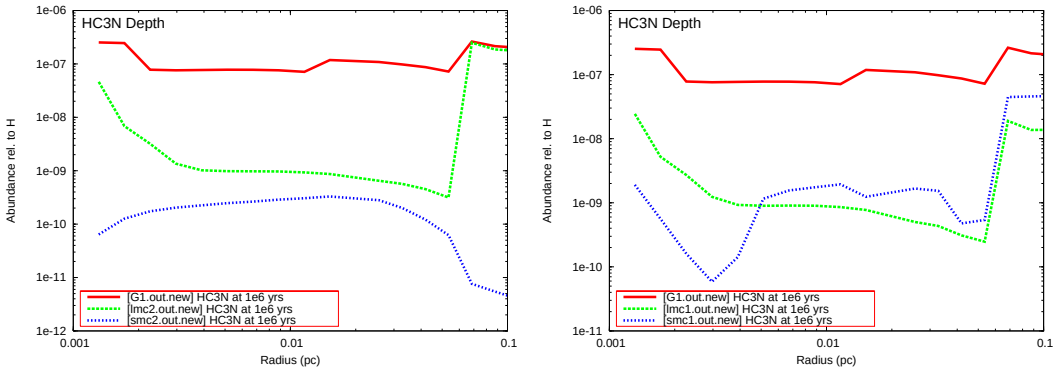

(a) HC_3N in models G, L2 and S2 at 10^6 years

(b) HC_3N in models G, L1 and S1 at 10^6 years

Figure 4.11: The fractional abundance of HC_3N to H in models G1, L2, S2, L1 and S1 at 10^6 years.

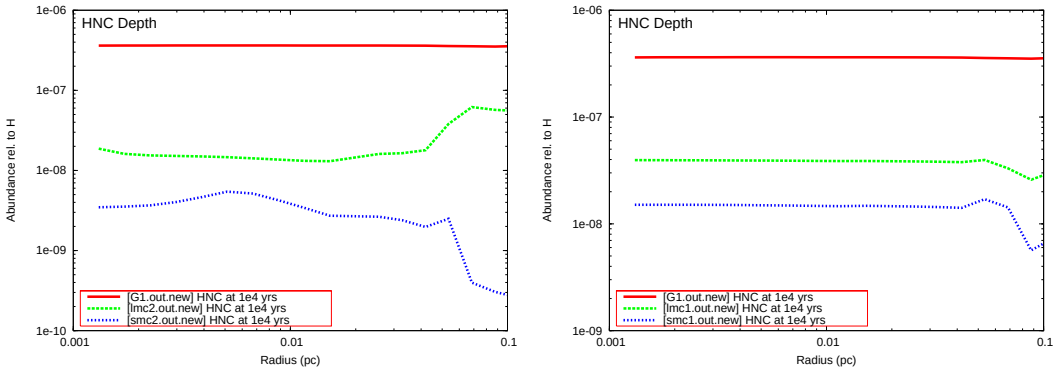

(a) HNC in models G, L2 and S2 at 10^4 years

(b) HNC in models G, L1 and S1 at 10^4 years

Figure 4.12: The fractional abundance of HNC to H in models G1, L2, S2, L1 and S1 at 10^4 years.

by Bayet et al. (2008) are less physically complex than those used in this thesis. The Bayet et al. (2008) models are comparable to one of the shells in the models used in this thesis - e.g. they contain a uniform temperature, density and set of chemical abundances. The Bayet models use the gas-phase chemical networks from Millar et al. (1997a) and Le Teuff et al. (2000), whereas the models in this thesis (hence-

forth JBCA[1] models) use the chemical reaction network of Woodall et al. (2007). As a benchmarking exercise, the Bayet models can be compared with the innermost shell of the G1 model from this thesis. The Bayet models chosen for comparison are Model 0 (a standard Galactic hot core) and Model 10, as this model is most similar to shell 1 in model G1 (henceforth, 1G1 or model 1G1) in terms of input abundances and physical conditions. Table 4.4 shows the physical and chemical abundance inputs for models 1G1, 0 and 10. A quick comparison reveals that the three models have many similarities, including the cosmic ray ionisation rate, and many of the input abundances. The most notable differences are the hot core temperature and the initial M (heavy metal) abundance. Model 1G1 represents a much cooler hot core than models 0 and 10. Model 1G1 also contains a much lower heavy metal abundance than models 0 and 10 – by a factor of 340. This means that model 1G1 transfers charge between species at a much lower rate than models 0 and 10. Model 10 contains the same input parameters as model 0, with the exception of the initial S abundance. The initial S abundance in model 10 is fairly similar to that seen in model 1G1, whereas the initial S abundance in model 0 is over an order of magnitude greater than that seen in 1G1. Figures 4.13 and 4.16 show the fractional abundances of various species with respect to time, for Models 0 and 10 amongst others. Figure 4.14(a) shows the fractional CS abundance in model 1G1 over the same time period. The general trend for the evolution of CS abundance with time in similar in models 1G1, 0 and 10. The fractional CS abundance in model 1G1 is in between the values seen in models 0 and 10. For example, at 10^4 years, the fractional CS abundance is around 3×10^{-9}, 2×10^{-8} and 3×10^{-10}, in models 1G1, 0 and 10 respectively.

Figure 4.14(b) shows how the CH_3CN fractional abundance changes with time in model 1G1. When compared with Figure 4.13, it can be seen that this species behaves differently in models 0 and 10. In model 1G1, the CH_3CN abundance peaks at steady state, whereas in models 0 and 10, the abundance peaks around 10^5 years before dropping off after this time. The peak fractional abundances seen are similar,

[1] Jodrell Bank Centre for Astrophysics

	Model 1G1	**Model 0 (ST)**	**Model 10**
Temperature (K)	179.4	300	300
CR ionisation rate (s^{-1})	1.33×10^{-17}	1.3×10^{-17}	1.3×10^{-17}
Grain number density/H nuclei density	1.33×10^{-12}	1.0×10^{-12}	1.0×10^{-12}
Number density (cm^{-3})	1.92×10^{7}	1×10^{7}	1×10^{7}
C/H	1.32×10^{-4}	1.4×10^{-4}	1.4×10^{-4}
O/H	3.19×10^{-4}	3.2×10^{-4}	3.2×10^{-4}
N/H	7.50×10^{-5}	6.5×10^{-5}	6.5×10^{-5}
He/H	1.00×10^{-1}	7.5×10^{-2}	7.5×10^{-2}
M/H*	1.50×10^{-8}	5.1×10^{-6}	5.1×10^{-6}
S/H	8.57×10^{-8}	1.4×10^{-6}	1.4×10^{-8}
O/C	2.4	2.3	2.3
Av (Magnitudes)	5540.6	581.1	581.1

Table 4.4: A comparison of Model 1G1 with Models 0 and 10 from Bayet et al. (2008). *The heavy metals (M) were included in the form of Fe for Model G1, and Mg for Models 0 and 10.

with values a little over 10^{-8}. The similarity of the underlying C abundance in the three models may explain the similar abundances produced, as this species contains two carbon atoms. The difference between the appearance time for the CH_3CN peak can be explained by the different physical conditions in the Bayet models compared with the models from this thesis (JBCA models).

Figure 4.14(c) shows the SO fractional abundance in model 1G1. By comparing with Figure 4.13, it can be seen that the SO is produced with a similar behaviour and fractional abundance in models 1G1 and 10. Model 0 has a fractional SO abundance, which is higher by around two orders of magnitude. This is caused by the higher initial S abundance in model 0, as seen in Table 4.4. The fractional SO_2 abundance is shown in Figure 4.14(d), for model 1G1. The behaviour here is different to that seen in the Bayet models, as the fractional abundance increases with time in the 1G1 model, but slightly decreases with time in the 0 and 10 models. At 10^4 years, the SO_2 fractional

abundance is similar in models 1G1 and 10, but by 10^6 years, the fractional abundance in 1G1 is closer to that seen in model 0. Overall, the fractional SO_2 abundance seen in model 1G1 compares reasonably well with the 0 and 10 models, when the differing underlying S abundance is considered.

Figure 4.14(e) shows the H_2CO fractional abundance in model 1G1 with respect to time. This species is more than an order of magnitude more abundant in model 1G1 than in models 0 and 10, at 10^4 years. However, by 10^6 years, the three models contain a similar H_2CO fractional abundance. H_2CO is formed on the grain surfaces in the collapse phase, and then destroyed in the gas phase of the hot core models. H_2CO is modelled differently in the gas-phase of the JBCA models, compared with that of the Bayet et al. (2008) models. Bayet et al. (2008) used the UDfA gas-phase chemical networks from Millar et al. (1997a) and Le Teuff et al. (2000), whereas the JBCA models use the UDfA chemical reaction network of Woodall et al. (2007). Woodall et al. (2007) implemented a large decrease to the reaction rate for H_2CO formation via reaction between C_2H_3 and O_2, as discussed in Section 3.3.2. Figure 4.14(e) shows that model 1G1 has a much higher fractional H_2CO abundance than models 0 and 10 (as seen in Figure 4.13) at 10^4 years. This demonstrates that the surface chemistry has a larger impact on this species than the gas-phase chemistry. The formation of H_2CO on grain surfaces is more efficient in model 1G1 than in models 0 and 10. Even at 10^6 years, after the H_2CO is desorbed and processed in the gas-phase, the fractional H_2CO abundance in model 1G1 is similar to that in models 0 and 10. If this species was purely formed and destroyed in the gas-phase, a higher abundance would be seen in models 0 and 10, as the gas-phase formation rate is much reduced in model 1G1. The H_2CO which forms on the grain surfaces increases the fractional gas-phase abundance in model 1G1.

The species CH_2CO is not included in the JBCA models, and so no comparison can be made with the Bayet models.

Figure 4.15(a) shows the fractional HCN abundance with respect to time, in model 1G1. At 10^4 years, the abundances in the three models are similar, with a fractional

abundance just below 10^{-6}. After around 4×10^4 years, the models diverge, as the HCN abundance in the 1G1 model slightly increases with time, whereas the HCN abundance in the 0 and 10 models falls by two orders of magnitude. The HNC fractional abundance in the three models is seen to be more similar than the HNC abundance, as seen in Figures 4.15(b) and 4.13. The fractional abundance in all three models is similar, with values ranging from $3–9\times10^{-7}$. The general trend in all three models is for the HNC fractional abundance to increase with time. HNC thus appears to be modelled in a similar manner in the Bayet and JBCA models.

The fractional OCS abundances from the three models can be compared in Figures 4.16 and 4.17(a). The species evolves in a similar manner in all three models. However, the fractional abundance in model 1G1 is much lower than models 0 and 10 at 10^4 years, by three and one orders of magnitude respectively. By 10^6 years, the fractional OCS abundance has risen to a value halfway between that seen in models 0 and 10, which corresponds to its intermediate underlying S abundance.

The fractional H_2O abundance corresponds almost perfectly between models 1G1, 0 and 10. This can be seen in Figures 4.16 and 4.17(b).

Figure 4.17(c) shows the time evolution of the fractional abundance of H_2S in model 1G1. When compared with Figure 4.16, it can be seen that the behaviour of this species is similar to that seen in models 0 and 10. The fractional abundance in 1G1 at 10^4 years is inbetween the values seen in models 0 and 10, which corresponds to the intermediate underlying S abundance in this model. However, the H_2S abundance in 1G1 drops off a little more quickly with time than in the 0 and 10 models. Overall, this species appears to be modelled in a similar fashion in the Bayet and JBCA models.

The H_2CS fractional abundance is seen in Figure 4.17(d), for model 1G1. This species behaves in a similar fashion in the Bayet and JBCA models, and again produced a fractional abundance somewhere between models 0 and 10, owing to the intermediate S abundance.

The fractional HCO^+ abundances from the Bayet and JBCA models can be seen in Figures 4.18(a) and 4.18(b) respectively. At 10^4 years, this species is around 35

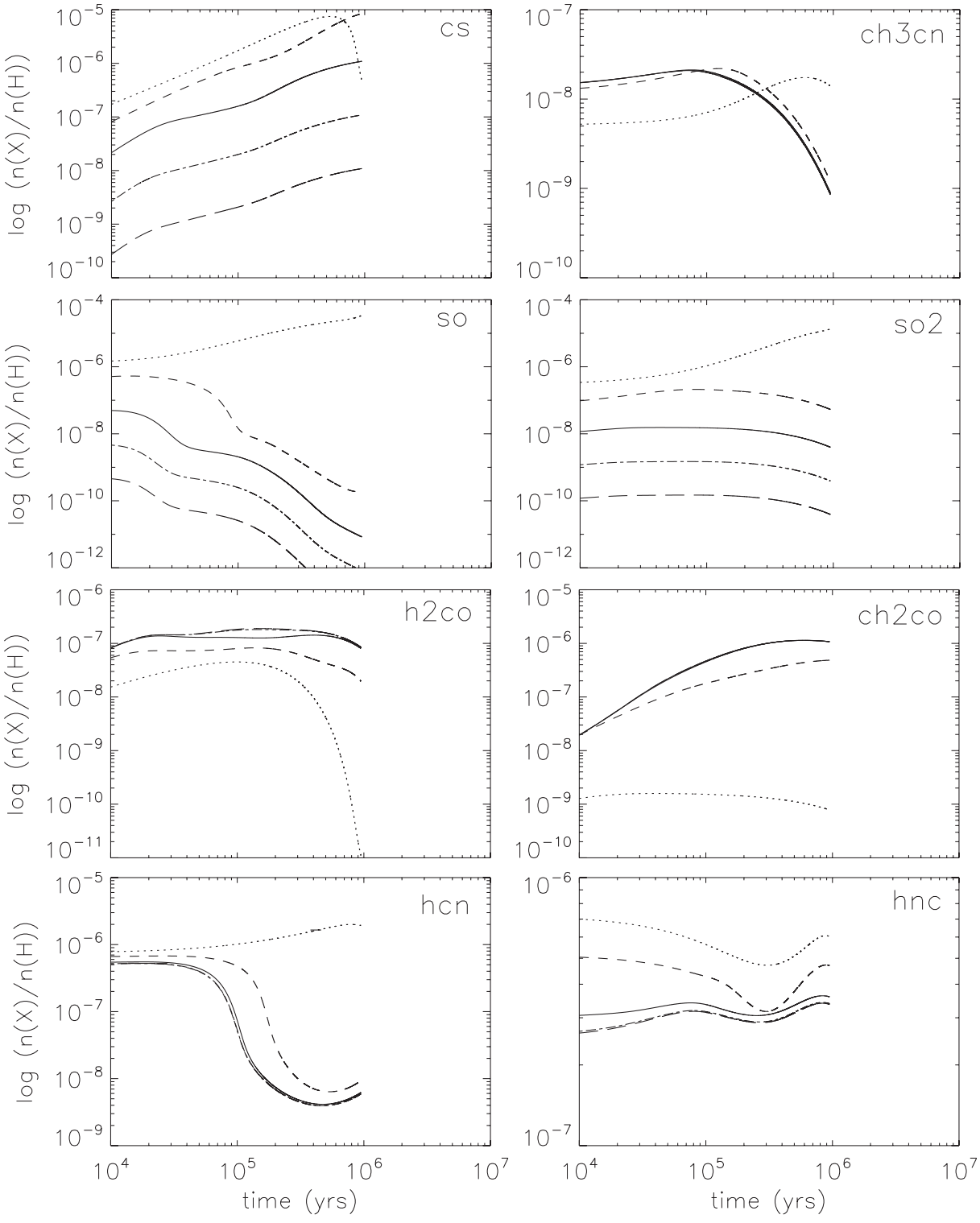

Figure 4.13: The fractional abundance of various species with respect to time, from Bayet et al. (2008), Figure 7. Model 0 is represented by the solid lines, model 10 is represented by the long-dashed lines.

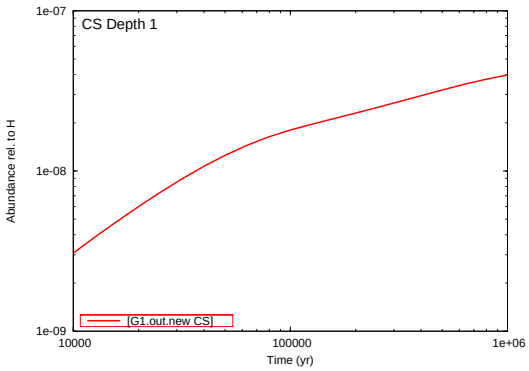

(a) CS

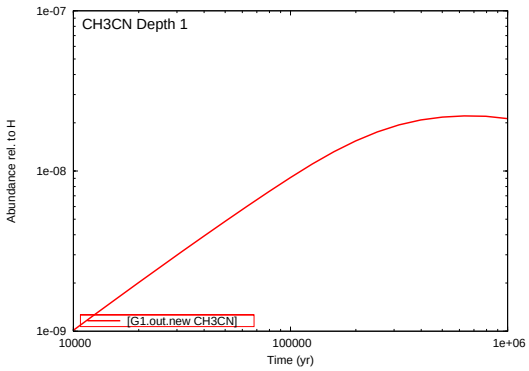

(b) CH_3CN

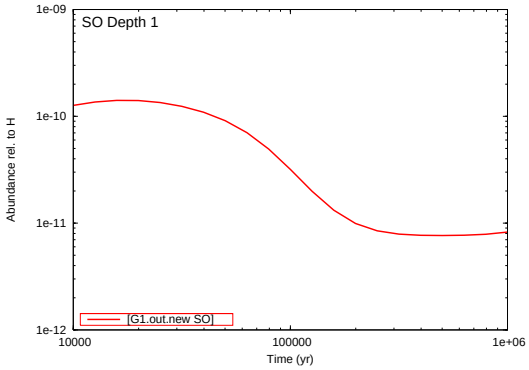

(c) SO

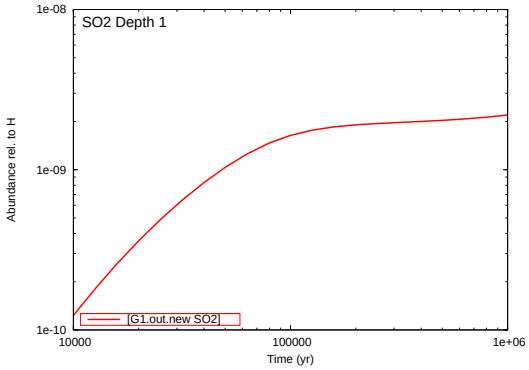

(d) SO_2

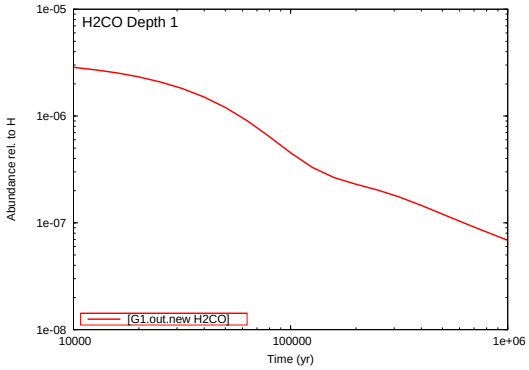

(e) H_2CO

Figure 4.14: The fractional abundance of various species with respect to time, from shell 1, model G1.

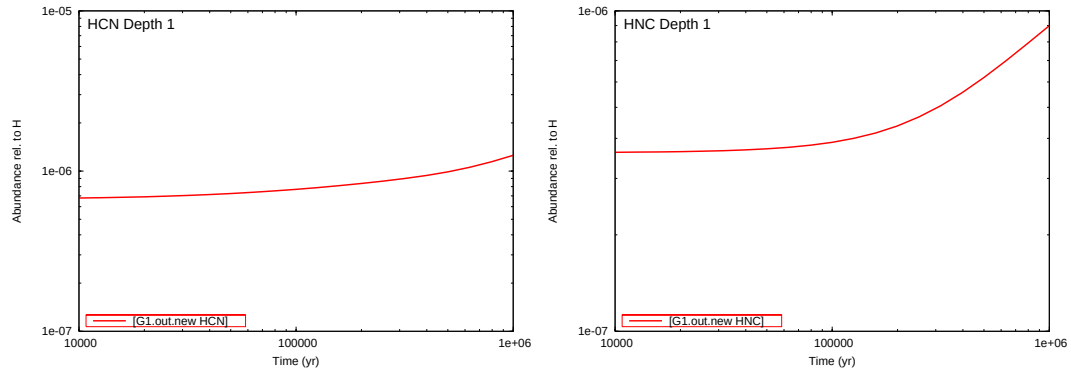

(a) HCN (b) HNC

Figure 4.15: The fractional abundance of HCN and HNC with respect to time, from shell 1, model G1.

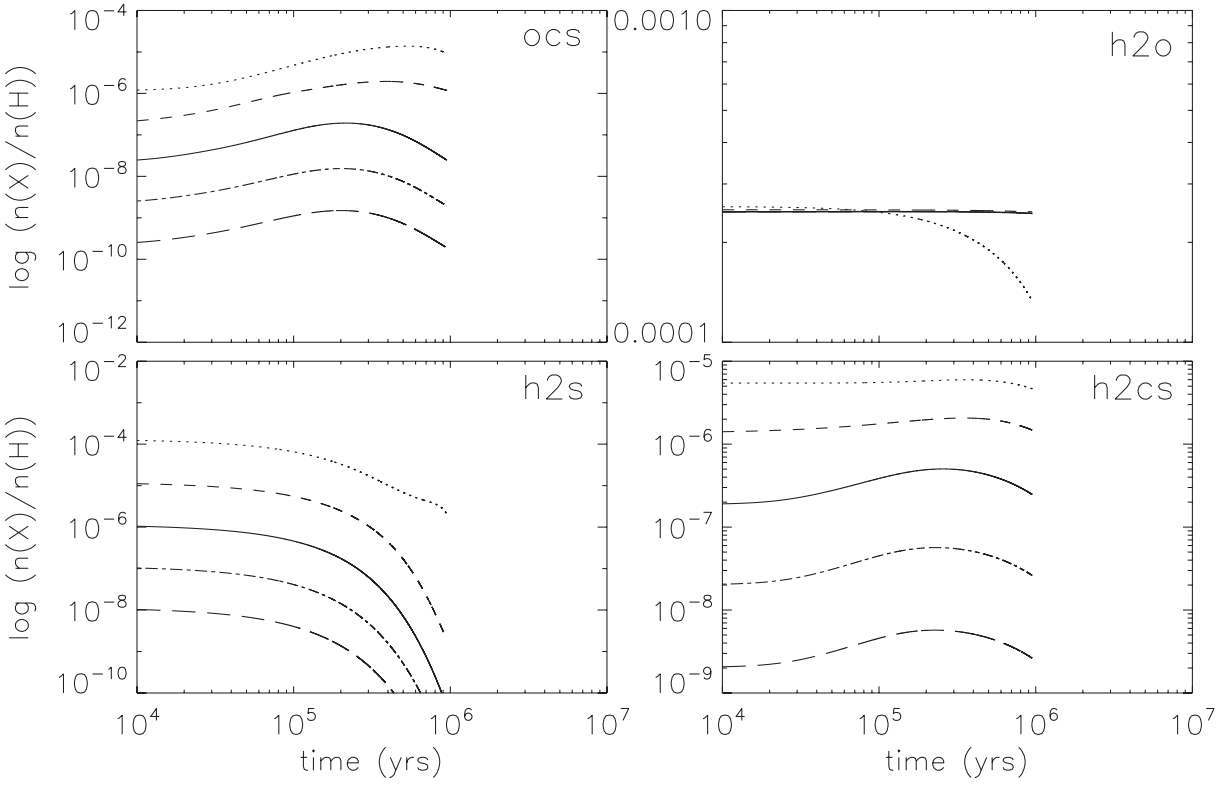

Figure 4.16: The fractional abundance of various species with respect to time, from Bayet et al. (2008), Figure 8. Model 0 is represented by the solid lines, model 10 is represented by the long-dashed lines.

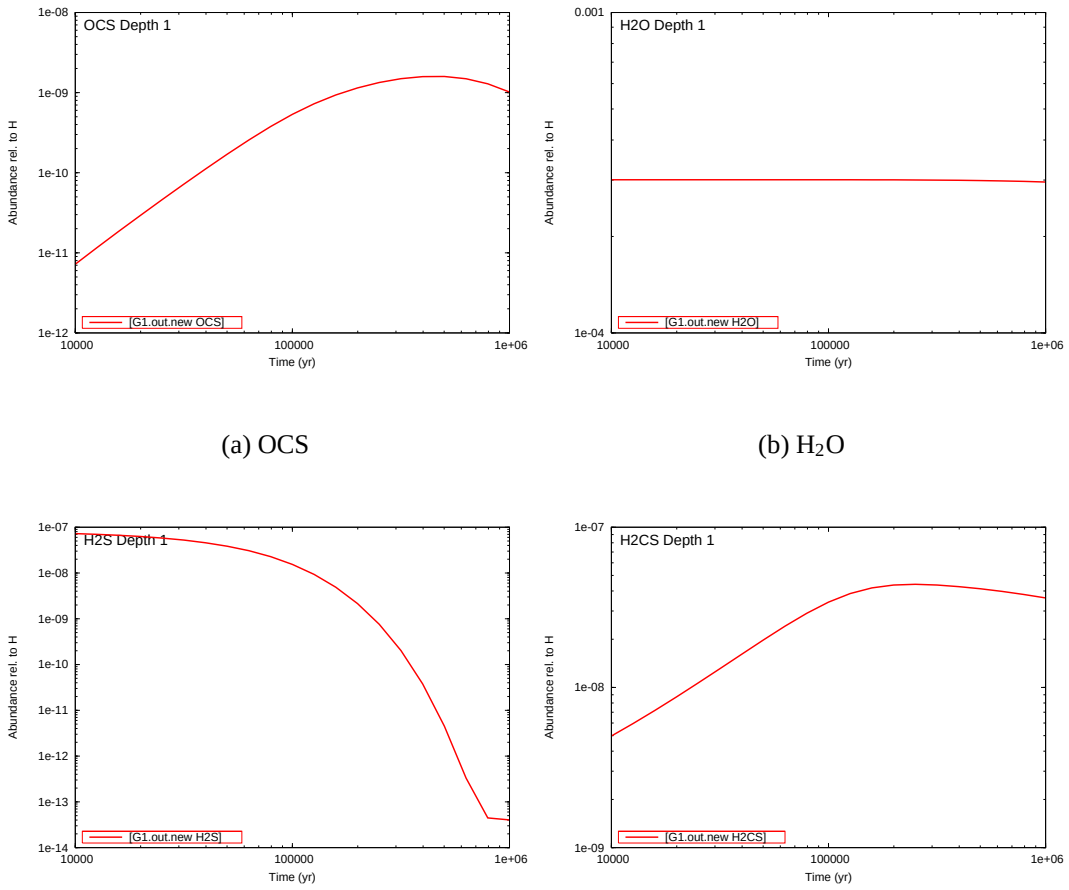

(a) OCS (b) H_2O

(c) H_2S (d) H_2CS

Figure 4.17: The fractional abundance of some more species with respect to time, from shell 1, model G1.

times more abundant in model 0 than in model 1G1. The fractional abundance seen in model 0 is rather insensitive to time, whereas in model 1G1 the fractional abundance increases by a factor of 3, by 10^6 years. The lower fractional abundance in model 1G1 is caused by the lower underlying abundance of heavy metals (see Table 4.4) in this model.

The CH_3OH fractional abundance for models 0 and 1G1 can be seen in Figures 4.19(a) and 4.19(b) respectively. The behaviour of the species is similar in both models – the species is steadily destroyed as time increases. However, model 0 has a lower CH_3OH

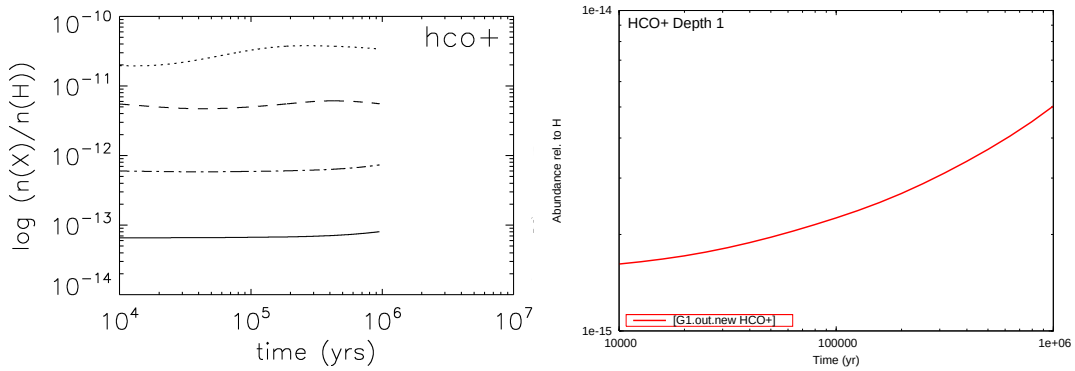

(a) Bayet et al. (2008) Model

(b) JBCA Model 1G1

Figure 4.18: The fractional abundance of HCO^+ to H with respect to time, from model 0 Bayet et al. (2008) and model 1G1. Figure 4.18(a) is taken from Bayet et al. (2008), Figure 1. Model 0 is represented by the solid line, model 10 is not shown in this image.

abundance than 1G1 at 10^4 years, and the fractional abundance in model 0 is also depleted by a larger factor than that of model 1G1 (almost three orders of magnitude in model 0, compared with around 2 orders of magnitude in model 1G1). The differences can be explained by the different gas-phase chemical networks used in the Bayet et al. (2008) and JBCA models. Bayet et al. (2008) used the UDfA gas-phase chemical networks from Millar et al. (1997a) and Le Teuff et al. (2000), whereas the JBCA models use the Woodall et al. (2007) UDfA. Two of the changes made to the UDfA by Woodall et al. (2007) strongly affected the formation/destruction of CH_3OH in the gas phase, as discussed in Section 3.3.2. These changes produce the differences seen in the CH_3OH chemistry between the Bayet et al. (2008) and JBCA models.

Overall Comparison with Bayet et al. (2008).

The JBCA model G1 is physically more complex than the Bayet et al. (2008) model, as the JBCA models have seventeen shells of differing temperature and density, whereas the Bayet et al. (2008) models consist of one ‘shell’ only. For this reason, only the innermost shell of model G1 was compared with the Bayet et al. (2008) models. In

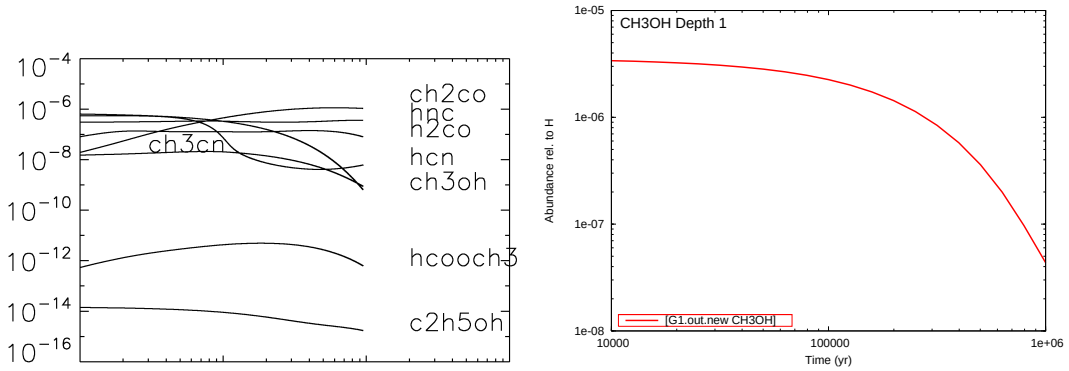

(a) Bayet et al. (2008) Model

(b) JBCA Model 1G1

Figure 4.19: The fractional abundance of CH_3OH to H with respect to time, from model 0 Bayet et al. (2008) and model 1G1. Figure 4.18(a) is taken from Bayet et al. (2008), Figure 3. Model 0 is represented by the solid line marked 'CH3OH' on the graph. Model 10 is not shown in this image.

general, the JBCA model 1G1 compares well with the Bayet models 0 and 10. The differences between the models can be accounted for, by looking at the different elemental input abundances as well as the different physical conditions on the models.

4.5 Comparison of the G1, L2 and S2 models

The purpose of the hot core modelling at varying metallicity was to try and identify whether some typical 'hot core' species could be used as metallicity tracer species. The models chosen for comparison were G1, L2 and S2. These models were chosen as their characteristics most closely resemble the environments they represent - e.g. a typical hot core in the Milky Way, the Large Magellanic Cloud and the Small Magellanic Cloud respectively. The input parameters used in the models can be seen in Table 4.1. The ratios of the underlying elemental abundances in these models can be seen in Table 4.5.

Model	O/C	N/C	C/S	C/Fe	O/N	N/S	O/(C+N+S+Fe)
G1	2.42	0.57	1540	8800	4.25	875	1.54
G TMC-1	2.41	0.29	1825	3476	8.22	535	1.86
L1	3.16	0.10	3453	7586	31.63	345	2.87
L2	3.16	0.10	3453	7586	31.63	345	2.87
S1	3.98	0.13	2742	13810	31.63	345	3.53
S2	3.98	0.13	2742	13810	31.63	345	3.53

Table 4.5: Some ratios for the initial elemental abundances in the Galactic, LMC and SMC models.

4.5.1 CO

As seen in Figure 4.20(a), the CO abundance is highest in model S2 for all depths at 10^4 years. The CO abundance in the S2 model is fairly flat, meaning that it does not vary much with increasing radius. At the outer edge of the hot core, the CO abundance decreases slightly. This is caused by CH_5^+ ions which react with CO to form HCO^+ and CH_4 in the outer shells. The G1 model shows the lowest CO abundance of the three models. Again, the abundance does not vary much with increasing radius, from the centre up to a distance of 0.06pc. After this, the CO abundance falls dramatically in the outer shells of the hot core. The L2 model shows an increasing CO abundance with increasing radius, apart from a drop in abundance at 0.04pc. The CO abundance increases in the outer shells, in direct contrast to the G1 and S2 models.

A comparison of the CO abundances in the three models suggests that the CO abundance is affected inversely by the combination of decreasing metallicity and the reduced dust/gas ratio. A quick comparison with Figure 4.20(b) shows that the change in metallicity alone produces quite a different plot. The G1, L1 and S1 models produce CO distributions of a similar shape, indicating that the chemical processes going on in the models are similar, particularly in the inner regions of the hot core. The lowest abundance is seen in the S1 model. This demonstrates that the large changes in CO abundance in the G1, L2 and S2 models come from an inverse dependence on the

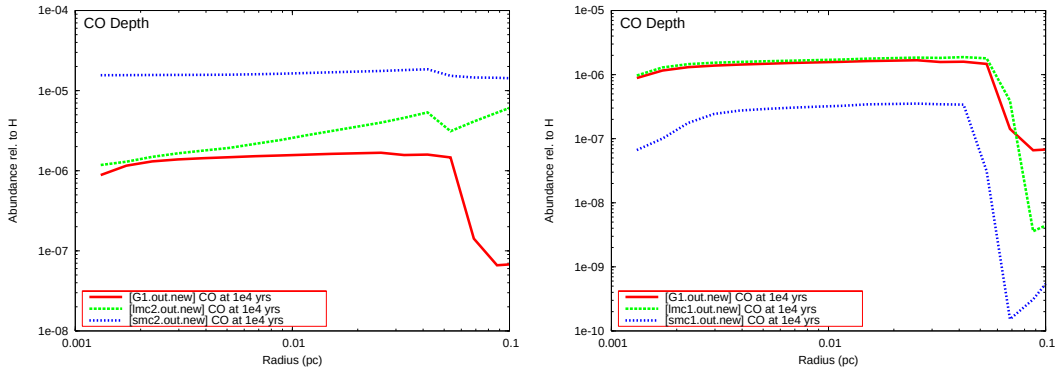

(a) CO in models G, L2 and S2 at 10^4 years (b) CO in models G, L1 and S1 at 10^4 years

Figure 4.20: The fractional abundance of CO to H in models G1, L2, S2, L1 and S1 at 10^4 years.

dust/gas ratio. The most strongly-affected regions of the hot core are the outer edges, as seen in Figure 4.20(a). If observations of hot cores in the Galaxy, the LMC and the SMC were made, Figure 4.20(a) implies that the Galactic and LMC hot cores may appear to be similar in CO abundance, particularly in the inner regions.

By 10^5 years, as seen in Figure 4.21(a) the CO abundance in the G1 model has increased across the whole hot core. This shows that CO is still being produced in all the shells of this model. The distribution of the CO remains similar to that seen at 10^4 years, with an almost constant fractional abundance of CO across the hot core up to around 0.06pc, and then a reduction in the CO abundance in the outermost shells. The flat fractional abundance in the inner shells at 10^4 and 10^5 years shows that the CO is produced in a fairly uniform manner, from shell to shell. The fractional abundance seen in the L2 model has also increased by 10^5 years, and the distribution of CO with radius remains similar. The fractional abundance of CO seen in the S2 model is very similar to that at 10^4 years. The fractional abundance in the outer shells has increased slightly, and now the fractional abundance seen across the whole radius is extremely similar. As the abundance has changed so little with time, it is possible that the CO chemistry was already approaching a steady state by 10^4 years in this model, at least

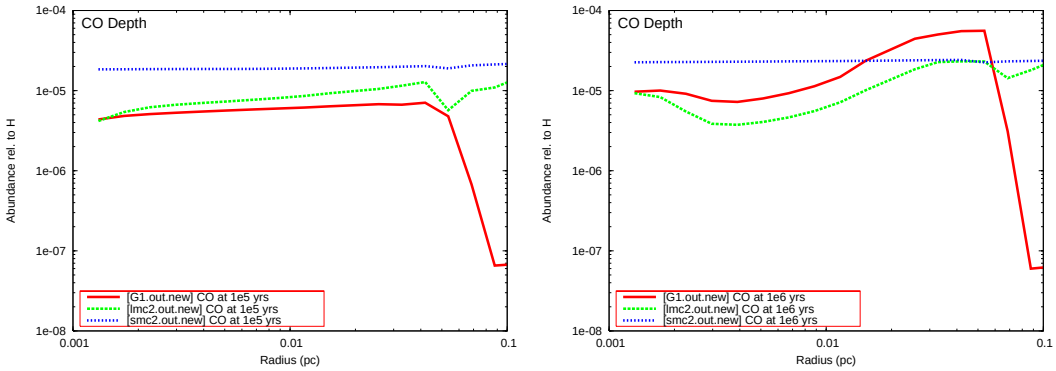

(a) CO in models G, L2 and S2 at 10^5 years (b) CO in models G, L2 and S2 at 10^6 years

Figure 4.21: The fractional abundance of CO to H in models G1, L2 and S2 at 10^5 and 10^6 years.

at intermediate radius.

When comparing the three data sets in Figure 4.21(a), it becomes apparent that the CO abundances in the three models are becoming more similar. This is particularly true for the G1 and L2 models. This demonstrates that at a typical hot core age of 10^5 years, CO may not be a useful tracer of metallicity. Figure 4.21(b) shows the fractional CO abundance in the three models at 10^6 years. The S2 model has the same fractional abundance of CO as seen at 10^4 and 10^5 years. The G1 and L2 results show that the chemistry in these models has evolved significantly. The CO abundance in G1 has increased for all radii, with the exception of the outermost shells where the abundance has remained constant. However, the CO abundance has not increased in a uniform manner, and some shells have produced more CO than others. The L2 model shows a similar pattern of behaviour to the G1 model, up to a radius of 0.05pc. After this point, the CO abundance in the L2 model has increased at the outer edges of the hot core, in direct contrast to the abundance seen in the G1 model.

The fractional abundance of CO at 10^6 years is fairly similar in the three models, so could not be used to distinguish the level of metallicity in a region. However the highest metallicity model (G1) has a distinctive pattern of CO distribution at all times.

There is a high abundance of CO in the inner regions, and a much lower abundance of CO at the edges. In the lower metallicity models (L2 and S2), a much flatter profile is seen for the CO abundance. This information on the distribution of the CO could be useful in determining the metallicity of a hot core.

Overall, it may not be possible to trace the underlying metallicity of a hot core using the fractional CO abundance, particularly at times beyond 10^4 years. This means that the fractional CO abundance is relatively independent of the underlying metallicity. The X–factor is the ratio between the integrated intensity of ^{12}CO J=1-0 [$W(^{12}\mathrm{CO})$] and the H_2 column density [$N(H_2)$] in a cloud (Pineda et al., 2008), and is defined as:

$$X = \frac{N(\mathrm{H_2})}{W(^{12}\mathrm{CO})} \tag{4.8}$$

If the fractional CO abundance is reasonably similar in clouds with different underlying metallicities, then the X–factor could be assumed to have a similar value in the Milky Way and galaxies with lower metallicity. This is a useful result.

4.5.2 HCO^+

As seen in Figure 4.22(a), the HCO^+ fractional abundance is clearly highest in the S2 model at 10^4 years. Even at the highest abundance in this model, it may be difficult to observe this species, as the abundances seen in all the models are extremely low. The highest abundance of HCO^+ in all models is seen at the outer edges of the hot core. The HCO^+ seems to be tracing the cooler, less dense gas. Figure 4.22(b) shows the models at 10^5 years. The fractional abundances seen have increased, particularly in the L2 model. However, the abundance is still highest in the S2 model and lowest in G1. By 10^6 years, the fractional abundances in all three models have increased as seen in Figure 4.22(c). If HCO^+ were observed in an extragalactic hot core, it would be likely that most of the emission would come from the outer layers of the hot core. If the HCO^+ abundance increases inversely with metallicity, it may be possible to observe HCO^+ in star-forming regions at very low metallicity/high redshift, as the HCO^+ abundance may be much higher in these regions.

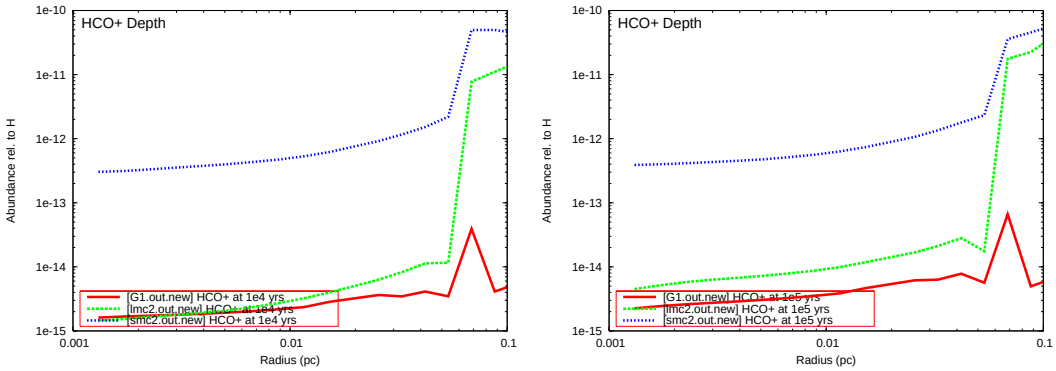

(a) 10^4 years (b) 10^5 years

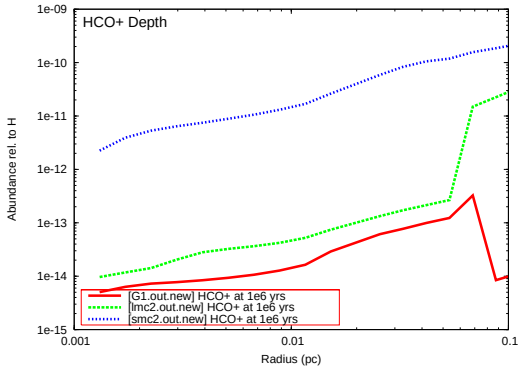

(c) 10^6 years

Figure 4.22: The fractional abundance of HCO^+ to H in models G1, L2 and S2 at 10^4, 10^5 and 10^6 years.

4.5.3 HCN

Figure 4.23(a) shows the HCN fractional abundance at 10^4 years. The abundance seen in the G1 model is constant from the inner radius of the hot core, up to a radius of 0.07pc. After this radius, the abundance swiftly drops in the outer shells. The fractional abundance seen in the L2 model is fairly constant, up to a radius of around 0.02pc. After this, the fractional abundance increases with radius up to the outer edge of the hot core. The HCN abundance seen in model L2 is lower than that seen in G1. This is due to the combined effect of the reduced N and C input abundances in

the L2 model (Table 4.1). It can be seen that the N input is approximately an order of magnitude lower in the L2 model, and the C input is around 50% lower in the L2 model. The fractional HCN abundances seen in the inner regions of the hot core are around five times bigger in the G1 model, when compared with the L2 model. As seen in Table 4.5, the N/C ratio is around five times higher in the G1 model, compared with the L2 model. The HCN abundance is tracing this ratio in the inner parts of the hot core, as the number of available nitrogen atoms per carbon atom limits how much HCN is produced in these hot, dense regions. The N/C ratio in the S2 model is very similar to that seen in the L2 model, and the HCN abundance in the inner shells of model is also very similar to that seen in L2. In the outer shells of models L2 and S2, the chemistry differs, as the HCN abundance drops in the S2 model, and increases in the L2 model. The distribution of HCN in the S2 hot core is analogous to that seen in the G1 model. If an observation of a hot core at 10^4 years were made, the HCN abundance could be used to identify whether the metallicity could be characterised as Galactic or sub-Galactic, and a lower limit could be estimated for the N/C ratio.

At 10^5 years, the HCN fractional abundances are as seen in Figure 4.23(b). The G1 fractional HCN abundance has increased slightly across the inner regions, from 6.7×10^{-7} to 7.4×10^{-7}, and has increased more dramatically in the outer shells, from 4.6×10^{-8} to 3.5×10^{-7}. This shows that HCN is being produced in the gas phase in all the shells across the G1 model. In contrast, the fractional abundances seen in the L2 model at this time have reduced, for all shells. This shows that net destruction of HCN is occurring in the gas phase. The majority of the HCN destruction occurs via the following reaction:

$$H_3O^+ + HCN \rightarrow HCNH^+ + H_2O \tag{4.9}$$

Similarly, in model S2 the fractional HCN abundance has reduced in the time period between 10^4 and 10^5 years, by almost an order of magnitude, for all shells. In this model, the HCN abundance is also reduced by reaction with the oxygen-bearing species H_3O^+. This reaction proceeds most quickly in the S2 model, then the L2 model,

and finally the G1 model. The reason for this is the underlying O/C ratio in the models. Table 4.5 shows that model S2 has the highest O/C ratio, and G1 the lowest. There is a higher concentration of free oxygen per unit carbon in the S2 model, and so higher quantities of oxygenated species such as H_3O^+ are able to form. This can be seen in Figures 4.24(a) and 4.24(b). A higher H_3O^+ concentration increases the rate of destruction of HCN, and so HCN is destroyed at a faster rate in the S2 model.

Figure 4.23(b) shows that at 10^5 years, the three models can be distinguished in terms of metallicity – e.g. the highest metallicity model produces the highest HCN abundance, and the lowest metallicity model produces the lowest HCN abundance. The fractional abundances seen in each model are reasonably flat, and the ranges in each model are distinct from one another. The reasonably large differences in abundance, from model to model, mean that HCN abundance could be used to estimate the underlying metallicity of a hot core, observed at an age of 10^5 years. The chemical behaviour of the HCN in each model is similar to that seen at 10^4 years, with a reduced HCN abundance in the outer shells for models G1 and S2, and an increased HCN abundance in the outer shells for model L2.

Figure 4.23(c) shows the fractional HCN abundances at 10^6 years. The chemical behaviour in the G1 model has changed, and the HCN abundance now peaks at the outer edge of the hot core, with a reduced abundance in the intermediate shells. The G1 model still contains the highest fractional abundance of HCN, and the abundance is still fairly consistent across the hot core. The L2 model shows a decreased abundance across most of the hot core, particularly in the intermediate shells where the abundance has decreased by a factor of fifty. The S2 model has considerably decreased in fractional HCN abundance - by a factor of two hundred in the innermost shell. The large reductions in fractional abundance in models L2 and S2 mean that the HCN abundance could still be used as a metallicity tracer at this time, provided the age of the hot core were known. The fractional abundances seen in each model are sufficiently different, and discrete, that the underlying metallicity could be estimated to within a certain limit from an observation.

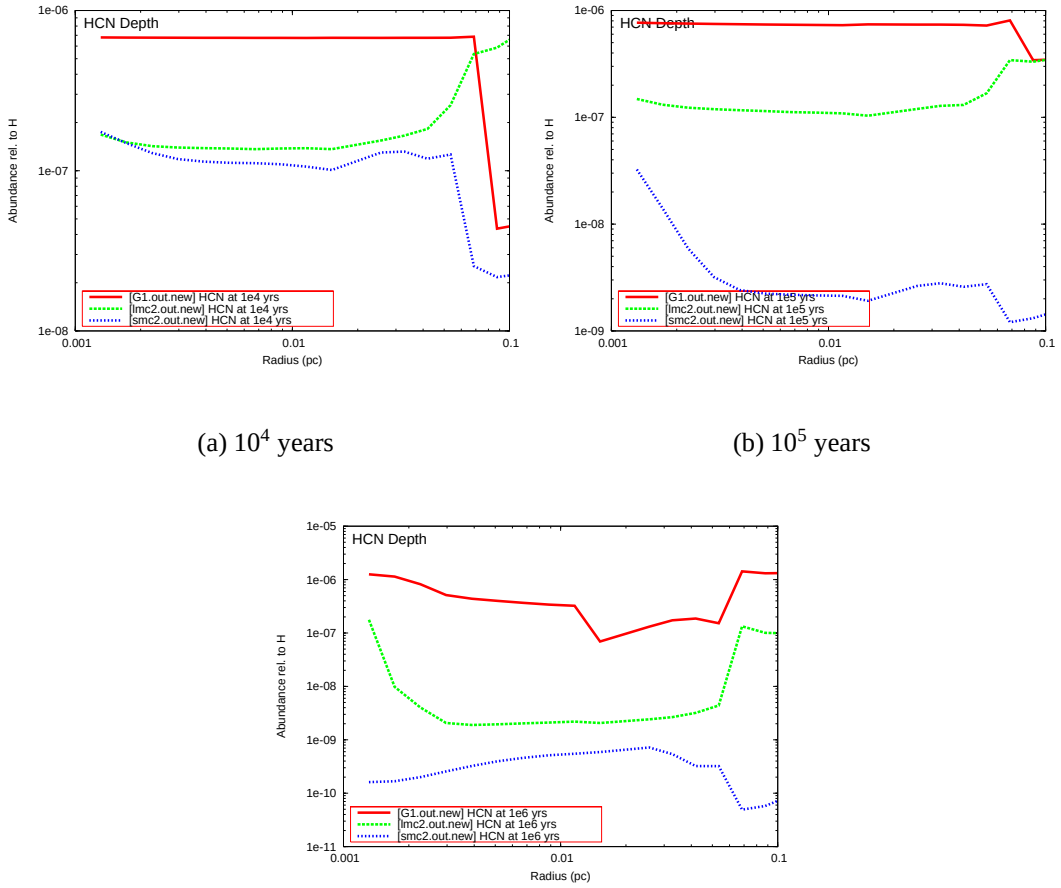

(a) 10^4 years (b) 10^5 years

(c) 10^6 years

Figure 4.23: The fractional abundance of HCN to H in models G1, L2 and S2 at 10^4, 10^5 and 10^6 years.

Overall, HCN is a potentially useful tracer of metallicity at all times. At early time, it appears to reflect the underlying N/C ratio. At later times, it can be used to determine the more general underlying metallicity of a hot core. A higher O/C ratio can be linked with a lower HCN abundance at later times.

4.5.4 HNC

Figure 4.25(a) shows the HNC fractional abundance in the three models at 10^4 years. The abundance seen in each model is distinct, and fairly constant across the hot core,

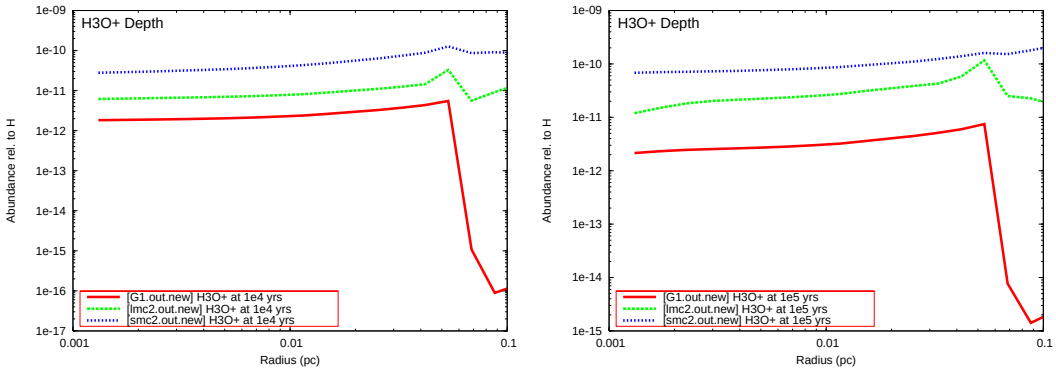

(a) 10^4 years (b) 10^5 years

Figure 4.24: The fractional abundance of H_3O^+ to H in models G1, L2 and S2 at 10^4 and 10^5 years.

and so potentially this species could be a useful metallicity tracer. The HNC abundance is about 26 times higher in model G1 compared with model L2, and 90 times higher than in model S2. The difference in metallicity is not as large as this, for any individual element or the elements combined. The HNC abundance is therefore not directly tracing the metallicity of the hot core, but providing an observable way in which the hot core could be characterised as high, medium, or low metallicity. This could be used to estimate limits of the underlying elemental abundances. As this species is not strongly affected by the changing dust/gas ratio, these results are a more direct measure of the changing elemental abundances.

At 10^5 years, the fractional abundances for the three models can be seen in Figure 4.25(b). The G1 HNC abundance has remained similar over the intervening time period. The abundance in L2 has increased by a factor of around five. The abundance in S2 has reamined fairly constant – with the exception of the inner shells where it has increased by a maxiumum factor of five. This shows that there is not much HNC produced in the gas phase in model G1, or the majority of the shells in model S2. The model L2 is producing HNC across the whole hot core, as is the inner part of model S2. There is no obvious reason for the different chemistries seen in the different

models in this case, and it is likely that a combination of factors lead to this result. Examples of these could include the differing N/C ratio (highest in model G1, lowest in L2), or the abundance of (C−N) available in the model at that time. The fractional HNC abundances seen in each model are still distinct enough that an HNC observation of a hot core could be used to determine its underlying metallicity, to a limited degree of accuracy. The abundances seen in each model are also fairly consistent, across the radius of the hot core.

At 10^6 years, the fractional HNC abundances are shown in Figure 4.25(c). At this time, the models produce very similar results for HNC and HCN, which can be seen by comparing Figure 4.25(c) with Figure 4.23(c). The main difference is in the outer shells of model L2, where more HCN than HNC is produced, by a factor of around 400. The similarities in the models can be explained, as the gas phase reactions which produce HCN and HNC tend to have a 50/50 branching ratio as to which species is formed. The HCN and HNC fractional abundances differ in the outermost shells of model L2. This is because in this model, at this time, the HNC and HCN are primarily destroyed by different mechanisms. HCN is destroyed by the following reactions:

$$H_3^+ + HCN \rightarrow HCNH^+ + H_2 \tag{4.10}$$

$$HCO^+ + HCN \rightarrow HCNH^+ + CO \tag{4.11}$$

Whereas HNC is solely destroyed by the following reaction:

$$HNC + CN \rightarrow NCCN + H \tag{4.12}$$

In models G1 and S2 in the same shell, at the same time, HCN and HNC are destroyed by the same mechanisms. In model G1, the species are destroyed by reaction with H_3^+, CH_5^+, $C_2H_3^+$ and $C_2H_5^+$. This demonstrates the effects of the increased C abundance in this model, as carbonaceous species are destroying the HCN and HNC. In model S2, at 10^6 years in the outermost shells, HCN and HNC are destroyed by H_3^+, H_3O^+ and HCO^+.

The fractional HNC abundances seen in the G1, L2 and S2 models at 10^6 years are less

easy to disentangle, as a fairly similar abundance is seen at the outer edge of models L2 and S2. However, it may still be possible to use this species as a metallicity tracer at this time, as the cumulative effect of all the shells in each model would produce a higher HNC abundance from an observer's point of view.

Overall, HNC appears to be a useful tracer of the underlying elemental abundances in a hot core, without being strongly affected by the gas/dust ratio in that region. However, HNC does not directly trace any one species or ratio, but rather a more general sense of the metallicity. As the relationship between underlying metallicity and HNC abundance is not obvious, the most useful way of interpreting an observation would be to try and produce a model in which the HNC abundance fits the observed value. This could provide some limiting values for the underlying elemental abundances in a hot core.

4.5.5 HNCO

The HNCO abundance for the three models at 10^4 years is shown in Figure 4.26(a). All three models show a similar behaviour for HNCO – it is fairly abundant in the inner shells, and the fractional abundance increases slightly before dropping off with increasing radius. The fractional abundance drops off most quickly at a radius of just over 0.04pc. The predicted HNCO fractional abundances in models L2 and S2 are very low – tending to values between 10^{-12} and 10^{-14}. It is unlikely that these abundances could be observed in an extragalactic hot core environment. The HNCO fractional abundance in the inner shells of the G1 model is around 10^{-10}, and it is likely that this could be observed in a Galactic hot core. Beyond a radius of 0.015pc, this abundance drops off fairly quickly. An observation of such a hot core would show the HNCO emission concentrated around the centre of the hot core. If an observation was made of an extragalactic hot core at 10^4 years, it is likely that the emission would be very weak, and concentrated around the centre. The HNCO fractional abundance is higher in model S2 than in model L2, for most of the hot core radius. This shows that the

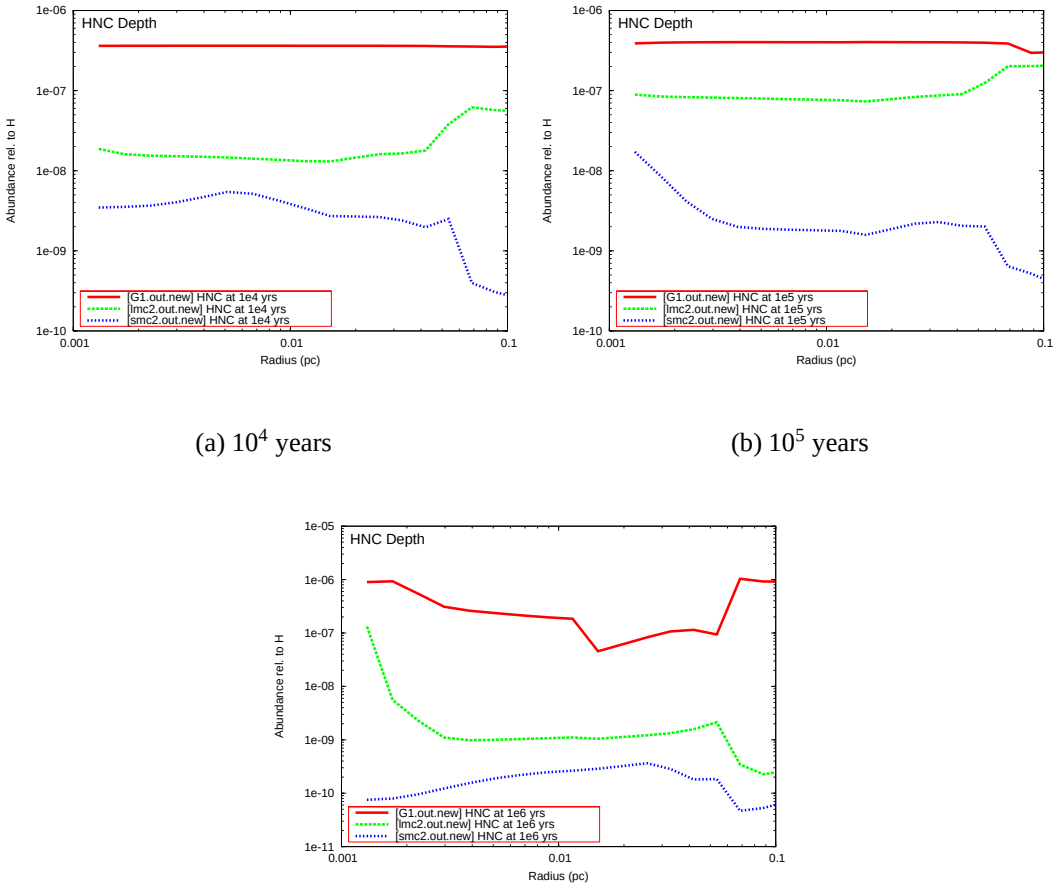

(a) 10^4 years (b) 10^5 years

(c) 10^6 years

Figure 4.25: The fractional abundance of HNC to H in models G1, L2 and S2 at 10^4, 10^5 and 10^6 years.

HNCO abundance is not directly tracing the metallicity of the hot core. If an extragalactic hot core observation were made, a fractional abundance of around 10^{-10} would imply that the metallicity of the hot core was similar to that in the Galactic model. If no HNCO were observed, it could indicate a hot core with a low underlying metallicity, where the HNCO abundance was not observable from Earth.

H2S in model 1G1 Figure 4.26(b) shows the fractional HNCO abundance in the three models at 10^5 years. The HNCO fractional abundance in model G1 has increased across the whole hot core radius, by around an order of magnitude. HNCO is there-

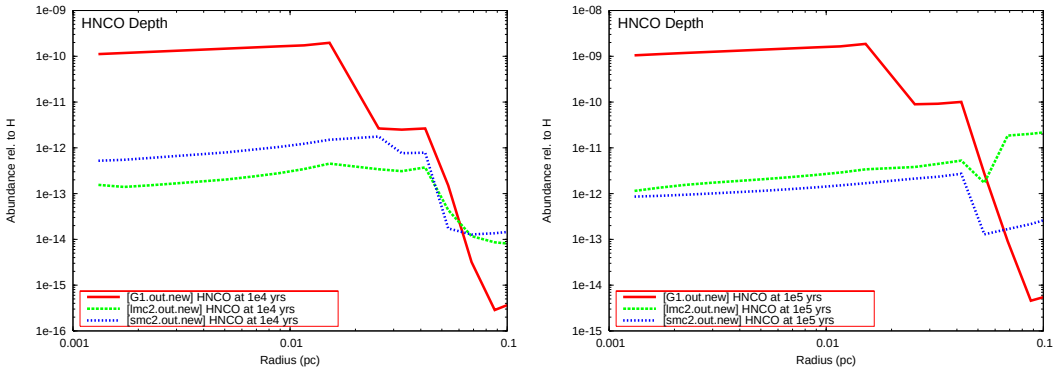

(a) 10^4 years (b) 10^5 years

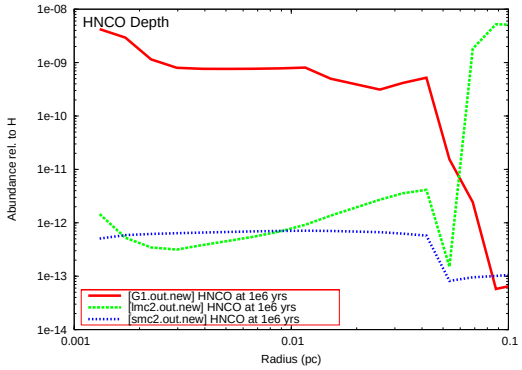

(c) 10^6 years

Figure 4.26: The fractional abundance of HNCO to H in models G1, L2 and S2 at 10^4, 10^5 and 10^6 years.

fore being produced in the gas phase, as a daughter product of HNCONH and HNCHO. These species are formed on the grain surfaces, and desorb when the protostar 'switches on'. The emission from this fractional abundance should be easily observed in a Galactic hot core. The distribution of the HNCO in the G1 hot core is similar to that seen at 10^4 years, with a high fractional abundance in the centre, which quickly tails off at a radius of 0.04pc. The behaviour in the L2 model has changed. The fractional abundance in the inner shells has increased by an order of magnitude, and in the outer shells by a factor of 3000. HNCO was produced across the whole hot core in this

model, between 10^4 and 10^5 years, as the grain species are processed. A less dramatic change occured in model S2 over this time period – the fractional HNCO abundance in the inner shells remained almost constant, and the greatest increase was seen in the outer shells where the fractional abundance increased by a factor of 20. The distribution of HNCO remains similar in model S2 at 10^4 and 10^5 years, with a reasonably flat abundance of HNCO across the inner and intermediate shells, and a reduction occuring at around 0.04pc.

At 10^6 years, the fractional HNCO abundance in the three models has evolved as seen in Figure 4.26(c). The HNCO abundance has again increased across the whole hot core in model G1, showing a net production of HNCO in every shell. The HNCO production at this stage appears to be governed by temperature or density, as Figure 4.26(c) appears to show a relationship between increasing radius and decreasing HNCO abundance. The most HNCO is produced in the hottest/densest shells, in the centre of the hot core. The temperature and density profile of the hot core can be seen in Figures 2.2(a) and 2.2(b) respectively. The behaviour of the HNCO fractional abundance in model L2 is an exaggerated version of that seen at 10^5 years. The highest abundance is seen in the outer shells. The fractional abundance in this region peaks at 5.2×10^{-9} – this value could potentially be observed from Earth, and would appear as a strong shell of HNCO in the outer parts of the hot core. However, it is unlikely that the chemistry would evolve to this stage. If an observation of such an HNCO distribution were made, it could be used to identify a highly evolved chemistry in a low metallicity hot core. The inner parts of the hot core at this time contain a similar abundance of HNCO to that seen at 10^5 years in the L2 model. In model S2, the fractional abundance in the hot core is similar to that seen at 10^5 years, which shows that some HNCO was produced in the gas phase before 10^5 years, and after this time little more was produced. The lower dust/gas ratio in model S2 (compared with G1 and L2) means that less of the parent species that form HNCO are formed on the dust grains, and so the HNCO production ceases at an earlier time in the S2 model. The HNCO chemistry therefore reaches a steady state at an earlier time in the S2 model than in the G1 and L2 models.

Overall, the fractional HNCO abundance could be used in hot cores (up to an age of around 10^5 years), to identify whether a hot core can be characterised as having 'Galactic metallicity' or 'low metallicity'. If no, or little, HNCO were observed, it would indicate that the hot core existed in a region of low metallicity. However, such an observation could not be used to constrain the metallicity level to a great level of precision.

4.5.6 HC_3N

At 10^4 years, the fractional abundance of HC_3N can be seen in Figure 4.27(a). To a certain extent the fractional abundance is determined by the dust/gas ratio, particularly in the inner shells, as discussed in Section 4.3.1. The behaviour seen in models G1 and L2 is similar, as the HC_3N abundance increases towards the edge of the hot core. In model S2, the abundance is fairly constant across the whole hot core, but there is a slight reduction at the outer edge. These different chemistries can be attributed to the dust/gas ratio, which is very low in model S2 compared with models G1 and L2, as seen in Table 4.1. If observations of extragalactic hot cores were made, it is likely that HC_3N would be observed, as the fractional abundances seen here are reasonably high in all models. At 10^4 years, a high fractional abundance appears linked to a lower gas/dust ratio.

Figure 4.27(b) shows the fractional HC_3N abundance at 10^5 years. The fractional abundance in model G1 has increased by almost two orders of magnitude. The fractional abundance in model L2 has remained similar in the inner shells, and has decreased in the outer shells. The fractional abundance in model S2 has decreased, by almost three orders of magnitude in the inner shells, and one order of magnitude at the outer shells. The fractional abundances seen in the three models are quite similar, and it is very unlikely that this species could be used to trace the elemental abundance or dust/gas ratio at this time. HC_3N could be used as a hot core tracer, as it is fairly abundant in all models, even at low metallicity.

By 10^6 years, the HC_3N fractional abundance appears to trace the underlying metallicity of the hot core. As seen in Figure 4.27(c), the highest fractional abundance is seen in the most metallic model, G1, and the lowest is seen in the lowest metallicity model, S2. The fractional abundances seen are fairly high, and should be possible to observe. As seen in Figure 4.11(b), similar results are produced at this time even when the same dust/gas ratio is used in each model. This implies that the most important factor here is the underlying elemental abundances. If a hot core was observed at an age of 10^6 years, the HC_3N abundance could be used to put limits on the underlying elemental abundances, using this model. The biggest change seen between Figures 4.27(b) and 4.27(c) is the increase in HC_3N abundance in model G1, across the whole hot core radius. This shows that HC_3N is efficiently produced in the gas phase in this model, between 10^5 and 10^6 years.

Overall, the fractional HC_3N abundance is not a useful metallicity tracer, unless the age of the hot core being observed is accurately known. However, HC_3N could be a useful hot core tracer, as in all three models at all times, it is produced with fractional abundances greater than 10^{-10}.

4.5.7 CH_3OH

Figure 4.28(a) shows that a high abundance of CH_3OH is produced in all three models at 10^4 years. An observation of CH_3OH in a hot core at this time would not provide useful information regarding the underlying elemental abundances or dust/gas ratio. However, CH_3OH could be used as a hot core tracer, as the fractional abundances seen are high in all three models. The CH_3OH is most abundant in the inner shells, up to a radius of 0.04pc, which corresponds to a temperature and density of 45K and $8\times10^{-6}cm^{-3}$, as seen in Figures 2.2(a) and 2.2(b) respectively. It would therefore appear that if a fractional CH_3OH abundance of around 10^{-5} is observed in a young star-forming region, this region is likely to have a temperature and density greater than or equal to 45K and $8\times10^{-6}cm^{-3}$ respectively. The species has almost exactly the same

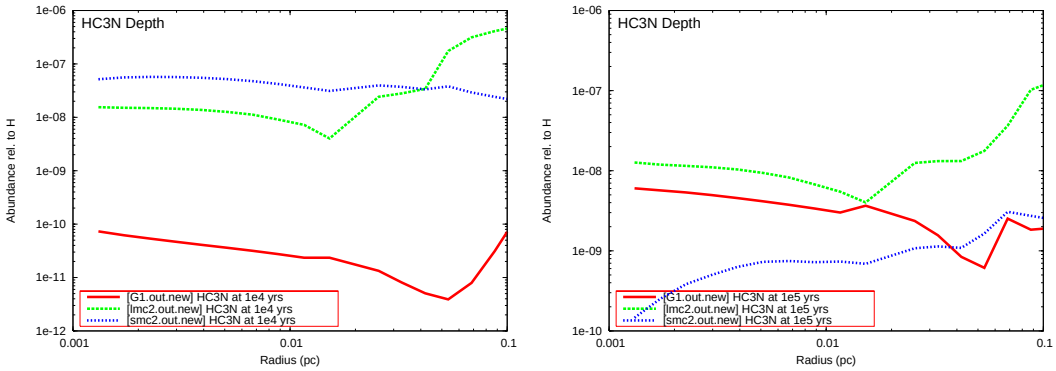

(a) 10^4 years (b) 10^5 years

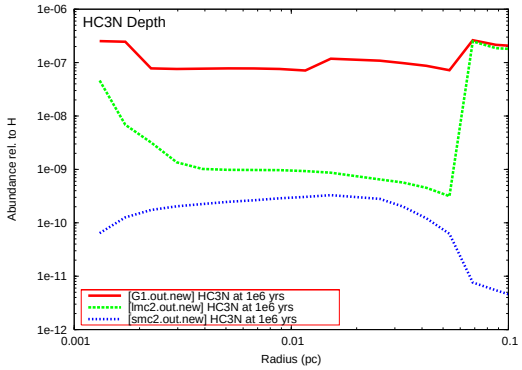

(c) 10^6 years

Figure 4.27: The fractional abundance of HC_3N to H in models G1, L2 and S2 at 10^4, 10^5 and 10^6 years.

abundance across the inner and intermediate shells of the hot core in each model. This is because the CH_3OH was formed on the dust grains. At temperatures above 45K, it is sublimated from the grain surfaces when the protostar "switches on". The methanol molecule then exists in the gas phase equally well in all shells up to a radius of 0.04pc and a time of 10^4 years, and so this flat distribution of methanol is seen across the shells.

By 10^5 years, the fractional abundance seen in model S2 has dropped by a factor of 750 in the inner part of the hot core. This can be seen in Figure 4.28(b). The methanol

is being destroyed very efficiently in this model. The reaction which destroys the most methanol at this stage, in all three models is:

$$H_3O^+ + CH_3OH \rightarrow CH_3OH_2^+ + H_2O \tag{4.13}$$

Models L2 and G1 also contain a reduced fractional abundance of CH_3OH in the inner and intermediate regions, both by less than an order of magnitude. Figures 4.29(a) and 4.29(b) show the ratio of CH_3OH/H_3O^+ in the three models, at 10^4 and 10^5 years respectively. It can be seen the ratio is lowest in model S2, at both times. This means that there is proportionally more H_3O^+ per CH_3OH molecule in model S2. This gives a greater rate of CH_3OH destruction, which can be seen by comparing Figure 4.28(a) with Figure 4.28(b).

In the outer regions of the hot core, the fractional CH_3OH abundance has increased in all three models between 10^4 and 10^5 years. This shows methanol is still being produced in the gas phase in these cooler, less dense regions. If a hot core was observed at this stage, it would be possible to identify if the region had very low metallicity, as the S2 model produces a much lower fractional abundance of methanol than the other two models.

Figure 4.28(c) shows the CH_3OH fractional abundance in each model at 10^6 years. By this stage, the fractional abundance has fallen in the inner shells for all models. The highest fractional abundance seen is lower than 10^{-7}, which is over an order of magnitude lower than that seen at 10^5 years in models G1 and L2. It may be possible to identify the different models and provide limits for their metallicity at this time, as the fractional abundances seen in the inner regions are quite different, with a higher abundance corresponding to a higher metallicity. However, there is some crossover between the models' fractional abundances at the outer edges.

Overall, this species is not a consistent metallicity tracer. At 10^4 years, the species is a good general tracer of hot cores, so if the age of a star-forming region were known it could be used to identify hot cores within it. CH_3OH could be used to determine if a region containing hot cores is at Galactic or very low metallicity at 10^5 years or later.

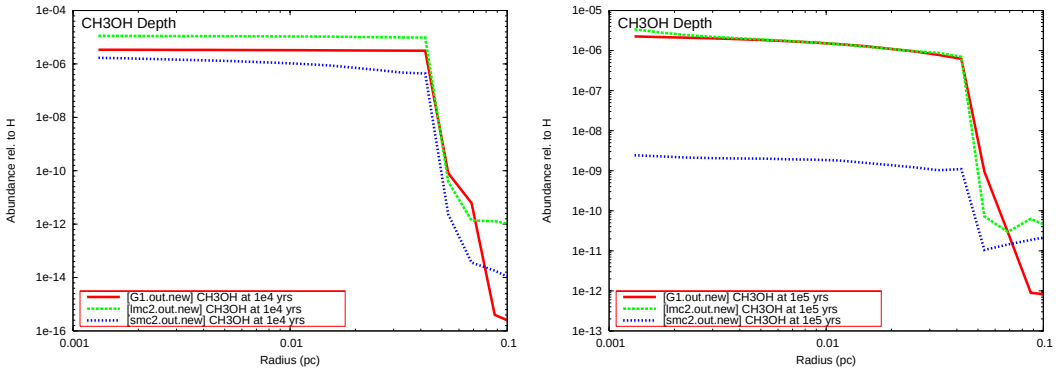

(a) 10^4 years (b) 10^5 years

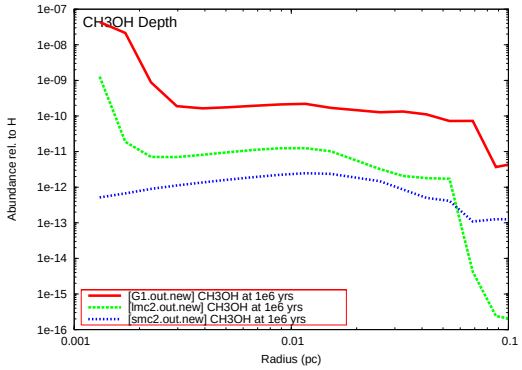

(c) 10^6 years

Figure 4.28: The fractional abundance of CH_3OH to H in models G1, L2 and S2 at 10^4, 10^5 and 10^6 years.

If no CH_3OH is observed in a hot core at low metallicity, it could be an indication that the chemistry is highly evolved. An example of this situation would be model S2 at 10^6 years.

4.5.8 CS

Figure 4.30(a) shows the fractional CS abundance at 10^4 years in the three models. In the inner regions of the hot core, the CS behaviour in model S2 is very different to that seen in models G1 and L2. The fractional abundance of CS in models G1 and L2 is

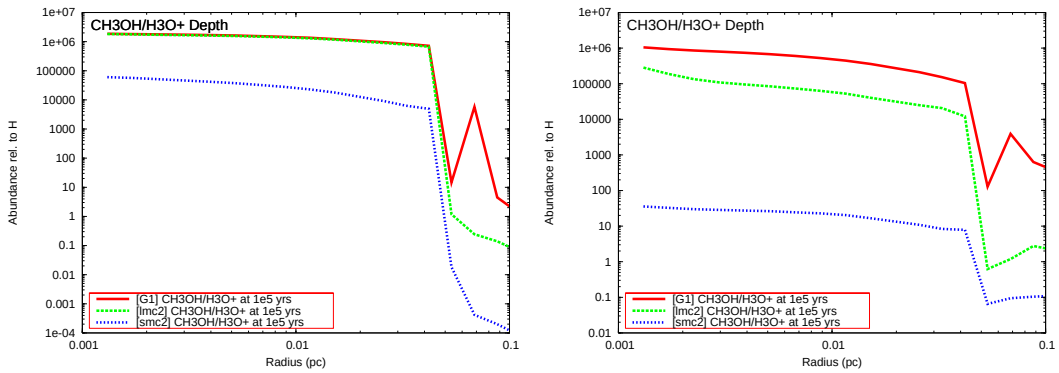

(a) 10^4 years (b) 10^5 years

Figure 4.29: The ratio of CH_3OH/H_3O^+ to H in models G, L2 and S2 at 10^4 and 10^5 years.

fairly high (over 1×10^{-9}) at the innermost shell of the hot core. This fractional abundance then decreases steadily, up to a radius of around 0.015pc in model L2 and 0.04pc in model G1. In contrast, the S2 model contains the lowest amount of CS in the innermost shell, with a fractional abundance of 4×10^{-13}. The fractional CS abundance then steadily grows as a function of radius, up to a maximum abundance which is reached between 0.02 and 0.03pc. Beyond this radius, the fractional abundance reaches a plateau, before falling in the outermost shells, from a radius of 0.07pc onwards. Over the whole hot core, in the G1 model, the fractional CS abundance is highest in the inner region. The fractional abundance drops fairly steadily with increasing radius, with a small increase in abundance starting at 0.04pc, which peaks around 0.06pc before rapidly dropping back down again. The fractional CS abundance seen in the L2 model follows a similar pattern to that seen in G1 in the inner regions of the hot core, as discussed above. Beyond a radius of around 0.015pc, the CS fractional abundance increases fairly rapidly in model L2. A peak is reached around 0.07pc, and after this the fractional abundance decreases. The behaviour seen in model L2 after 0.015pc is more similar to that of model S2 than model G1.

The type of chemistry seen in model G1 is very different to that seen in S2. G1 contains a fairly steady fractional CS abundance, which is highest in the innermost shells.

In this model, the CS could be said to be tracing the temperature/density, to a small extent, as the fractional abundance tends to decrease with decreasing temperature and density. Over the whole hot core radius, the fractional abundance drops by a factor of 50. In the S2 model, the fractional CS abundance is lowest in the inner regions of the hot core. The abundance grows steadily with radius, up to around 0.025pc where it plateaus and then decreases. The fractional abundances in this model range from 4×10^{-13} to 7.4×10^{-9}, so model S2 shows a much wider variance in fractional abundances than models G1 and L2. The chemistry seen in model L2 is a combination of the chemistries seen in models G1 and S2. Up to a radius of 0.015pc, model L2 behaves in a similar fashion to model G1, and beyond this radius model L2 resembles model S2 in terms of behaviour.

The reduction in fractional CS abundance in all three models at 0.07pc occurs as at this radius, the CS is able to condense onto the dust grains, as seen in Figure 4.30(b), which shows the fractional abundance of CS on the grain surfaces in each model.

Figure 4.30(c) shows the fractional CS abundance in models G1, L1 and S1 at 10^4 years. In these models, the dust/gas ratio is kept constant. It can be seen that the CS fractional abundance is a metallicity tracer under these conditions, as the CS abundance is highest in G1 (the most metallic model) and lowest in S2 (the least metallic model) at all radii. This graph provides a sharp contrast to Figure 4.30(a), which shows models G1, L2 and S2 at the same time. The differences between the two figures can be explained by the changing dust/gas ratio in models L2 and S2. This shows that the dust/gas ratio has a far greater effect on the chemistry than changing the input abundances alone. The chemistry in models G1, L1 and S1 appears to be similar, as the fractional abundance distributions in the three models are similar across the hot core at 10^4 years. The differing chemistries in models G1, L2 and S2 are caused by the changing dust/gas ratio, as shown in Table 4.1. Figure 4.31(a) shows how the fractional CS abundances in models G1, L2 and S2 have evolved, at 10^5 years. The fractional abundance in the G1 model has increased across most of the hot core, with the exception of the outer shells where the CS abundance has remained constant. This shows that CS is

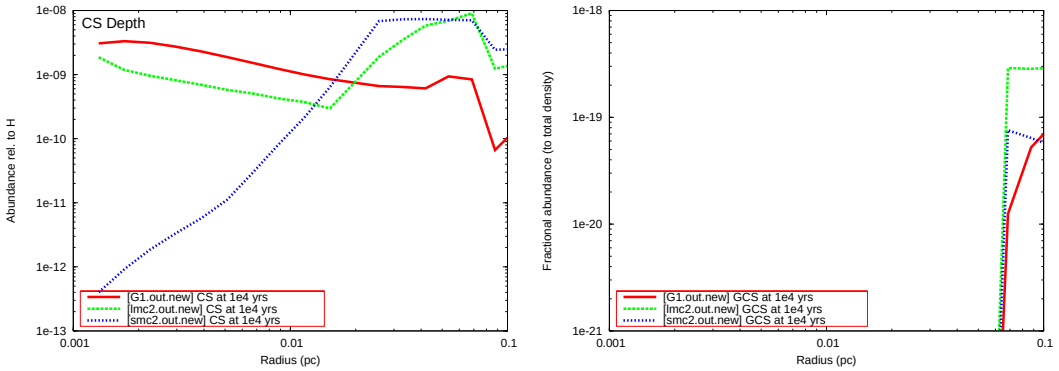

(a) CS in models G1, L2 and S2

(b) Grain surface bound CS in models G1, L2 and S2

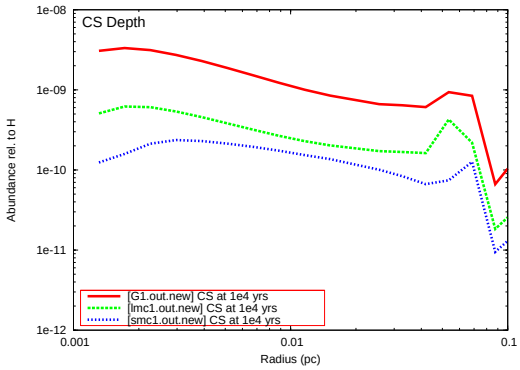

(c) CS in models G1, L1 and S1

Figure 4.30: The fractional abundance of CS and GCS (grain surface bound CS) to H in models G1, L2, S2, L1 and S1 at 10^4 years.

being actively produced in the gas phase in the G1 model between 10^4 and 10^5 years. In the L2 model, the fractional abundance has increased slightly in the inner regions, and decreased slightly in the outer regions. The fractional abundance in this model is now reasonably constant across the hot core radius. In the S2 model, the fractional CS abundance has decreased at all radii, except for the outermost shells where the fractional abundance has remained constant.

Figure 4.31(b) shows the fractional CS abundances in the models at 10^6 years. In the

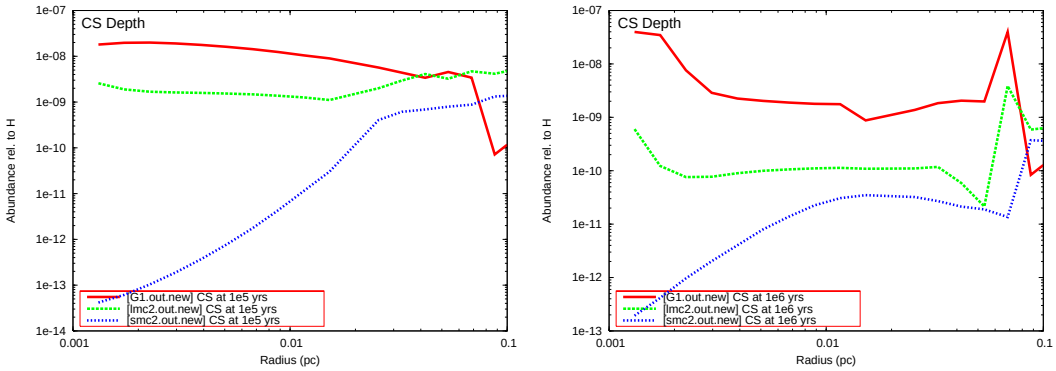

(a) 10^5 years (b) 10^6 years

Figure 4.31: The fractional abundance of CS to H in models G1, L2 and S2 at 10^5 and 10^6 years.

G1 model, the fractional CS abundance has increased in the inner and outer regions, and decreased in the intermediate hot core regions. The fractional abundances seen in model L2 have decreased for most of the hot core radius, showing that CS is being destroyed in the L2 model by this time. In model S2, the fractional CS abundance has increased in the inner regions, and decreased towards the outer regions.

Tables 4.6 and 4.7 show the main species which destroy and produce CS at 10^4, 10^5 and 10^6 years in models G1, L2 and S2. It can be seen that CS is destroyed in model S2 almost solely by atomic oxygen. This is because the oxygen is comparatively more abundant in the S2 model than in the other models, and so more atomic oxygen per unit species (not including H_2) exists, and is able to destroy other species. The underlying ratio of (O)/(C+N+S+Fe) is highest in model S2 and lowest in G1, as seen in Table 4.5. This results in atomic oxygen (and some oxygen-bearing species) being comparatively more abundant in model S2, and explains the very different behaviour seen in this model, particularly at early time, when the CS is models G1 and L2 is mostly destroyed by carbon-bearing species, H_3O^+, and H_3^+. The three models behave in a more similar fashion at 10^6 years, when the chemistry has evolved so that in the majority of shells, the CS destruction is dominated by atomic O or oxygen-bearing H_3O^+. Table

4.7 shows that in the outer shells, for all models at all times, all the CS is formed on the grains, and thermally desorbed into the gas-phase. The formation of CS in the inner and intermediate shells is not dominated by a particular species. Many of the gas phase formation routes involve species which have formed on the grain surfaces and then been desorbed when the protostar 'switched on', before being broken down into smaller species and finally CS. Examples of species which have been processed in this way include H_3CS^+ and H_2CS.

Overall, for models G1, L2 and S2, the fractional CS abundance is not a straightforward metallicity tracer. This species is very sensitive to changes in the dust/gas ratio, and if a hot core were observed with a very low CS abundance in the inner regions (or no CS abundance was observed in the inner regions), it could indicate that the hot core had a very low dust/gas ratio. This is independent of the age of the hot core, and so is quite a useful diagnostic. The fractional CS abundance seen in all three models at all three times, in the outer regions of the hot core, cannot be used to identify the underlying metallicity or dust/gas ratio of the model. The values seen in the graphs are similar in the three models, at each time stage. CS is therefore most useful to an observer who is trying to interpret the dust/gas ratio in a hot core. If the CS fractional abundance is seen to be strongest at the edges of the hot core, the dust/gas ratio is very low. If the CS fractional abundance is reasonably constant across the hot core radius, the dust/gas ratio is likely to be Galactic or similar.

4.5.9 NH_3

Figure 4.32(a) shows the fractional NH_3 abundance at 10^4 years in models G1, L2 and S2. It can be seen that the highest fractional abundance is seen in model G1, across the whole hot core. The next highest fractional abundance is seen in model L2, and the lowest fractional abundance in model S2. At 10^4 years, the NH_3 abundance is thus tracing the underlying metallicity of the models, to some extent. The NH_3 is equally abundant across the whole hot core in model G1. In model L2, the fractional abund-

			Distance from protostar (pc)	
Model	**Time (years)**	**1.31×10^{-3}**	**1.16×10^{-2}**	**1.12×10^{-1}**
G1	10^4	C_2H(12%), H_3^+(11%), H_3O^+(51%), CRPHOT(18%)	C_2H(11%), H_3^+(11%), H_3O^+(54%), CRPHOT(14%)	N(6%), C_2H(25%), H_3^+(54%)
	10^5	C_2H(10%), H_3^+(10%), H_3O^+(55%), CRPHOT(18%)	C_2H(8%), H_3^+(10%), H_3O^+(62%), CRPHOT(12%)	C_2H(10%), H_3^+(72%)
	10^6	C_2H(6%), H_3^+(8%), H3O+(69%), CRPHOT(12%)	H_3O^+(96%)	H_3^+(81%)
L2	10^4	C_2H(7%), H_3^+(7%), H_3O^+(74%)	C_2H(6%), H_3^+(7%), H_3O^+(73%)	O(100%)
	10^5	H_3O^+(86%)	H_3O^+(91%)	O(14%), H_3^+(25%), H_3O^+(14%), HCO^+(38%)
	10^6	H_3O^+(97%)	H_3O^+(95%)	C_2H (87%), H_3^+(7%)
S2	10^4	O(100%)	O(100%)	O(100%)
	10^5	O(100%)	O(100%)	O(100%)
	10^6	O(99%)	O (99%)	O (98%)

Table 4.6: How CS is destroyed in models G1, L2 and S2 at various times and radii. The numbers in brackets are the percentage of CS which is destroyed by that species at that time. CRPHOT represents a cosmic ray photon breaking up the CS molecule.

			Distance from protostar (pc)	
Model	**Time (years)**	**1.31×10^{-3}**	**1.16×10^{-2}**	**1.12×10^{-1}**
G1	10^4	C_2H(95%)	C_2H(94%)	THERM(100%)
	10^5	C_2H(33%), HCS(8%), HCS^+(36%), H_2CS(18%)	C_2H(29%), HCS^+(32%), H_3CS^+(5%), H_2CS(28%)	THERM(100%)
	10^6	HCS^+(76%), H_2CS(15%)	HCS^+(19%), H_3CS^+(12%), H_2CS(53%)	THERM(100%)
L2	10^4	HCS^+(29%), H_3CS^+(15%), H_2CS(45%)	CH_2(54%), HCS^+(9%), H_3CS^+(15%), H_2CS(18%)	THERM (100%)
	10^5	HCS^+(55%), H_3CS^+(9%), H_2CS(29%)	HCS^+(47%), H_3CS^+(10%), H_2CS(35%)	THERM (100%)
	10^6	HCS^+(17%), H_3CS^+(12%), H_2CS(38%)	HCS^+(18%), H_2CS^+(6%), H_3CS^+(24%), H_2CS(43%)	THERM (100%)
S2	10^4	SO (85%), H_3CS^+(7%)	SO(84%), H_3CS^+(7%)	THERM (100%)
	10^5	H_3CS^+(59%), H_2CS^+(9%), H_2CS(18%)	HCS^+(6%), H_2CS^+(7%), H_3CS^+(50%), H_2CS^+(9%) H_2CS(19%)	THERM(100%)
	10^6	H_2CS^+(7%), H_3CS^+(73%), H_2CS(9%)	HCS(6%), HCS^+(16%), H_2CS^+(7%), H_3CS^+(62%),	THERM(100%)

Table 4.7: The species from which CS is formed in models G1, L2 and S2 at various times and radii. The numbers in brackets are the percentage of CS which is produced by that species at that time. THERM represents thermal desorption from the grain surfaces.

ance drops slightly at the outer edge of the hot core. In model S2, the fractional NH_3 abundance drops considerably at the outer edge of the hot core. This reduction in NH_3 in the lower metallicity models occurs as NH_3 is destroyed by H_3O^+ in these regions. The H_3O^+ abundance is much higher in the outer shells of models L2 and S2 than G1. This is caused by a much higher abundance of atomic oxygen in the outer shells of models L2 and S2. The atomic oxygen in these models reacts to form OH/OH^+, and finally H_3O^+, which goes on to destroy ammonia. In model G1, there is much less atomic oxygen in the outer shells, and the O atoms present tend to react with nitrogen/nitrogen-bearing species, to form neutral species such as NO and HNO. At 10^4 years, the NH_3 abundance could be used as a metallicity tracer, as the three models produce fractional abundances which somewhat reflect the underlying level of metallicity in that model. The underlying ratio of nitrogen in models G1/L2 is 9.45, as seen in Table 4.1. The NH_3 ratio in the two models (from the inner shells of the hot core at 10^4 years) is 9, which reflects the underlying ratio of nitrogen abundances in the models. However, the underlying nitrogen abundance in models G1/S2 is $\sim$ 24, whereas the ratio of NH_3 in models G1/S2 (inner shells, 10^4 years) is $\sim$ 75. The NH_3 abundance does not directly trace the underlying nitrogen abundance in this case. At 10^4 years, the fractional NH_3 abundance contains 80% of the underlying nitrogen in models G1 and L2. At the same time, in model S2, only 25% of the underlying nitrogen exists as NH_3. Ammonia forms in the grain surfaces, and the lower fraction of nitrogen in the S2 model shows that the dust/gas ratio also has an effect on the formation of this species.

Figure 4.32(b) shows how the fractional NH_3 abundance in the three models has evolved, by 10^5 years. The fractional abundances in models G1 and L2 are similar to those seen at 10^4 years, albeit slightly lower. The fractional abundance in model S2 is much lower across the whole hot core radius. This change occurs as follows:

In both models, when NH_3 is destroyed, it tends to form NH_4^+. This occurs almost

100% of the time in S2, and over 80% of the time in model G1. The following reaction:

$$NH_4^+ + e^- \rightarrow NH_2 \tag{4.14}$$

has a branching ratio of 0.31 in the models (the NH_4^+ ion forms NH_3 with a branching ratio of 0.69). However, in model S2, NH_2 almost always goes on to react with atomic oxygen, giving the following products:

$$NH_2 + O \rightarrow \{OH, NO, HNO\} \tag{4.15}$$

Whereas in model G1, NH_2 reacts with H_2 97% the time, producing ammonia:

$$NH_2 + H_2 \rightarrow NH_3 \tag{4.16}$$

Thus, in model G1 (and L2), the ammonia abundance is maintained at a reasonably high level between 10^4 and 10^5 years. In model S2, the ammonia is destroyed by atomic oxygen over this time period. In models G1 and L2, a greater proportion of the atomic oxygen has reacted to form NO, HNO and other nitrogen-bearing species. The reduced underlying nitrogen abundance in model S thus has two effects on the NH_3 abundance:

1. Less NH_3 can be formed, as there is less nitrogen to incorporate into this molecule

2. The NH_3 which is formed is much more likely to be destroyed. This is because there is a higher fractional atomic oxygen abundance, as there is less nitrogen in the model and so lower abundance of species such as HNO and NO are able to form.

At 10^5 years, NH_3 could be used as a metallicity tracer, as the three models produce fractional abundances which reflect the level of metallicity in the model, and can easily be distinguished from one another.

Figure 4.32(c) shows the fractional NH_3 abundance in the models at 10^6 years. The fractional abundances in models G1 and L2 have drastically dropped. This is because

by this time, a large quantity of the available nitrogen is locked up in the N_2 molecule. This can be seen in Figure 4.32(d), which shows the fractional N_2 abundance in the models at 10^6 years. The fractional NH_3 abundance in model S2 is extremely similar at 10^5 and 10^5 years. The same species and reactions are destroying and producing NH_3 at both times. The nitrogen chemistry in this model approaches steady state at an earlier time than models G1 and L2. At 10^6 years, NH_3 may not be such a useful tracer of the underlying metallicity of a hot core, as the fractional NH_3 abundances in the three models are more similar than at earlier times.

Overall, the fractional NH_3 abundance is a fairly useful metallicity tracer. If the dust/gas ratio in other galaxies is similar to that in the Milky Way (or reduced by a factor of up to four, as in the L2 model) then the fractional NH_3 abundance directly traces the underlying nitrogen abundance at 10^4 years. If a much lower NH_3 abundance is seen at this time, it is likely that this is caused by a reduction in the dust/gas ratio as well as a lower underlying nitrogen abundance. At 10^5 years, an extremely low NH_3 abundance could indicate a high atomic oxygen abundance in a hot core. A sub-Galactic NH_3 fractional abundance at this time can also indicate a lower underlying nitrogen abundance, coupled with a Galactic/sub-Galactic dust/gas ratio. By 10^6 years, the usefulness of NH_3 as a metallicity tracer has diminished, as the chemistry becomes more complicated with respect to radius in the higher metallicity models.

4.5.10 Behaviour in the outermost shells

In many of the models, for most species, at most times, it can be seen that the outermost shells of the hot core contain slightly unusual fractional abundances. For example, Figure 4.26(a) shows that the fractional HNCO abundance decreases with increasing radius at 10^4 years in model G1, but the fractional abundance can be seen to increase in the outermost shells. In other cases, a fractional abundance which has been steadily increasing can be seen to reach a plateau. An example of this can be seen in Figure 4.22(a), where the fractional HCO^+ abundance at 10^4 years in model S2 reaches a plat-

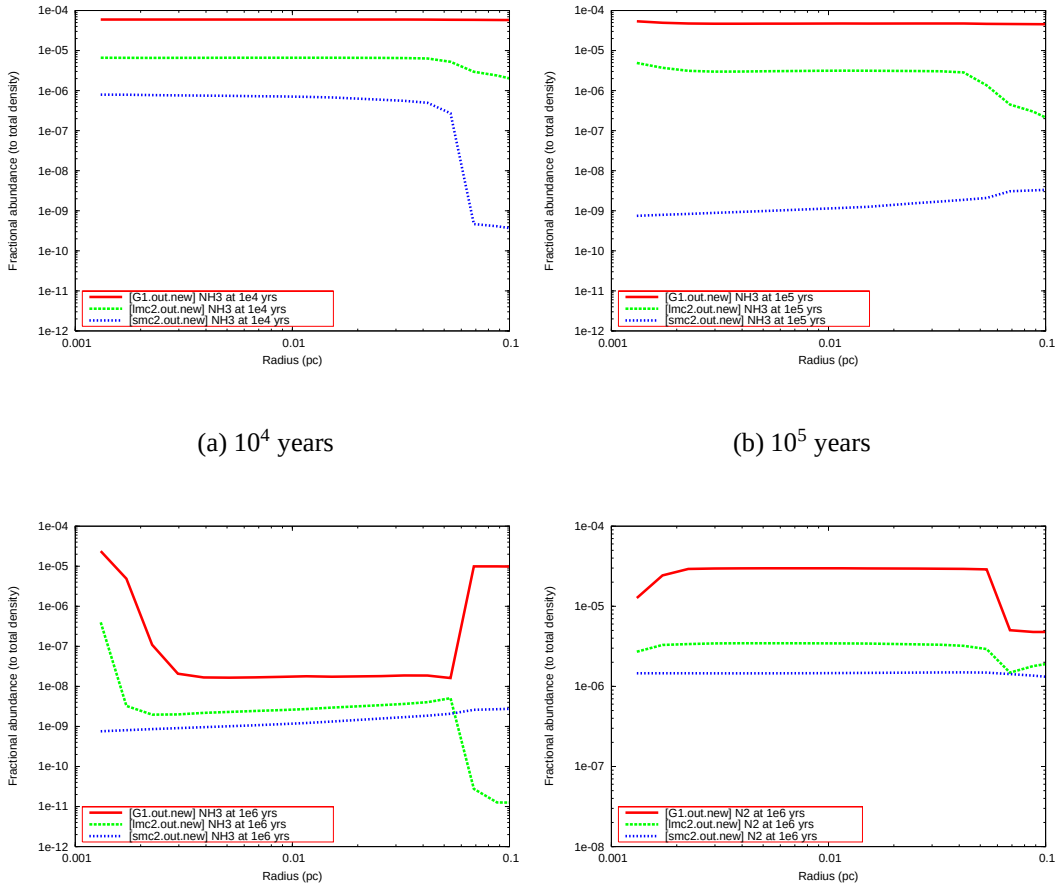

(a) 10^4 years

(b) 10^5 years

(c) 10^6 years

(d) 10^6 years

Figure 4.32: The fractional abundance of NH_3 to H in models G1, L2 and S2 at 10^4, 10^5 and 10^6 years, and N_2 at 10^6 years.

eau at a radius of 0.07pc. The reason for this unusual behaviour is due to a change in the type of chemistry which occurs. In the inner and intermediate shells, the high temperatures and densities ensure a typical 'hot core' chemistry is seen. In the outer shells, the cooler, less dense regime begins to resemble a dark cloud, and the chemistry changes accordingly. In the outer shells, the fractional ionisation is higher and so the chemistry changes as ion-neutral reactions occur more frequently than neutral-neutral reactions (which dominate in the inner and intermediate shells). As the shell model does not allow interaction between shells (chemical or physical), the chemistry seen in this outer

region does not smoothly integrate with the hot core chemistry. Instead, the differences between the chemical regimes are starkly visible, and produce these jumps/plateaux in fractional abundance for some species. Beyond the outer shells, more shells of lower temperature and density exist within the model (although the results are not displayed). As the shell models are calculated independently from one another, these further shells have no effect on the shells which are shown in this thesis. Each shell is calculated as a single point hot core model, with the same radiation field affecting each model. In each shell, the high visual extinction is assumed to prevent photoreactions occurring – all of the shells have a visual extinction greater than $2000 A_V$, as shown in Table 2.4. These high visual extinctions ensure that no significant photochemistry occurs in any of the shells modelled.

The different type of chemistry occurring in the outer shells appears to lead to some very drastic changes in the modelled abundances. This is because the shells are separated in log space, and the figures in this chapter use a log scale. As the shell number increases, the shell radius also increases, and the outer two shells actually represent a fairly large proportion of the model.Figure 4.33 shows the fractional abundances seen for CO in model G1, on a log scale and a linear scale. It can be seen that, when shown on a linear scale, the change in the fractional CO abundance appears less sudden.

In this thesis, where possible, I have described and discussed the overall chemistry of a region, rather than these extreme changes in the outer shells. This is because a hot core is characteristically described as being hot and dense. At the point where the chemical regime changes, it could be argued that these regions are not part of the hot core, but instead the surrounding dark cloud.

4.5.11 Comparison with the results of those of Bayet et al. (2008)

As discussed in Section 4.4, Bayet et al. (2008) modelled hot cores at low metallicity. Bayet et al. (2008) used these models to identify several species which could be used as metallicity tracers in hot cores. The Bayet et al. (2008) models included:

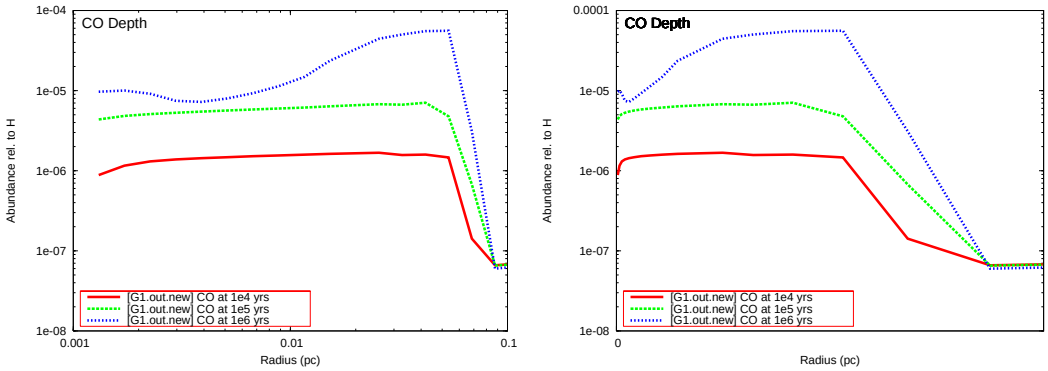

(a) Log Scale (b) Linear Scale

Figure 4.33: The fractional abundance of CO to H in model G1 at 10^4, 10^5 and 10^6 years, on a log scale and a linear scale.

1. Depleted models – models which had reduced initial elemental abundances (by a common factor, e.g. 1/10, 1/100) but standard/Galactic physical parameters

2. Low–metallicity models – models which had reduced initial elemental abundances and reduced dust/gas ratio and H_2 formation rate

3. Differing–ratio models – models in which the ratios of the elemental abundances were changed with respect to one another

A comparison of the common species examined in this thesis and by Bayet et al. (2008) is shown in Table 4.8.

It can be seen that the JBCA and Bayet et al. (2008) models disagree about which species are useful metallicity tracers. This could be caused by a number of factors, including:

1. The differing physical complexity of the models

2. The different gas-phase chemistry used – the Bayet et al. (2008) models use a less recent UDfA release than the models in this thesis. This is particularly

	JBCA	Depleted	Low–metallicity	Differing–ratio
CO	Does not trace metallicity	Traces metallicity	Traces metallicity	Traces C
CS	Traces dust/gas in inner regions	Traces metallicity	Traces metallicity	Reduced by high underlying O
CH3OH	Traces metallicity beyond 10^5 years	Traces metallicity up to 10^5 years	Traces metallicity up to 10^5 years	Mainly traces C
HCN	Traces N/C, then general metallicity	Does not trace metallicity	Does not trace metallicity	Traces N
HNC	Traces metallicity	Does not trace metallicity	Does not trace metallicity	Traces N
HCO+	Inversely traces metallicity	Inversely traces metallicity	Inversely traces metallicity	Anticorrelates with O

Table 4.8: A comparison of the common species examined in this thesis and by Bayet et al. (2008). The species are analysed for their metallicity tracing abilities.

important for methanol, as the gas-phase modelling of this species was changed in the UDfA Rate 06 release which is used in this thesis.

3. Differences in the surface chemistry used in the models

4. Different interpretations of "metallicity" – Bayet et al. (2008) describes CO as a poor metallicity tracer, but goes on to say it traces the underlying carbon abundance in a region. In this thesis, that would be considered a good tracer.

The models agree that HCO^+ is a good inverse tracer of metallicity. The disagreement between the models over CH_3OH can be explained by the different versions of the UDfA used for the gas-phase chemical reaction networks. Although Bayet et al. (2008) consider HCN and HNC poor metallicity tracers, they found that these species trace the underlying nitrogen abundance in a hot core. The results of this thesis show that HCN and HNC are good tracers of general metallicity. The differences between the results of the JBCA and Bayet et al. (2008) models show that more benchmarking is needed to fully explain the differences produced by different hot core models.

4.6 Summary of Comparisons between G1, L2 and S2

The results from models G1, L2 and S2 show that lowering the metallicity changes the chemistry in a hot core. A reduction in the initial elemental abundances does not directly translate into an equal reduction in the fractional abundances of the gas and grain phase species. For example, if the underlying nitrogen abundance in a region is halved, the fractional abundance of NH_3 is not automatically halved. The interdependencies of the reaction network are complex, and a change in the underlying elemental abundances can cause different reactions and rates to dominate the chemistry. Generally, it can be seen that lowering the dust/gas ratio has a more profound effect than altering the input elemental abundances, for most species. Table 4.9 summarises which species can be thought of as potential metallicity tracers.

Species	Potential metallicity tracer?
CO	Probably not – similar abundances in models G1, L2, S2
HCO^+	Possible inverse tracer - could trace cooler, less dense gas in outer shells
HCN	Yes – traces lower limit for N/C ratio at 10^4 years. After this, traces metallicity generally. A low abundance is linked to a high O/C ratio
HNC	Yes – traces underlying elemental abundances, not dust/gas
HNCO	Possibly – could identify Galactic or sub-Galactic metallicity up to 10^5 years
HC_3N	Possibly – if hot core age accurately known, could trace dust/gas at 10^4 years or elemental abundances at 10^6 years
CH_3OH	Possibly – if age of hot core is over 10^5 years, could identify Galactic or sub-Galactic metallicity
CS	Possibly – inner region observations can determine if dust/gas ratio is Galactic or sub-Galactic
NH_3	Yes – traces underlying N abundance in more metallic models at 10^4 & 10^5 years. Reveals low dust/gas ratio in very low metallicity model

Table 4.9: Possible metallicity tracers in the Multidepth hot core model

5

RATRAN modelling of low metallicity hot cores.

5.1 Radiative Transfer

The radiative transfer equation describes how radiation travelling through a medium is affected by the processes of absorption, emission and scattering. The equation of radiative transfer is as follows: (using notation from Dyson & Williams 1997)

$$\frac{dI_\nu}{ds} = -\kappa_\nu I_\nu + j_\nu \tag{5.1}$$

where the specific intensity, I_ν, is the energy (erg) per second in the frequency range ν, v + dν (Hz), crossing unit area (cm^2) in unit solid angle (sr); s is the path length (cm), and κ_ν is the absorption coefficient (including scattering) per unit path length. The emissivity, j_ν, is defined so that j_ν dV dν dΩ dt is the energy emitted by the volume dV in the frequency range dν during the time dt over a solid angle dΩ.

The optical depth is defined:

$$\tau_\nu = \int \kappa_\nu ds \tag{5.2}$$

Using $d\tau_\nu = \kappa_\nu ds$ from equation 5.2, equation 5.1 can be written as:

$$\frac{dI_\nu}{d\tau_\nu} = S_\nu - I_\nu \tag{5.3}$$

where the source function, $S_\nu \equiv \frac{j_\nu}{\kappa_\nu}$, is independent of the optical depth. The values for j_ν and κ_ν can vary throughout the absorbing region. Equation 5.3 is a linear ODE and can be integrated, using e^{τ_ν} as the integrating factor. This gives:

$$I_\nu = I_{\nu 0} e^{-\tau_\nu} + \int_0^{\tau_\nu} S_\nu \exp[-(\tau_\nu - \tau'_\nu)]\, d\tau'_\nu \tag{5.4}$$

The specific flux, F_ν, is the specific intensity, I_ν, integrated over all solid angles $d\Omega$:

$$F_\nu = \int_\Omega I_\nu d\Omega \tag{5.5}$$

The local mean intensity of the radiation field, J_ν, is defined as follows, and can be thought of as the specific flux at a particular point in space:

$$J_\nu = \frac{\int_\Omega I_\nu d\Omega}{\int_\Omega d\Omega} = \frac{1}{4\pi} \int_\Omega I_\nu d\Omega \tag{5.6}$$

This integration extends to infinity.

5.2 RATRAN

RATRAN is a non-LTE radiative transfer code (available online, Hogerheijde & van der Tak 2000) which can be used for spherically symmetric sources, such as the Multidepth Hot Core Model. The code can also be used for cylindrically symmetric sources. RATRAN uses an accelerated Monte Carlo method. In order to use a Monte Carlo approach, RATRAN models the source as a grid of small cells. Within each cell, the physical properties (e.g. density, temperature, molecular abundance) are kept constant. The cells are assumed to be very small, as Hogerheijde & van der Tak (2000) describe that, "the molecular excitation can be represented by a single value in each cell, which requires instantaneous spatial and velocity mixing of the gas". The Monte Carlo method calculates the local mean intensity of the radiation field, J_ν, in each cell, *i*, by summing the radiation received from all the other cells in the source. The radiation received from each shell is weighted by the solid angle subtended by that cell in relation to cell *i*. J_ν is calculated for a number of paths through the source, using the

CMB radiation as a boundary condition for the source. Accelerated Lambda Iteration (ALI) is used to expedite the convergence of the model at high optical depth, by separating the incident (CMB) and locally produced radiation fields. ALI uses 'operator splitting' to speed up the iteration to convergence by approximating the mathematical operator, Λ, which acts on the source function, S_ν to calculate J_ν. Λ is a matrix which describes how the radiation field in cell *i* depends on each of the other cells in the source. The approximated value, Λ*, is often chosen to be the diagonal or tri-diagonal part of the operator Λ, as this quickly leads to a convergence. The addition of ALI to the Monte Carlo method is useful when using RATRAN in conjunction with the hot core model results, as the optical depths can become large in the inner regions of the hot core.

5.2.1 Using RATRAN

RATRAN Hogerheijde & van der Tak (2000) can be used online or offline, to calculate line profiles for various interstellar species. A spherical model of a hot core was used, as described in Section 2.4.2. Different RATRAN inputs were taken from each shell of the hot core model, in order to model the integrated intensities of various transitions for a number of species. The RATRAN inputs used in this thesis are as follows, generalised for a shell, *x*:

1. Shell number – Identifies how shells are positioned with respect to one another
2. Density (cm^{-3}) – The H_2 density in shell *x* of the hot core model
3. Temperature (K) – The gas (and dust) temperature in shell *x* of the hot core model
4. Abundance (cm^{-3}) – The abundance of a species in shell *x* at a specified time
5. Inner radius (cm) – The inner radius of shell *x*, with respect to the internal protostar

6. Outer radius (cm) – The outer radius of shell *x*, with respect to the internal protostar

7. Line width (km s^{-1}) – Assumed value of 0.9 for all shells

8. Line velocity (km s^{-1}) – Assumed value of 0 for all shells

The value estimated by RATRAN is J_ν – this is the observed flux/intensity seen from a spectral line by an observer. It is measured in K km s^{-1}. J_ν was plotted as a function of projected radius/offset for the hot core models G1, L2 and S2, at 10^4, 10^5 and 10^6 years, for several transitions of some hot core species.

5.3 Modelling the expected line intensity for several hot core species

The species chosen for modelling were commonly observed hot core species which can be modelled with RATRAN . The transitions examined were chosen as they are of frequencies which can be observed at mm and sub-mm wavelengths. The RATRAN output consists of line profiles for each transition. The results shown in this section are the integrated intensities of these line profiles. Integrating the line profiles means that information regarding the internal velocity structure is lost. However, given the poor observational constraints of the line widths and velocities of hot cores in other galaxies, it is inappropriate to consider them in detail in the RATRAN modelling.
Table 5.1 lists the frequency and excitation temperature for the RATRAN modelled transitions of the species considered. Table 5.2 gives the opacity outputs from the RATRAN modelling using the G1 model.

Transition	Freq (Ghz)	E_u/k(K)
HNCO		
4(0,4) – 3(0,3)	87.93	10.55
4(1,3) – 3(1,2)	88.24	53.86
5(2,4) – 4(2,3)	109.87	186.1
^{13}CS		
2 – 1	46.25	2.22
3 – 2	92.49	6.66
5 – 4	184.98	22.19
7 – 6	277.46	46.61
CS		
2 – 1	48.99	2.35
3 – 2	97.98	7.05
5 – 4	195.95	23.51
7 – 6	293.91	49.37
C^{18}O		
2 – 1	109.78	5.27
3 – 2	219.56	15.81
4 – 3	329.33	31.61
5 – 4	439.09	52.68
CO		
2 – 1	115.27	5.53
3 – 2	230.54	16.6
4 – 3	345.8	33.19
5 – 4	461.04	55.32
H^{13}CN		
2 – 1	86.34	4.14
3 – 2	172.68	12.43
4 – 3	259.01	24.86
NH_3		
3(1,1) – 3(1,0)	22.23	144.03
3(2,1) – 3(2,0)	22.83	128.07
2(1,1) – 2(1,0)	23.10	58.32
1(1,1) – 1(1,0)	23.69	1.14
2(2,1) – 2(2,0)	23.72	42.32
4(4,1) – 4(4,0)	24.14	178.39
5(5,1) – 5(5,0)	24.53	273.24

Table 5.1: The frequency and excitation temperature for the RATRAN modelled transitions of various species.

5.4 Results from the Galactic Model

5.4.1 ^{13}CS

Figure 5.1 shows the RATRAN-modelled intensity of some observable rotational transitions of ^{13}CS at 10^4 years. The intensities were produced using RATRAN and the fractional abundances/physical conditions from model G1. The figure shows that the peak intensity of the hot core increases as the rotational transition number increases. A similar peak intensity of around 17 K km s^{-1} is observed at J=7-6 and J=5-4, the

G1 Model	Opacities		
	10^4 years	10^5 years	10^6 years
^{13}CS			
1 – 0	0.02	0.06	0.10
2 – 1	0.05	0.19	0.38
3 – 2	0.09	0.39	0.75
5 – 4	0.20	0.84	1.38
7 – 6	0.26	1.07	1.41
C^{18}O			
1 – 0	0.05	0.14	0.83
2 – 1	0.16	0.45	2.78
3 – 2	0.29	0.79	4.74
4 – 3	0.42	1.03	5.78
5 – 4	0.53	1.14	5.64
HCN			
1 – 0	3156.00	3918.00	4086.00
3 – 2	19880.00	24320.00	23590.00
4 – 3	26000.00	31420.00	28540.00
H^{13}CN			
1 – 0	9.91	12.27	12.76
3 – 2	62.35	75.91	73.62
4 – 3	81.03	97.59	88.54
HC^{15}N			
1 – 0	42.55	52.73	54.97
3 – 2	267.20	326.30	316.40
4 – 3	348.60	420.70	381.80
HNC			
1 – 0	2470.00	2576.00	3293.00
3 – 2	14840.00	15580.00	18510.00
4 – 3	18680.00	19710.00	21890.00
HN^{13}C			
1 – 0	33.36	34.75	44.24
3 – 2	199.90	209.60	248.10
4 – 3	250.70	264.40	292.70
H^{15}NC			
1 – 0	7.90	8.23	10.38
3 – 2	47.40	49.29	58.33
4 – 3	59.20	62.41	68.49
HNCO			
4(0,4) – 3(0,3)	0.05	0.39	0.33
4(1,3) – 3(1,2)	0.02	0.02	0.02
5(2,4) – 4(2,3)	0.03	0.03	0.03
NH_3			
3(1,1) – 3(1,0)	945.80	750.90	25.39
3(2,1) – 3(2,0)	5282.00	4191.00	163.00
2(1,1) – 2(1,0)	8101.00	6417.00	426.40
1(1,1) – 1(1,0)	55320.00	43760.00	4028.00
2(2,1) – 2(2,0)	47490.00	37610.00	2762.00
4(4,1) – 4(4,0)	6751.00	5363.00	128.10
5(5,1) – 5(5,0)	1847.00	1466.00	11.40

Table 5.2: Opacities in Model G1 RATRAN outputs

highest transition levels modelled.

Figure 5.2 shows the intensities for the same transitions in the same model at 10^5 years. The intensities have increased by a factor of a few in the time period from 10^4 to 10^5 years. This corresponds with the increase in the fractional ^{13}CS abundance between 10^4 and 10^5 years, as seen in Figures 5.1(f) and 5.2(f) (G1 is represented by the red line). At 10^5 years, the intensities again increase as the J transitions increase, with the highest intensities being seen at J=7-6 and J=5-4. The peak intensities for these transitions are around 77 K km s^{-1}.

Figure 5.3 shows the intensities for the same transitions in model G1 at 10^6 years. The intensity at 10^6 years no longer increases as the J number of the transitions increases. The highest intensities are seen at J=5-4 and J=3-2. Figure 5.3(f) shows that the fractional CS abundance has reduced in the intermediate shells of the hot core, since 10^5 years. However, in the inner shells the fractional CS abundance has increased, and the fractional abundance also sharply increases at a hot core radius of 0.05-0.07pc. This increase causes a peak in the intensity at an offset/projected radius of around 0.06pc, rather than at a projected radius of zero (the 'centre' of the hot core). In all the ^{13}CS results, the intensity falls sharply at a radius of around 0.08pc. As this gas is only observed in the inner regions of the hot core, it can be used a dense gas tracer. The intensity of the ^{13}CS emission changes with time, for each transition. A very low intensity of ^{13}CS is seen in a very young hot core. The highest intensities are seen at 10^5 years. At 10^6 years, the fractional CS abundance leads to a bright shell of CS surrounding a less bright inner region. These characteristic ^{13}CS intensity patterns could be used to constrain the age of a hot core.

5.4.2 C^{18}O

Figures 5.4, 5.5 and 5.6 show the intensities produced by the rotational transitions J=1-0, J=2-1, J=3-2, J=4-3 and J=5-4 for C^{18}O at 10^4, 10^5 and 10^6 years respectively, using fractional abundances from model G1. At 10^4 years, the highest intensity is seen

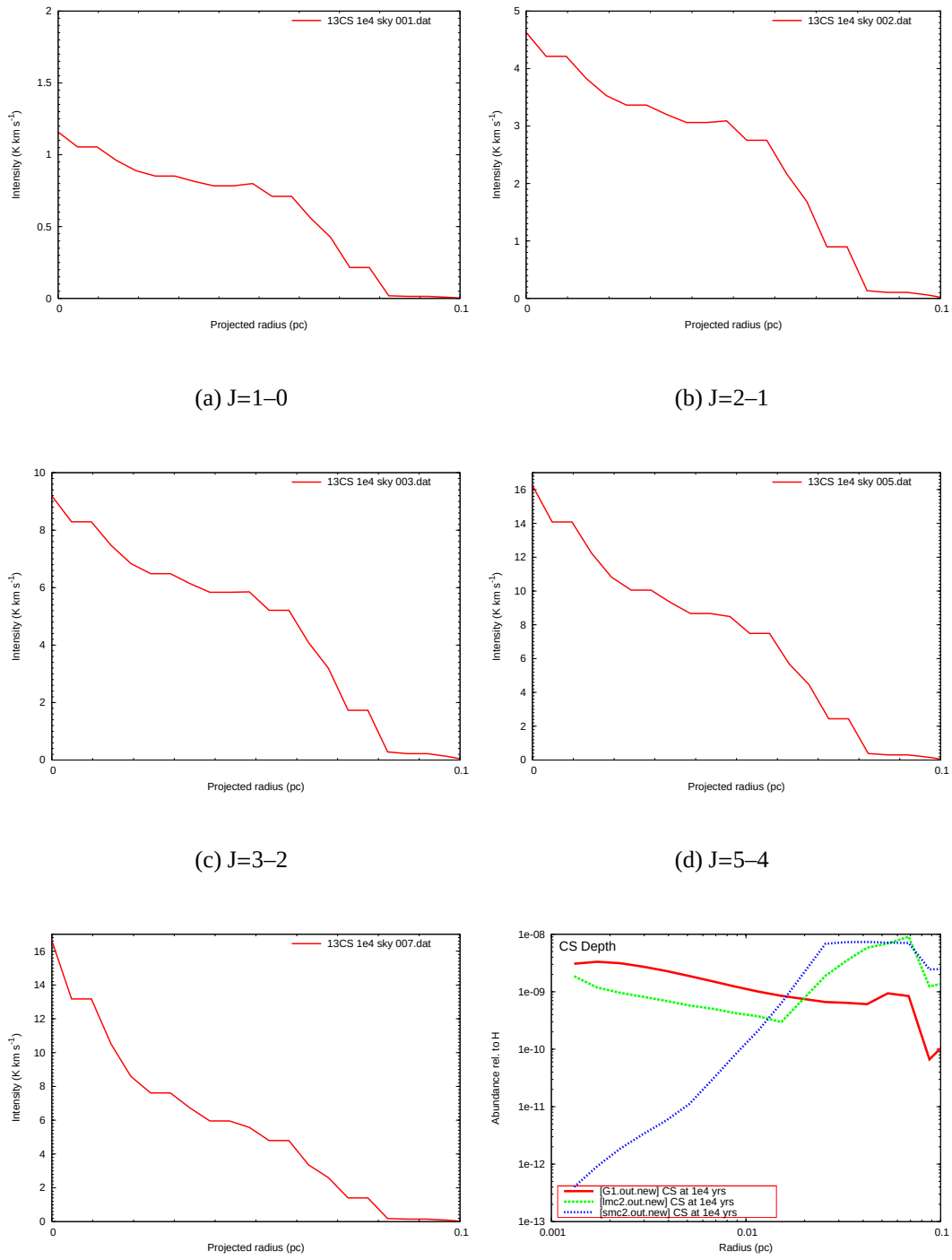

(a) J=1–0 (b) J=2–1

(c) J=3–2 (d) J=5–4

(e) J=7–6 (f) CS fractional abundance

Figure 5.1: The intensity of some observable rotational transitions of ^{13}CS, and the fractional CS abundance, from the G1 model at 10^4 years.

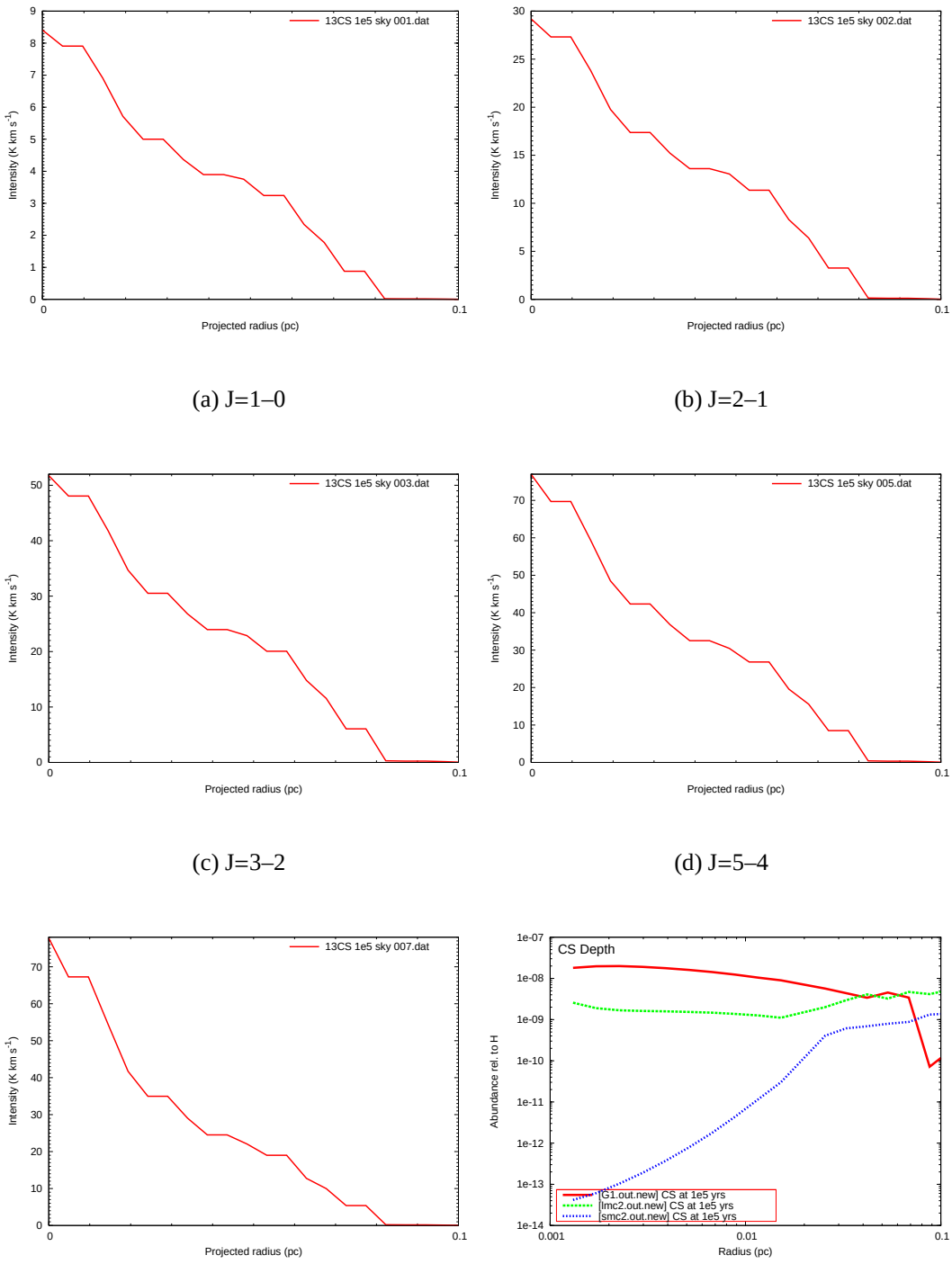

(a) J=1–0 (b) J=2–1

(c) J=3–2 (d) J=5–4

(e) J=7–6 (f) CS fractional abundance

Figure 5.2: The intensity of some observable rotational transitions of ^{13}CS, and the fractional CS abundance, from the G1 model at 10^5 years.

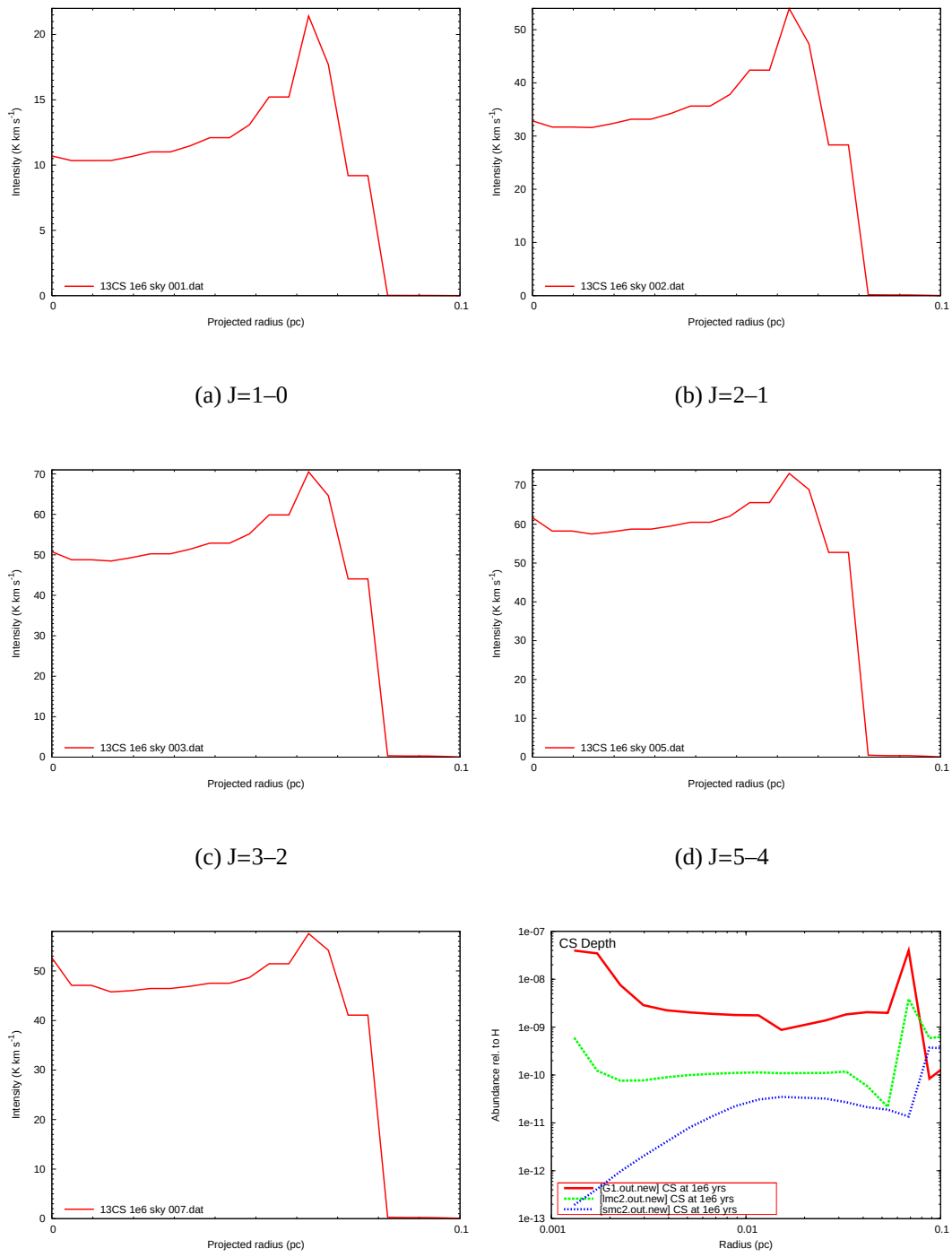

(a) J=1–0 (b) J=2–1

(c) J=3–2 (d) J=5–4

(e) J=7–6 (f) CS fractional abundance

Figure 5.3: The intensity of some observable rotational transitions of ^{13}CS, and the fractional CS abundance, from the G1 model at 10^6 years.

at J=4-3, with a peak value of 26 K km s^{-1}. Similar intensities are seen at J=3-2 and J=5-4.

Figure 5.5 shows that by 10^5 years, the peak intensities have grown by a factor of 3 or 4. This corresponds with the increase in the CO fractional abundance over this time period, which can be seen by comparing the red line in Figure 5.4(f) with that in Figure 5.5(f). The highest peak value at of 63 K km s^{-1} is seen at J=4-3 at 10^5 years. A similar intensity is seen at J=3-2.

At 10^6 years, most of the transitions have started to show self-absorption to some extent, as seen in Figure 5.6. The intensity seen for each transition at this time has increased since 10^5 years, in most cases by a factor less than two. However, the intensity at J=1-0 has increased by a factor greater than four. The change in fractional abundance between 10^5 and 10^6 years can be seen by comparing the red line in Figure 5.5(f) with that in Figure 5.6(f). The fractional CO abundance has increased by a factor of a few over this time period. The optical depths of all the transitions have increased, as can be seen in Table 5.2, and all except J=1-0 are now somewhat optically thick. The increased optical depth of the higher transitions causes the emission to be redistributed between the different rotational transitions at this time, which is why the J=1-0 transition intensity has increased so much more than the other transition intensities. The highest intensities (just over 100 K km s^{-1}) are now seen at J=3-2 and J=2-1, although similar intensities are seen at J=4-3.

The $C^{18}O$ emission could be used to identify the age of a Galactic hot core. The intensity of each transition increases with time, and so a brighter hot core should be older and more chemically evolved than a similar sized hot core with a lower $C^{18}O$ intensity, for these rotational transitions. The presence of self-absorption in the emission spectra could reveal a highly evolved chemistry in an ‘old’ hot core.

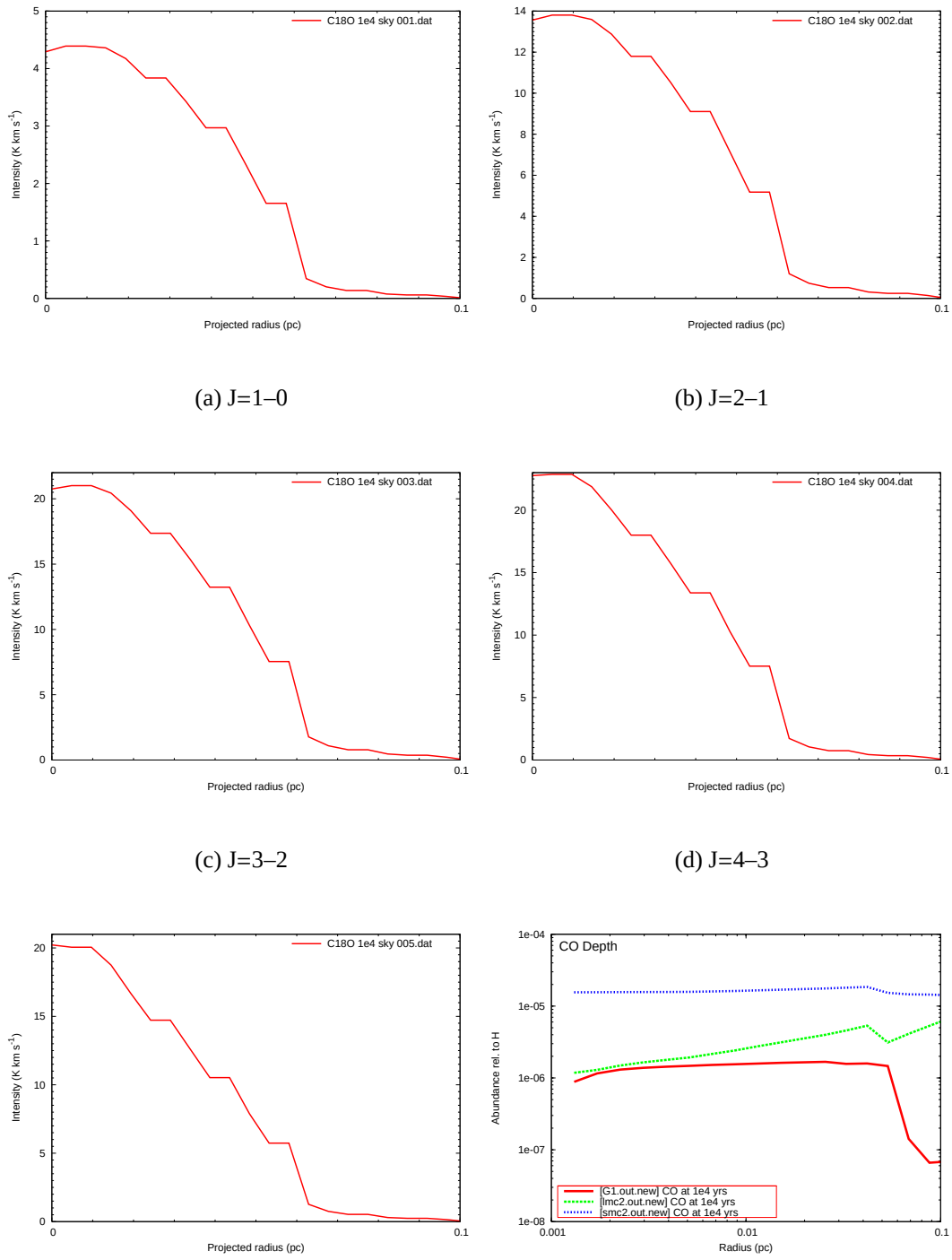

(a) J=1–0 (b) J=2–1

(c) J=3–2 (d) J=4–3

(e) J=5–4 (f) CO fractional abundance

Figure 5.4: The intensity of some observable rotational transitions of $C^{18}O$, and the fractional CO abundance, from the G1 model at 10^4 years.

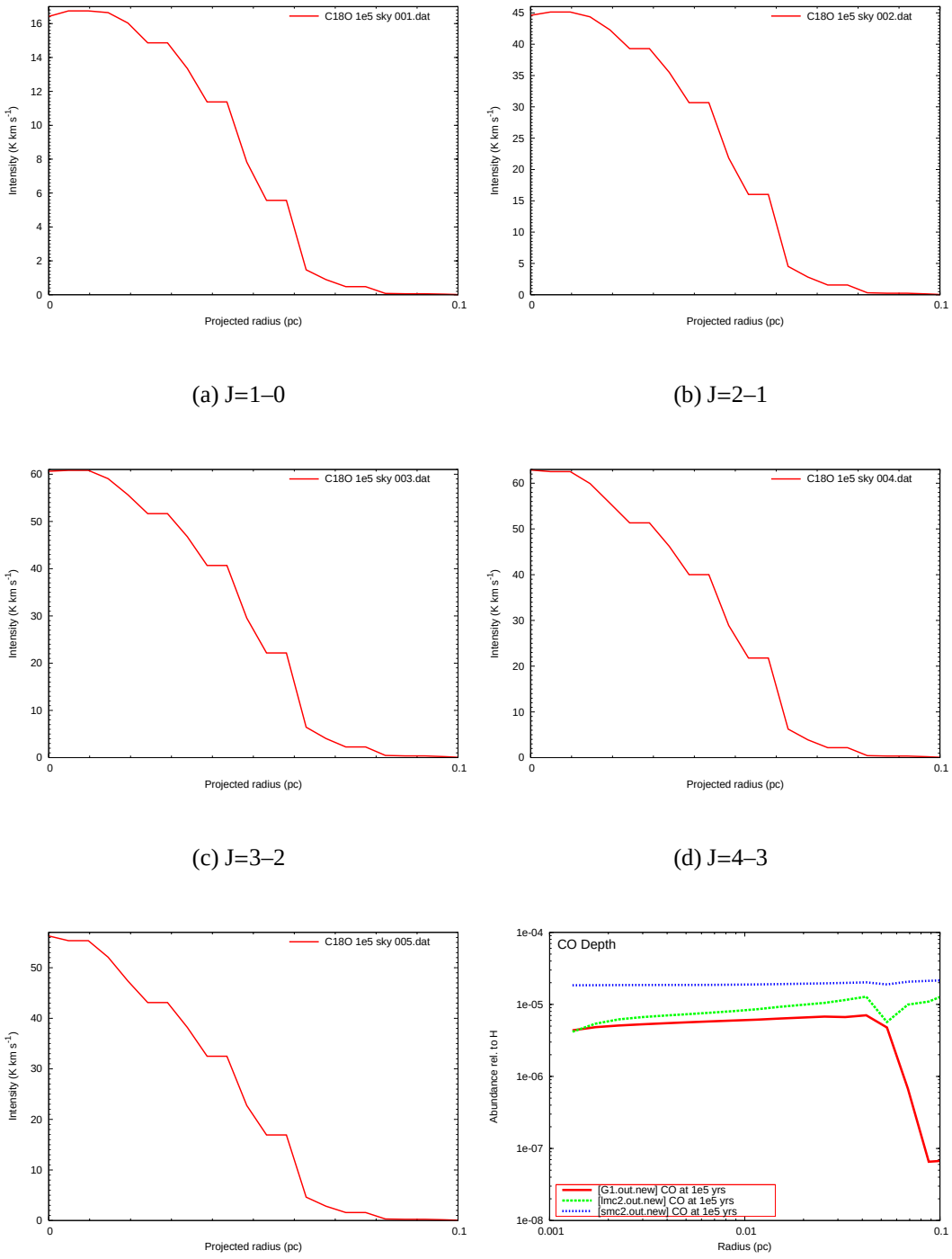

(a) J=1–0 (b) J=2–1

(c) J=3–2 (d) J=4–3

(e) J=5–4 (f) CO fractional abundance

Figure 5.5: The intensity of some observable rotational transitions of $C^{18}O$, and the fractional CO abundance, from the G1 model at 10^5 years.

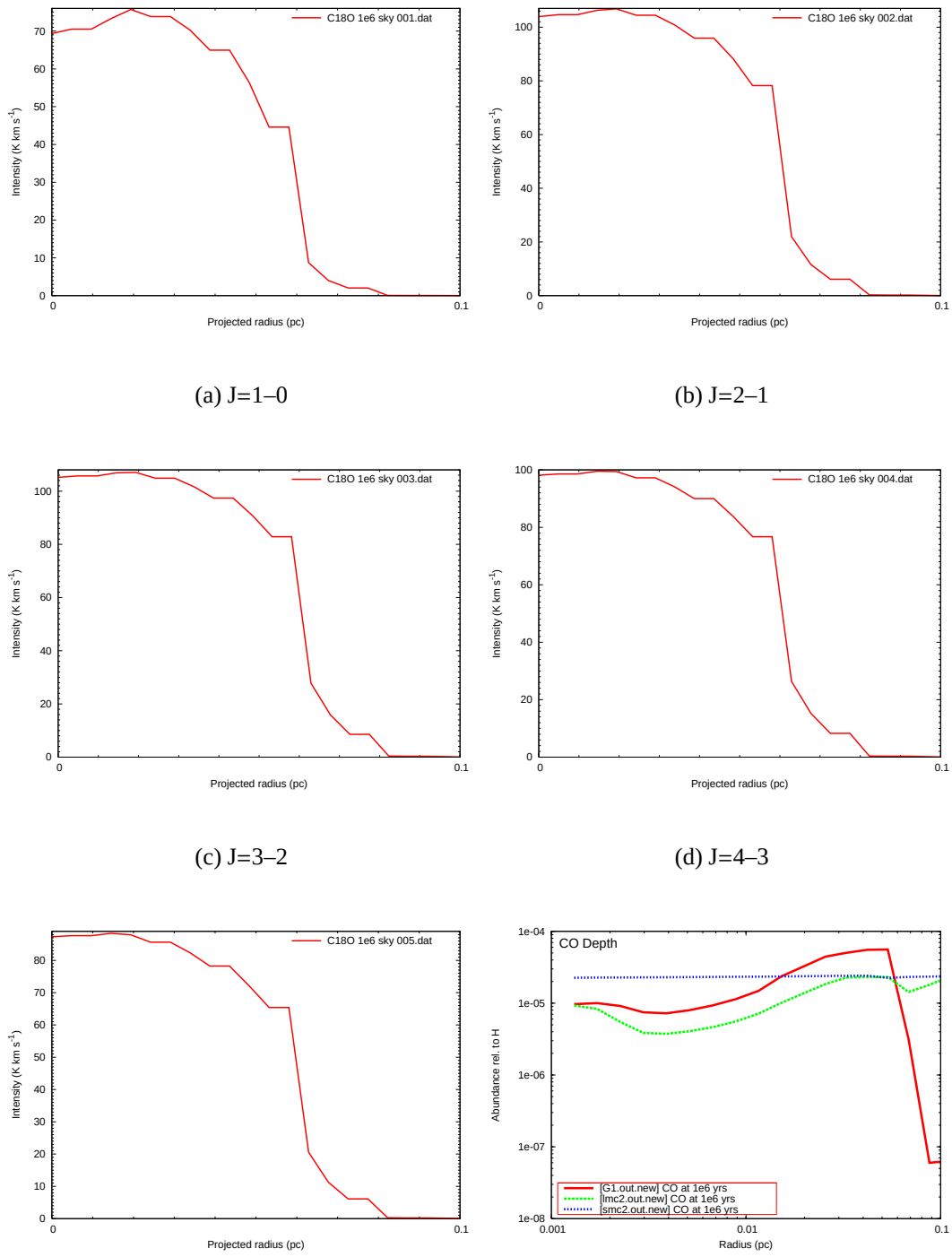

(a) J=1–0 (b) J=2–1

(c) J=3–2 (d) J=4–3

(e) J=5–4 (f) CO fractional abundance

Figure 5.6: The intensity of some observable rotational transitions of $C^{18}O$, and the fractional CO abundance, from the G1 model at 10^6 years.

5.4.3 HCN, $H^{13}CN$ and $HC^{15}N$

The HCN emission modelled by RATRAN is extremely optically thick, as seen in Table 5.2. Figures 5.7, 5.8 and 5.9 show the intensity produced by the J=1-0, J=3-2 and J=4-3 transitions of HCN from model G1 at 10^4, 10^5 and 10^6 years respectively. Figure 5.7 shows that at 10^4 years, the intensity produced by these three transitions is very high. The highest peak intensity is seen for the J=1-0 transition (182 K km s^{-1}), closely followed by the J=3-2 transition (181 K km s^{-1}), and then the J=4-3 transition (173 K km s^{-1}). The fractional HCN abundance abundance at 10^4 years is seen in Figure 5.13(d). It can be seen that the fractional abundance falls sharply at a radius of 0.07pc in the hot core. This is reflected in the intensity profiles for each transition, as the intensity begins to drop more rapidly around a projected radius of 0.07pc. Even at the outer edge of the hot core, the HCN intensity is high at 10^4 years. Each HCN transition has an intensity greater than 120 K km s^{-1} at this point.

Figure 5.8 shows the intensity profiles for the same rotational HCN transitions in model G1 at 10^5 years. The peak values for each transition are almost exactly the same. At the outer edge of the hot core, the intensity has increased for each transition. This is caused by an increase in the fractional HCN abundance at the edge of the hot core between 10^4 and 10^5 years, which can be seen by comparing Figure 5.13(d) with Figure 5.14(d).

Figure 5.9 shows the same HCN transitions at 10^6 years, using results from the G1 model. As in ^{13}CS and $C^{18}O$, self-absorption has started to occur for all the rotational transitions at this time. The extent of the self-absorption is small, and is roughly equal at each transition. The intensity profile for each transition at this time is almost flat-topped. The intensity for each transition has actually increased between 10^5 and 10^6 years, as can be seen at the outer edge of the hot core. The self-absorption effects mask the intensity increase in the centre of the hot core, resulting in the flat-topped profile.

Throughout the times examined, the highest intensities are seen at J=1-0 and J=3-2, although the intensities seen at J=4-3 are of a similar magnitude. The peak intensities do not change much with time. The intensity seen at the outer hot core edges does

increase with time, in line with the fractional HCN abundance in the G1 model. HCN could be used as a tracer of hot cores in general, as strong emission is seen throughout the whole time period. HCN emission could be used to estimate the age of a hot core, to some extent. If the HCN intensity drops off fairly rapidly at the outer hot core edge, the hot core could be said to be young ($\sim 10^4$ years). If the HCN intensity drops off smoothly at the outer edge, the hot core could be identified as being older ($\sim 10^5$ years). A flat-topped intensity profile could indicate a highly evolved hot core ($\sim 10^6$ years). However, the similar intensities seen for all rotational transitions at all the times examined could make it difficult to estimate a hot core's age.

Figures 5.10–5.15 show some rotational transitions of $H^{13}CN$ and $HC^{15}N$ at 10^4, 10^5 and 10^6 years. Table 5.2 shows that these species are optically thick at all times examined, in model G1. The patterns of behaviour seen are the same as those seen for HCN, although the peak intensities are somewhat lower for $H^{13}CN$ (around 140 K km s^{-1}), and lower still for $HC^{15}N$ (around 120 K km s^{-1}). These isotopologues could be used as hot core tracers, as they show strong emission across the whole hot core radius at all times examined. However, this emission comes from the outer shells, and so these species cannot be used to probe the internal hot core structure.

5.4.4 $H^{15}NC$ and $HN^{13}C$

Table 5.2 shows that the RATRAN modelling of HNC produced extremely high opacities – for this reason, the HNC result graphs are not included in this thesis. The intensities from the rotational transitions of $H^{15}NC$ (an isotopologue of HNC) from model G1, are seen in Figures 5.16, 5.17 and 5.18. High intensities are seen at each rotational transition analysed, namely J=1-0, J=3-2 and J=4-3. The highest peak intensity, 120 K km s^{-1}, is seen for J=3-2. The intensity is reduced with increasing projected radius/offset, although the intensities seen at the outer edge of the hot core are still high for each transition (between 80 and 100 K km s^{-1}).

There is little difference between the intensities at 10^4 and 10^5 years, as seen in Fig-

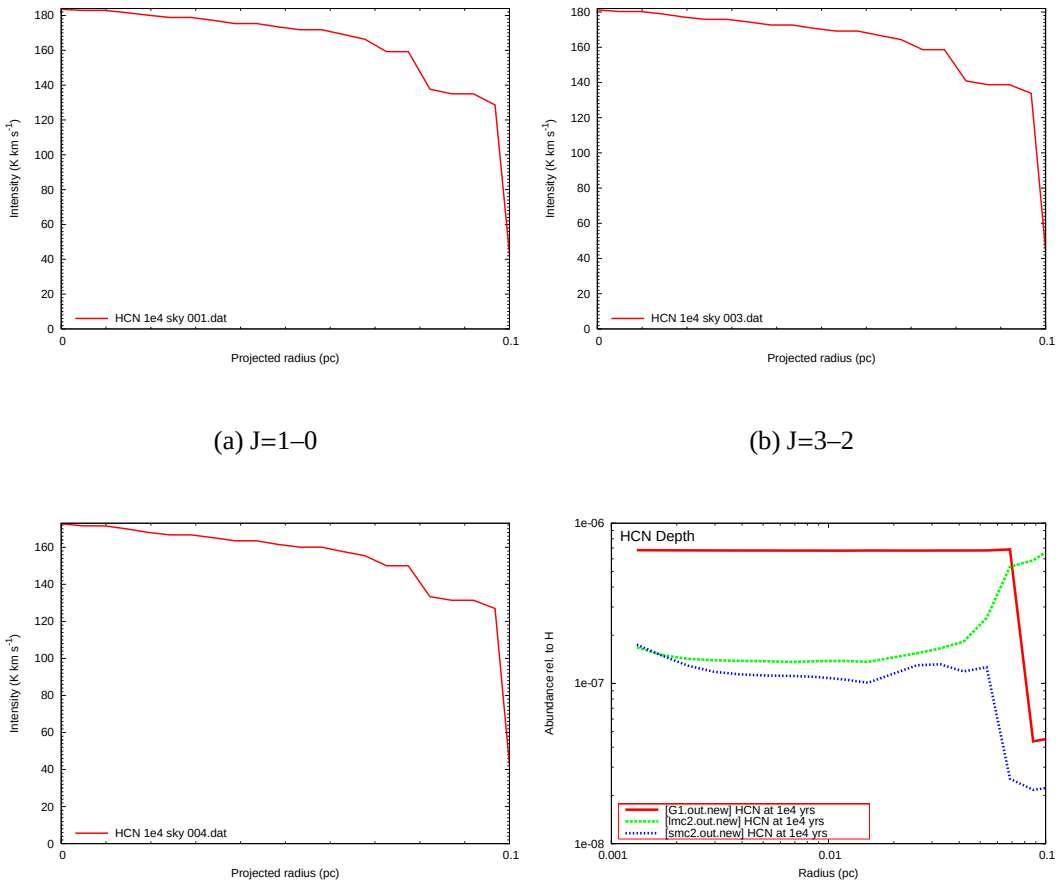

(a) J=1–0

(b) J=3–2

(c) J=4–3

(d) HCN fractional abundance

Figure 5.7: The intensity of some observable rotational transitions of HCN, and the fractional HCN abundance, from the G1 model at 10^4 years.

ures 5.16 and 5.17. This is caused by the almost identical fractional HNC abundances across the hot core radius at 10^4 and 10^5 years, as seen in Figures 5.19(d) and 5.20(d). At 10^6 years, self-absorption of the rotational $H^{15}NC$ transition lines occurs, as seen in Figure 5.18. The intensities at this time have increased, for each transition, as can be seen at the outer hot core edge. The fractional HNC abundance has increased between 10^5 and 10^6 years, for most of the hot core radius, as can be seen by comparing Figure 5.20(d) with Figure 5.21(d). This accounts for the increased $H^{15}NC$ intensity. A similar amount of self-absorption is seen for each transition.

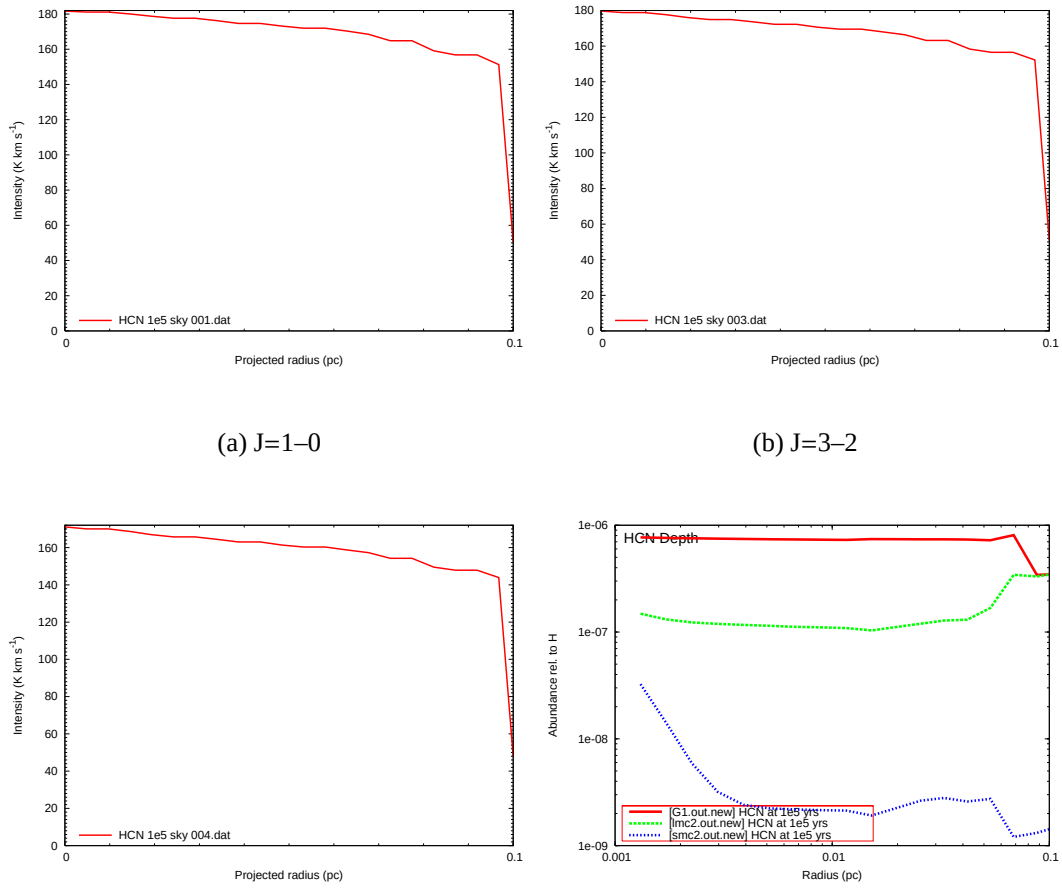

(a) J=1–0

(b) J=3–2

(c) J=4–3

(d) HCN fractional abundance

Figure 5.8: The intensity of some observable rotational transitions of HCN, and the fractional HCN abundance, from the G1 model at 10^5 years.

Overall, the rotational $H^{15}NC$ transitions could not be used to estimate the age of a hot core to a great degree of accuracy. If self-absorbed line profiles were observed, it would indicate that the hot core had an evolved chemistry and was likely to be at least 10^6 years old. At 10^4 and 10^5 years, the line profiles are so similar that they could not be differentiated from one another, and so a hot core of either age would appear the same when observed in $H^{15}NC$.

Another HNC isotopologue, $HN^{13}C$, was also modelled using RATRAN. The results are shown in Figures 5.19, 5.20 and 5.21. The results were similar to those seen for

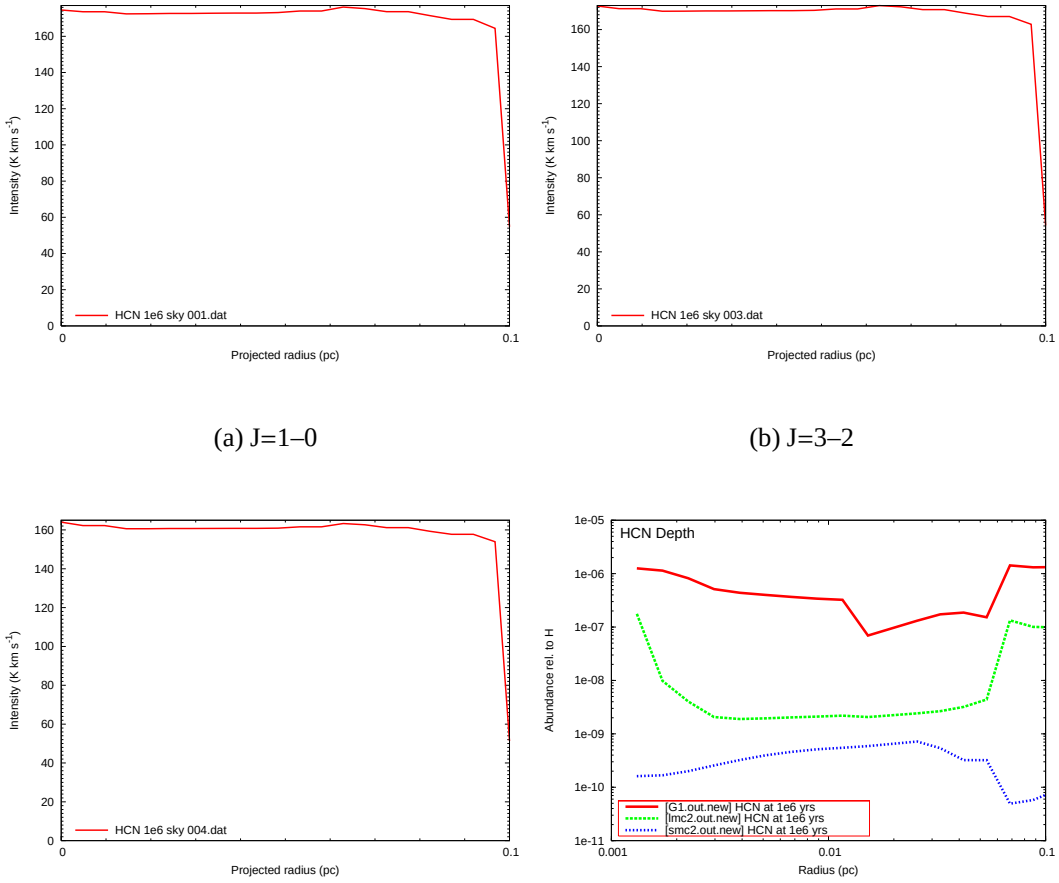

(a) J=1–0

(b) J=3–2

(c) J=4–3

(d) HCN fractional abundance

Figure 5.9: The intensity of some observable rotational transitions of HCN, and the fractional HCN abundance, from the G1 model at 10^6 years.

$H^{15}NC$, in terms of behaviour. The intensities seen were slightly higher, as $HN^{13}C$ is more abundant than $H^{15}NC$. The high integrated intensities of HNC, $H^{15}NC$ and $HN^{13}C$ for all transitions at all times examined, means that these species could be used as general tracers of hot cores. Like HCN and its isotopologues, these species trace the gas in the outer shells of the hot core, and so does not probe the inner regions.

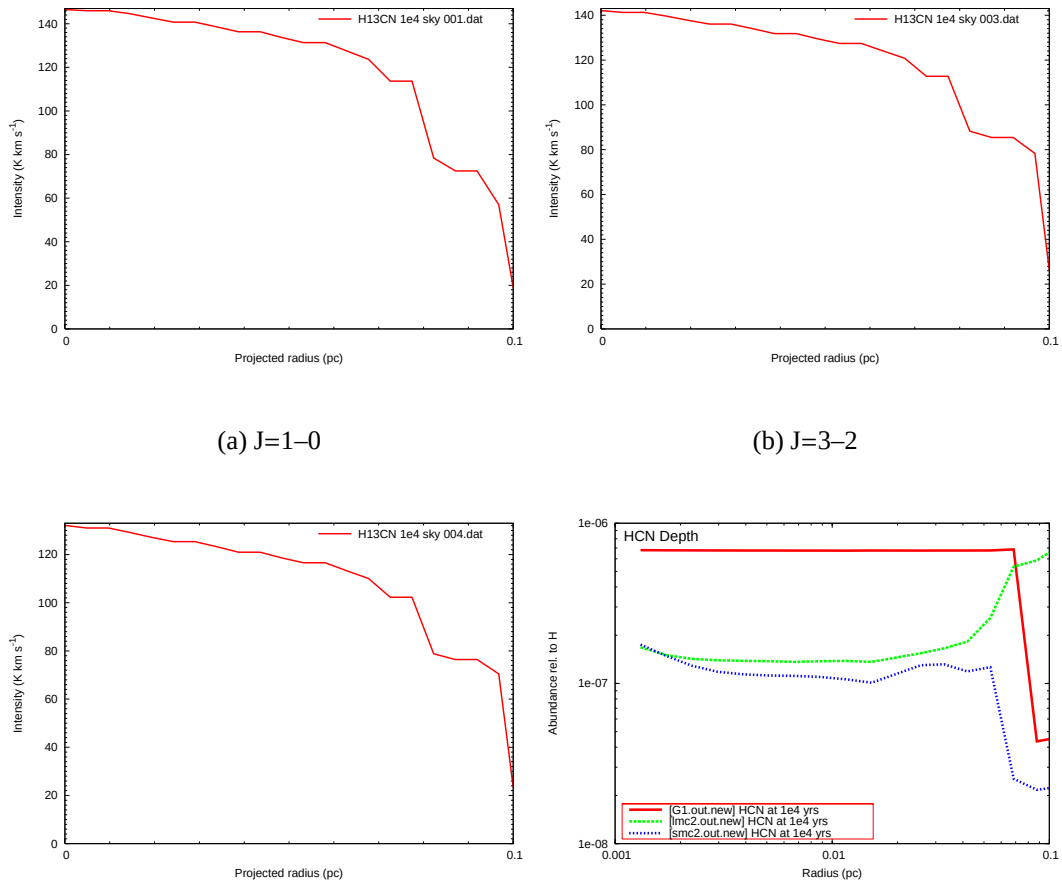

(a) J=1–0 (b) J=3–2

(c) J=4–3 (d) HCN fractional abundance

Figure 5.10: The intensity of some observable rotational transitions of $H^{13}CN$, and the fractional HCN abundance, from the G1 model at 10^4 years.

5.4.5 HNCO

The intensities of some RATRAN modelled hyperfine HNCO transitions are shown in Figures 5.22, 5.23 and 5.24. The transitions examined are 4(0,4)-3(0,3), 4(1,3)-3(1,2) and 5(2,4)-4(2,3). These transitions were chosen as they are at observable frequencies, as shown in Table 5.1.

Figure 5.22 shows the modelled intensities at 10^4 years. The highest peak intensity of 9.4 K km s^{-1} is seen at the transition 4(0,4)-3(0,3). A very low peak intensity of less than 0.2 K km s^{-1} is seen for 4(1,3)-3(1,2) - this may not be observable. No emission

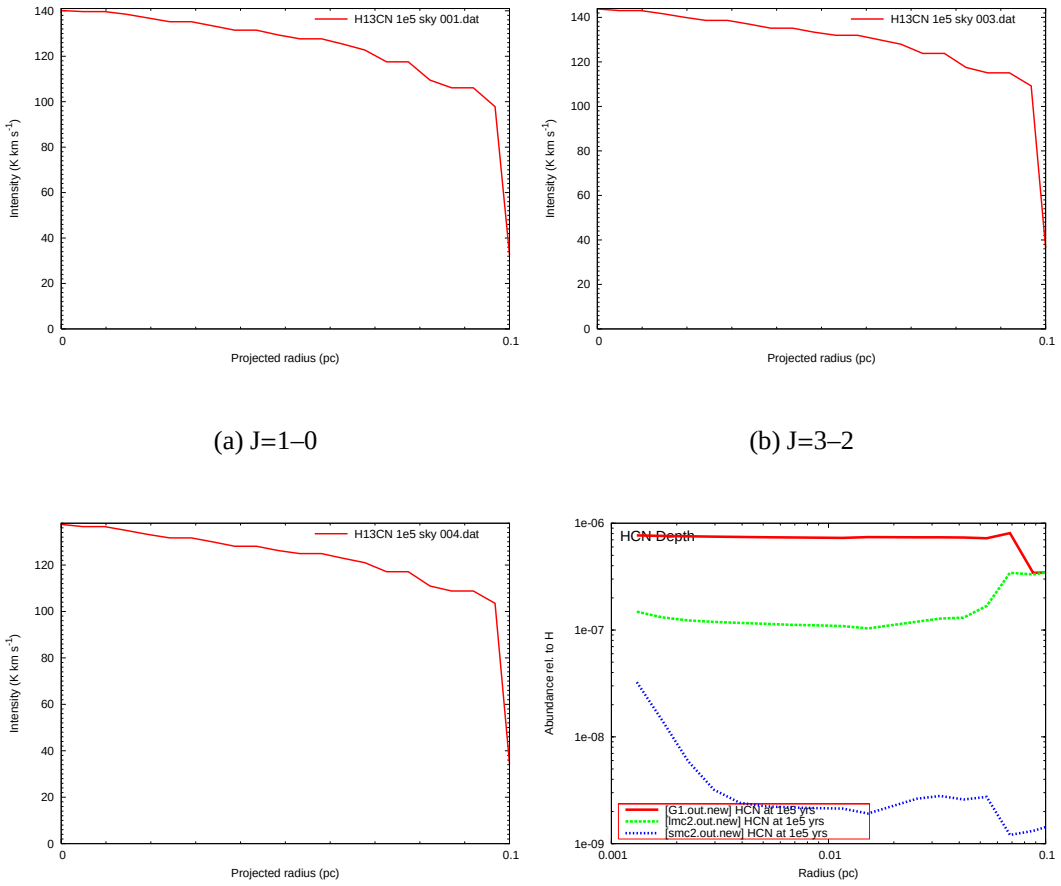

(a) J=1–0

(b) J=3–2

(c) J=4–3

(d) HCN fractional abundance

Figure 5.11: The intensity of some observable rotational transitions of $H^{13}CN$, and the fractional HCN abundance, from the G1 model at 10^5 years.

is seen for 5(2,4)-4(2,3). For 4(0,4)-3(0,3) and 4(1,3)-3(1,2), the emission is seen for a very small offset/projected radius (0.045pc and 0.02pc respectively). These rotational HNCO transitions therefore only trace the very hot, dense gas in the centre of the hot core. Figure 5.22(d) shows that a high fractional HNCO abundance is seen across the inner hot core regions, up to a radius of 0.015pc. The fractional abundance then drops, but remains relatively high up to a radius of 0.04pc. This is the region traced by the 4(0,4)-3(0,3) and 4(1,3)-3(1,2) transitions.

Figure 5.23 shows the modelled rotational HNCO transitions from model G1 at 10^5

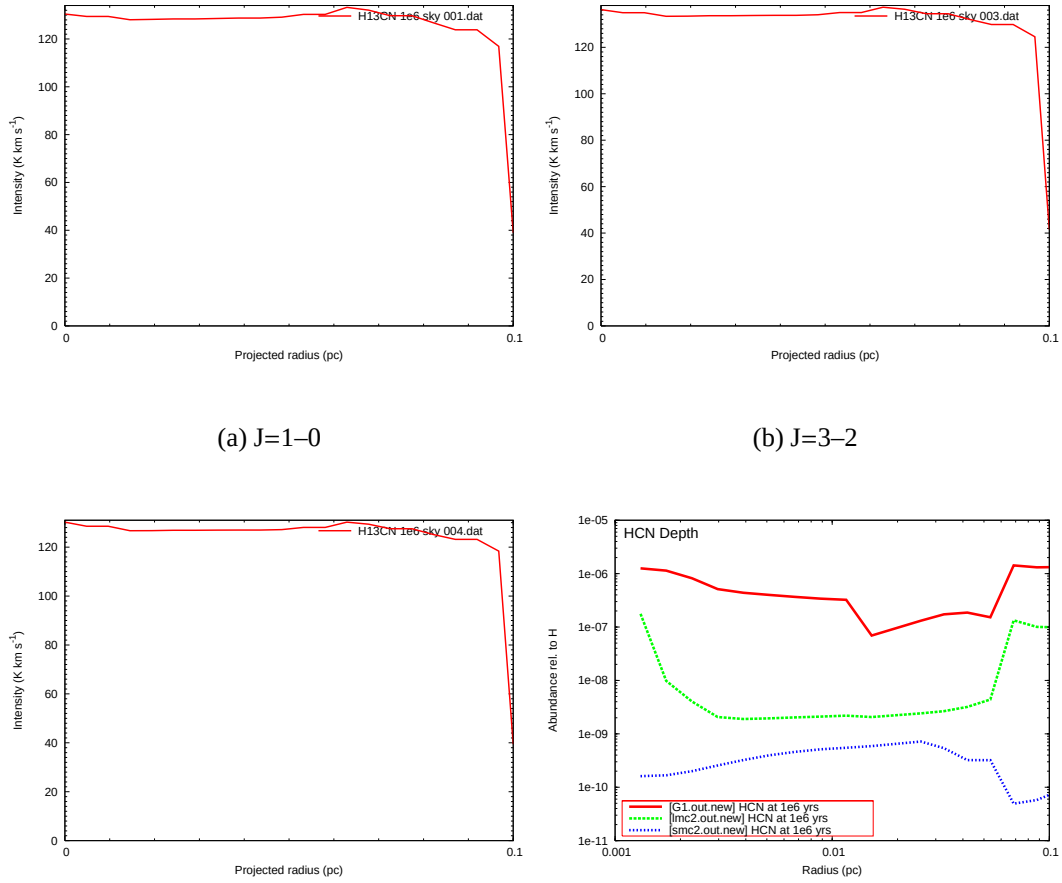

(a) J=1–0 (b) J=3–2

(c) J=4–3 (d) HCN fractional abundance

Figure 5.12: The intensity of some observable rotational transitions of $H^{13}CN$, and the fractional HCN abundance, from the G1 model at 10^6 years.

years. The peak intensities for 4(0,4)-3(0,3) and 4(1,3)-3(1,2) have increased, by factors of 7 and 39 respectively, and the emission is now visible across a larger projected radius/offset. The highest peak intensity is still seen at 4(0,4)-3(0,3). The fractional HNCO abundance in the inner hot core regions has increased by around one order of magnitude over this time period, as seen by comparing Figure 5.22(d) with Figure 5.23(d). The amount of emission has been redistributed between the different rotational transitions at this time, as the opacity of the 4(0,4)-3(0,3) transition has increased since 10^4 years, from 0.05 mag to 0.39 mag. This is why the 4(1,3)-3(1,2)

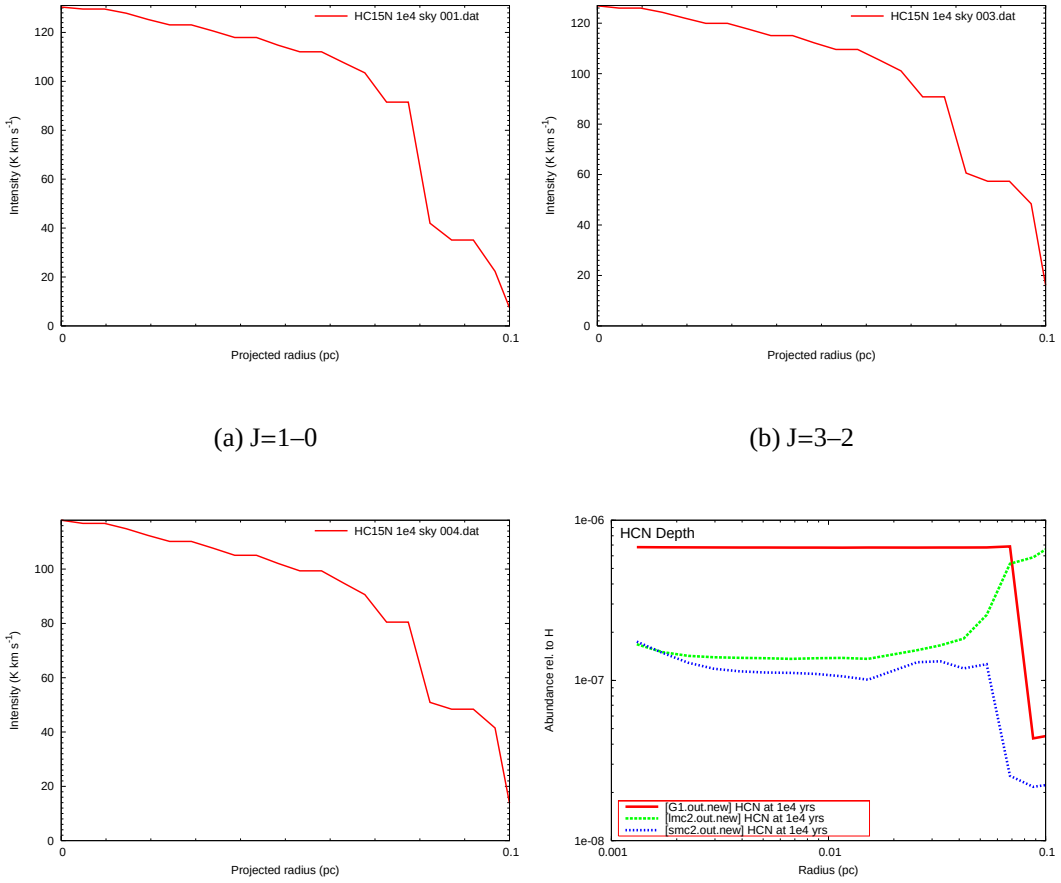

(a) J=1–0

(b) J=3–2

(c) J=4–3

(d) HCN fractional abundance

Figure 5.13: The intensity of some observable rotational transitions of $HC^{15}N$, and the fractional HCN abundance, from the G1 model at 10^4 years.

transition intensity has increased so much more than the 4(0,4)-3(0,3) intensity. As the optical depths of the lower rotational transition lines increase, the emission becomes redistributed, and so comparatively more emission is seen from the higher rotational transitions. Hence, a larger proportional increase is seen in the intensity of the 4(1,3)-3(1,2) line between 10^4 and 10^5 years, than the 4(0,4)-3(0,3) line.

Figure 5.24 shows the G1 modelled rotational HNCO transitions at 10^6 years. The peak intensities have decreased at this time. The fractional HNCO abundance, as seen in Figure 5.24(d), has increased in the inner regions of the hot core at this time. The de-

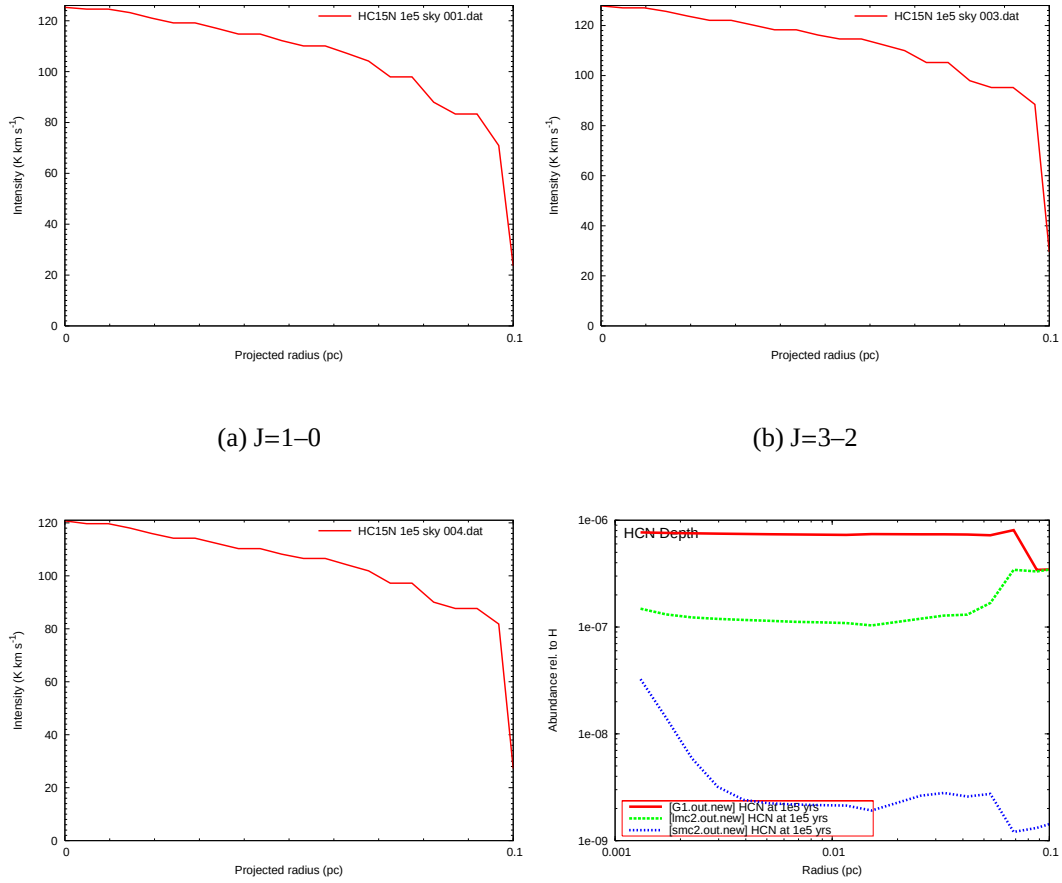

(a) J=1–0 (b) J=3–2

(c) J=4–3 (d) HCN fractional abundance

Figure 5.14: The intensity of some observable rotational transitions of $HC^{15}N$, and the fractional HCN abundance, from the G1 model at 10^5 years.

crease in intensity is caused by a further redistribution of the emission. More emission is coming from higher rotational transition lines, which have a lower optical depth. Overall, HNCO is not a very useful tracer of the age of a hot core. The emission seen at 10^5 and 10^6 years is not sufficiently different to distinguish between the two times. However, a very low intensity could indicate a very young hot core. More importantly, HNCO appears to be a good tracer of the hottest, densest gas in the centre of a hot core, at all times examined. HNCO could therefore be used as a dense/hot gas tracer.

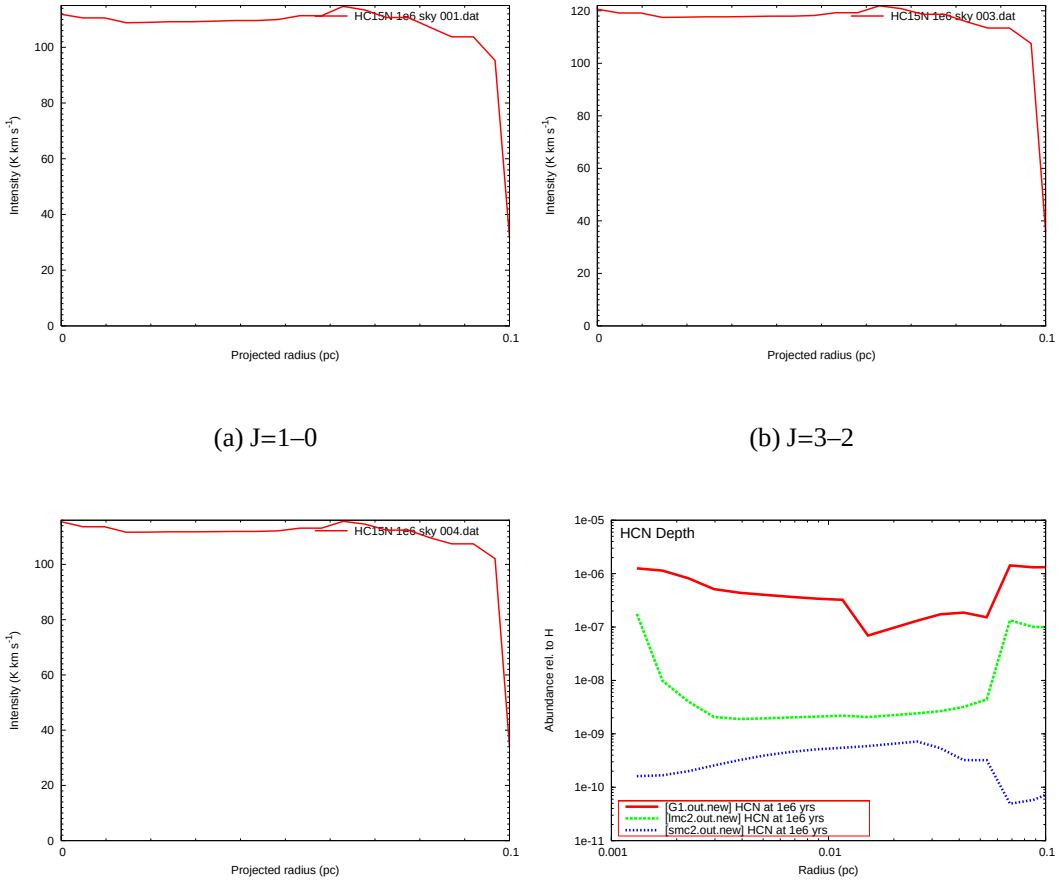

(a) J=1–0

(b) J=3–2

(c) J=4–3

(d) HCN fractional abundance

Figure 5.15: The intensity of some observable rotational transitions of $HC^{15}N$, and the fractional HCN abundance, from the G1 model at 10^6 years.

5.4.6 NH_3

Figures 5.25 and 5.26 shows some observable inversion transitions of para-NH_3. Table 5.2 shows that the opacity for this species is very high, particularly for the metastable transitions 1(1,1)–1(1,0), 2(2,1)–2(2,0), 4(4,1)–4(4,0) and 5(5,1)–5(5,0). For all the transitions examined, the integrated intensity is very high, with peak values in the range 190–235 K km s^{-1}. All the transitions also show extended emission, with a high intensity across the whole hot core. Figure 5.25(f) shows that the fractional NH_3 abundance in model G1 at 10^4 years is consistently high across the whole hot core

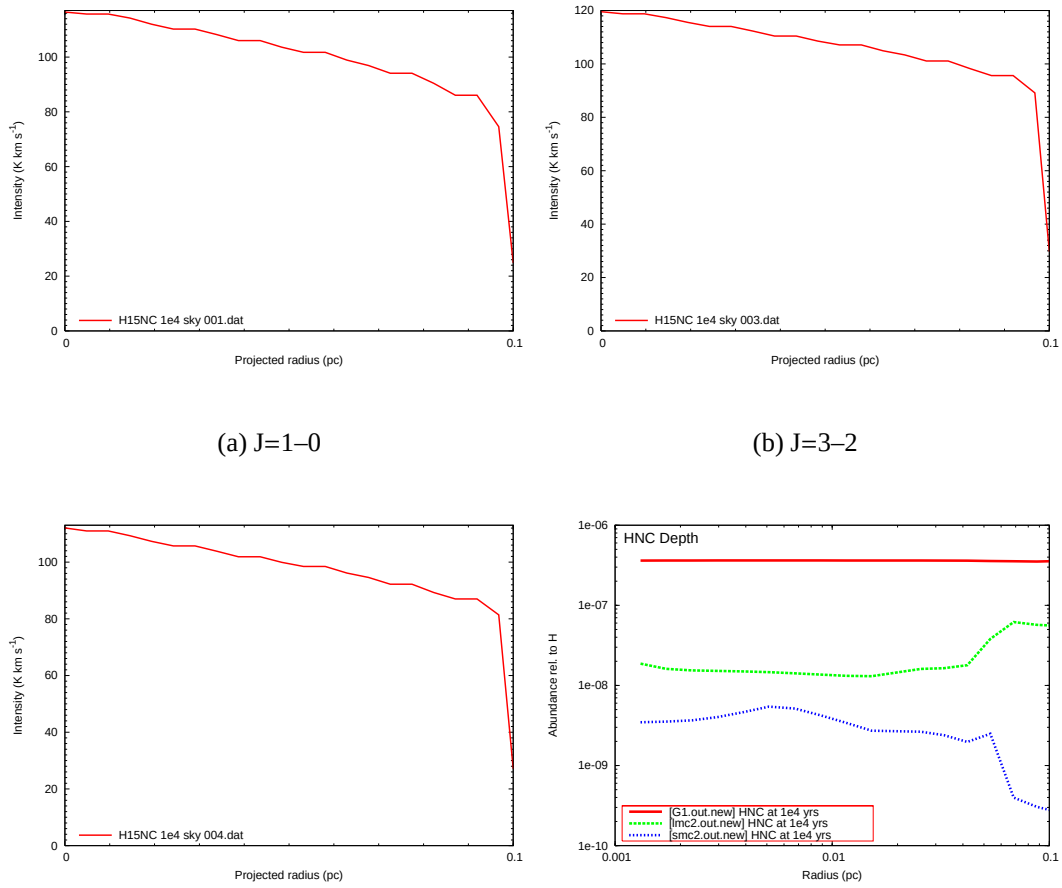

(a) J=1–0 (b) J=3–2

(c) J=4–3 (d) HNC fractional abundance

Figure 5.16: The intensity of some observable rotational transitions of $H^{15}NC$, and the fractional HNC abundance, from the G1 model at 10^4 years.

radius. This causes the strong, extended emission seen from the inversion transitions. Figures 5.27 and 5.28 show the same transitions at 10^5 years. The peak intensities are extremely similar to those seen at 10^4 years for all transitions. The fractional NH_3 abundance is very similar in model G1 at 10^4 and 10^5 years, as can be seen by comparing Figure 5.25(f) with Figure 5.27(f). Although the fractional abundance is slightly lower at 10^5 years, the integrated intensity values do not reflect this, as the NH_3 has a very high opacity at both 10^4 and 10^5 years, as seen in Table 5.2. The high opacity means that the emission is optically thick, and so even though the fractional NH_3

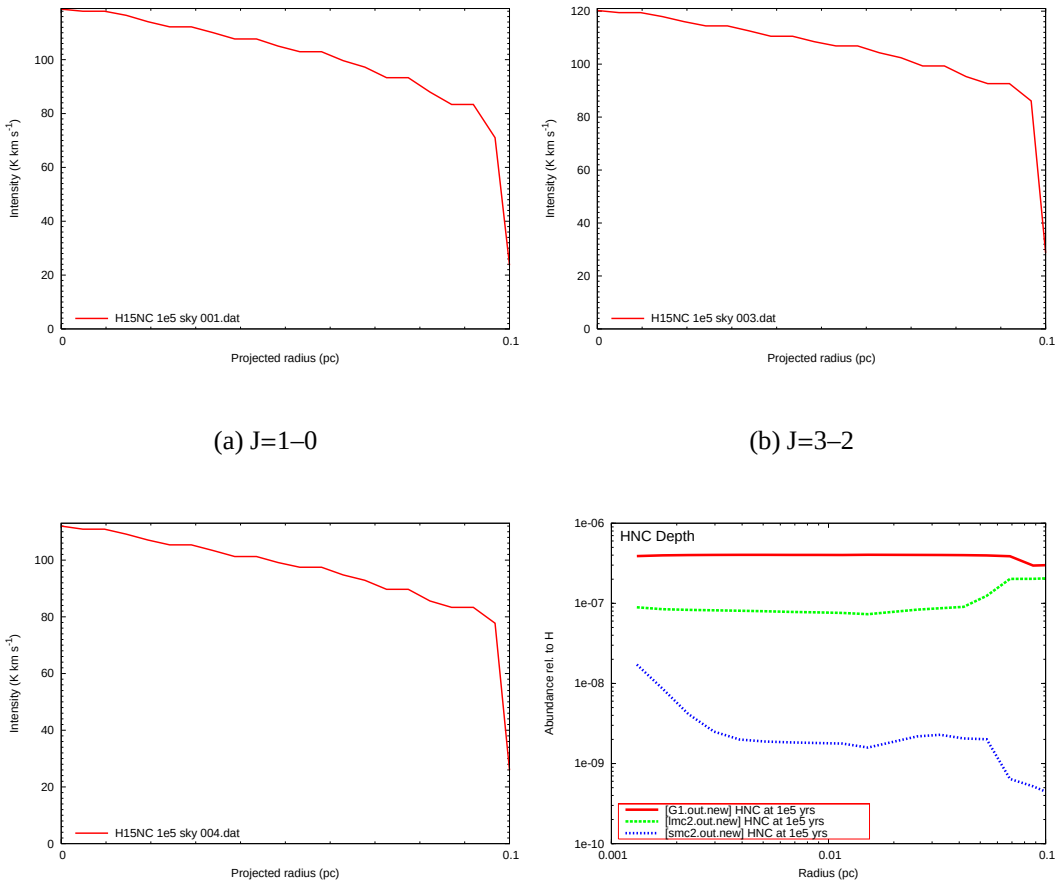

(a) J=1–0

(b) J=3–2

(c) J=4–3

(d) HNC fractional abundance

Figure 5.17: The intensity of some observable rotational transitions of $H^{15}NC$, and the fractional HNC abundance, from the G1 model at 10^5 years.

abundance is reduced, this is not reflected in the integrated intensity, as the emission is undergoing self-absorption at 10^4 and 10^5 years.

Figures 5.29 and 5.30 show the para-NH_3 inversion transitions at 10^6 years. It can be seen in Table 5.2 that at 10^6 years, the opacity of the NH_3 emission has considerably reduced. The most optically thin lines are 3(1,1)-3(1,0) and 5(5,1)-5(5,0). The fractional NH_3 abundance at 10^6 years is much reduced in the intermediate shells, as seen in Figure 5.29(f). The metastable transitions, particularly 1(1,1)-1(1,0) and 2(2,1)-2(2,0), still have a high opacity at 10^6 years. As a function of projected radius, the intensity is

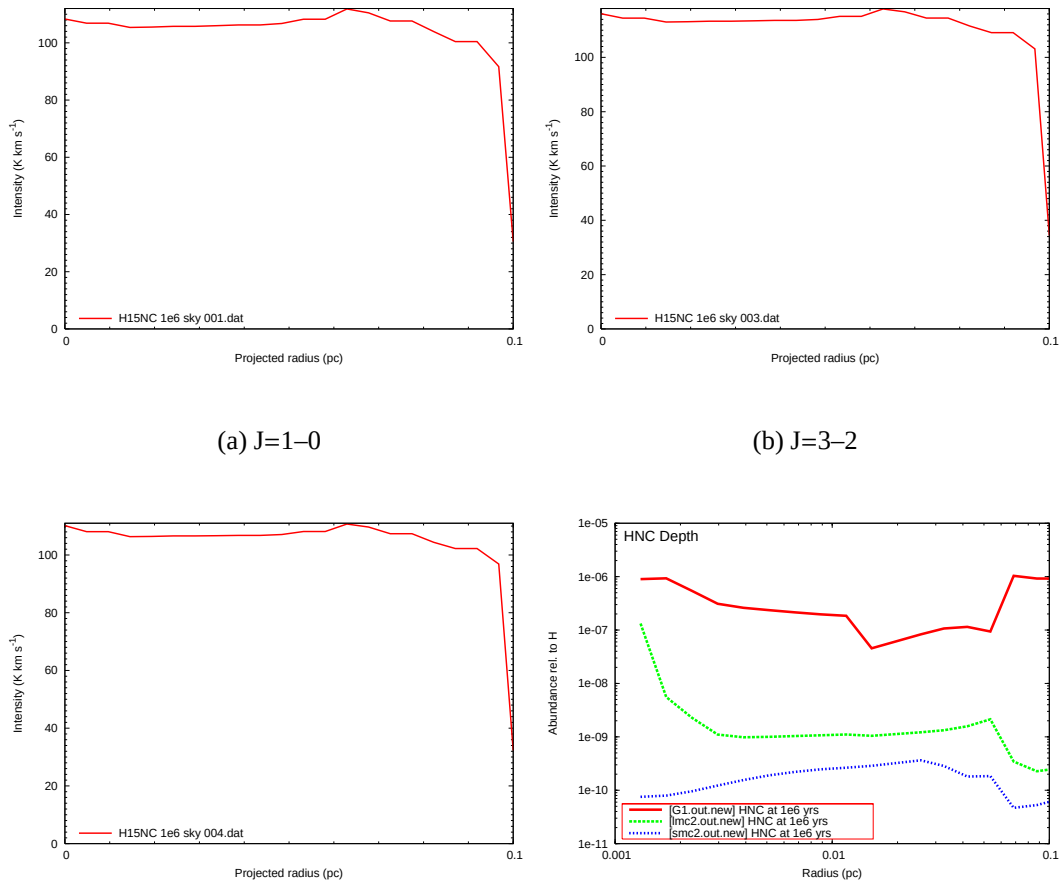

(a) J=1–0 (b) J=3–2

(c) J=4–3 (d) HNC fractional abundance

Figure 5.18: The intensity of some observable rotational transitions of $H^{15}NC$, and the fractional HNC abundance, from the G1 model at 10^6 years.

fairly constant for many of the transitions examined. These transitions are tracing the high fractional NH_3 abundance in the outer shells of the hot core, which can be seen in Figure 5.29(f). The inversion transitions 4(4,1)-4(4,0) and 5(5,1)-5(5,0) both trace gas with a higher temperature, as seen in Table 5.1, and so contain emission from more central regions of the hot core.

NH_3 is not a useful tracer of the age of a hot core. Ammonia is highly abundant in the hot core at all times examined, and so the emission produced has a consistently high intensity at all times. NH_3 could be used as a tracer of the outer regions of hot cores,

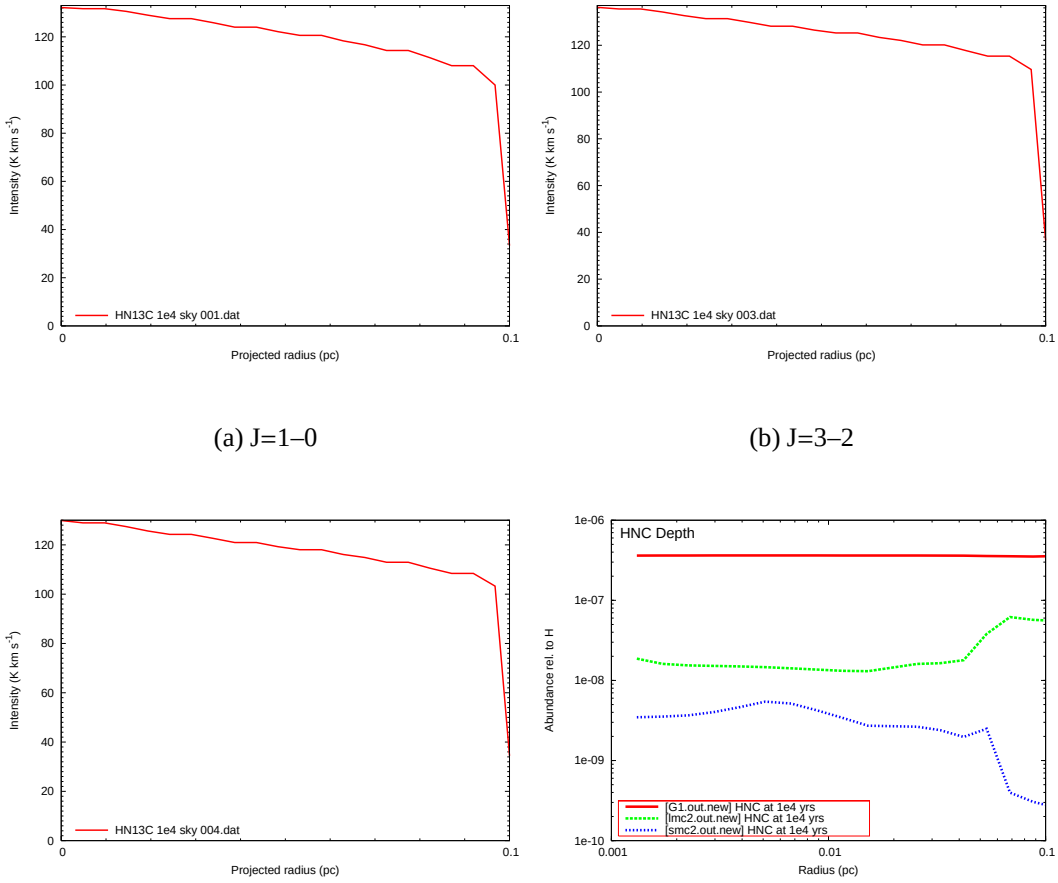

(a) J=1–0

(b) J=3–2

(c) J=4–3

(d) HNC fractional abundance

Figure 5.19: The intensity of some observable rotational transitions of $HN^{13}C$, and the fractional HNC abundance, from the G1 model at 10^4 years.

to determine the extent of the gas.

5.5 A comparison of the RATRAN outputs at varying metallicity

The species chosen for modelling were determined on the following bases:

1. They can be observed in hot cores

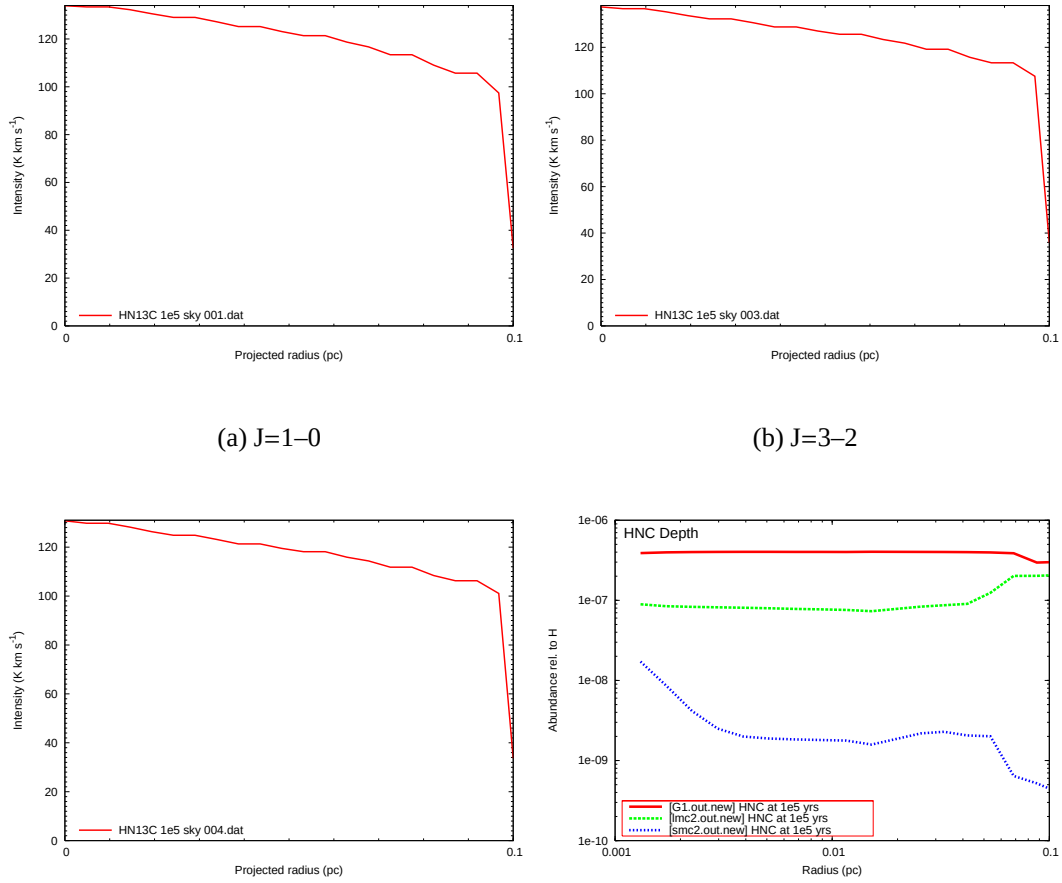

(a) J=1–0 (b) J=3–2

(c) J=4–3 (d) HNC fractional abundance

Figure 5.20: The intensity of some observable rotational transitions of $HN^{13}C$, and the fractional HNC abundance, from the G1 model at 10^5 years.

2. If possible, the lines were not too optically thick

3. It was possible to obtain observed estimates for the isotopic ratios (e.g. $^{13}C/^{12}C$) in the LMC and SMC

It was necessary to model isotopologues of common species, as their non-isotopic counterparts were extremely optically thick. The isotopic ratios used are shown in Table 5.3. Tables 5.4, 5.5 and 5.6 show the peak optical depth for the transitions and species examined, at 10^4, 10^5 and 10^6 years respectively.

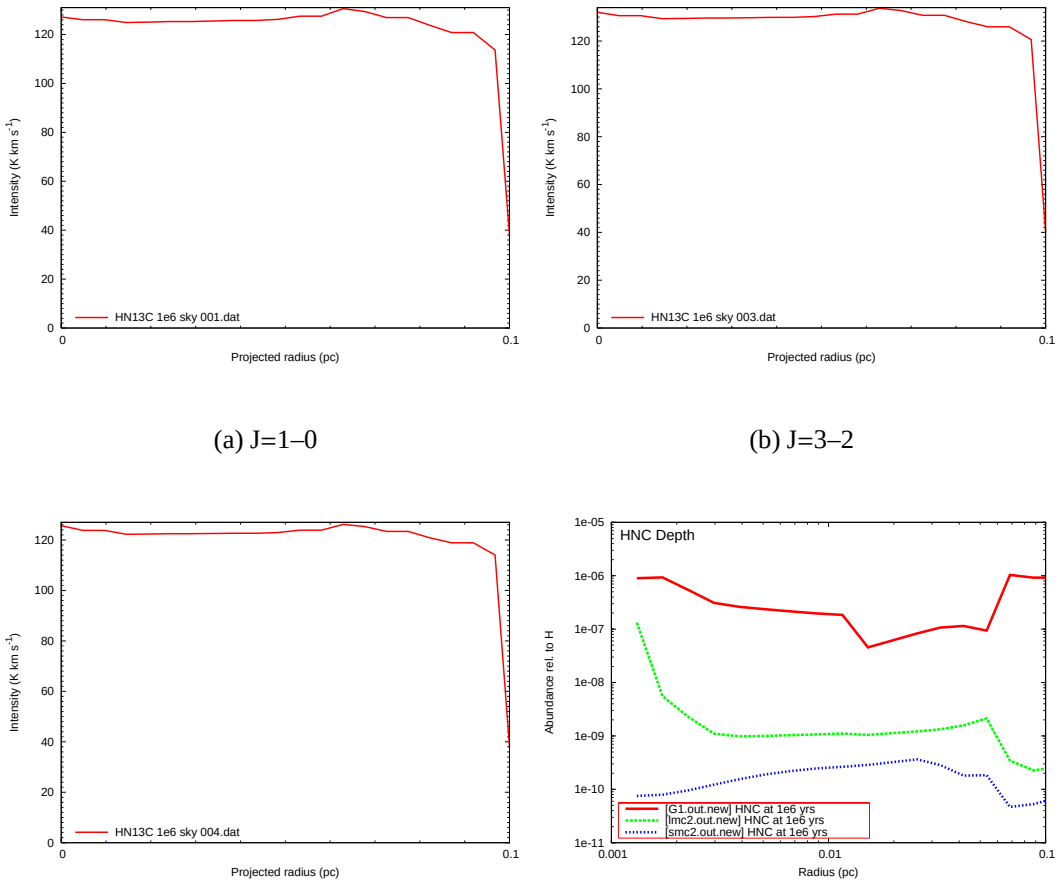

(a) J=1–0 (b) J=3–2

(c) J=4–3 (d) HNC fractional abundance

Figure 5.21: The intensity of some observable rotational transitions of $HN^{13}C$, and the fractional HNC abundance, from the G1 model at 10^6 years.

	G1	**L2**	**S2**
$^{12}C/^{13}C$	76[1]	49[2]	50[3]
$^{16}O/^{18}O$	430[4]	2000[5]	-

Table 5.3: Isotopic ratios used in the RATRAN modelling of G1, L2 and S2. [1] Stahl et al. (2008); [2] Wang et al. (2009a); [3] Chin et al. (1998); [4] Polehampton et al. (2005); [5] Wang et al. (2009b).

10^4 years	**Opacities**		
	G1	**L2**	**S2**
^{13}CS			
1 – 0	0.02	0.08	0.10
2 – 1	0.05	0.30	0.35
3 – 2	0.09	0.61	0.71
5 – 4	0.20	1.16	1.38
7 – 6	0.26	1.23	1.49
C^{18}O			
1 – 0	0.05	0.05	-
2 – 1	0.16	0.16	-
3 – 2	0.29	0.27	-
4 – 3	0.42	0.38	-
5 – 4	0.53	0.48	-
H^{13}CN			
1 – 0	42.55	43.57	10.07
3 – 2	267.20	254.60	63.87
4 – 3	348.60	311.60	83.83
HN^{13}C			
1 – 0	33.36	5.73	0.19
3 – 2	199.90	33.18	2.33
4 – 3	250.70	39.73	3.17
HNCO			
4(0,4) – 3(0,3)	0.05	0.02	0.02
4(1,3) – 3(1,2)	0.02	0.02	0.02
5(2,4) – 4(2,3)	0.03	0.03	0.03
NH$_3$			
3(1,1) – 3(1,0)	945.98	94.55	9.11
3(2,1) – 3(2,0)	5282.00	515.00	46.69
2(1,1) – 2(1,0)	8101.00	709.80	53.49
1(1,1) – 1(1,0)	55320.00	4379.00	275.10
2(2,1) – 2(2,0)	47490.00	4045.00	287.80
4(4,1) – 4(4,0)	6751.00	697.40	66.36
5(5,1) – 5(5,0)	1847.00	198.40	19.38

Table 5.4: Opacities at 10^4 years

10^5 years	**Opacities**		
	G1	**L2**	**S2**
^{13}CS			
1 – 0	0.06	0.07	0.03
2 – 1	0.19	0.25	0.07
3 – 2	0.39	0.50	0.14
5 – 4	0.84	0.97	0.28
7 – 6	1.07	1.04	0.31
C^{18}O			
1 – 0	0.14	0.09	-
2 – 1	0.45	0.28	-
3 – 2	0.79	0.48	-
4 – 3	1.03	0.62	-
5 – 4	1.14	0.71	-
H^{13}CN			
1 – 0	52.73	27.86	0.22
3 – 2	326.30	164.00	2.33
4 – 3	420.70	201.90	3.08
HN^{13}C			
1 – 0	34.75	20.56	0.17
3 – 2	209.60	118.90	2.03
4 – 3	264.40	144.10	2.68
HNCO			
4(0,4) – 3(0,3)	0.39	0.03	0.02
4(1,3) – 3(1,2)	0.02	0.02	0.02
5(2,4) – 4(2,3)	0.03	0.03	0.03
NH$_3$			
3(1,1) – 3(1,0)	750.90	40.97	0.02
3(2,1) – 3(2,0)	4191.00	218.30	0.12
2(1,1) – 2(1,0)	6417.00	274.20	0.50
1(1,1) – 1(1,0)	43760.00	1533.00	3.23
2(2,1) – 2(2,0)	37610.00	1521.00	2.14
4(4,1) – 4(4,0)	5363.00	308.70	0.18
5(5,1) – 5(5,0)	1466.00	90.41	0.04

Table 5.5: Opacities at 10^5 years

10^6 years	Opacities		
	G1	L2	S2
^{13}CS			
1 – 0	0.10	0.03	0.01
2 – 1	0.38	0.08	0.03
3 – 2	0.75	0.16	0.05
5 – 4	1.38	0.32	0.10
7 – 6	1.41	0.34	0.14
C^{18}O			
1 – 0	0.83	0.14	-
2 – 1	2.78	0.45	-
3 – 2	4.74	0.76	-
4 – 3	5.78	0.95	-
5 – 4	5.64	0.99	-
H^{13}CN			
1 – 0	54.97	6.67	0.04
3 – 2	316.40	37.70	0.52
4 – 3	381.80	44.41	0.75
HN^{13}C			
1 – 0	44.24	0.12	0.03
3 – 2	248.10	1.55	0.40
4 – 3	292.70	2.05	0.55
HNCO			
4(0,4) – 3(0,3)	0.33	1.18	0.02
4(1,3) – 3(1,2)	0.02	0.03	0.02
5(2,4) – 4(2,3)	0.03	0.03	0.03
NH$_3$			
3(1,1) – 3(1,0)	25.39	0.04	0.02
3(2,1) – 3(2,0)	163.00	0.28	0.11
2(1,1) – 2(1,0)	426.40	0.66	0.48
1(1,1) – 1(1,0)	4028.00	3.26	2.99
2(2,1) – 2(2,0)	2762.00	2.70	2.00
4(4,1) – 4(4,0)	128.10	0.34	0.18
5(5,1) – 5(5,0)	11.40	0.08	0.04

Table 5.6: Opacities at 10^6 years

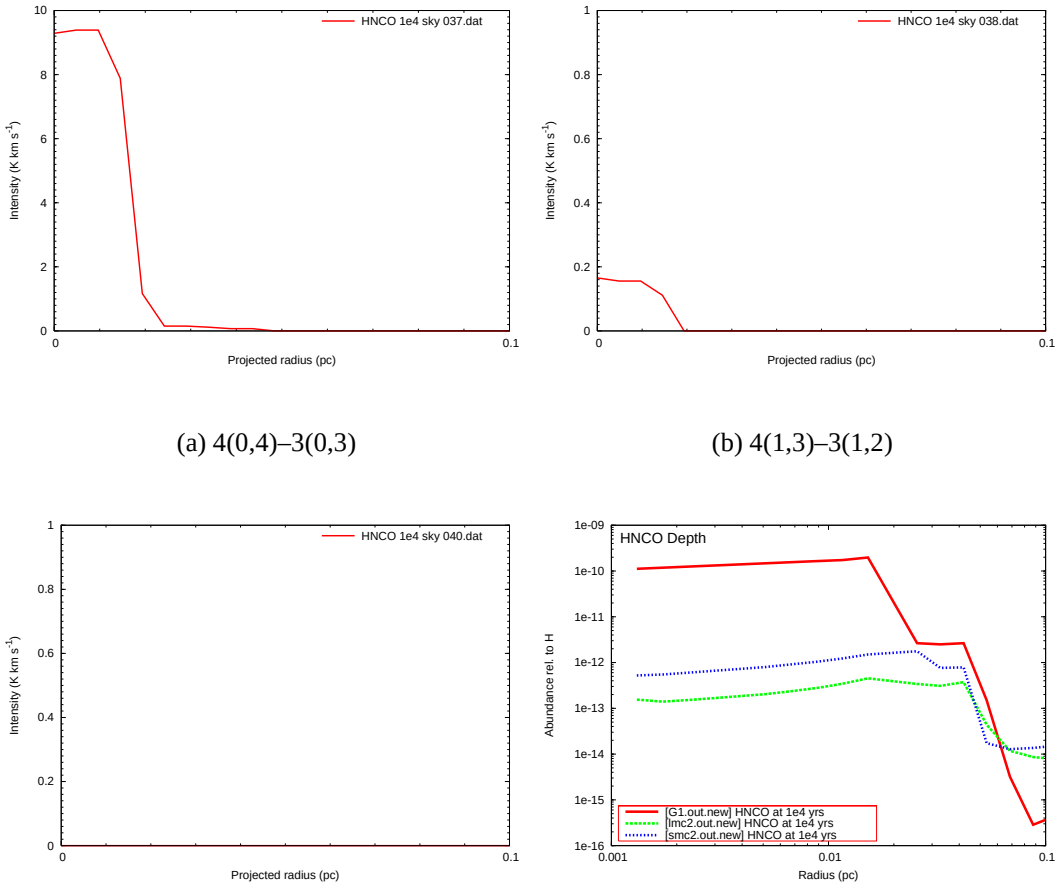

(a) 4(0,4)–3(0,3)

(b) 4(1,3)–3(1,2)

(c) 5(2,4)–4(2,3)

(d) HNCO fractional abundance

Figure 5.22: The intensity of some observable rotational transitions of HNCO, and the fractional HNCO abundance, from the G1 model at 10^4 years.

5.5.1 ^{13}CS

Figure 5.31 shows the comparative intensity of the rotational transitions J=1-0, J=2-1, J=3-2, J=5-4 and J=7-6 in models G1, L2 and S2, at 10^4 years. At this time, the intensity is much higher in models S2 and L2 than in model G1, for all transitions. The highest intensity is seen in the model S2 results, although similar intensities are seen from the L2 results. The lower intensity in model G1 is partly down to the ^{12}C/^{13}C ratio in the various galaxies, as seen in Table 5.3. In G1, a ^{12}C/^{13}C ratio of 76 was used to estimate the fractional ^{13}CS abundance, whereas in models L2 and S2, the ^{12}C/^{13}C ra-

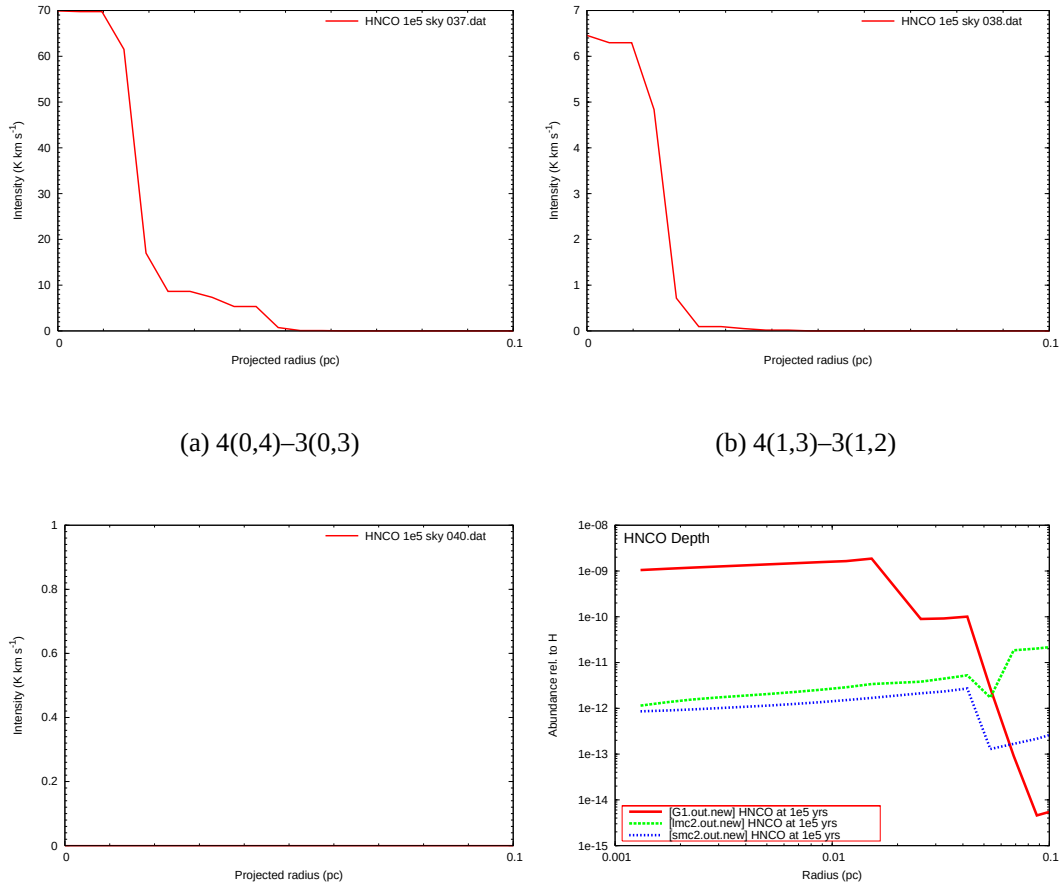

(a) 4(0,4)–3(0,3)

(b) 4(1,3)–3(1,2)

(c) 5(2,4)–4(2,3)

(d) HNCO fractional abundance

Figure 5.23: The intensity of some observable rotational transitions of HNCO, and the fractional HNCO abundance, from the G1 model at 10^5 years.

tios used were 49 and 50 respectively. The ratios used result in less ^{13}CS being present in model G1 compared with models L2 and S2, as a proportion of the total CS in the model at a particular time. Figure 5.31(f) shows the fractional CS abundance in each model at 10^4 years, as a function of distance. In the inner regions of the hot core, there is a much higher fractional CS abundance in model G1 than model S2, by over three orders of magnitude. However, in the mid-outer shells of the hot core, there is more CS in models S2 and L2 than in model G1. It is apparent that the intensity profiles for the rotational transitions are showing the emission from the outer shells rather than the

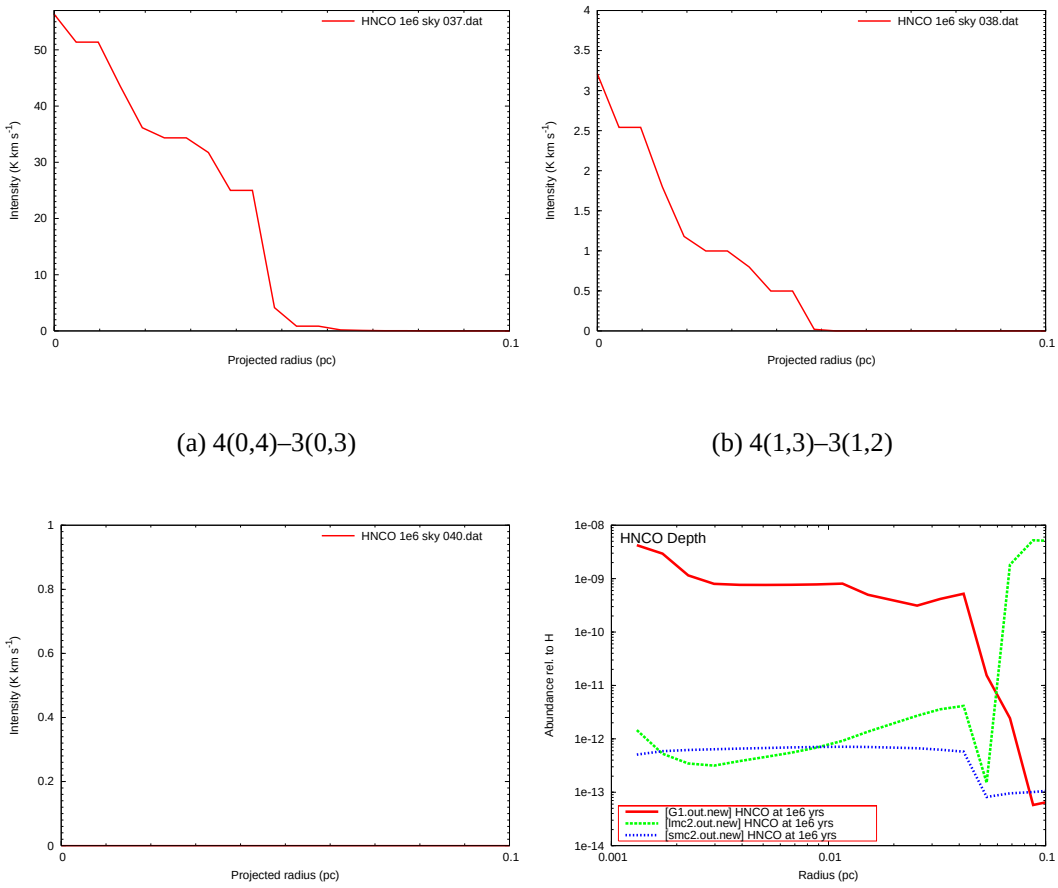

(a) 4(0,4)–3(0,3)

(b) 4(1,3)–3(1,2)

(c) 5(2,4)–4(2,3)

(d) HNCO fractional abundance

Figure 5.24: The intensity of some observable rotational transitions of HNCO, and the fractional HNCO abundance, from the G1 model at 10^6 years.

inner part of the hot core. The high intensity seen in models L2 and S2 comes from the shells which are between 0.02 and 0.07pc from the centre of the hot core, and the gas in the inner region of the hot core is not seen. This results in limb brightening of the emission profile, as the intensity peaks at a projected radius away from the centre of the hot core. This would appear as a brighter ring of intensity surrounding a less bright centre in an observation. If the observation had perfect resolution this ring could be seen. However, in a less resolved image the limb brightening effects may be smoothed away. Table 5.4 shows that the J=5-4 and J=7-6 transitions are slightly optically thick

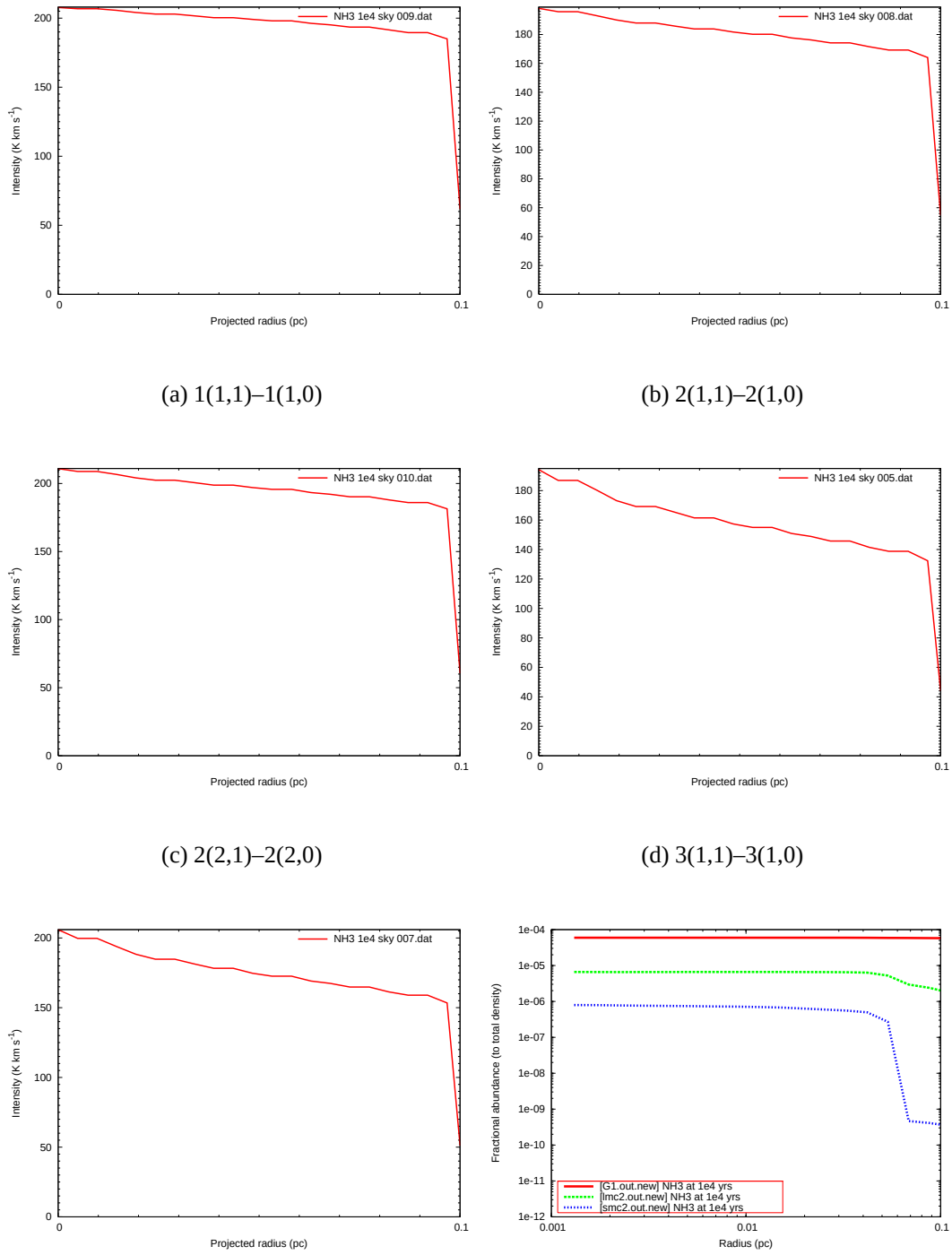

(a) 1(1,1)–1(1,0)

(b) 2(1,1)–2(1,0)

(c) 2(2,1)–2(2,0)

(d) 3(1,1)–3(1,0)

(e) 3(2,1)–3(2,0)

(f) NH_3 fractional abundance

Figure 5.25: The intensity of some observable inversion transitions of NH_3, and the fractional NH_3 abundance, from model G1 at 10^4 years.

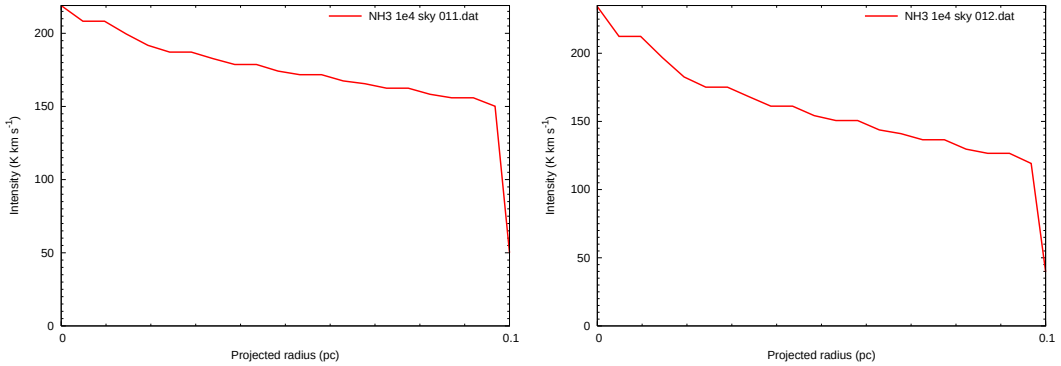

(a) 4(4,1)–4(4,0) (b) 5(5,1)–5(5,0)

Figure 5.26: The intensity of some more observable inversion transitions of NH_3, and the fractional NH_3 abundance, from models G1, L2 and S2 at 10^4 years.

in models L2 and S2. All of the transitions from model G1 are optically thin. The intensity produced by the model G1 results is much lower than the other models. The transitions with the highest intensities are J=5-4 and J=7-6 in all three models. The peak intensities for these transitions are ~15 K km s^{-1} in G1, 50-60 K km s^{-1} in L2 and 60-70 K km s^{-1} in S2.

Figure 5.32 shows the same transitions for models G1, L2 and S2 at 10^5 years. The intensities from the S2 model results have dramatically decreased over the time period since 10^4 years, with a peak value of 14 K km s^{-1} seen for the most intense transition, a factor of five lower than that seen at 10^4 years. This corresponds to the drop in fractional CS abundance in the mid-outer shells of this model, as can be seen by comparing Figure 5.31(f) with Figure 5.32(f). At 10^4 years, the fractional CS abundance at a radius of 0.07pc is ~7×10^{-9}, whereas at 10^5 years this has dropped to 1×10^{-9} at the same radius. This factor of seven reduction in fractional CS abundance in the outer shells matches well with the reduction in peak intensity of J=5-4, which falls by a factor of five over this time period. The fractional CS abundance in the inner shells of the hot core has also decreased, although this has less of an effect on the intensity as the fractional abundance is very low at 10^4 and 10^5 years.

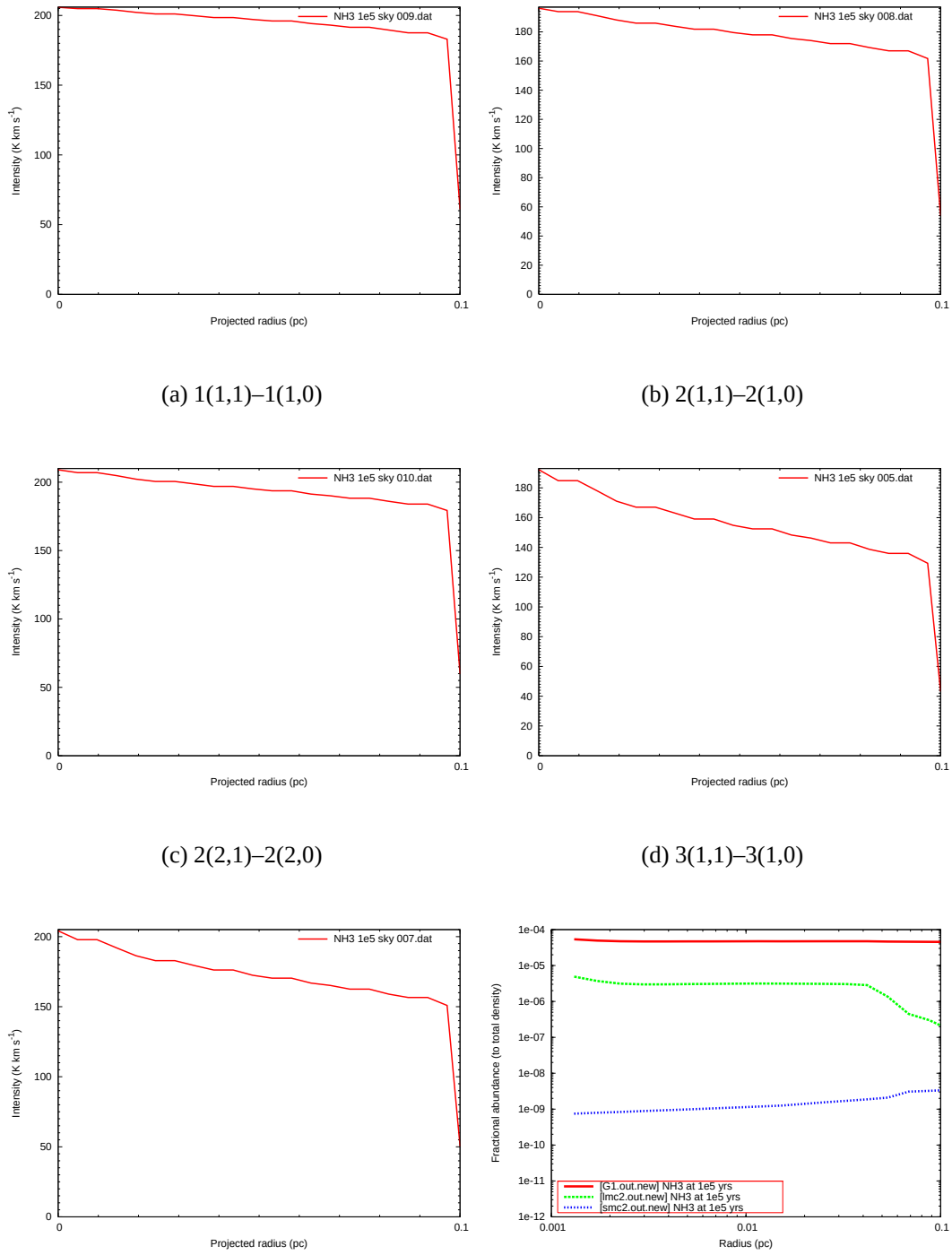

(a) 1(1,1)–1(1,0)

(b) 2(1,1)–2(1,0)

(c) 2(2,1)–2(2,0)

(d) 3(1,1)–3(1,0)

(e) 3(2,1)–3(2,0)

(f) NH_3 fractional abundance

Figure 5.27: The intensity of some observable rotational transitions of NH_3, and the fractional NH_3 abundance, from the G1 model at 10^5 years.

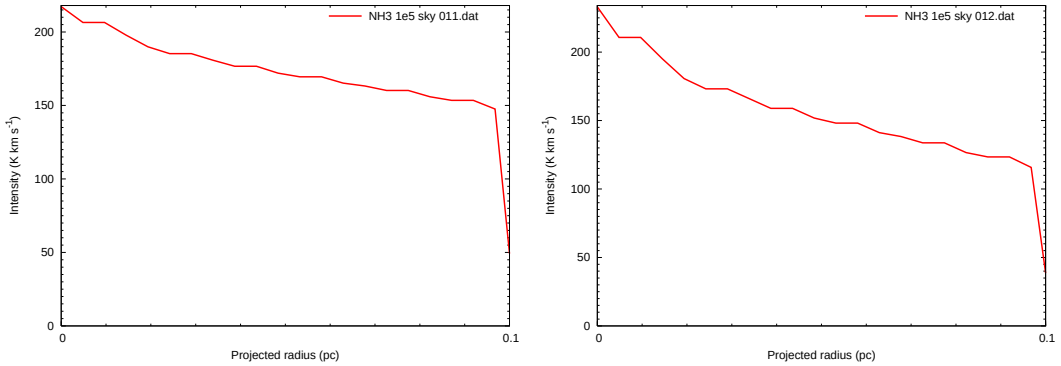

(a) 4(4,1)–4(4,0)

(b) 5(5,1)–5(5,0)

Figure 5.28: The intensity of some more observable rotational transitions of NH_3 at 10^5 years.

Figure 5.32 shows that the intensities produced by the G1 model results at 10^5 years have increased in the time period since 10^4 years. The peak intensity of the most intense transition (J=5-4) has increased by a factor of 4.75. Figures 5.31(f) and 5.32(f) show that the fractional CS abundance in model G1 has increased over this time period, by a factor of around 6.7 in the inner shell. The increase in intensity can be attributed to this increase in fractional abundance. All of the transitions are optically thin in model G1 at this time, with the exception of J=7-6 which is slightly optically thick. The L2 results produce emission with a similar intensity at 10^4 and 10^5 years, for all transitions. This is because the fractional CS abundance in model L2 is similar at 10^4 and 10^5 years. Overall, at 10^5 years, the highest peak intensities are seen in the results from model G1, for all rotational transitions considered. However, this emission quickly drops off, and is less extended that that seen from models L2 and S2. The G1 emission traces the whole hot core radius, whereas the L2 and S2 emission traces the outer shells of the hot core.

Figure 5.33 shows the intensity of the same rotational transitions in the three models at 10^6 years. The G1 and L2 models show an intensity peak at a projected radius of ~0.07pc. This is caused by the correpsonding peak in the fractional CS abundance in these models, as seen in Figure 5.33(f). If observed with infinite resolution, a hot

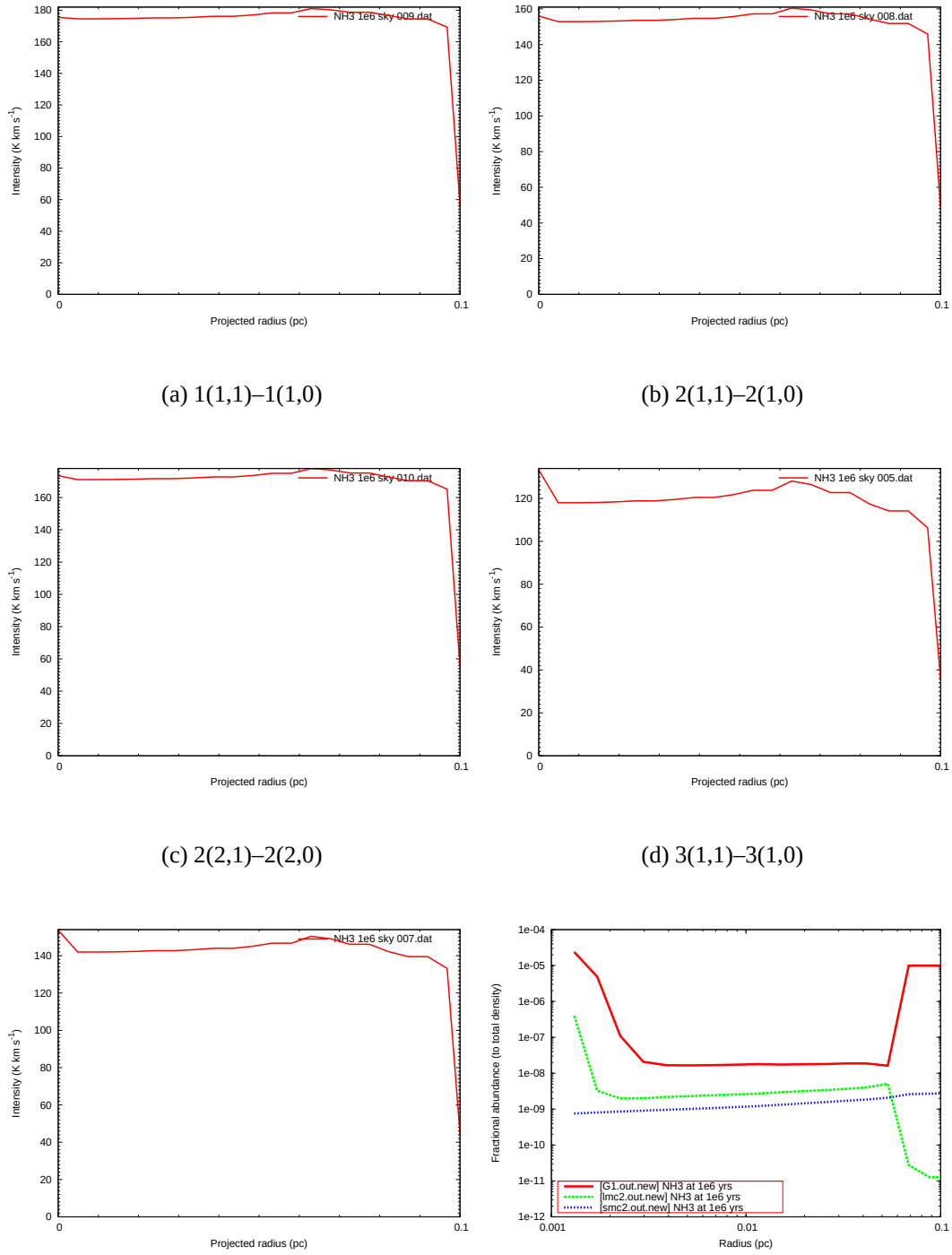

(a) 1(1,1)–1(1,0)

(b) 2(1,1)–2(1,0)

(c) 2(2,1)–2(2,0)

(d) 3(1,1)–3(1,0)

(e) 3(2,1)–3(2,0)

(f) NH_3 fractional abundance

Figure 5.29: The intensity of some observable rotational transitions of NH_3, and the fractional NH_3 abundance, from the G1 model at 10^6 years.

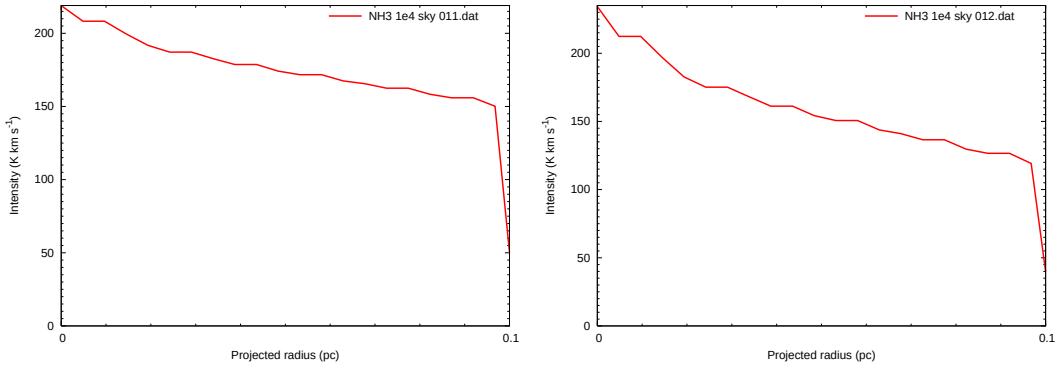

(a) 4(4,1)–4(4,0) (b) 5(5,1)–5(5,0)

Figure 5.30: The intensity of some more observable rotational transitions of NH_3 at 10^6 years.

core of this age would show a bright ring of ^{13}CS, at around 0.06pc from the inner part of the hot core. The intensities seen in the model S2 transitions are extremely low, with peak intensity values below 2 K km s^{-1}. The fractional CS abundance in model S2 has decreased at 10^6 years when compared with that at 10^5 years, particularly at a distance of 0.01-0.08pc. The fractional abundance in this region has decreased by over an order of magnitude. This explains the large drop in intensity over this time period, in model S2, as almost all of the intensity at 10^5 years comes from these mid-outer shells. The intensities seen for models G1 and L2 are lower at 10^6 years than at 10^5 years. This is because the fractional CS abundances in both models are reduced across most of the hot core, as can be seen by comparing Figure 5.32(f) with Figure 5.33(f). The exception to this statement is the 0.07pc peak. The peak forms as CS is still thermally desorbing from the grain surfaces at 10^6 years in all three models at a distance of 0.07pc. However, the species which destroy CS, e.g. C_2H, atomic O, as shown in Table 4.6, are approaching chemical equilibrium at this time. Thermally desorbed CS thus causes an increase in the fractional CS abundance at this time and radius.

The intensities of the rotational ^{13}CS transitions seen in the three models at the three times provide some interesting illustrations of the effects of the underlying chemistry

on the intensity profiles. A hot core at Galactic metallicity is seen to produce an increasing ^{13}CS intensity with increasing time. The opposite is true for the lower metallicity models, where the ^{13}CS intensity is dramatically reduced as the hot core chemistry evolves. These results could prove useful as a means of determining the comparative age/chemical evolution of a group of hot cores. If several hot cores were observed in the LMC (or SMC), a high ^{13}CS intensity would indicate that a hot core was young, and a low ^{13}CS intensity would indicate an older hot core. At each of the times examined (particularly 10^4 and 10^5 years), the ^{13}CS emission is seen to be more extended in models L2 and S2, when compared with model G1. The emission from models L2 and S2 is tracing the mid-outer shells of the hot core, rather than the central region. The emission from model G1 is tracing ^{13}CS from a more central region. This information could be used when making observations of hot cores at low metallicity, as if it were assumed that the ^{13}CS traces the central parts of the hot core, then it could be thought that low metallicity hot cores are extremely large, owing to the extended ^{13}CS emission. This is not the case, as the underlying models show.

5.5.2 C^{18}O

Figure 5.34 shows the J=1-0, J=2-1, J=3-2, J=4-3 and J=5-4 rotational transitions of C^{18}O at 10^4 years, in models G1 and L2. The results from model S2 have not been analysed, as a reliable estimate for the ^{16}O/^{18}O ratio in the SMC could not be found. The CO abundances from models G1 and L2 were reduced using ^{16}O/^{18}O ratios of 430 and 2000, respectively, as seen in Table 5.3. It can be seen in Figure 5.34(f) that the fractional CO abundance in model G1 is similar to that of model L2 in the inner regions of the hot core. The fractional abundance in L2 grows with increasing radius from the protostar, whereas the G1 fractional abundance remains quite flat with increasing radius, up to 0.05pc. The most noticeable difference in CO abundance between the two models is at a radius of 0.05pc, where the fractional CO abundance increases in L2, but falls sharply in G1. This difference in fractional abundance in the outer shells results

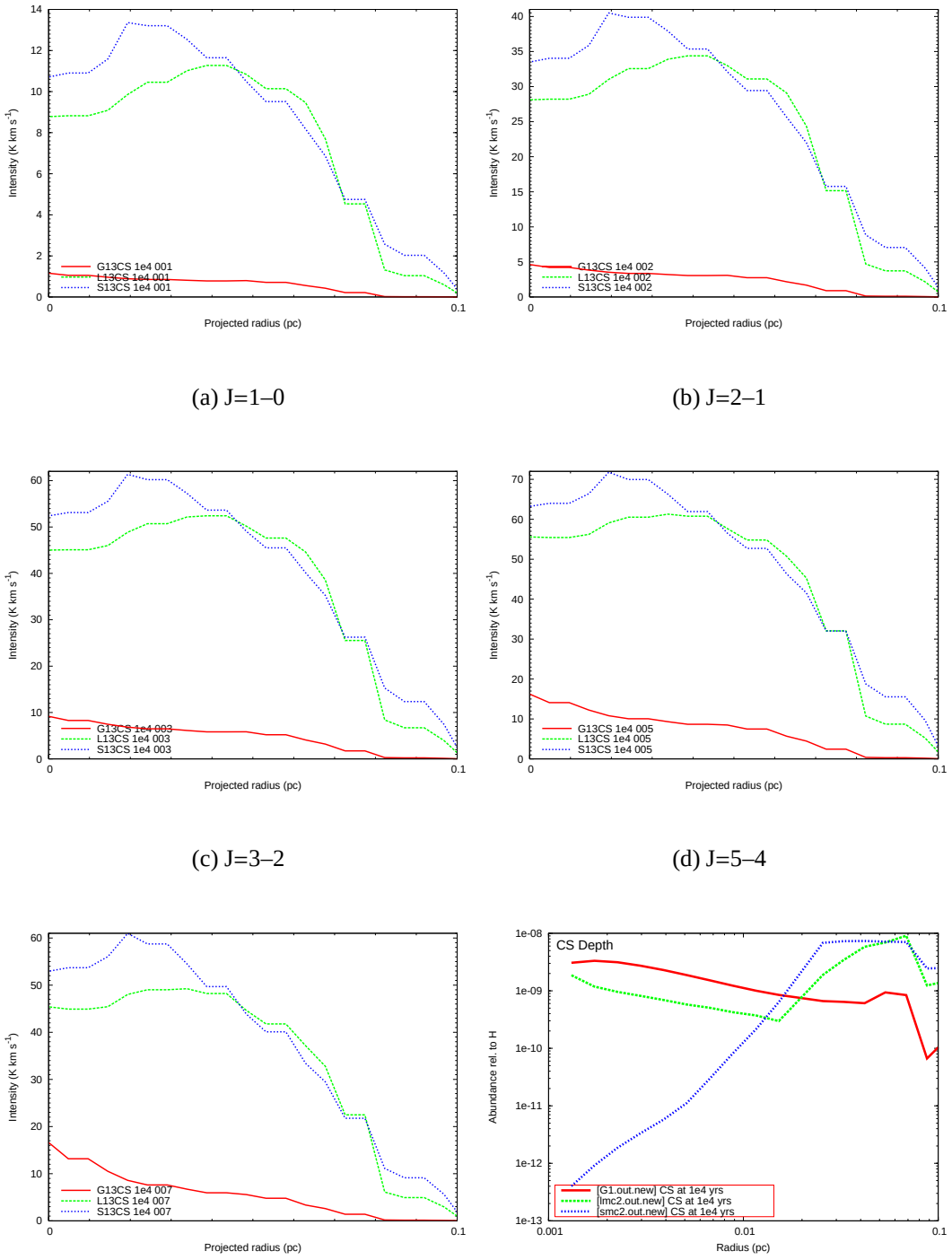

(a) J=1–0 (b) J=2–1

(c) J=3–2 (d) J=5–4

(e) J=7–6 (f) CS fractional abundance

Figure 5.31: The intensity of some observable rotational transitions of ^{13}CS, and the fractional CS abundance, from models G1, L2 and S2 at 10^4 years. For the G1 results, a ^{12}C/^{13}C ratio of 76 was used to estimate the fractional ^{13}CS abundance Stahl et al. (2008). For L2, a ^{12}C/^{13}C ratio of 49 was used Wang et al. (2009a), and for S2 a ratio of 50 was used Chin et al. (1998).

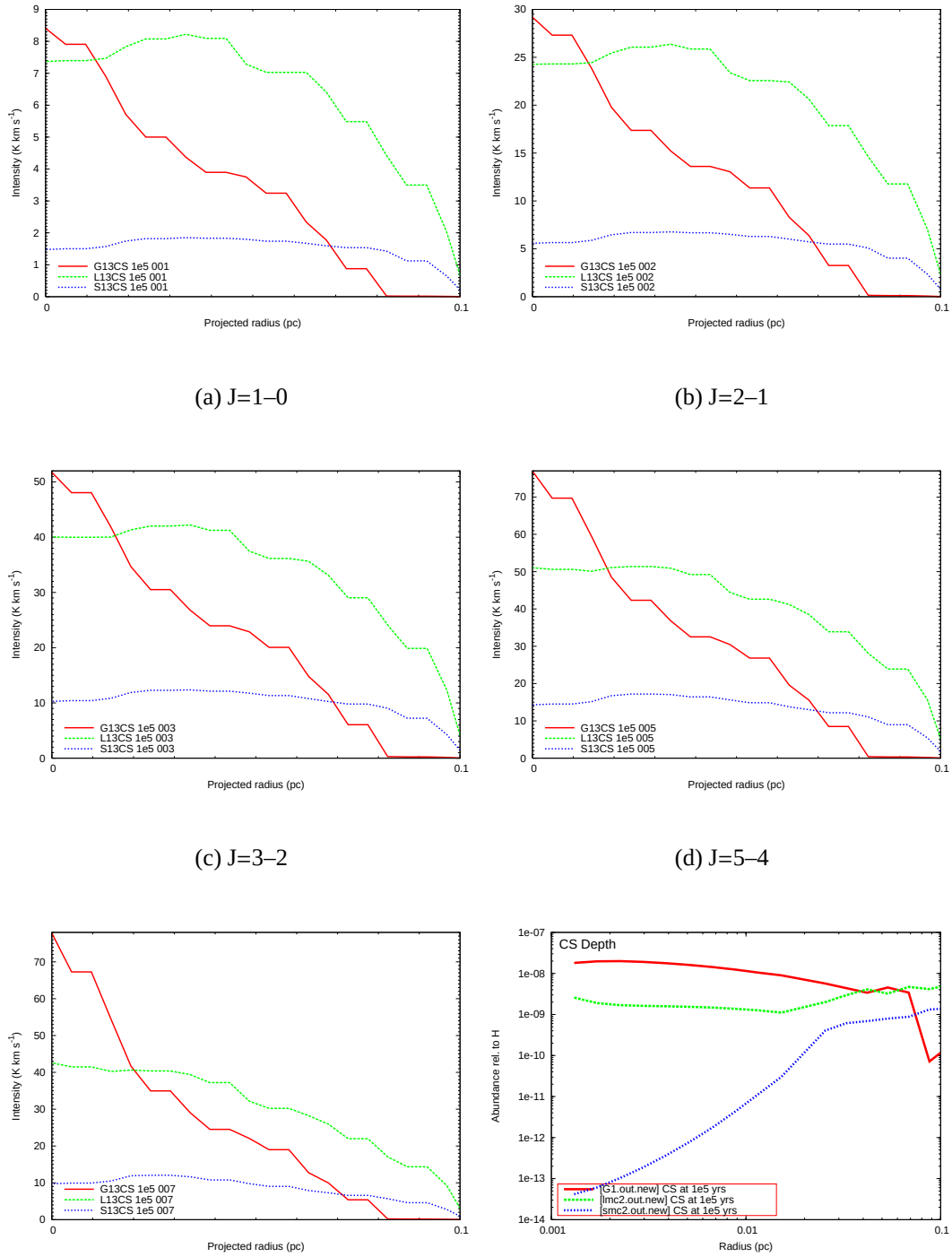

(a) J=1–0 (b) J=2–1

(c) J=3–2 (d) J=5–4

(e) J=7–6 (f) CS fractional abundance

Figure 5.32: The intensity of some observable rotational transitions of ^{13}CS, and the fractional CS abundance, from models G1, L2 and S2 at 10^5 years. For the G1 results, a ^{12}C/^{13}C ratio of 76 was used to estimate the fractional ^{13}CS abundance Stahl et al. (2008). For L2, a ^{12}C/^{13}C ratio of 49 was used Wang et al. (2009a), and for S2 a ratio of 50 was used Chin et al. (1998).

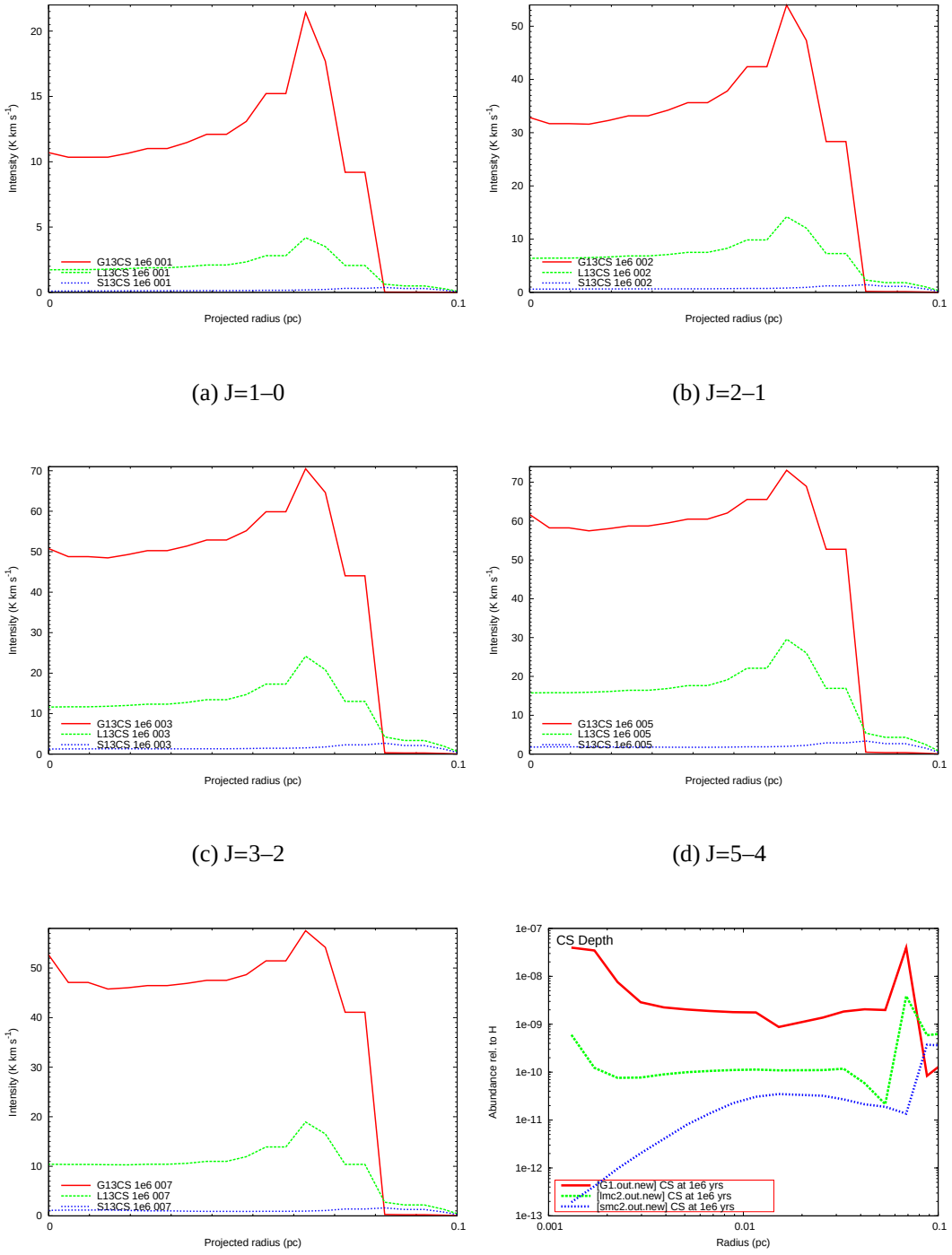

(a) J=1–0

(b) J=2–1

(c) J=3–2

(d) J=5–4

(e) J=7–6

(f) CS fractional abundance

Figure 5.33: The intensity of some observable rotational transitions of ^{13}CS, and the fractional CS abundance, from models G1, L2 and S2 at 10^6 years. For the G1 results, a ^{12}C/^{13}C ratio of 76 was used to estimate the fractional ^{13}CS abundance Stahl et al. (2008). For L2, a ^{12}C/^{13}C ratio of 49 was used Wang et al. (2009a), and for S2 a ratio of 50 was used Chin et al. (1998).

in the emission from model L2 being much more extended than that of G1, for all the transitions examined. The peak intensity for each transition is lower in model L2 than in G1. This is because the $^{16}O/^{18}O$ ratio is higher in the LMC, and so the proportion of ^{18}O is lower in the L2 model, which results in a lower intensity being modelled. The highest peak intensity in both models is seen for the transition J=4-3. The emission from both models is optically thin, as seen in Table 5.4.

Figure 5.35 shows the same transitions in models G1 and L2, at 10^5 years. The peak intensity for each transition in both models has increased since 10^4 years, by a range of factors between two and four. The highest peak intensity is again at the J=4-3 transition. The peak emission remains higher in model G1, and the emission is still more extended in model L2. Figure 5.34(f) shows that the fractional CO abundance in both models has increased across most of the hot core radius, since 10^4 years. This increase is of a similar magnitude to the intensity increase in the same time period. At the outer edge of the hot core, the fractional CO abundance in model G1 is the same at 10^4 and 10^5 years, whereas the fractional CO abundance in the outer shells of model L2 increases over this time period. This results in the continuation of the more extended emission seen in model L2, compared with G1. At 10^5 years, the emission from the J=5-4 and J=4-3 transitions has become optically thick in model G1. Figures 5.35(d) and 5.35(e) show a flattening in the region of the peak intensity for these transitions, which is caused by self-absorption. All of the transitions from model L2 are optically thin at this time.

Figure 5.36 shows the $C^{18}O$ rotational transitions at 10^6 years, in models G1 and L2. It can be seen that again, for all transitions, the highest peak intensity is in model G1, and the L2 emission is more extended. The highest peak intensity in model G1 is at the J=2-1 transition, and in model L2 it is at the J=3-2 and J=4-3 transitions. Figure 5.36(f) shows that the fractional CO abundance in G1 has increased at a radius of 0.05pc, since 10^5 years, by an order of magnitude. This increase results in an increased intensity at a higher projected radius, as the mid-outer shells of the hot core contribute more to the intensity profile. This also results in a flattening of the profile, as the mid-outer

shells shield the contribution of the inner shells. Some self-absorption occurs, as the emission has become optically thick for all the transitions except J=1-0, as seen in Table 5.6. Figure 5.36(f) shows that the fractional CO abundance in model L2 has increased slightly across most of the hot core radius, since 10^5 years. This causes the intensity for each transition to be slightly higher at 10^6 years compared with that at 10^5 years. The intensity profiles from model L2 remain fairly flat and extended. The emission remains optically thin. Overall, it appears that the $C^{18}O$ emission from a hot core brightens as the hot core chemistry evolves, in both models. This could be used to differentiate between older and younger hot cores which are observed in the same galaxy. Observers should note that the extended emission in model L2 traces the outer shells of the hot core. The extended emission reflects the distribution of the underlying fractional abundance in the model, rather than the physical size of the hot core, which is the same in models G1 and L2.

5.5.3 $H^{13}CN$

Figure 5.37 shows the emission from the J=1-0, J=3-2 and J=4-3 rotational transitions from models G1, L2, and S2 at 10^4 years. The $^{12}C/^{13}C$ ratios used to reduce the HCN abundances from the three models are the same as were used for the ^{13}CS modelling. The peak intensities are very high for all three models and all transitions, with values ranging from 120–140 K km s^{-1}. Table 5.4 shows that all the transitions in the three models produce optically thick emission at 10^4 years. In the outer shells of the hot core, more emission is seen from model L2 than models G1 and S2. Figure 5.37(d) shows that the fractional HCN abundance in model L2 increases towards the edge of the hot core, whereas models G1 and S2 exhibit sharp dips in the fractional HCN abundance in the outer shells. This outer-shell emission in model L2 causes the more intense extended emission seen in Figure 5.37. The intensity profiles for the rotational transitions from model L2 are very flat. This is because the emission from the outer shells shields the emission from the inner regions. The $H^{13}CN$ emission in this model is thus tracing

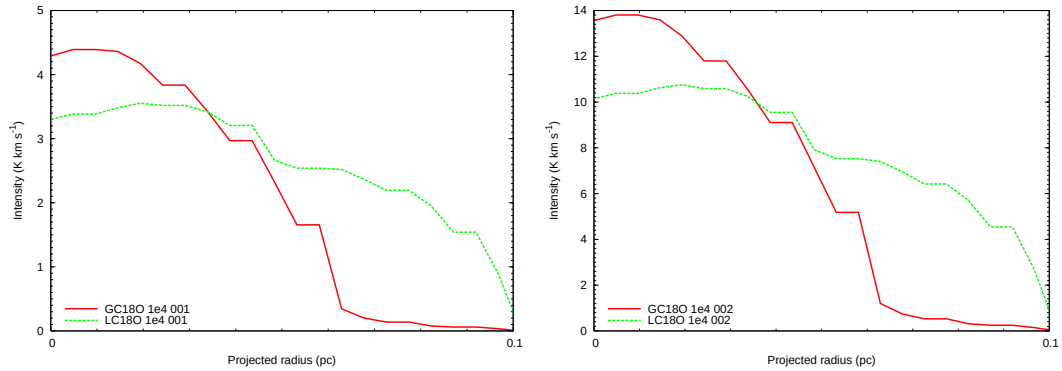

(a) J=1–0

(b) J=2–1

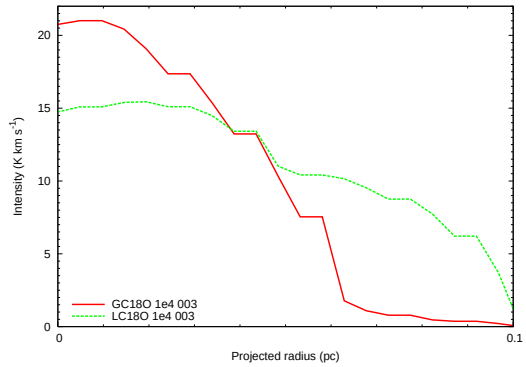

(c) J=3–2

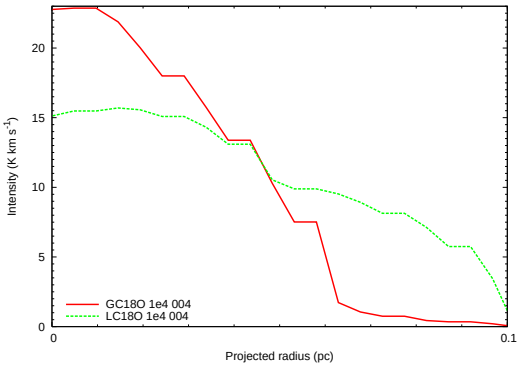

(d) J=4–3

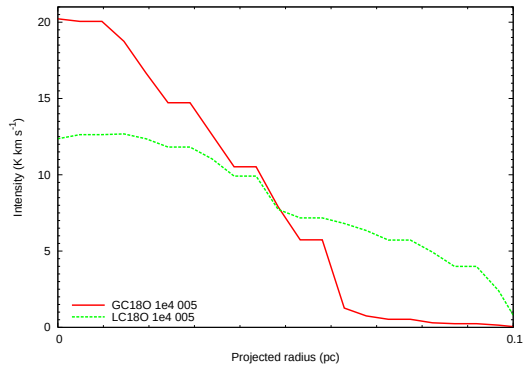

(e) J=5–4

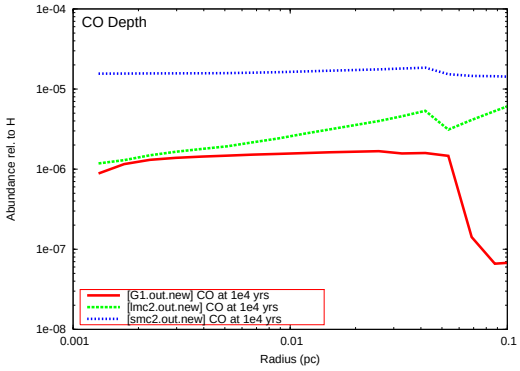

(f) CO fractional abundance

Figure 5.34: The intensity of some observable rotational transitions of $C^{18}O$, and the fractional CO abundance, from the G1 and L2 models at 10^4 years. The CO abundances from models G1 and L2 were reduced using $^{16}O/^{18}O$ ratios of 430 and 2000 respectively. These ratios were taken from Polehampton et al. (2005) and Wang et al. (2009b).

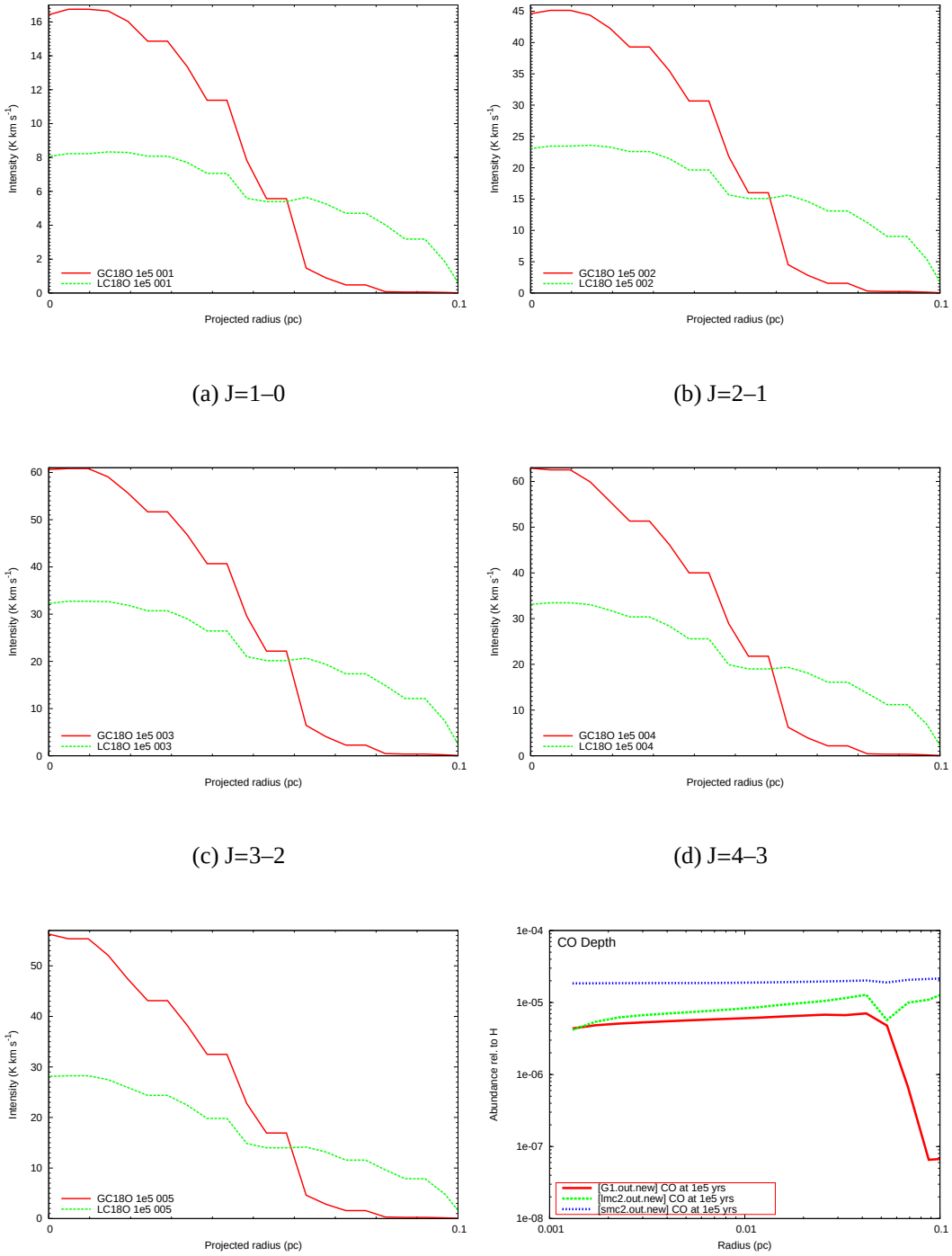

(a) J=1–0 (b) J=2–1

(c) J=3–2 (d) J=4–3

(e) J=5–4 (f) CO fractional abundance

Figure 5.35: The intensity of some observable rotational transitions of $C^{18}O$, and the fractional CO abundance, from the G1 and L2 models at 10^5 years. The CO abundances from models G1 and L2 were reduced using $^{16}O/^{18}O$ ratios of 430 and 2000 respectively. These ratios were taken from Polehampton et al. (2005) and Wang et al. (2009b).

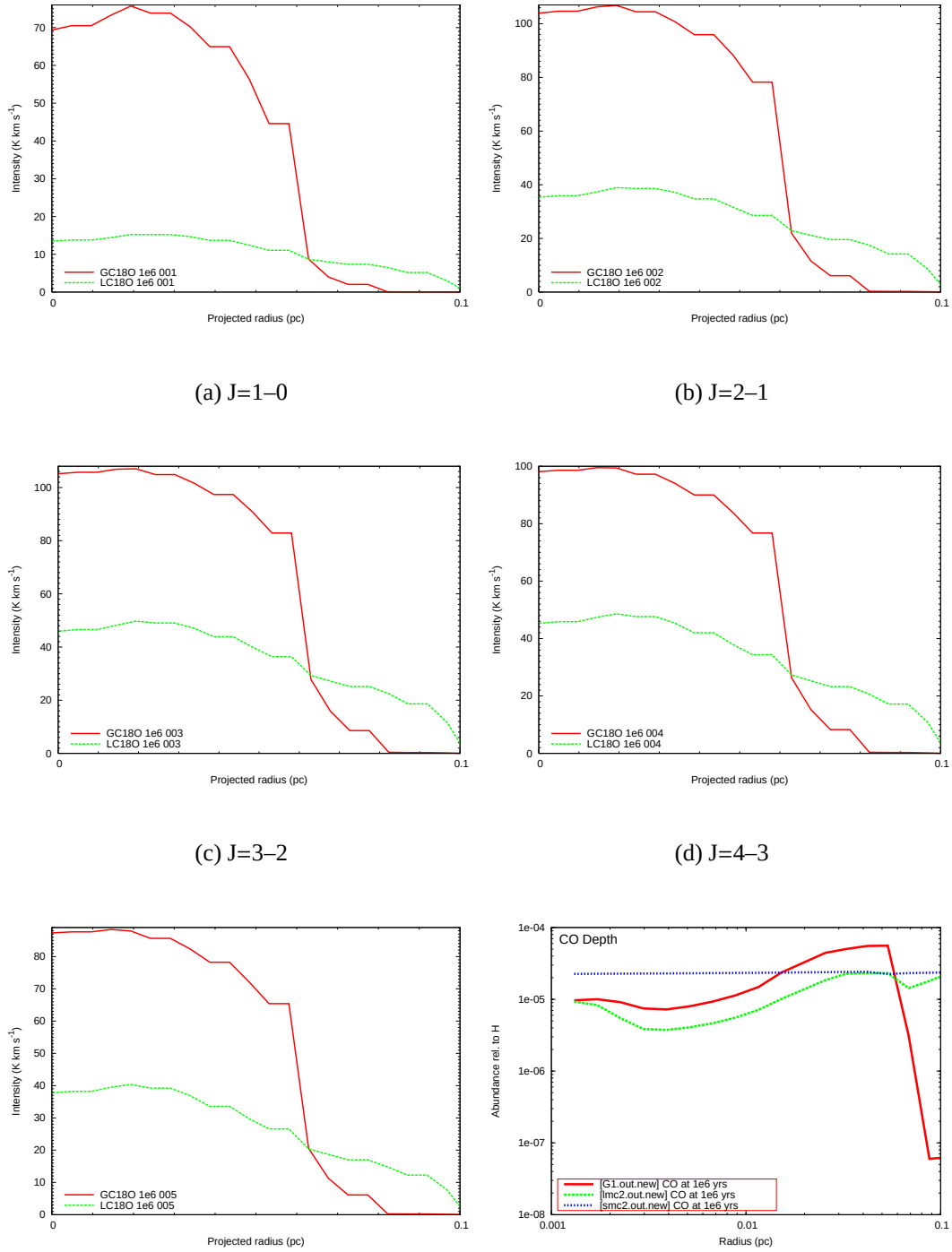

(a) J=1–0 (b) J=2–1

(c) J=3–2 (d) J=4–3

(e) J=5–4 (f) CO fractional abundance

Figure 5.36: The intensity of some observable rotational transitions of $C^{18}O$, and the fractional CO abundance, from the G1 and L2 models at 10^6 years. The CO abundances from models G1 and L2 were reduced using $^{16}O/^{18}O$ ratios of 430 and 2000 respectively. These ratios were taken from Polehampton et al. (2005) and Wang et al. (2009b).

the outer shells of the hot core. The intensity profiles produced by models G1 and S2 are also fairly flat. The fractional HCN abundances for these models, seen in Figure 5.37(d), are fairly flat across most of the hot core. The emission seen does not come from the central regions, as the high $H^{13}CN$ abundances in the mid-outer shells cause the transition lines to become optically thick. At 10^4 years, all the emission from the transitions is tracing the outer and mid-outer shells.

Figure 5.38 shows the same transitions for models G1, L2 and S2 at 10^5 years. The intensity seen from the transitions of model G1 is very similar to that seen at 10^4 years. The peak intensities are almost identical, the main changes occur at the projected radii/offsets after 0.07pc, where the intensity increases between 10^4 and 10^5 years. This is caused by an increase in the fractional HCN abundance in the outer shells of model G1, as can be seen by comparing Figure 5.37(d) with Figure 5.38(d). It can also be seen that the fractional HCN abundance across the hot core remains similar this time period, up to a radius of 0.07pc. As the peak intensity does not increase over this time period, but the intensity at a greater projected radius/offset does, it can be concluded that the line is saturated. Self absorption prevents the intensity increasing at small projected radii, whereas at larger projected radii, the effects of the increased fractional abundance in the outer shells can be seen as the intensity increases. The fractional HCN abundance drops slightly across the whole hot core radius in model L2 between 10^4 and 10^5 years. This is translated as a very slight drop in intensity for all transitions, as the optical depth of the lines remains high. Observationally, a hot core at the metallicity of model L2 would look the same at 10^4 and 10^5 years. The intensities of the transitions modelled using the S2 results drop dramatically between 10^4 and 10^5 years, by factors in the range 1.6–3.25. This corresponds to a large drop in the fractional HCN abundance, which occurs in this model over this time period, in the middle and outer shells of the hot core. This can be seen by comparing Figure 5.37(d) with Figure 5.38(d). The J=1-0 emission is optically thin at 10^5 years in model S2.

Figure 5.39 shows the same transitions for the three models at 10^6 years. Self-absorption can be seen in the intensity profiles produced using the G1 and L2 models, as the in-

tensity dips at the lowest projected radii. The intensity profiles from these models are very flat, as the emission seen comes from the outer shells. Figure 5.39(d) shows that the fractional HCN abundance in model G1 has increased at the inner and outer edges of the hot core, but reduced in the middle shells. Model L2 has a reduced HCN abundance across the whole hot core, except for the innermost shell which has the same fractional abundance at 10^5 and 10^6 years. The fractional abundance in model S2 has fallen across the whole hot core, particularly in the inner shells. The intensities produced by models L2 and S2 have reduced since 10^5 years. For all transitions examined, the intensities produced by the three models are distinct from one another, and the underlying metallicity could potentially be estimated by comparing observations from the Milky Way and the LMC or SMC.

The $H^{13}CN$ emission is optically thick for many of the transitions examined. This species could be used to trace the extent of the outer shells of a hot core, but it does not provide information about the inner shells in models G1 and L2. The $H^{13}CN$ intensity is fairly consistent over time in a hot core with Galactic metallicity, although self-absorption does somewhat reduce the intensity by 10^6 years. The $H^{13}CN$ intensity produced using the model L2 results is also similar at 10^4 and 10^5 years, although again after this time it is reduced by a factor of around 20%. The $H^{13}CN$ intensity in model S2 changes dramatically with time. This species could be used as a ‘chemical clock’ in low metallicity regions, to comparatively estimate the ages amongst a group of hot cores.

5.5.4 $HN^{13}C$

Figure 5.40 shows the rotational transitions J=1-0, J=3-2 and J=4-3 for $HN^{13}C$ in models G1, L2 and S2, at 10^4 years. The peak intensities are highest in model G1, and lowest in S2. This matches the variation in the fractional abundances in the models, as can be seen in Figure 5.40(d). The emission in models G1 and L2 is more extended than that in model S2. This is because the outer shells of models G1 and L2 contain

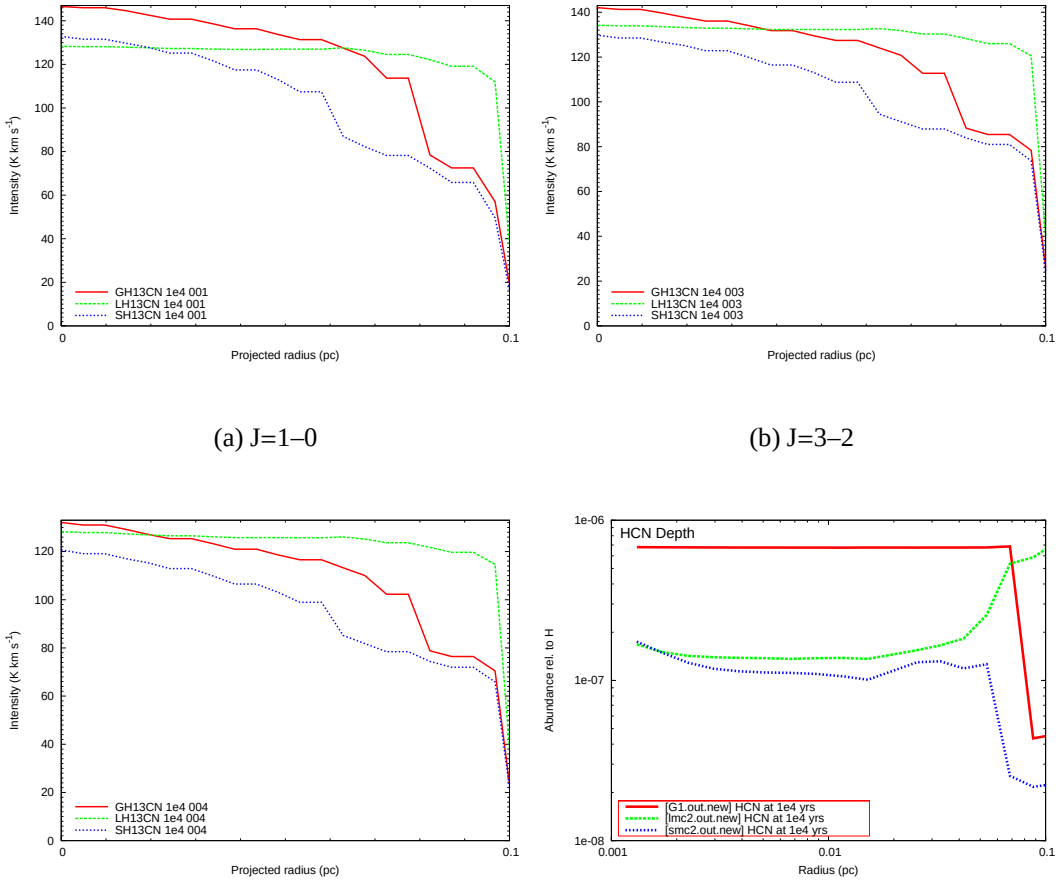

(a) J=1–0

(b) J=3–2

(c) J=4–3

(d) HCN fractional abundance

Figure 5.37: The intensity of some observable rotational transitions of $H^{13}CN$, and the fractional HCN abundance, from models G1, L2 and S2 at 10^4 years. For the G1 results, a $^{12}C/^{13}C$ ratio of 76 was used to estimate the fractional ^{13}CS abundance Stahl et al. (2008). For L2, a $^{12}C/^{13}C$ ratio of 49 was used Wang et al. (2009a), and for S2 a ratio of 50 was used Chin et al. (1998).

a high HNC abundance, and so the emission is tracing the gas in the outer shells. The optical thickness of the emission from the outer shells prevents the emission from the inner shells being observed. Model S2 shows a sharp drop in fractional HNC abundance at a radius of 0.055pc. This corresponds to a sharp drop in intensity at a projected radius of 0.55pc, as the outer shells of model S2 do not contribute much $HN^{13}C$ emis-

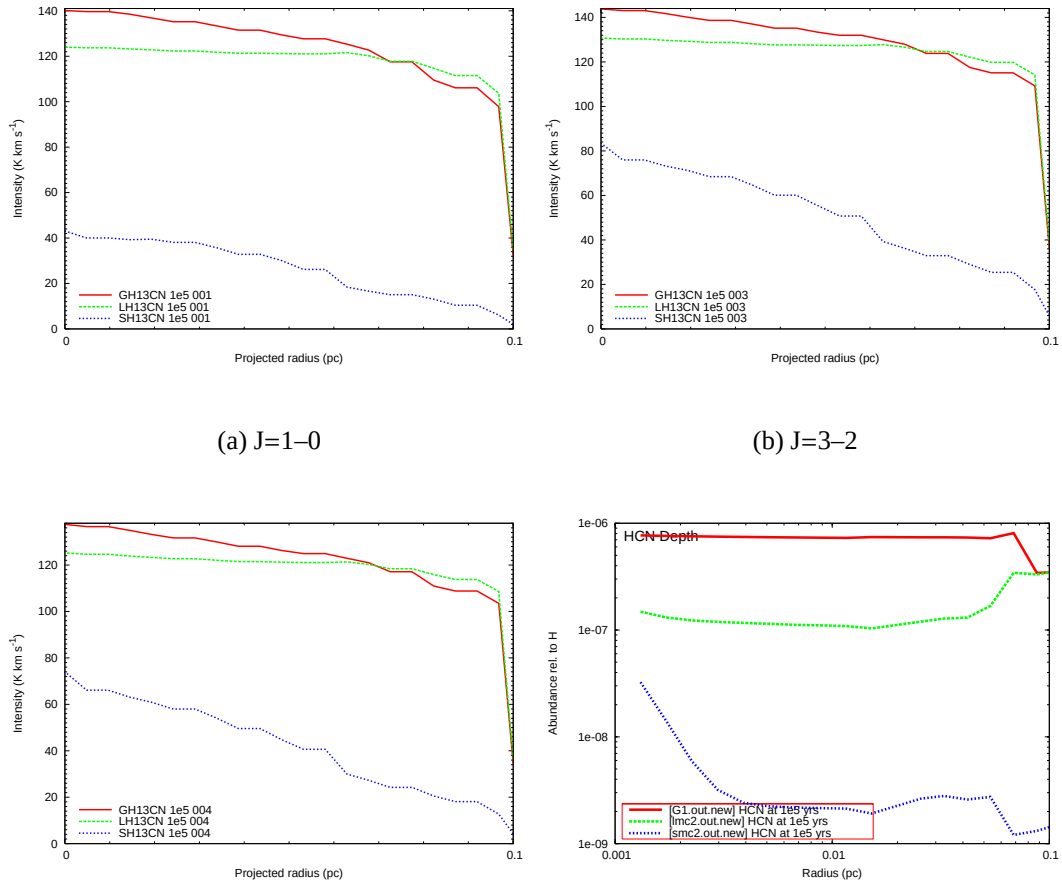

(a) J=1–0 (b) J=3–2

(c) J=4–3 (d) HCN fractional abundance

Figure 5.38: The intensity of some observable rotational transitions of $H^{13}CN$, and the fractional HCN abundance, from models G1, L2 and S2 at 10^5 years. For the G1 results, a $^{12}C/^{13}C$ ratio of 76 was used to estimate the fractional ^{13}CS abundance Stahl et al. (2008). For L2, a $^{12}C/^{13}C$ ratio of 49 was used Wang et al. (2009a), and for S2 a ratio of 50 was used Chin et al. (1998).

sion. The intensity ranges produced by the three models for each transition are distinct from one another, and somewhat reflect the underlying metallicity of the model from which they are calculated. However, almost all of the transitions are optically thick at 10^4 years, as seen in Table 5.4, and so the emission seen traces only the outer shells of the hot core. If the age of a hot core could be accurately estimated to be 10^4 years, the

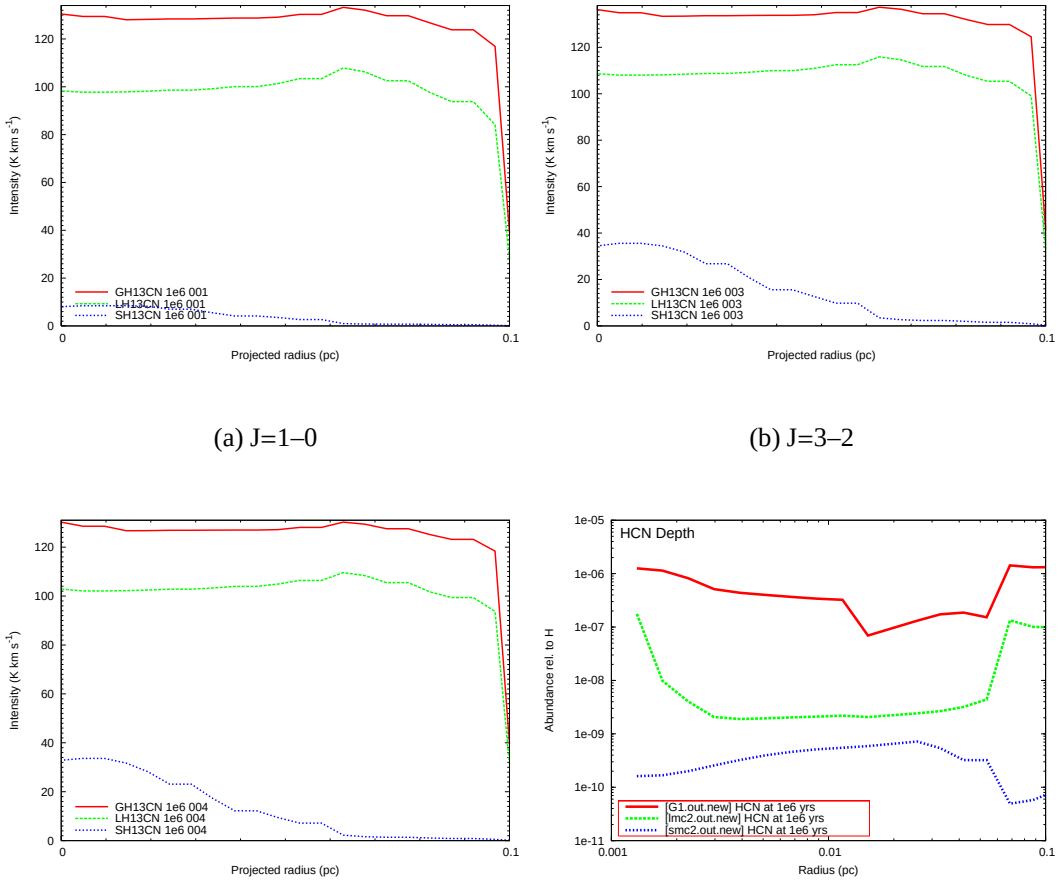

(a) J=1–0

(b) J=3–2

(c) J=4–3

(d) HCN fractional abundance

Figure 5.39: The intensity of some observable rotational transitions of $H^{13}CN$, and the fractional HCN abundance, from models G1, L2 and S2 at 10^6 years. For the G1 results, a $^{12}C/^{13}C$ ratio of 76 was used to estimate the fractional ^{13}CS abundance Stahl et al. (2008). For L2, a $^{12}C/^{13}C$ ratio of 49 was used Wang et al. (2009a), and for S2 a ratio of 50 was used Chin et al. (1998).

$HN^{13}C$ intensity could be used to estimate the underlying metallicity, using the transitions shown in Figure 5.40.

Figure 5.41 shows the same transitions at 10^5 years, for models G1, L2 and S2. The fractional HNC abundance in model G1 is almost identical at 10^4 and 10^5 years. This is reflected in the intensity profiles for the G1 $HN^{13}C$ transitions, which are also al-

most identical at 10^4 and 10^5 years. The intensity profiles produced using the model L2 results increase between 10^4 and 10^5 years. This corresponds to an increase in fractional HNC abundance across the whole hot core, as seen by comparing Figure 5.40(d) with Figure 5.41(d). The intensity profiles for models G1 and L2 at 10^5 years are very similar. However, Figure 5.41(d) shows that the fractional HNC abundance in the models is different, by a factor of 2–3. The similar intensity profiles occur as the outermost shells of the models contain very similar fractional HNC abundances. Most of the emission seen comes from these shells, as the high fractional abundance produces a high optical depth. The emission from the intermediate and central shells of the hot core is barely seen, as the optical thickness of the outer shells shields the internal emission. At very low projected radii/offsets, there is some difference in intensity between models G1 and L2. This difference is caused by the emission from the mid/inner shells hot core, as a small amount of this intensity is able to penetrate the optically thick outer shells to reach the observer. The intensities seen from the transitions modelled using the S2 results are of a similar magnitude to those seen at 10^4 years. The fractional HNC abundance in model S2 has increased in the inner regions, and decreased in the intermediate shells, since 10^4 years. The peak intensity values at 10^5 years are slightly lower than those seen at 10^4 years. This shows that the emission is tracing the intermediate regions rather than the inner shells, as this decrease corresponds with the decreased fractional abundance in the intermediate shells, rather than the increased fractional HNC abundance in the inner shells.

Figure 5.42 shows the rotational $HN^{13}C$ transitions for the models at 10^6 years. The intensities seen from the three models at this time can be easily distinguished from one another. The intensities associated with model G1 are very high. They are slightly reduced from those seen at 10^5 years. This is caused by the reduction in fractional HNC abundance in the intermediate shells which occurs over this time period. The fractional HNC abundance in the inner and outer shells increases between 10^5 and 10^6 years. It can be seen that almost all the intensity is coming from the outermost shells, as the intensity profile is almost rectangular. The emission is tracing the outer shells

only. The lines are self absorbed, as can be seen in the inner 0.06pc where the intensity slightly dips. The intensity profiles produced using model L2 are much reduced when compared with those at 10^5 years. The J=1-0 transition is optically thin at 10^6 years, and so the emission seen comes from the whole hot core. The intensity peaks at a projected radius of zero, which corresponds with a peak in fractional HCN abundance at the centre of the hot core (shown in Figure 5.42(d)). The intensities created from the model S2 results are lower at 10^6 years than at 10^5 years, by factors ranging from 2-4. This corresponds to a large drop in the fractional HNC abundance in model S2, as seen by comparing Figure 5.41(d) with Figure 5.42(d). The $HN^{13}C$ emission from this model at 10^6 years is optically thin, and can thus be used to reveal the distribution of $HN^{13}C$ in the hot core.

The $HN^{13}C$ intensity in model G1 is fairly consistent with time – a similar intensity is seen at all times considered, and the emission seen comes from the outer shells of the hot core. The $HN^{13}C$ intensity in model L2 increases by around 20% between 10^4 and 10^5 years, before significantly decreasing after this time. The $HN^{13}C$ intensity in model S2 is fairly similar at 10^4 and 10^5 years, and after this time the intensity falls dramatically. This information could be used to identify older hot cores, as the low intensities for all transitions considered in models L2 and S2 indicate a hot core age of $\geq 10^6$ years. If hot cores at low metallicity with low $HN^{13}C$ intensities are observed, this species could be used to probe the structure and inner shells of the hot core, as the models predict these rotational transitions will be optically thin.

5.5.5 HNCO

Figure 5.43 shows the hyperfine 4(0,4)-3(0,3), 4(1,3)-3(1,2) and 5(2,4)-4(2,3) HNCO transitions at 10^4 years in models G1, L2 and S2. It can be seen that the 5(2,4)-4(2,3) transition does not produce observable intensities in any of the models. Model G1 produces peak intensities of 9.3 and 0.16 K km s^{-1} for 4(0,4)-3(0,3) and 4(1,3)-3(1,2) respectively. This emission traces the central shells of the hot core only. Figure 5.43(d)

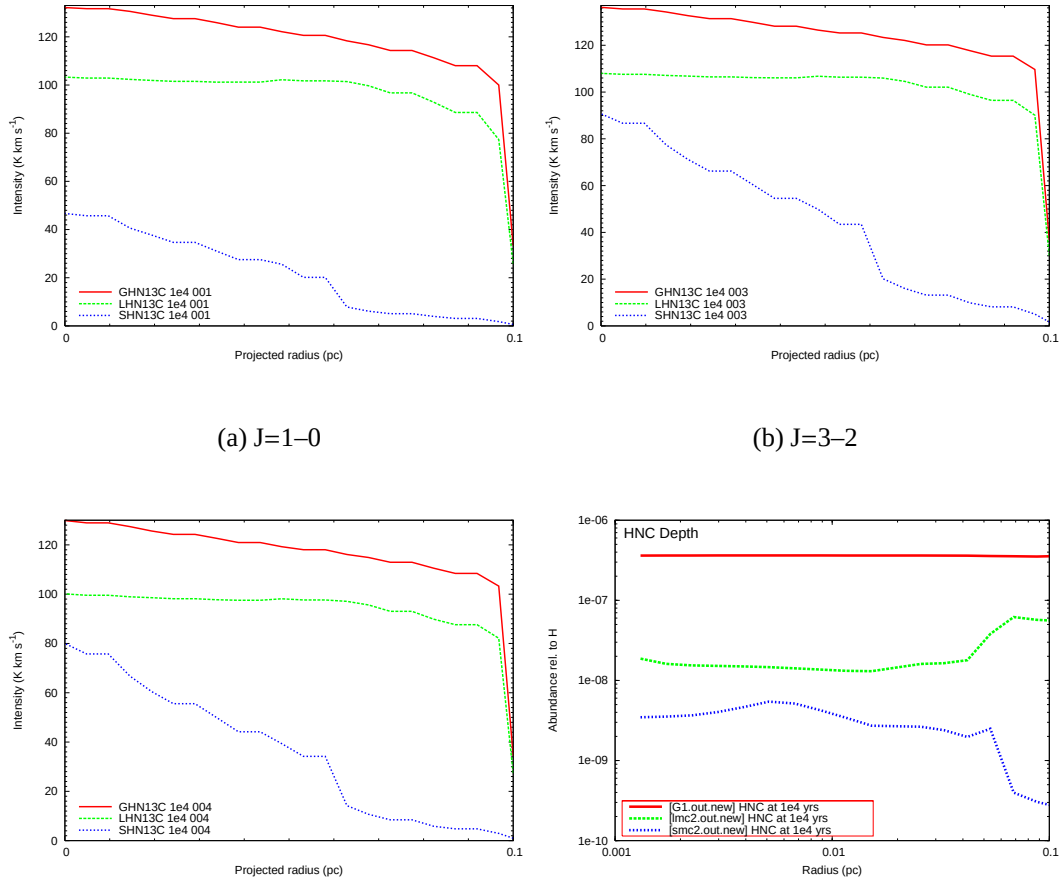

(a) J=1–0

(b) J=3–2

(c) J=4–3

(d) HNC fractional abundance

Figure 5.40: The intensity of some observable rotational transitions of $HN^{13}C$, and the fractional HNC abundance, from models G1, L2 and S2 at 10^4 years. For the G1 results, a $^{12}C/^{13}C$ ratio of 76 was used to estimate the fractional ^{13}CS abundance Stahl et al. (2008). For L2, a $^{12}C/^{13}C$ ratio of 49 was used Wang et al. (2009a), and for S2 a ratio of 50 was used Chin et al. (1998).

shows the fractional HNCO abundance in the models at this time. It can be seen that model G1 has a much higher fractional HNCO abundance in the inner shells than models L2 and S2, by over two orders of magnitude. This is why the intensity is so much stronger in the results from model G1. The 4(0,4)-3(0,3) and 4(1,3)-3(1,2) transitions trace the inner region of the hot core, up to a radius of around 0.02pc. The models thus

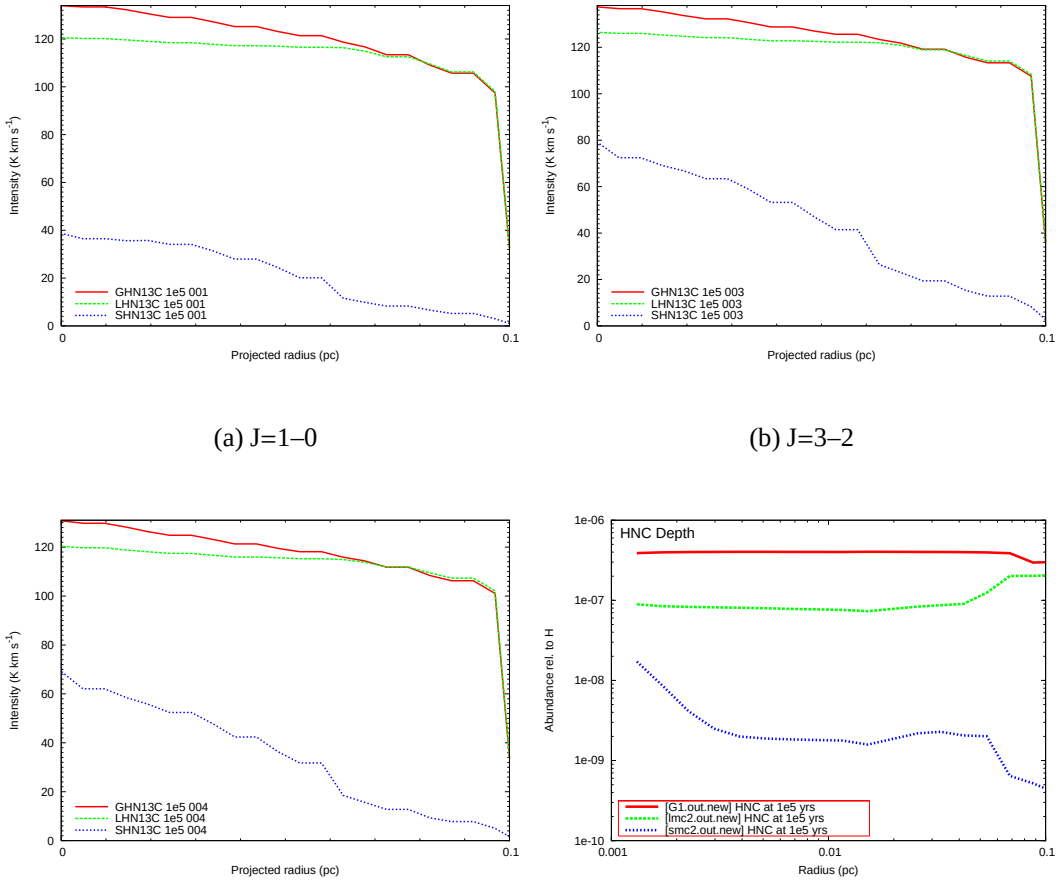

(a) J=1–0 (b) J=3–2

(c) J=4–3 (d) HNC fractional abundance

Figure 5.41: The intensity of some observable rotational transitions of $HN^{13}C$, and the fractional HNC abundance, from models G1, L2 and S2 at 10^5 years. For the G1 results, a $^{12}C/^{13}C$ ratio of 76 was used to estimate the fractional ^{13}CS abundance Stahl et al. (2008). For L2, a $^{12}C/^{13}C$ ratio of 49 was used Wang et al. (2009a), and for S2 a ratio of 50 was used Chin et al. (1998).

indicate that it should not be possible to observe HNCO in a young hot core with a low underlying metallicity.

Figure 5.44 shows the same transitions for models G1, L2 and S2 at 10^5 years. The HNCO intensity in model G1 has increased considerably since 10^4 years. The peak intensities at 10^5 years are 70 K km s^{-1} for 4(0,4)-3(0,3) and 6.4 K km s^{-1} for 4(1,3)-

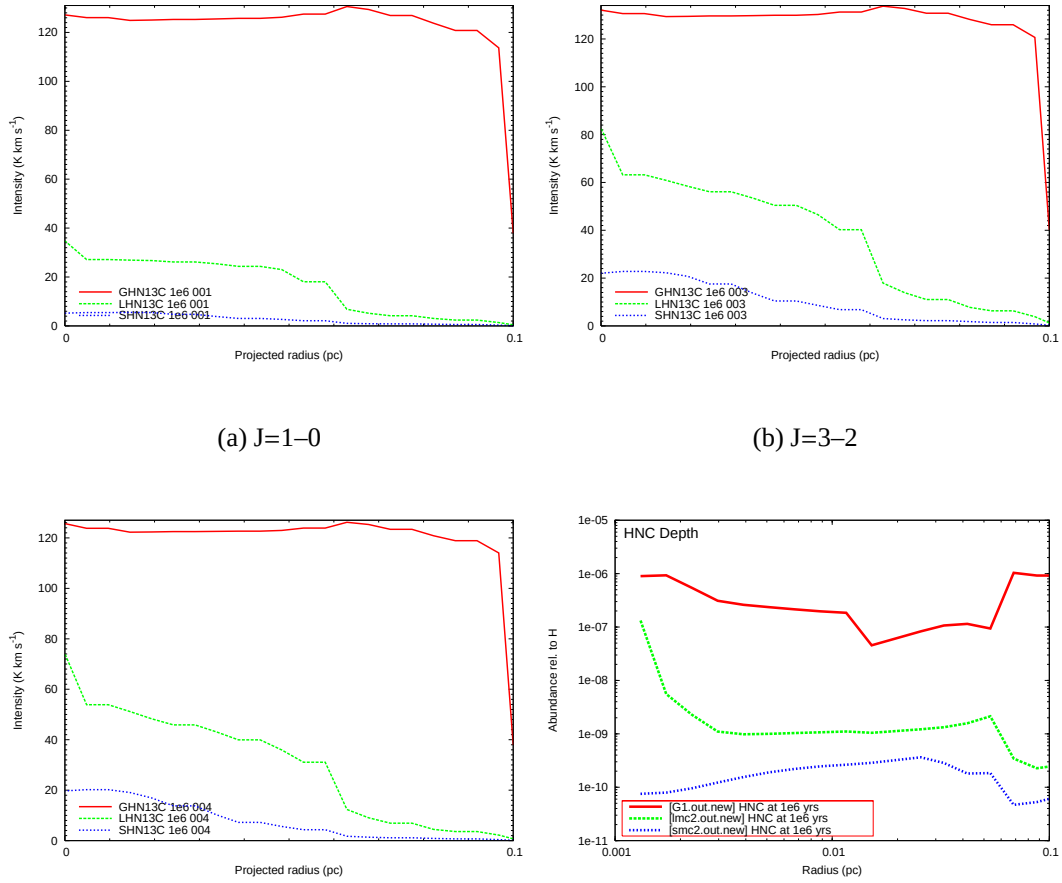

(a) J=1–0 (b) J=3–2

(c) J=4–3 (d) HNC fractional abundance

Figure 5.42: The intensity of some observable rotational transitions of HN^{13}C, and the fractional HNC abundance, from models G1, L2 and S2 at 10^6 years. For the G1 results, a ^{12}C/^{13}C ratio of 76 was used to estimate the fractional ^{13}CS abundance Stahl et al. (2008). For L2, a ^{12}C/^{13}C ratio of 49 was used Wang et al. (2009a), and for S2 a ratio of 50 was used Chin et al. (1998).

3(1,2). These values represent respective increases of 750% and 400%, when compared with the values at 10^4 years. The fractional HNCO abundance in model G1 increases by around one order of magnitude in the inner regions of the hot core over the time period between 10^4 and 10^5 years, as seen by comparing Figure 5.43(d) with Figure 5.44(d). The 4(0,4)-3(0,3) transition is tracing a larger part of the hot core at

10^5 years, as the emission has extended to a projected radius of 0.05pc. The HNCO is tracing gas in which the fractional HNCO abundance is greater than 10^{-10} in this model. Some emission is seen from model L2 at 10^5 years, for the transition 4(0,4)-3(0,3) only. The emission is extended, and has almost constant intensity across the whole projected radius. The intensity is very low, with an average value around 1.5 K km s^{-1}. This emission is tracing the HNCO from the outer shells of the hot core. Figure 5.44(d) shows that the peak fractional HNCO abundance is seen in the outer shells of the hot core, with an approximate value of 2×10^{-11}. This is the gas which the 4(0,4)-3(0,3) transition is tracing. No emission is seen from the S2 model. The transition 5(2,4)-4(2,3) again does not produce any observable intensities from any of the models at 10^5 years.

Figure 5.45 shows the same HNCO transitions for models G1, L2 and S2 at 10^6 years. The intensity for the transition 4(0,4)-3(0,3) in model G1 is fairly similar to that seen at 10^5 years, although its peak value has reduced to around 56 K km s^{-1} and the emission is slightly more extended. These changes are caused by changes in the fractional HNCO abundance in G1, at a radius of around 0.05pc. The 4(1,3)-3(1,2) intensity for model G1 is also reduced, and slightly extended. No 5(2,4)-4(2,3) emission is seen for this model. The intensities for the transitions using the results from model L2 have greatly increased since 10^5 years. The peak intensity for 4(0,4)-3(0,3) is over 120 K km s^{-1} – this line is optically thick, so self-absorption could be masking an even higher peak intensity. The intensity increase is caused by a large increase in the fractional HNCO abundance at 10^6 years in the outer shells of model L2, which can be seen by comparing Figure 5.44(d) with Figure 5.45(d). This increase occurs at a hot core radius of around 0.065pc. The intensity profiles show some limb-brightening effects, which are caused by the high intensity coming from the outer shells. All three transitions are seen in the model L2 results, although the 5(2,4)-4(2,3) transition is very weak, with an intensity of around 0.04 K km s^{-1}.

The model results indicate that HNCO may only be observable in hot cores with Galactic metallicity, at times up to 10^5 years. At 10^6 years, a great deal of HNCO

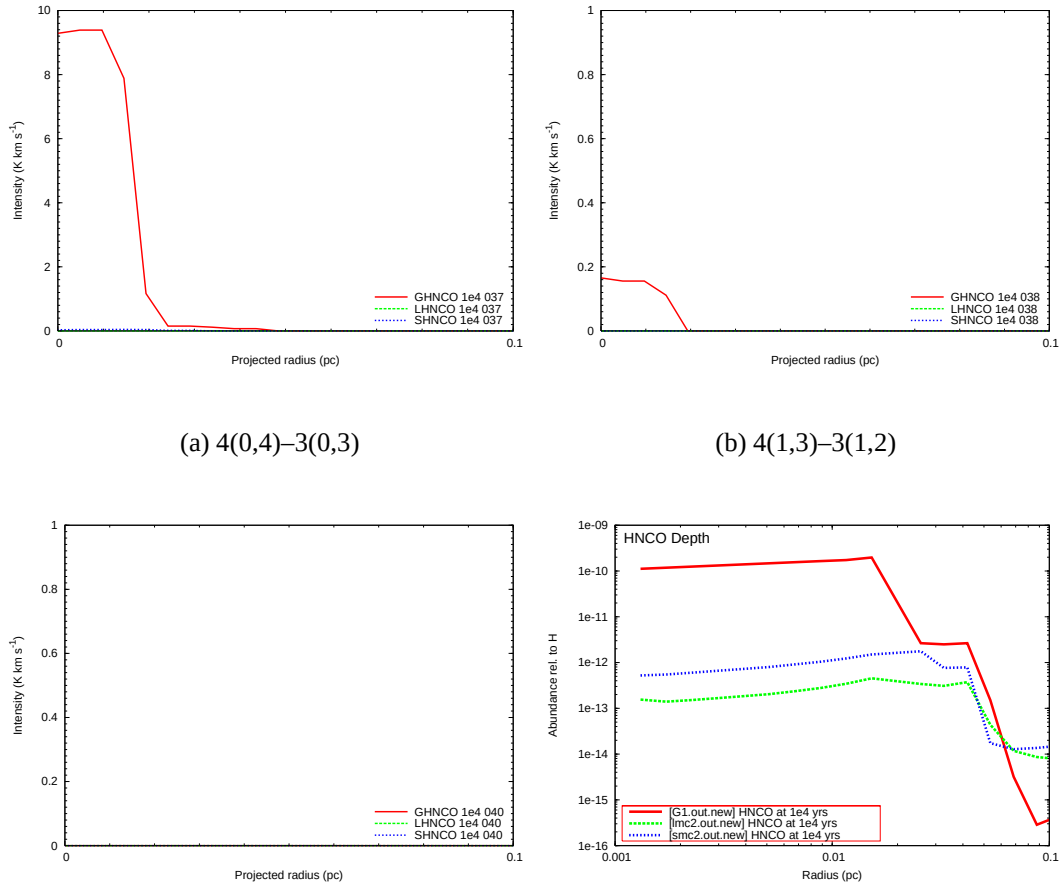

(a) 4(0,4)–3(0,3)

(b) 4(1,3)–3(1,2)

(c) 5(2,4)–4(2,3)

(d) HNCO fractional abundance

Figure 5.43: The intensity of some observable rotational transitions of HNCO, and the fractional HNCO abundance, from models G1, L2 and S2 at 10^4 years.

emission is seen in model L2. If strong HNCO emission were to be observed in a low metallicity hot core, it would indicate a highly evolved chemistry, and a hot core age $\sim 10^6$ years.

5.5.6 NH_3

Figures 5.46 and 5.47 show some inversion transitions of para-NH_3 from models G1, L2 and S2 at 10^4 years. All three models produce high peak intensities for all trans-

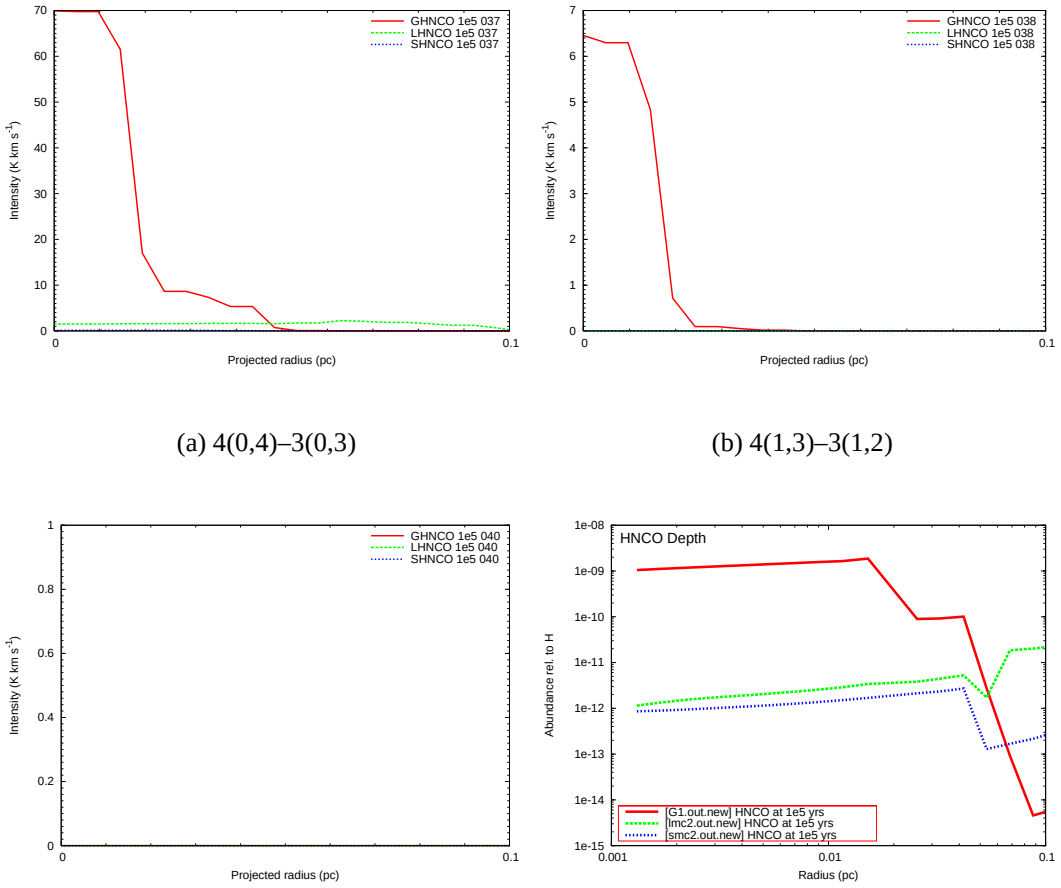

(a) 4(0,4)–3(0,3)

(b) 4(1,3)–3(1,2)

(c) 5(2,4)–4(2,3)

(d) HNCO fractional abundance

Figure 5.44: The intensity of some observable rotational transitions of HNCO, and the fractional HNCO abundance, from models G1, L2 and S2 at 10^5 years.

itions. The emission from models G1 and L2 is more extended than that from model S2, for all transitions. This is because the outer shells of model S2 contain much less NH_3 than the outer shells of models G1 and L2, as can be seen in Figure 5.46(f). The metastable transitions 1(1,1)-1(1,0) and 2(2,1)-2(2,0) have the flattest intensity profiles, as the bulk of the emission seen in these models is from the outer shells of the hot core. 3(1,1)-3(1,0) is potentially the most useful metallicity tracer transition at 10^4 years, as the peak intensities differ between the models by around 20 K km s^{-1}, and the intensities decrease with decreasing metallicity, across the whole projected radius.

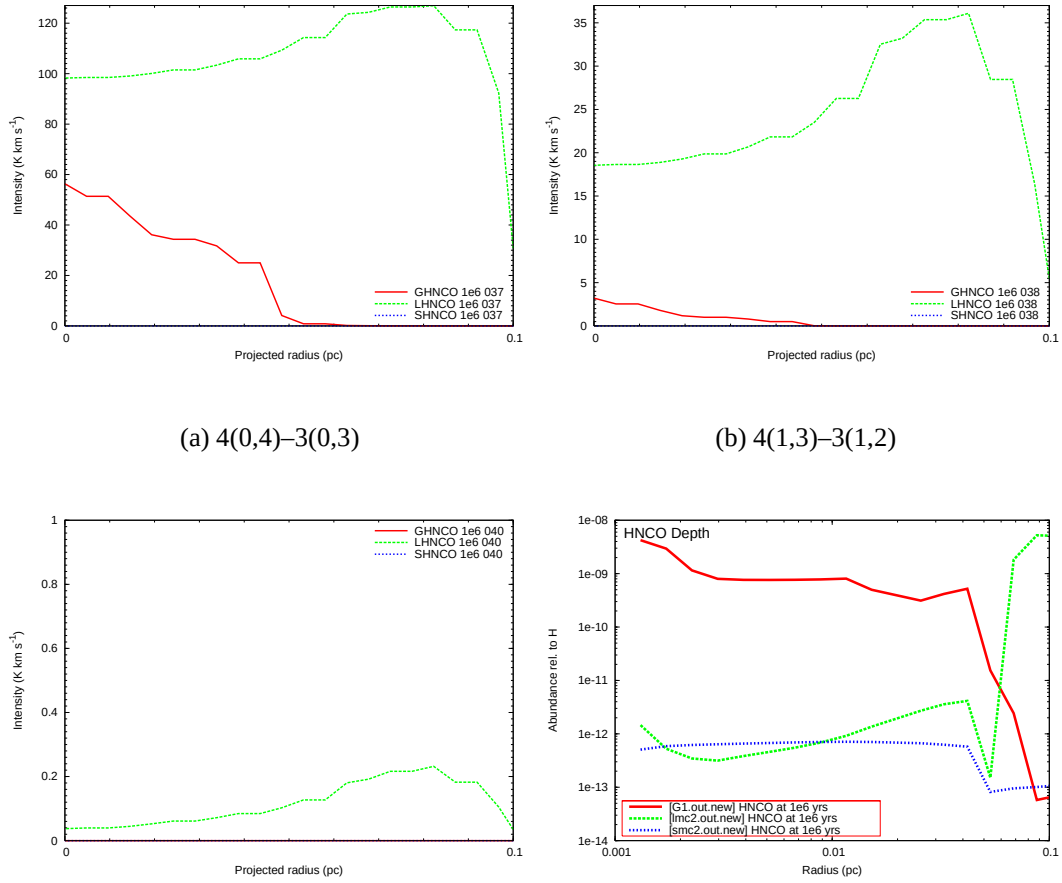

(a) 4(0,4)–3(0,3)

(b) 4(1,3)–3(1,2)

(c) 5(2,4)–4(2,3)

(d) HNCO fractional abundance

Figure 5.45: The intensity of some observable rotational transitions of HNCO, and the fractional HNCO abundance, from models G1, L2 and S2 at 10^6 years.

All the transitions in all the models have a high peak integrated intensity at 10^4 years, which means that NH_3 could be used a general tracer to locate hot cores at this time, independently of metallicity. All of the transitions in the three models are optically thick at 10^4 years, as seen in Table 5.4. The emission seen comes from the outer shells of the hot core.

Figures 5.48 and 5.49 show the same transitions at 10^5 years. The intensities produced by the different models are easily discernable at this time, as the peak intensities differ dramatically for some transitions, e.g. 3(2,1)-3(2,0) in Figure 5.46(e). The opacities

for the different transitions in the three models at 10^5 years can be seen in Table 5.5. The emission from models G1 and L2 is optically thick, particularly for the metastable transitions 1(1,1)-1(1,0) and 2(2,1)-2(2,0). The emission from model S2 is optically thin for some transitions, although the 1(1,1)-1(1,0) and 2(2,1)-2(2,0) transitions are optically thick. Figure 5.48(f) shows the fractional NH_3 abundance in each model at 10^5 years. The low fractional abundance in model S2 results in the much lower intensities produced by this model. At 10^5 years, it should be possible to identify hot cores at lower metallicity from the intensity of the NH_3 emission. The emission from all three models at this time is similarly extended, and much of it comes from the mid-outer shells of the hot core.

Figures 5.50 and 5.51 show the same inversion transitions for the three models at 10^6 years. The peak intensities for many of the transitions have decreased. This is caused by a reduction in the fractional NH_3 abundance in the intermediate shells in models G1 and L2, as seen in Figure 5.50(f). Transitions 4(4,1)-4(4,0) and 5(5,1)-5(5,0) have consistent, and high, peak intensities for the models at 10^6 years. These transitions trace the hottest, densest gas, as shown in Table 5.1. The consistency of these results can be explained as the temperature profile of the hot core model is the same for G1, L2, and S2, and it does not change with time. These transitions trace the inner shells of the hot core. It is not possible to easily distinguish the peak intensities of the different models from one another. However, these transitions could be used as tracers of hot, dense gas. The other transitions can be used in a more general result. The intensities seen are confusing, as for many transitions model S2 has a higher peak intensity than model L2. This is because these transitions are tracing the outer shells of the hot core, and as Figure 5.50(f) shows, in the outer shells, model S2 has a higher fractional NH_3 abundance than model L2. However, as a general rule, the G1 intensities are much higher than the sub-Galactic model intensities. Observations of NH_3 in an evolved hot core could thus be used to identify if such regions have sub-Galactic metallicity.

Overall, NH_3 is potentially a useful tracer of hot cores. High intensities are seen for many of the transitions, and so this species could be used to identify hot cores at low or

high metallicity. At 10^4 years, the extent and intensity of the emission can be used to distinguish between the models, and hence the underlying metallicity. The most useful transition at this time is 3(1,1)-3(1,0). At 10^5 years, many of the transitions (for example, 1(1,1)-1(1,0)) can be used to comparatively estimate the underlying metallicity of a hot core. The emission from the non-metastable transitions in model S2 is very low at this time. Such low intensity levels could be used to identify a hot core with very low metallicity. At 10^6 years, The inversion transitions can be used to identify whether a hot core has Galactic or sub-Galactic metallicity. The transitions 4(4,1)-4(4,0) and 5(5,1)-5(5,0) can be used to trace the densest, hottest gas at this time, independently of the underlying metallicity level.

5.5.7 Summary

Most of the RATRAN-modelled species are optically thick, for all three models at all three times. This means that the emission is tracing the temperature structure rather than the fractional abundance of the species. The use of rarer isotopologues would remove this problem, and allow the inner regions of extragalactic hot cores to be probed. However, for this to be possible, accurate values of common isotopic ratios in the galaxies modelled would need to be determined. For example if the $^{32}S/^{34}S$ ratio were known, $C^{34}S$ could be used to model and observe the inner regions of hot cores at varying metallicity. It would also be useful to know the $^{14}N/^{15}N$ ratio, so that species such as $HC^{15}N$ could be modelled. The results obtained often trace gas in the outer hot core shells. However, it should be noted that more extended emission does not always mean that a hot core is larger. In the context of these models, extended emission indicates high fractional abundances in the outer shells of a hot core. These results could be cautiously used by observers to determine the extent of the outer shells of a hot core. Many of the results can also be used to comparatively age hot cores, within a group. For example, if several hot cores were observed in the same region in another galaxy, the observed intensity of species such as $C^{18}O$ and $H^{13}CN$ could be used to determine

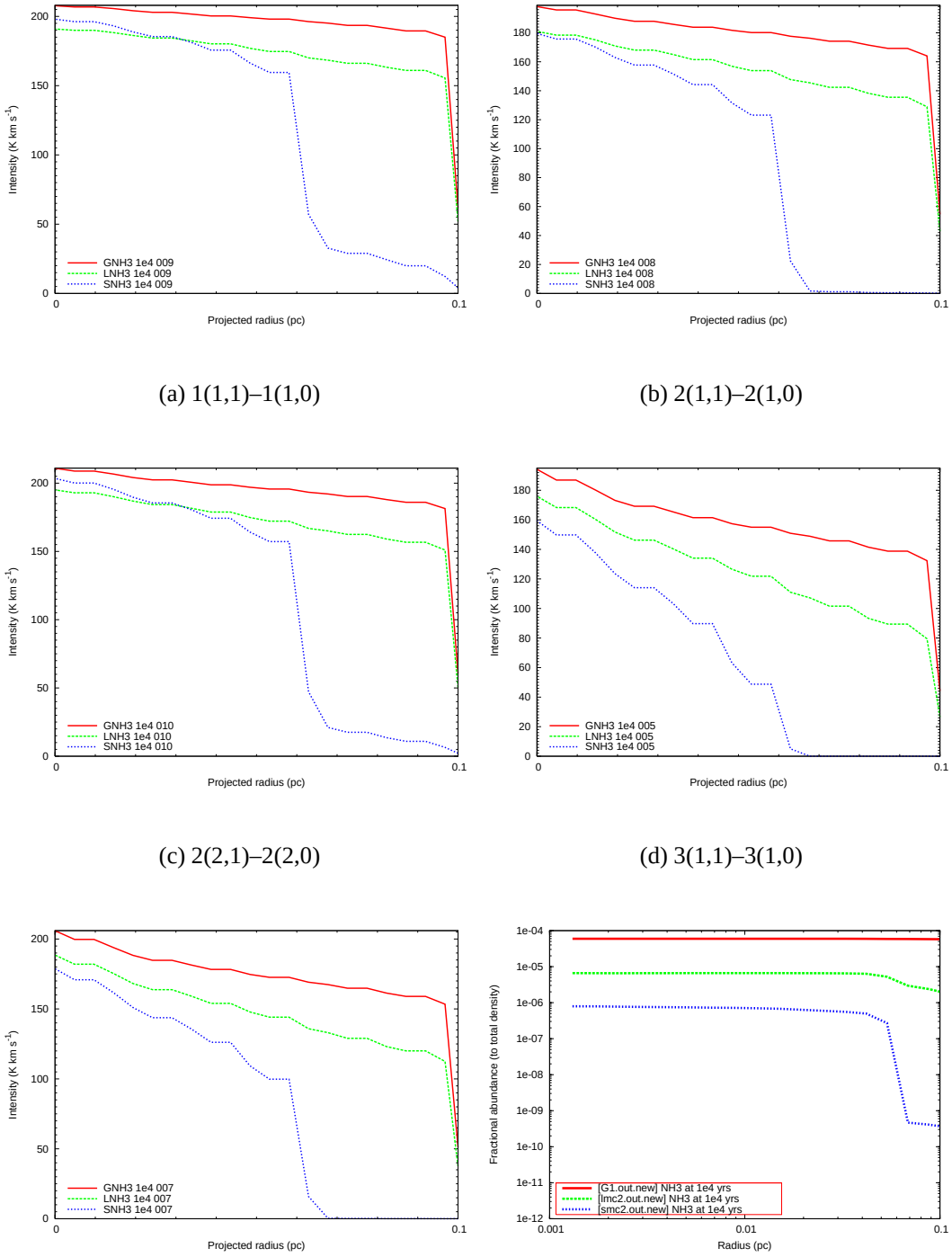

(a) 1(1,1)–1(1,0)

(b) 2(1,1)–2(1,0)

(c) 2(2,1)–2(2,0)

(d) 3(1,1)–3(1,0)

(e) 3(2,1)–3(2,0)

(f) NH_3 fractional abundance

Figure 5.46: The intensity of some observable inversion transitions of NH_3, and the fractional NH_3 abundance, from models G1, L2 and S2 at 10^4 years.

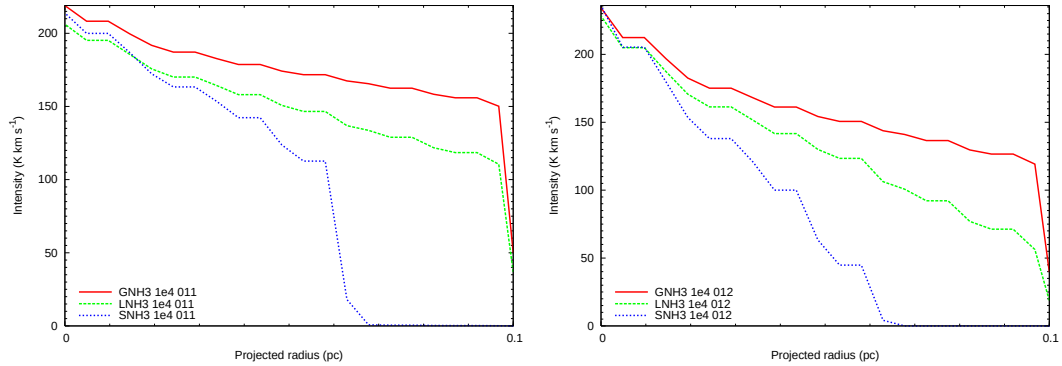

(a) 4(4,1)–4(4,0) (b) 5(5,1)–5(5,0)

Figure 5.47: The intensity of some more observable inversion transitions of NH_3, and the fractional NH_3 abundance, from models G1, L2 and S2 at 10^4 years.

the order of age/evolution of the hot cores.

Table 5.5.7 summarises the RATRAN modelled species, and how useful they are as metallicity tracers in hot cores.

Species	Metallicity Tracer?
^{13}CS	Could identify hot cores at very low metallicity at all times examined
C^{18}O	Could identify sub-Galactic metallicity at all times, but extent of emission may not indicate size of hot core
H^{13}CN	Could identify regions of very low metallicity from 10^5 years onwards
HN^{13}C	10^4 years – traces underlying metallicity level
	10^5 years – can identify regions with very low metallicity
	10^6 years – can identify regions with sub-Galactic metallicity
HNCO	No observable emission could indicate a young hot core at low metallicity
	If observed, emission may not indicate size or metallicity of hot core
NH_3	10^4–10^5 years – emission could reveal underlying metallicity level of hot core
	1e6 years – Could identify regions with sub-Galactic metallicity

Table 5.7: A summary of the RATRAN modelled species, and their ability to trace the underlying metallicity of a hot core

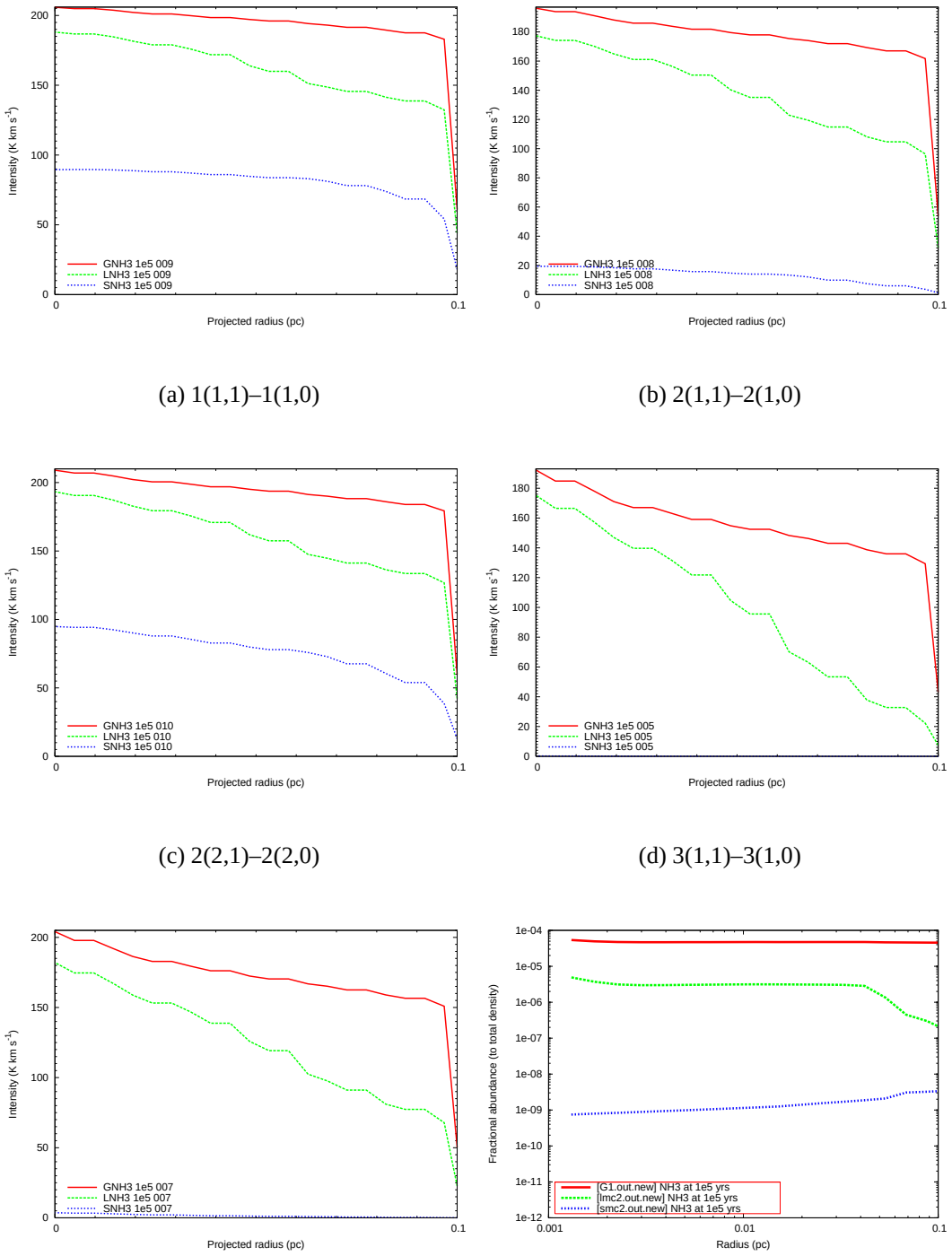

(a) 1(1,1)–1(1,0)

(b) 2(1,1)–2(1,0)

(c) 2(2,1)–2(2,0)

(d) 3(1,1)–3(1,0)

(e) 3(2,1)–3(2,0)

(f) NH_3 fractional abundance

Figure 5.48: The intensity of some observable rotational transitions of NH_3, and the fractional NH_3 abundance, from models G1, L2 and S2 at 10^5 years.

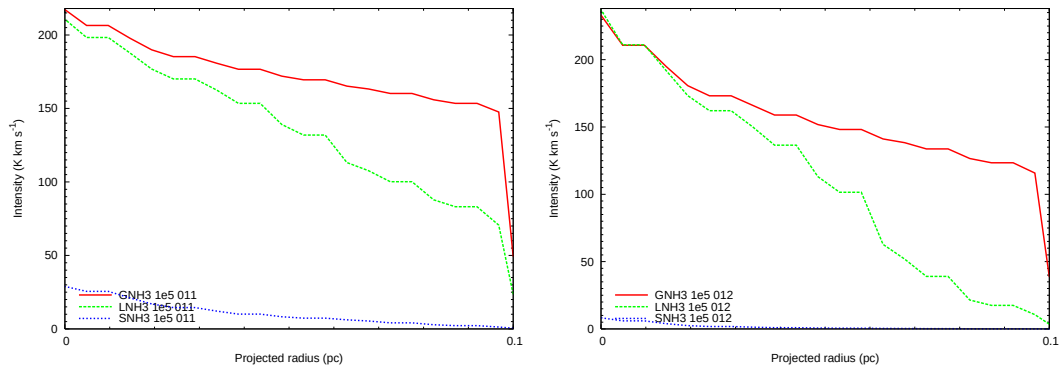

(a) 4(4,1)–4(4,0) (b) 5(5,1)–5(5,0)

Figure 5.49: The intensity of some more observable rotational transitions of NH_3 from models G1, L2 and S2 at 10^5 years.

5.5.8 Feasibility of Extragalactic Hot Core Observations

The intensities and structures predicted in this chapter may not be resolvable in high redshift galaxies, owing to the great distance between the Earth and such galaxies. However, in the LMC and SMC the individual hot cores could be resolved using ALMA. The online ALMA Sensitivity Calculator [1] can be used to estimate whether a predicted intensity can be observed within other galaxies. For example, the HNC integrated intensity in the LMC for the J=3–2 transition at 10^6 years peaks at 80 K km s^{-1}, as seen in Figure 5.42(b). The LMC is at a distance of roughly 50kpc, and the predicted structure has a diameter of around 0.12pc. This corresponds to a 0.5 arcsecond area in the sky. ALMA will be able to resolve an area of 1 arcsecond as standard, and 0.1 arcsecond resolution should also be easily achieved. The predicted structure will only fill 1/4 of the beam at 1” resolution. At a line width of 10 km s^{-1}, using 1” resolution, a 10 sigma detection should be possible within minutes.

Although it will be possible to observe the predicted intensities with ALMA, it will be more challenging (but not impossible) to resolve the finer structure within a hot cores – for example, limb brightening effects. With a resolution of 0.1”, it should be possible

[1] http://www.eso.org/sci/facilities/alma/observing/tools/etc/

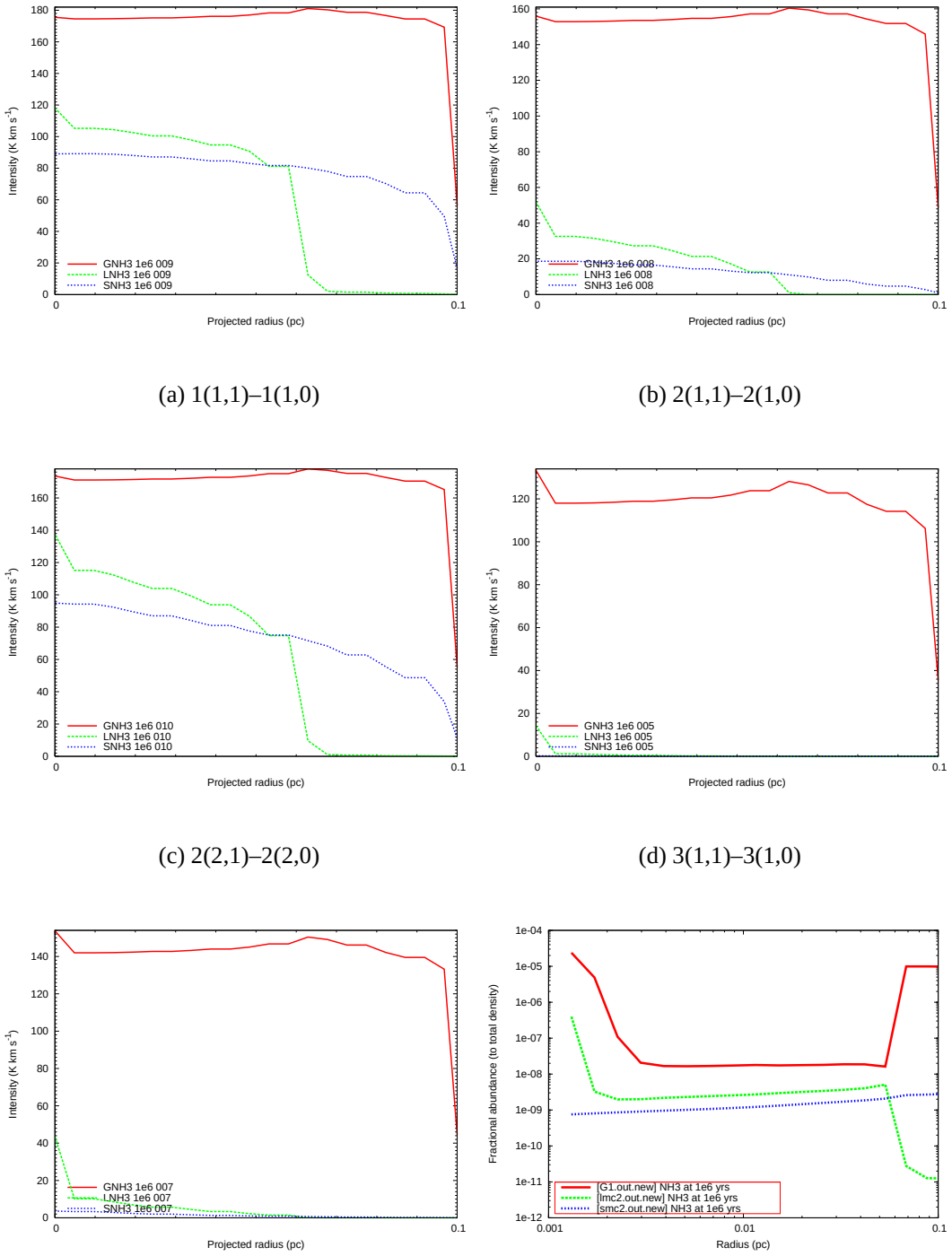

(a) 1(1,1)–1(1,0)

(b) 2(1,1)–2(1,0)

(c) 2(2,1)–2(2,0)

(d) 3(1,1)–3(1,0)

(e) 3(2,1)–3(2,0)

(f) NH_3 fractional abundance

Figure 5.50: The intensity of some observable rotational transitions of NH_3, and the fractional NH_3 abundance, from models G1, L2 and S2 at 10^6 years.

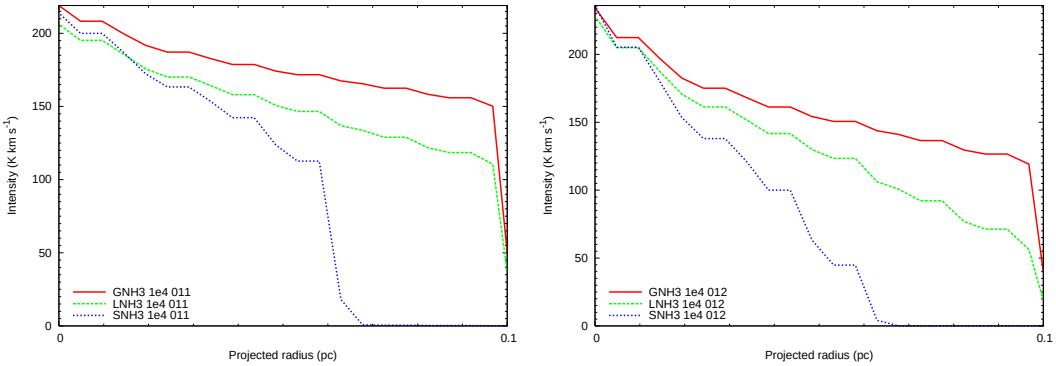

(a) 4(4,1)–4(4,0) (b) 5(5,1)–5(5,0)

Figure 5.51: The intensity of some more observable rotational transitions of NH_3 from models G1, L2 and S2 at 10^6 years.

to resolve the structure to some extent.

6

Summary and Conclusions

6.1 Dark Cloud Modelling

In the pseudo-time-dependent gas-phase dark cloud chemical modelling in Chapter 3, thirty-nine species were considered as possible tracers of the underlying metallicity in a dark cloud. The results of the analysis are summarised in Tables 6.1 – 6.3. The majority of the species do not trace the underlying metallicity of the cloud. The complex interplay between the various reactions in a chemical network creates a chemistry in which species are highly interdependent, and simple scaling of the fractional abundances with the underlying abundances does not occur. For instance, if the underlying abundance of nitrogen is halved, the resulting fractional abundance of ammonia is not automatically halved.

The nitrogen-bearing species are shown in Table 6.1. The most useful species are those which contain both carbon and nitrogen - namely HCN, HNC, HC_3N and CH_3CN. Observations of these species in a dark cloud could allow upper limits for the underlying metallicity to be estimated, provided the chemistry had not reached steady state (typically at times $>10^7$ years). The combination of both carbon and nitrogen in these species traces the underlying metallicity in a general sense, but does not trace the underlying abundance of any particular element. The result is interesting as, of the species ex-

amined, those which contain either nitrogen or carbon do not trace the underlying metallicity, in a general or specific sense. The two elements in combination are able to trace the general metallicity level, as both elements must have a certain abundance in order to form species such as HCN and HC_3N in the quantities produced by the models. In Section 3.4.3 it was discussed that the species NH_3, HCN, HNC, NS, CN, NH_2CN, and CH_3CN trace the underlying N/O ratio at steady state. If a dark cloud were determined to be at chemical equilibrium, observations of these species could perhaps be used to estimate the underlying N/O ratio in the cloud. However, it is unlikely that a dark cloud would reach a gas-phase chemical equilibrium similar to that seen in the model, in the presence of dust grains. Depletion of gas-phase species onto the dust grain surfaces would occur before a steady state chemistry could be reached.

None of the hydrocarbon species examined are useful metallicity tracers. This is

Species	**Early-time tracer?**	**Steady state tracer?**
NH_3	No	No
HCN	Yes – provides lower limit	No
HNC	Yes – provides lower limit	No
HC_3N	Yes – provides lower limit	No – low abundance
NS	No	No
NO	No	No
CN	No	No
NH_2CN	No	No
CH_2NH	No	No
CH_3CN	Yes – provides lower limit	No
N_2H^+	No	Possibly

Table 6.1: A summary of the observed extragalactic nitrogen-bearing species and their potential as metallicity tracers.

because the carbon in the model becomes locked up in the stable CO molecule in increasing amounts, with increasing time. The hydrocarbons form at early time, and peak

in abundance between 10^3 and 10^6 years. These species are then destroyed, and the freed carbon goes on to form CO. Similar fractional abundances of each hydrocarbon form in each model, regardless of the underlying metallicity. At early time and steady state, the fractional abundances of the hydrocarbons in each model do not reflect the underlying metallicity of the cloud.

The oxygen-bearing species are shown in Table 6.2. Many of these species do not trace the underlying metallicity. CO^+ and HCO could potentially trace the underlying metallicity at steady state, but the low fractional abundances seen make this an unlikely eventuality. H_2CO inversely traces the underlying metallicity at steady state. If an observation showed H_2CO to be abundant in a dark cloud, this could indicate a low underlying metallicity. H_2O traces the underlying metallicity at steady state. H_2O is highly abundant in the Galactic, LMC and SMC models, and could potentially be observed. OH is the most useful oxygen-bearing metallicity tracer. It inversely traces the underlying metallicity of a dark cloud from 3×10^5 years onwards. Observations of this species could be used to estimate a range of values for the underlying metallicity of a dark cloud.

The sulphur-bearing species are shown in Table 6.3. All of the species shown trace

Species	**Early-time tracer?**	**Steady state tracer?**
H_2O	No	Yes
H_3O^+	No	No
CO^+	No	No – low abundance
H_2CO	No	Yes – could provide lower limit
HOC^+	No	No
CH_3OH	No	No
HCO	Possibly	No – low abundance
HCO^+	No	No
OH	No	Yes

Table 6.2: A summary of the oxygen-bearing species and their potential as metallicity tracers.

the underlying metallicity of the cloud at steady-state. However, H_2S, C_2S and H_2CS all have low steady-state fractional abundances (in the range 10^{-12}–10^{-10}), and so it may not be possible to observe these species in extragalactic dark clouds. OCS appears to be the best metallicity tracer amongst the sulphur-bearing species. It reaches steady-state chemistry before the other sulphur-bearing species. The fractional OCS abundances are reasonably high in each model, and the values from the different models can easily be distinguished from one another at steady state.

The best metallicity tracers in the dark cloud models are ratios of various species to

Species	**Early-time tracer?**	**Steady state tracer?**
SO	No	Yes
SO_2	No	Yes
CS	No	Yes
H_2S	No	Possibly – low abundance
C_2S	No	No – low abundance
H_2CS	No	Possibly – low abundance
OCS	No	Yes

Table 6.3: A summary of the sulphur-bearing species and their potential as metallicity tracers.

CO. Table 6.4 lists the species, and which aspect of metallicity they are able to trace. The HCO^+/CO ratio can be used to trace the underlying heavy metal abundance from 10^5 years onwards. This complements the work done by Caselli et al. (1998), who constructed a formula to determine the underlying heavy metal abundance from this ratio, at steady-state. The CO/H_3O^+ and OH/CO ratios can be used to estimate the underlying carbon abundance of a dark cloud, from 3×10^4 years and 10^5 years onwards respectively. The CO/H_3O^+ ratio is more useful than the OH/CO ratio, as it is valid from an earlier time point in the chemical ago of the dark cloud in question. If observations of the same cloud were made at different frequencies, both ratios could be used to provide an estimated range for the underlying carbon abundance of the cloud.

Table 6.5 shows some inferences which could be made using observations of a dark

Species	**Metallicity tracer?**
HCO^+/CO	Traces underlying heavy metal abundance from 10^5 years onwards
CO/H_3O^+	Constrains range for underlying carbon abundance from 3×10^4 years onwards
OH/CO	Constrains range for underlying carbon abundance from 10^5 years onwards

Table 6.4: A summary of some ratios of species and their potential as metallicity tracers.

cloud in the Milky Way or another galaxy.

Overall, the dark cloud models allow the identification of several useful metallicity

Species	**Observed fractional abundance or ratio**	**Inference**
HCN	10^{-8}	Metallicity ≥ model DC3
OH	2×10^{-7}	Metallicity ≥ model S
OCS	4×10^{-10}	If cloud is at steady state – metallicity similar to model LMC
HCO^+/CO	3×10^{-4}	If cloud age $>10^5$ years – M abundance in range $(2.73–4.34)\times10^{-10}$
CO/H_3O^+	8000	If cloud age > 3×10^5 years – underlying C abundance in range $(2.62–2.69)\times10^{-5}$
OH/CO	4000	If cloud age $>10^6$ years – underlying C abundance in range $(1.1–1.2)\times10^{-4}$

Table 6.5: Some example inferences which could be made from dark cloud observations

tracer species, and many more species which are not useful in this capacity. Species which are not useful metallicity tracers can be used in other ways, such as tracing the location/extent or the chemical age of dark clouds. The species which appear to trace the underlying metallicity at steady state may not be useful in practice, as dark clouds may not reach a gas-phase chemical equilibrium in the same way the chemical models do, owing to the depletion of gas-phase species onto dust grain surfaces. Ratios such

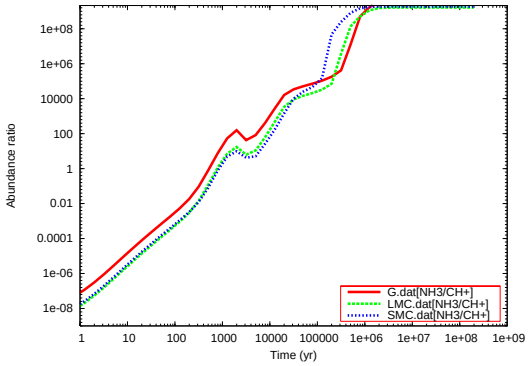

(a) NH_3/C^+ in models G, L and S

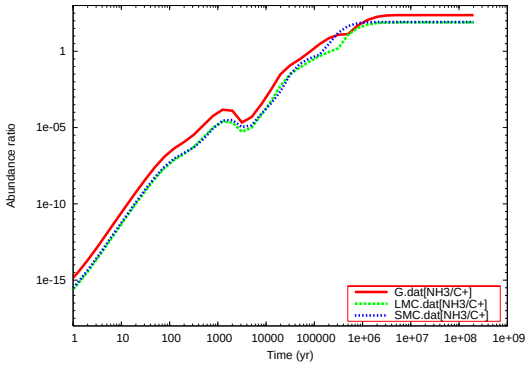

(b) NH_3/CH^+ in models G, L, S and DC1-DC6.

Figure 6.1: The NH_3/C^+ and NH_3/CH^+ ratios in models G, L and S. These ratios appear to be largely independent of underlying metallicity. If observed, these ratios could be used to estimate the age of a dark cloud.

as NH_3/CH^+ and NH_3/C^+ can be used to estimate the chemical age of a dark cloud, regardless of the underlying metallicity, as seen in Figures 6.1(a) and 6.1(b) respectively. If these ratios can be determined for a cloud, it may be possible to estimate the cloud age, and thus more accurately use the metallicity tracer species to determine the underlying metallicity of the cloud.

6.2 Hot Core Modelling

Chapter 4 described the use of a two-phase gas-grain chemical hot core model, which was used in an attempt to identify potential metallicity tracer species in hot cores. Table 6.6 summarises the species analysed, and their potential as hot core metallicity tracers. CO was the least useful species examined – this molecule does not appear to trace the underlying metallicity of a hot core. HCO^+ was also not a very useful metallicity tracer. The majority of the HCO^+ gas exists in the cooler, less dense gas in the outer parts of the hot core. This species could inversely trace the underlying metallicity to

some degree, but only in the gas in the outer shells of the hot core. It could be argued that these shells are less important/interesting than the inner shells, which are closer to the protostar.

HCN is able to trace a lower limit for the N/C ratio at 10^4 years. At times beyond 10^5 years, this species traces the general underlying metallicity of the hot core. HNC is preferable to HCN as a metallicity tracer, as it is useful from 10^4 years onwards. HNC traces the underlying metallicity of the hot core, rather than the dust/gas ratio. HNC is a useful metallicity tracer, as the fractional abundances seen are fairly constant across the hot core in each model, and the fractional abundances in each model are easily distinguished from one another.

The fractional HNCO abundance in a hot core could be used to identify whether the region existed at Galactic or sub-Galactic metallicity, at times up to 10^5 years. CH_3OH could also be used to determine if a hot core existed at Galactic or sub-Galactic metallicity, at 10^5 years.

The fractional HC_3N abundance could be used to estimate the dust/gas ratio in a hot core at 10^4 years, or to estimate the underlying metallicity at 10^6 years. HC_3N can only be used as a metallicity tracer if the age of the hot core can be relatively accurately determined. The fractional CS abundance from the inner regions of the hot core can be used to determine if the dust/gas ratio is Galactic or sub-Galactic. For this result to be useful, the CS emission would have to be optically thin, in order that the gas from the most central regions of the hot core could be observed. This may be possible if observing an isotopologue, such as $C^{34}S$. $C^{32}S$ is likely to optically thick at all of the metallicities modelled, as this species is highly abundant in the hot core models.

The fractional NH_3 abundance traces the underlying nitrogen abundance in the higher metallicity models (G1 and L2) up to 10^5 years. The low NH_3 fractional abundances seen in the S2 model reveal the low dust/gas ratio in this model. Low fractional NH_3 abundances can be used to infer a low dust/gas ratio at 10^4, 10^5 and 10^6 years. The relationship between the NH_3 abundance and the underlying nitrogen, at early times, in the G1 and L2 models appears to be very precise. However, it is possible that the

modelling of the grain-surface NH_3 formation is somewhat over-simplified. The grain surface model results in 80% of the adsorbed nitrogen atoms becoming fully hydrogenated, forming NH_3. This may not be the case in reality, as the material which exists in a core prior to collapse is likely to have been processed in the gas-phase, and the majority of the nitrogen may not initially exist as atomic nitrogen.

Many of the species are most useful as metallicity tracers when the chemical age of the hot core is accurately known. Several authors have discussed how the chemical age of a hot core could be determined. Charnley (1997) originally suggested the idea of using ratios of sulphur-bearing species as 'chemical clocks' (namely, SO/H_2S and SO/SO_2) in order to determine the age of a hot core. Wakelam et al. (2004) further analysed the sulphur chemistry in hot core chemical models, and concluded that the use of sulphur-bearing species as chemical clocks was not straightforward.

Rodgers & Charnley (2001) argued that the NH_3/CH_3OH ratio could be used to estimate the chemical age of a hot core under specific circumstances, but this ratio is also sensitive to the hot core temperature, and grain mantle composition. For these reasons, this species is not a useful tracer of the hot core age.

Chapman et al. (2009) found that the fractional abundances of the larger cyanopolyynes (e.g. HC_5N, HC_7N) peaked in their hot core model at $\sim 10^{4.5}$ years. The cyanopolyynes were found to be rapidly destroyed by $10^{5.5}$ years. The observation of these species in a hot core could therefore be used to constrain the chemical age of the hot core.

If a reliable 'chemical clock' can be identified for hot cores (independent of the underlying metallicity), observations of the hot core metallicity tracer species discussed in Chapter 4 will be much easier to interpret. Of the species examined, HNC and NH_3 are the most useful metallicity tracers in a hot core of indeterminate age. Table 6.7 gives some example inferences which could be deduced from the listed fractional abundances, if observed.

Species	Potential metallicity tracer?
CO	Probably not – similar abundances in models G1, L2, S2
HCO^+	Possible inverse tracer – could trace cooler, less dense gas in outer shells
HCN	Yes – traces lower limit for N/C ratio at 10^4 years. After this, traces metallicity generally
HNC	Yes – traces underlying elemental abundances, not dust/gas. Most useful before 10^6 years
HNCO	Possibly – could identify Galactic or sub-Galactic metallicity up to 10^5 years
HC_3N	Possibly – if hot core age accurately known, could trace dust/gas at 10^4 years or elemental abundances at 10^6 years
CH_3OH	Possibly – if hot core age is 10^5 years, could identify Galactic or sub-Galactic metallicity
CS	Possibly – inner region observations can determine if dust/gas ratio is Galactic or sub-Galactic
NH_3	Yes – traces underlying N abundance in more metallic models at 10^4 and 10^5 years. Reveals low dust/gas ratio in very low metallicity model, at all times.

Table 6.6: Possible metallicity tracers in the Multidepth hot core model

Species	**Observed fractional abundance**	**Inference**
HCN	7×10^{-7}	At 10^4 years – an N/C ratio ~0.57
HNC	5×10^{-8}	At 10^4 or 10^5 years – an L2 model type metallicity
HNCO	1×10^{-12}	At 10^4 or 10^5 years – sub-Galactic metallicity
CH_3OH	2×10^{-6}	At 10^5 years – metallicity ≥ L2 model
NH_3	6×10^{-4}	At 10^4 or 10^5 years – a G1 model type metallicity

Table 6.7: Some example inferences which could be made from hot core observations

6.3 RATRAN Modelling of Hot Cores

The RATRAN results model the integrated intensities which could be observed from hot cores with varying underlying metallicity (as modelled in this thesis). The species and transitions chosen for modelling are thought to be abundant, and observable in hot cores. $^{12}C/^{13}C$ and $^{16}O/^{18}O$ ratios were used in order to deplete the hot core fractional abundances, so that the RATRAN modelled results were not too optically thick. The ratios used have a profound effect on the results – for example, the fractional CO abundance in model L2 is higher than that in G1 at 10^4 years, as seen in Figure 4.20(a). However, a higher $^{12}C/^{13}C$ ratio was assumed for the LMC compared with the Galactic value – this led to lower predicted peak intensities of $C^{18}O$ at 10^4 years in model L2 than in model G1, as seen in Figure 5.34. Figure 5.34 also shows that large regions of extended emission do not necessarily indicate large regions of extended density. The $C^{18}O$ emission is more extended for model L2 than model G1. However, this does not indicate that the hot core itself is larger/more extended. The hot core model in both cases is exactly the same size, and has the same density and temperature profiles. The more extended emission in model L2 is caused by the fractional CO abundance only.

Table 6.8 summarises the species modelled using RATRAN, and their ability to trace the underlying metallicity of a hot core. The most useful metallicity tracer species are $HN^{13}C$ and NH_3. These species could both be used to identify regions with very low underlying metallicity. If the age of the hot core could be constrained, all of the species could be used to estimate the underlying metallicity much more accurately. Isotopomers such as $^{15}NH_3$ are likely to be optically thin when observed in hot cores. Estimates of the $^{14}N/^{15}N$ ratio in the LMC and SMC would allow $^{15}NH_3$ to be modelled using RATRAN. Optically thin species such as $^{15}NH_3$ could be used to probe the hot, dense, inner shells of the hot cores.

Table 6.9 lists some example integrated intensities for some of the species modelled, along with the inferences which could be made if these values were observed.

Species	Metallicity Tracer?
^{13}CS	Could identify hot cores at very low metallicity at all times examined
C^{18}O	Could identify sub-Galactic metallicity at all times, but extent of emission may not indicate size of hot core
H^{13}CN	Could identify regions of very low metallicity from 10^5 years onwards
HN^{13}C	10^4 years – traces underlying metallicity level
	10^5 years – can identify regions with very low metallicity
	10^6 years – can identify regions with sub-Galactic metallicity
HNCO	If no emission is observed this could indicate a young hot core at low metallicity
	If observed, emission may not indicate size or metallicity of hot core
NH$_3$	10^4–10^5 years – emission could reveal underlying metallicity level of hot core
	10^6 years – Could identify regions with sub-Galactic metallicity

Table 6.8: A summary of the RATRAN modelled species, and their ability to trace the underlying metallicity of a hot core

Species	Observed intensity	Inference
^{13}CS	More extended emission in LMC/SMC than Milky Way	^{13}CS could be tracing outer shells of gas. Use C^{34}S to investigate further
	At 10^5 years, J=1-0 intensity < 2 Kkms^{-1}	Underlying metallicity is similar to model S2
C^{18}O	More extended emission in LMC/SMC than Milky Way	C^{18}O could be tracing outer shells of gas. Use ^{13}C^{18}O to investigate further
H^{13}CN	At times ≥ 10^5 years, J=1-0 intensity in range 130–140 Kkms^{-1}	G1 type metallicity
	At times ≥ 10^5 years, J=1-0 intensity in range 95–125 Kkms^{-1}	LMC type metallicity
	At times ≥ 10^5 years, J=1-0 intensity in range 10–45 Kkms^{-1}	Low metallicity, possibly similar to SMC model
HN^{13}C	At 10^4-10^6 years, intensity > 125 Kkms^{-1} for J=1-0, J=3-2 or J=4-3	G1 type metallicity
	At 10^4-10^5 years, intensity < 50 Kkms^{-1} for J=1-0	S2 type metallicity
	At 10^6 years, intensity < 120 Kkms^{-1} for J=1-0,J=3-2 or J=4-3	Sub-Galactic metallicity
HNCO	At 10^4-10^5 years, intensity < 5 Kkms^{-1} for 4(0,4)-3(0,3)	Sub-Galactic metallicity
NH3	At 10^5 years, intensity < 100 Kkms^{-1} for 1(1,1)-1(1,0) or 2(2,1)-2(2,0)	S2 type metallicity
	At 10^6 years, peak intensity > 120 Kkms^{-1} for 3(1,1)-3(1,0)	G1 type metallicity
	At 10^6 years, peak intensity < 20 Kkms^{-1} for 3(1,1)-3(1,0)	Sub-Galactic metallicity

Table 6.9: Some example inferences which could be made from observations of various transition intensities in hot cores

6.4 Future Work

Throughout this thesis, an emphasis has been made on producing observable model outputs. The species discussed as metallicity tracers in Chapters 3 and 4 have all been observed in extragalactic regions[1]. The particular transitions of the species modelled using RATRAN in Chapter 5 have all been observed in hot cores (e.g. Olmi et al. 2003; Johnstone et al. 2003; Bayet et al. 2009). It should therefore be possible to test the predictions made in this thesis, through the observation of star-forming regions in the Milky Way and the Magellanic Clouds.

Hot core models could be built to include less common isotopes, such as ^{13}C and ^{15}N. These models could be used to produce fractional abundances of isotopomers such as $^{15}NH_3$ and HN^{13}C. The less abundant isotopomers are more likely to be optically thin than their more common counterparts (e.g. HN^{13}C is less common than HNC). If more fully modelled, these isotopomers could be used to probe the inner regions of hot cores in the Milky Way, and other galaxies. However, credible hot core models would only be possible for galaxies in which ratios such as ^{14}N/^{15}N can be estimated, to a reasonable degree of accuracy.

The RATRAN results presented here are not convolved with telescope beams. This could be done for sub-mm/mm telescopes (e.g. JCMT) which are able to observe the modelled species in hot cores, at mm and sub-mm wavelengths. The model results could then be more directly compared with observations of suitable regions in the Milky Way, the LMC and the SMC.

In reality, hot cores and dark clouds do not exist in isolation. They are component parts of larger star-forming regions, which comprise of many parts, including photon-dominated regions (henceforth PDRs), dark clouds, hot cores and HII regions. An ensemble-model of a star-forming region could be made. This would include proportional representation of fractional abundances taken from PDR, hot core and dark cloud models. Ensemble-models could be run with varying underlying metallicities.

[1] www.astro.uni-koeln.de/site/vorhersagen/molecules/extragalactic

The resulting fractional abundances could be used to identify which species and ratios could be used as metallicity tracers in star-forming regions in other galaxies. Different species are likely to predominantly exist in certain regions within the ensemble-model – these species could be used to trace the type of gas in which the emission originates. For example, HCO^+ is likely to be more typically observed in a PDR than a hot core.

It is thought that HCN/HCO^+ emission ratio can be used to differentiate between starburst and AGN galaxies. HCO^+ is thought to be more abundant than HCN in starburst galaxies (Krips et al. 2006;Wang et al. 2004) whereas HCN is thought to be more abundant in galaxies with an AGN (Imanishi et al. 2007;Kohno et al. 2008). Observations of the HCN/HCO^+ ratio, or the fractional abundances of these species, could be used in conjunction with the hot core models to further explore the validity of using these species as identifiers of galaxy type.

The wider motivation behind this work is a desire to increase understanding of how individual star forming regions have evolved, and influenced galaxies, over cosmological timescales. New telescopes, such as ALMA, will allow radiation from distant galaxies to be resolved at a higher level of detail than is currently possible. Comparisons of the results presented in this thesis with ALMA observations of the Milky Way, LMC and SMC could be made. It is hoped that these model results will aid observers' understanding of star-forming regions at low metallicity, and help to interpret their results.

Bibliography

Allen M. & Robinson G.W. The molecular composition of dense interstellar clouds. *ApJ*, vol. 212:396–415 (Mar. 1977).

Alves J., Lada C.J., & Lada E.A. Correlation between Gas and Dust in Molecular Clouds: L977. *ApJ*, vol. 515:265–274 (Apr. 1999).

Banerji M., Viti S., Williams D.A., & Rawlings J.M.C. Timescales for Low-Mass Star Formation in Extragalactic Environments: Implications for the Stellar Initial Mass Function. *ApJ*, vol. 692:283–289 (Feb. 2009).

Bayet E., Aladro R., Martín S., Viti S., & Martín-Pintado J. Extragalactic CS Survey. *ApJ*, vol. 707:126–136 (Dec. 2009).

Bayet E., Bell T., Viti S., Rawlings J., Roueff E., & Williams D. Modelling the chemistry of external galaxies. In *Molecules in Space and Laboratory* (Dec. 2007).

Bayet E., Viti S., Williams D.A., & Rawlings J.M.C. Molecular Tracers of High-Mass Star Formation in External Galaxies. *ApJ*, vol. 676:978–990 (Apr. 2008).

Bel N., Viala Y.P., & Guidi I. Chemical equilibrium from diffuse to dense clouds. II Interstellar clouds in the Magellanic clouds. *A&A*, vol. 160:301–309 (May 1986).

Bertoldi F., Cox P., Neri R., Carilli C.L., Walter F., Omont A., Beelen A., Henkel C., Fan X., Strauss M.A., & Menten K.M. High-excitation CO in a quasar host galaxy at z =6.42. *A&A*, vol. 409:L47–L50 (Oct. 2003).

Brandner W., Clark J.S., Stolte A., Waters R., Negueruela I., & Goodwin S.P. Intermediate to low-mass stellar content of Westerlund 1. *A&A*, vol. 478:137–149 (Jan. 2008).

Brown P.D. The grain-surface formation of complex molecules. *MNRAS*, vol. 243:65–71 (Mar. 1990).

Brown P.D., Charnley S.B., & Millar T.J. A model of the chemistry in hot molecular cores. *MNRAS*, vol. 231:409–417 (Mar. 1988).

Cappa de Nicolau C.E. & Poppel W.G.L. OH- and HI-observations of the CrA dark cloud complex. *A&AS*, vol. 88:615–624 (Jun. 1991).

Caselli P. Chemical Processes in Star Forming Regions. In M. S. N. Kumar, M. Tafalla, & P. Caselli, editor, *Cores to Clusters: Star Formation with Next Generation Telescopes*, pp. 47–+ (Nov. 2005).

Caselli P., Hasegawa T.I., & Herbst E. Chemical differentiation between star-forming regions - The Orion Hot Core and Compact Ridge. *ApJ*, vol. 408:548–558 (May 1993).

Caselli P., Walmsley C.M., Terzieva R., & Herbst E. The Ionization Fraction in Dense Cloud Cores. *ApJ*, vol. 499:234–+ (May 1998).

Chapman J.F., Millar T.J., Wardle M., Burton M.G., & Walsh A.J. Cyanopolyynes in hot cores: modelling G305.2+0.2. *MNRAS*, vol. 394:221–230 (Mar. 2009).

Charnley S.B. Hot Core Chemistry. *Ap&SS*, vol. 224:251–254 (Feb. 1995).

Charnley S.B. Sulfuretted Molecules in Hot Cores. *ApJ*, vol. 481:396–+ (May 1997).

Charnley S.B., Tielens A.G.G.M., & Millar T.J. On the molecular complexity of the hot cores in Orion A - Grain surface chemistry as 'The last refuge of the scoundrel'. *ApJL*, vol. 399:L71–L74 (Nov. 1992).

Chin Y., Henkel C., Millar T.J., Whiteoak J.B., & Marx-Zimmer M. Molecular abundances in the Magellanic Clouds. III. LIRS36, a star-forming region in the Small Magellanic Cloud. *A&A*, vol. 330:901–909 (Feb. 1998).

Crutcher R.M., Troland T.H., Goodman A.A., Heiles C., Kazes I., & Myers P.C. OH Zeeman observations of dark clouds. *ApJ*, vol. 407:175–184 (Apr. 1993).

Dickens J.E., Irvine W.M., Snell R.L., Bergin E.A., Schloerb F.P., Pratap P., & Miralles M.P. A Study of the Physics and Chemistry of L134N. *ApJ*, vol. 542:870–889 (Oct. 2000).

Dowell J.D., Buckalew B.A., & Tan J.C. The Initial Cluster Mass Function of Super Star Clusters in Irregular and Spiral Galaxies. *AJ*, vol. 135:823–835 (Mar. 2008).

Dyson J.E. & Williams D.A. *The physics of the interstellar medium* (1997).

Elmegreen B.G. Magnetic diffusion and ionization fractions in dense molecular clouds - The role of charged grains. *ApJ*, vol. 232:729–739 (Sep. 1979).

García-Rojas J., Esteban C., Peimbert A., Rodríguez M., Peimbert M., & Ruiz M.T. The chemical composition of the Galactic H II regions M8 and M17. A revision based on deep VLT echelle spectrophotometry. *Revista Mexicana de Astronomia y Astrofisica*, vol. 43:3–31 (Apr. 2007).

Garnett D.R. Element Abundances in Magellanic Cloud H II Regions from Carbon to Argon. In Y.-H. Chu, N. Suntzeff, J. Hesser, & D. Bohlender, editor, *New Views of the Magellanic Clouds*, vol. 190 of *IAU Symposium*, pp. 266–+ (1999).

Garrod R.T., Weaver S.L.W., & Herbst E. Complex Chemistry in Star-forming Regions: An Expanded Gas-Grain Warm-up Chemical Model. *ApJ*, vol. 682:283–302 (Jul. 2008).

Geppert W.D., Hamberg M., Thomas R.D., Österdahl F., Hellberg F., Zhaunerchyk V., Ehlerding A., Millar T.J., Roberts H., Semaniak J., Ugglas M.A., Källberg A., Si-

monsson A., Kaminska M., & Larsson M. Dissociative recombination of protonated methanol. *Chemical Evolution of the Universe, Faraday Discussions, volume 133, 2006, p.177*, vol. 133:177–+ (2006).

Hartquist T.W. & Williams D.A. Cosmic-Ray Induced Desorption and High Depletions in Dense Cores. *MNRAS*, vol. 247:343–+ (Nov. 1990).

Hasegawa T.I. & Herbst E. New gas-grain chemical models of quiescent dense interstellar clouds - The effects of H2 tunnelling reactions and cosmic ray induced desorption. *MNRAS*, vol. 261:83–102 (Mar. 1993a).

Hasegawa T.I. & Herbst E. Three-Phase Chemical Models of Dense Interstellar Clouds - Gas Dust Particle Mantles and Dust Particle Surfaces. *MNRAS*, vol. 263:589–+ (Aug. 1993b).

Hasegawa T.I., Herbst E., & Leung C.M. Models of gas-grain chemistry in dense interstellar clouds with complex organic molecules. *ApJS*, vol. 82:167–195 (Sep. 1992).

Heaton B.D., Little L.T., & Bishop I.S. The 'ultracompact hot core' of G34.3+0.15 - Arcsecond resolution ammonia observations. *A&A*, vol. 213:148–154 (Apr. 1989).

Herbst E. & Klemperer W. The Formation and Depletion of Molecules in Dense Interstellar Clouds. *ApJ*, vol. 185:505–534 (Oct. 1973).

Herbst E. & Leung C.M. Effects of large rate coefficients for ion-polar neutral reactions on chemical models of dense interstellar clouds. *ApJ*, vol. 310:378–382 (Nov. 1986).

Herbst E. & Leung C.M. Gas-phase production of complex hydrocarbons, cyanopolynes, and related compounds in dense interstellar clouds. *ApJS*, vol. 69:271–300 (Feb. 1989).

Hirota T., Ikeda M., & Yamamoto S. Mapping Observations of DNC and $HN^{13}C in Dark Cloud Cores. ApJ, vol. 594 : 859 - -868(Sep. 2003)$.

Hogerheijde M.R. & van der Tak F.F.S. An accelerated Monte Carlo method to solve two-dimensional radiative transfer and molecular excitation. With applications to axisymmetric models of star formation. *A&A*, vol. 362:697–710 (Oct. 2000).

Imanishi M., Nakanishi K., Tamura Y., Oi N., & Kohno K. Millimeter Interferometric HCN(1-0) and HCO^+(1 – 0)$Observations of Luminous Infrared Galaxies.$ $AJ, vol.$134 : 2366 – −2384($Dec.$2007).

Johnstone D., Boonman A.M.S., & van Dishoeck E.F. Astrochemistry of sub-millimeter sources in Orion. Studying the variations of molecular tracers with changing physical conditions. *A&A*, vol. 412:157–174 (Dec. 2003).

Kobulnicky C. & Johnson K.E. Finding Signatures of the Youngest Starbursts. *ArXiv Astrophysics e-prints* (Nov. 2000).

Kohno K., Nakanishi K., Tosaki T., Muraoka K., Miura R., Ezawa H., & Kawabe R. Dense gas in normal and active galaxies. *Ap&SS*, vol. 313:279–285 (Jan. 2008).

Krips M., Neri R., Garcia-Burillo S., Combes F., Martin S., Eckart A., Petitpas G., & Peck A. A HCN and HCO+ Multi-transition Line Survey in Active Galaxies: AGN versus Starburst Environments. In *Bulletin of the American Astronomical Society*, vol. 38 of *Bulletin of the American Astronomical Society*, pp. 1060–+ (Dec. 2006).

Langer W.D. Electron abundances and ionization rates in interstellar clouds. In D. C. Black & M. S. Matthews, editor, *Protostars and Planets II*, pp. 650–667 (1985).

Langer W.D. & Graedel T.E. Ion-molecule chemistry of dense interstellar clouds - Nitrogen-, oxygen-, and carbon-bearing molecule abundances and isotopic ratios. *ApJS*, vol. 69:241–269 (Feb. 1989).

Le Teuff Y.H., Millar T.J., & Markwick A.J. The UMIST database for astrochemistry 1999. *A&AS*, vol. 146:157–168 (Oct. 2000).

Lebouteiller V., Bernard-Salas J., Brandl B., Whelan D.G., Wu Y., Charmandaris V., Devost D., & Houck J.R. Chemical Composition and Mixing in Giant H II Regions: NGC 3603, 30 Doradus, and N66. *ApJ*, vol. 680:398–419 (Jun. 2008).

Leung C.M., Herbst E., & Huebner W.F. Synthesis of complex molecules in dense interstellar clouds via gas-phase chemistry - A pseudo time-dependent calculation. *ApJS*, vol. 56:231–256 (Oct. 1984).

Lintott C.J., Viti S., Williams D.A., Rawlings J.M.C., & Ferreras I. Hot cores: probes of high-redshift galaxies? *MNRAS*, vol. 360:1527–1531 (Jul. 2005).

Luca A., Voulot D., & Gerlich D. Dissociative recombination of protonated methanol. *WDS'02 Proceedings of Contributed Papers* (2002).

MacDonald G.H., Gibb A.G., Habing R.J., & Millar T.J. A 330-360 GHz spectral survey of G 34.3+0.15. I. Data and physical analysis. *A&AS*, vol. 119:333–367 (Oct. 1996).

McKee C.F. Photoionization-regulated star formation and the structure of molecular clouds. *ApJ*, vol. 345:782–801 (Oct. 1989).

Meyer D.M., Cardelli J.A., & Sofia U.J. The Abundance of Interstellar Nitrogen. *ApJL*, vol. 490:L103+ (Nov. 1997).

Meyer D.M., Jura M., & Cardelli J.A. The Definitive Abundance of Interstellar Oxygen. *ApJ*, vol. 493:222–+ (Jan. 1998).

Millar T.J., Defrees D.J., McLean A.D., & Herbst E. The sensitivity of gas-phase models of dense interstellar clouds to changes in dissociative recombination branching ratios. *A&A*, vol. 194:250–256 (Apr. 1988).

Millar T.J., Farquhar P.R.A., & Willacy K. The UMIST Database for Astrochemistry 1995. *A&AS*, vol. 121:139–185 (Jan. 1997a).

Millar T.J. & Freeman A. Chemical modelling of molecular sources. I - TMC-1. II - L183. *MNRAS*, vol. 207:405–423 (Mar. 1984).

Millar T.J. & Herbst E. Chemical modelling of dark clouds in the LMC and SMC. *MNRAS*, vol. 242:92–97 (Jan. 1990).

Millar T.J., Leung C.M., & Herbst E. How abundant are complex interstellar molecules? *A&A*, vol. 183:109–117 (Sep. 1987).

Millar T.J., MacDonald G.H., & Gibb A.G. A 330-360 GHz spectral survey of G 34.3+0.15. II. Chemical modelling. *A&A*, vol. 325:1163–1173 (Sep. 1997b).

Millar T.J. & Nejad L.A.M. Chemical modelling of molecular sources. IV - Time-dependent chemistry of dark clouds. *MNRAS*, vol. 217:507–522 (Nov. 1985).

Millar T.J. & Williams D.A. *Dust and chemistry in astronomy* (Jan. 1993).

Minh Y.C. & van Dishoeck E.F., editors. *Astrochemistry: From Molecular Clouds to Planetary Systems*, vol. 197 of *IAU Symposium* (2000).

Nomura H. & Millar T.J. The physical and chemical structure of hot molecular cores. *A&A*, vol. 414:409–423 (Feb. 2004a).

Nomura H. & Millar T.J. The physical and chemical structure of hot molecular cores. *A&A*, vol. 414:409–423 (Feb. 2004b).

Okada Y., Onaka T., Miyata T., Okamoto Y.K., Sakon I., Shibai H., & Takahashi H. Si and Fe Depletion in Galactic Star-forming Regions Observed by the Spitzer Space Telescope. *ApJ*, vol. 682:416–433 (Jul. 2008).

Olmi L., Cesaroni R., Hofner P., Kurtz S., Churchwell E., & Walmsley C.M. High resolution observations of the hot core in G29.96-0.02. *A&A*, vol. 407:225–235 (Aug. 2003).

Oppenheimer M. & Dalgarno A. The Fractional Ionization in Dense Interstellar Clouds. *ApJ*, vol. 192:29–32 (Aug. 1974).

Pineda J.E., Caselli P., & Goodman A.A. CO Isotopologues in the Perseus Molecular Cloud Complex: the X-factor and Regional Variations. *ApJ*, vol. 679:481–496 (May 2008).

Polehampton E.T., Baluteau J., & Swinyard B.M. Oxygen isotopic ratios in galactic clouds along the line of sight towards ¡ASTROBJ¿Sagittarius B2¡/ASTROBJ¿. *A&A*, vol. 437:957–965 (Jul. 2005).

Rae J.G.L., Bell N., Hartquist T.W., Pilling M.J., & Ruffle D.P. Reduced networks governing the fractional ionisation in interstellar molecular clouds. *A&A*, vol. 383:738–746 (Feb. 2002).

Rodgers S.D. & Charnley S.B. Chemical Differentiation in Regions of Massive Star Formation. *ApJ*, vol. 546:324–329 (Jan. 2001).

Ruffle D.P., Hartquist T.W., Caselli P., & Williams D.A. The sulphur depletion problem. *MNRAS*, vol. 306:691–695 (Jul. 1999).

Savage B.D. & Sembach K.R. Interstellar Abundances from Absorption-Line Observations with the Hubble Space Telescope. *ARA&A*, vol. 34:279–330 (1996).

Scoville N.Z. & Kwan J. Infrared sources in molecular clouds. *ApJ*, vol. 206:718–727 (Jun. 1976).

Shalabiea O.M. The effect of the initial elemental abundance on gas-grain chemical models. *A&A*, vol. 370:1044–1055 (May 2001).

Spitzer L. *Physical processes in the interstellar medium* (1978).

Stahl O., Casassus S., & Wilson T. Interstellar $^{12}C/^{13}C\,from CH^{+}\,absorption lines$: $results\,from\,an\,extended\,survey. A\&A, vol.$477 : 865 – –875($Jan.$2008).

Stanimirovic S., Staveley-Smith L., van der Hulst J.M., Bontekoe T.R., Kester D.J.M., & Jones P.A. Cool dust and gas in the Small Magellanic Cloud. *MNRAS*, vol. 315:791–807 (Jul. 2000).

Suzuki H., Yamamoto S., Ohishi M., Kaifu N., Ishikawa S., Hirahara Y., & Takano S. A survey of CCS, HC3N, HC5N, and NH3 toward dark cloud cores and their production chemistry. *ApJ*, vol. 392:551–570 (Jun. 1992).

Thampi R.S. & Dave H. Spectroscopic study of submillimeter lines from dark, quiescent clouds. In *36th COSPAR Scientific Assembly*, vol. 36 of *COSPAR, Plenary Meeting*, pp. 914–+ (2006).

Tideswell D.M., Fuller G.A., Millar T.J., & Markwick A.J. The abundance of HNCO and its use as a diagnostic of environment. *A&A*, vol. 510:A85+ (Feb. 2010).

Tielens A.G.G.M. *The Physics and Chemistry of the Interstellar Medium* (Sep. 2005).

van der Tak F.F.S. Hot Molecular Cores and High Mass Star Formation. In M. G. Burton, R. Jayawardhana, & T. L. Bourke, editor, *Star Formation at High Angular Resolution*, vol. 221 of *IAU Symposium*, pp. 59–+ (Sep. 2004).

Viti S., Caselli P., Hartquist T.W., & Williams D.A. Chemical signatures of shocks in hot cores. *A&A*, vol. 370:1017–1025 (May 2001).

Viti S. & Williams D.A. Time-dependent evaporation of icy mantles in hot cores. *MNRAS*, vol. 305:755–762 (May 1999).

Wakelam V., Caselli P., Ceccarelli C., Herbst E., & Castets A. Resetting chemical clocks of hot cores based on S-bearing molecules. *A&A*, vol. 422:159–169 (Jul. 2004).

Wakelam V., Herbst E., & Selsis F. The effect of uncertainties on chemical models of dark clouds. *A&A*, vol. 451:551–562 (May 2006).

Wang M., Chin Y., Henkel C., Whiteoak J.B., & Cunningham M. Abundances and Isotope Ratios in the Magellanic Clouds: The Star-Forming Environment of N 113. *ApJ*, vol. 690:580–597 (Jan. 2009a).

Wang M., Chin Y., Henkel C., Whiteoak J.B., & Cunningham M. Abundances and Isotope Ratios in the Magellanic Clouds: The Star-Forming Environment of N 113. *ApJ*, vol. 690:580–597 (Jan. 2009b).

Wang M., Henkel C., Chin Y., Whiteoak J.B., Hunt Cunningham M., Mauersberger R., & Muders D. Dense gas in nearby galaxies. XVI. The nuclear starburst environment in NGC 4945. *A&A*, vol. 422:883–905 (Aug. 2004).

Watt G.D. Time-dependent chemistry. II - Dependence of the chemistry on the initial C/O abundance ratio. *MNRAS*, vol. 212:93–103 (Jan. 1985).

Wiebe D., Semenov D., & Henning T. Reduction of chemical networks. I. The case of molecular clouds. *A&A*, vol. 399:197–210 (Feb. 2003).

Williams D.A. & Hartquist T.W. On C(o) and CO in dense interstellar clouds - Evidence that cloud material is frequently shocked. *MNRAS*, vol. 210:141–145 (Sep. 1984).

Woodall J., Agúndez M., Markwick-Kemper A.J., & Millar T.J. The UMIST database for astrochemistry 2006. *A&A*, vol. 466:1197–1204 (May 2007).

Young J.S., Goldsmith P.F., Langer W.D., Wilson R.W., & Carlson E.R. Physical conditions and carbon monoxide abundance in the dark cloud B5. *ApJ*, vol. 261:513–531 (Oct. 1982).